

# **Spin Labeling of and EPR Spectroscopic Studies on functional Oligonucleotides**

Dissertation

zur Erlangung des Doktorgrades (Dr. rer. nat.)  
der Mathematisch-Naturwissenschaftlichen Fakultät  
der Rheinischen Friedrich-Wilhelms-Universität Bonn

vorgelegt von  
**Christine Wübben**  
aus Euskirchen

Bonn, 2021



Angefertigt mit Genehmigung der Mathematisch-Naturwissenschaftlichen Fakultät der Rheinischen Friedrich-Wilhelms-Universität Bonn.

1. Gutachter: Prof. Dr. Olav Schiemann

2. Gutachterin: Prof. Dr. Stephanie Kath-Schorr

Tag der Promotion: 23.04.2021












Erscheinungsjahr: 2021



Die vorliegende Arbeit wurde am *Institut für physikalische und theoretische Chemie* der *Rheinischen Friedrich-Wilhelms-Universität Bonn* in der Zeit von November 2016 bis Februar 2021 unter der Leitung von *Prof. Dr. Olav Schieman*n angefertigt.



Parts of this thesis have been published in:

-  C. Wuebben, M. F. Vicino, M. Mueller, O. Schiemann, *Nucleic Acids Research* **2020**  
48, 10518-10526.
-  H. Rosenbach, J. Borggräfe, J. Victor, C. Wuebben, O. Schiemann, W. Hoyer, G. Steger, M. Etzkorn, I. Span, *Biological Chemistry* **2020**, 402, 99-111.
-  C. Wuebben, S. Blume, D. Abdullin, D. Brajtenbach, F. Haege, S. Kath-Schorr, O. Schiemann, *Molecules* **2019**, 24, 1-13.
-  S. Blume, *Bachelor Thesis*, Rheinische Friedrich-Wilhelms-Universität Bonn, **2019**.
-  F. Schmidt, *Bachelor Thesis*, Rheinische Friedrich-Wilhelms-Universität Bonn, **2019**.
-  F. Haege, *Master Thesis*, Rheinische Friedrich-Wilhelms-Universität Bonn, **2019**.
-  M. Wittig, *Bachelor Thesis*, Rheinische Friedrich-Wilhelms-Universität Bonn, **2019**.
-  M. Stockmeier, *Bachelor Thesis*, Rheinische Friedrich-Wilhelms-Universität Bonn,  
**2019**.
-  M. F. Vicino, *Master Thesis*, Rheinische Friedrich-Wilhelms-Universität Bonn, **2018**.
-  M. Mueller, *Bachelor Thesis*, Rheinische Friedrich-Wilhelms-Universität Bonn, **2018**.
-  D. Brajtenbach, *Bachelor Thesis*, Rheinische Friedrich-Wilhelms-Universität Bonn,  
**2017**.





## Abstract

Within the last three decades, the central dogma of molecular biology has been extended in the sense that RNA is not only the molecule from which the genetic information is translated into proteins but is involved in many functions in cells. In order to gain an understanding of the function of the various RNAs on a molecular level, methods are required for studying their structures, since structure and function are inextricably interwoven. One of these methods is electron paramagnetic resonance (EPR) spectroscopy, which is employed here as the main tool because it has no size restriction and the RNA can be studied in solution. The work reported in this thesis had three major aims: (1) To establish a “click”-chemistry based site-directed spin labeling strategy for RNA with a new *gem*-diethyl nitroxide spin label and to characterize its EPR properties. The idea being that such a *gem*-diethyl nitroxide label would be suited for *in cell* measurements on RNA. (2) To use this labeling strategy in combination with Q-band Pulsed Electron-Electron Double Resonance (PELDOR or DEER) spectroscopy to experimentally test the proposed switching mechanism of the Guanidine-II riboswitch. (3) To quantify the number and affinity of Mn<sup>2+</sup> ion binding sites in the 10-23 DNAzyme using continuous wave (cw) X-band EPR spectroscopy.

The labeling strategy was successfully implemented and EPR measurements revealed that this spin label on RNA has a surprisingly long relaxation time  $T_M$ . Additionally, the PELDOR measurements on the truncated hairpins **P1** and **P2** of the Guanidine-II riboswitch were successful, proving that **P1** and **P2** do indeed form the proposed kissing hairpin **P1 | P2**. However, for the full-length riboswitch mainly intermolecular interactions were resolved making the identification of the anticipated intrastrand **P1 | P2** interaction impossible. Finally, a reproducible protocol for the quantification of Mn<sup>2+</sup> ion binding sites was established in the lab and was successfully applied to different forms of the 10-23 DNAzyme, supporting the structural/catalytic importance of these ions for this DNAzyme. Thus, the presented work contributes to a deeper understanding of oligonucleotide structure and function.



## Danksagung

Obwohl mein Name alleine auf dieser Arbeit steht, kann ich nicht behaupten, dass ich als Einzelkämpfer durch diese Zeit gegangen bin. Deshalb möchte mich an dieser Stelle bei einigen Leuten bedanken, die mich während dieser Zeit unterstützt haben.

Zunächst möchte ich mich an dieser Stelle bei Prof. Dr. Olav Schiemann dafür bedanken, dass ich meine Promotion in seinem Arbeitskreis anfertigen durfte. Ich kann unbestritten sagen, dass ich viel gelernt habe, und diese Möglichkeit und die geschöpfte Erfahrung weiß ich sehr zu schätzen.

Prof. Dr. Stephanie Kath-Schorr danke ich dafür, dass sie ein Vorbild für jede junge Wissenschaftlerin ist. Ich konnte mich stets auf ihre persönliche und fachliche Unterstützung verlassen, und natürlich danke ich ihr für die Übernahme der Zweitkorrektur.

Prof. Dr. Dirk Menche danke ich für sein fortwährendes Interesse an meiner Forschung und seiner Unterstützung im Rahmen des Mentorentreffens der BIGS-Chemistry. Zudem möchte ich mich bei Ihm und bei Prof. Dr. Ulrike Thoma für die Teilnahme an der Prüfungskommission bedanken.

Wenn aus Arbeitskollegen Freunde werden, weiß man, dass man eine wirklich gute Zeit hatte. Für diese schöne Zeit und die Unterstützung, danke ich denen die sich angesprochen fühlen, und besonders hervorheben möchte ich: Tobias Hett, der mir beigebracht hat, wie ich eigenständig EPR Messungen durchführe, sowie immer ein offenes Ohr für mich hatte, aber auch Jonas Brode, Dr. Andreas Meyer, Nico Fleck, Martin F. Peter, Jean Jacques Jassoy, Maria F. Vicino und Janin Glänzer. Zudem danke ich für ihre stetige Hilfe: PD Dr. Gregor Hagelüken, Nicole Florin, Gabriele Alonso Rodrigues, Dr. Dinar Abdullin, Hamed Alaei und Rolf Paulig.

Während meiner Zeit hatte ich die Freude, mit vielen Studierenden in Rahmen ihrer Abschlussarbeiten zusammenarbeiten zu dürfen. Für ihr Mitwirken an meiner Doktorarbeit möchte ich mich bedanken: Maria F. Vicino, Marcel Müller, Sam Thilmany, Felix Schmidt, Simon Blume, Florian Haege, Moritz Wittig, Max Stockmeier und Dominik Brajtenbach.

Zudem durfte ich mehrere Kooperationen führen, die alle in Publikationen geendet haben. Für den wissenschaftlichen Austausch danke ich an dieser Stelle Prof. Dr. Stephanie Kath-Schorr und ihrem Arbeitskreis, vor allem Dr. Frank Eggert, Dr. Christof Domnick, Lisa Bornewasser und Hannah Depmeier. Zudem Jun.-Prof. Dr. Ingrid Span, Dr. Manuel Etzkorn, sowie Dr. Hannah Rosenbach und Dr. Julian Victor, als auch Prof. Dr. Michael Famulok und Dr. Mark Kerzhner.

Ich möchte mich ebenso bei den Mitarbeiterinnen und Mitarbeitern der zentralen Einrichtungen der chemischen Institute bedanken. Allen voran Dr. Senada Nozinovic, für die Einführung in NMR Messungen und ihr Vertrauen, mich diese eigenständig durchführen zu lassen. Mein Dank gilt auch PD Dr. Marianne Engeser und der Abteilung für Massenspektrometrie für die Durchführung der Messungen am Guanidine-II Riboswitch.

Zudem danke ich der BIGS Chemistry für die Aufnahme in der Graduiertenschule, und Prof. Dr. Andreas Gansäuer für seine aufmunternden Worte.

Außerdem bedanke ich mich an dieser Stelle bei der GDCh und der DFG für die Förderung zum Besuch diverser Konferenzen, sowie der Universität Bonn für die Vergabe der Stipendien.

Abschließend danke ich den wichtigsten Menschen in meinem Leben dafür, dass sie immer für mich da sind und ich weiß, dass das nicht nur eine Floskel ist: meinem langjährigen Freund Sven Ullrich, meinen Schwestern Katharina und Anika Wübben, meiner Mama Jutka Ürmenyi Pinter und ihrem Freund Volker Bolg, meinem Papa Dr. Peter Wübben und Dr. Stefanie Alexandra Meißner.

# Table of content

<b>1. Introduction</b>	<b>1</b>
<b>1.1 Nucleic acids</b>	<b>1</b>
<b>1.2 Riboswitches</b>	<b>2</b>
1.2.1 Transcription control	3
1.2.2 Translation control	3
1.2.3 The first riboswitches	4
1.2.4 Overview of riboswitch classes	5
<b>1.3 The Guanidine-I riboswitch   The ykkC motif</b>	<b>7</b>
1.3.1 Challenges of ligand identification	7
<b>1.4 The Guanidine-II riboswitch   The mini-ykkC motif</b>	<b>8</b>
<b>1.5 Catalytically active RNA and DNA</b>	<b>11</b>
<b>1.6 Structure and dynamic investigation of nucleic acids</b>	<b>12</b>
<b>1.7 EPR spectroscopy</b>	<b>16</b>
1.7.1 Theoretical background	16
1.7.1.1 Dipolar electron spin electron spin interaction	22
1.7.1.2 The spin Hamiltonian concept	23
1.7.2 Pulsed EPR	23
1.7.2.1 The Hahn echo experiment	24
1.7.2.2 Relaxation	24
1.7.2.3 The pulsed electron-electron double resonance experiment	26
<b>1.8 Site directed spin labeling</b>	<b>28</b>
1.8.1 3' and 5' spin labeling	28
1.8.2 Phosphate spin labeling	29
1.8.3 Ribose spin labeling	30
1.8.4 Nucleobase spin labeling	30
1.8.5 Non-covalent spin label	33
1.8.6 Spin labeling of long RNA strands	34
1.8.7 Trityl spin labeling	36
1.8.8 Gd <sup>3+</sup> and Cu <sup>2+</sup> spin labeling	37
<b>2. Aim of the Study</b>	<b>40</b>
<b>3. Results and Discussion</b>	<b>41</b>

<b>3.1</b>	<b>Spin labeling of RNA with a <i>gem</i>-diethyl nitroxide via Click-chemistry</b>	<b>41</b>
3.1.1	The spin labeling reaction	41
3.1.2	Test for structural perturbation	43
3.1.3	EPR characteristics	44
3.1.3.1	Temperature-dependent 2PESEEM measurements	44
3.1.3.2	Solvent-dependent 2PESEEM measurements	46
3.1.3.3	Magnetic field-dependent 2PESEEM measurements	48
3.1.3.4	Inversion recovery measurement	49
3.1.4	PELDOR measurements	50
3.1.5	Conversion of distance and angular distributions into label conformers	53
3.1.6	Implication of the long phase memory time	55
3.1.7	Investigation of the spin label stability	55
3.1.8	Analysis of <i>in cell</i> measurements	56
<b>3.2</b>	<b>The Guanidine-II Riboswitch</b>	<b>57</b>
3.2.1	Analysis of the truncated hairpin P2U14	57
3.2.1.1	Spin labeling	57
3.2.1.2	PELDOR measurements	59
3.2.1.3	EPR analysis of fast versus slow annealed P2U14	61
3.2.1.4	Other methods to investigate fast versus slow annealed P2	63
3.2.2	Analysis of the truncated hairpin P1U18	67
3.2.2.1	Spin labeling	67
3.2.2.2	PELDOR measurements	69
3.2.2.3	<sup>1</sup> H-NMR measurements	71
3.2.3	Analysis of the hetero hairpin mixture P1U18   P2U14	72
3.2.3.1	PELDOR measurements	72
3.2.4	Analysis of the truncated hairpin P1U20	73
3.2.4.1	Spin labeling	74
3.2.4.2	PELDOR measurements	74
3.2.5	Analysis of the hetero hairpin mixture P1U20   P2U14	75
3.2.5.1	PELDOR measurements	75
3.2.6	Analysis of the singly labeled full-length riboswitch	78
3.2.6.1	Spin labeling	79
3.2.6.2	Test for structural perturbation	81
3.2.6.3	PELDOR measurements	83
3.2.7	Analysis of the doubly labeled full-length riboswitch	86
3.2.7.1	Spin labeling	86
3.2.7.2	Test for structural perturbation	87

3.2.7.3	PELDOR measurements	88
3.2.7.4	Analysis of the linker length	92
3.2.7.5	Analysis of the kissing hairpin length	94
3.2.8	Analysis of the doubly labeled full-length riboswitch with additional SDS	97
3.2.8.1	Spin labeling reaction	97
3.2.8.2	PELDOR measurements	98
<b>3.3</b>	<b>Mn<sup>2+</sup> binding study</b>	<b>100</b>
3.3.1	Protocol for the cwEPR Mn <sup>2+</sup> -titration	101
3.3.2	Data analysis and measurements conducted on the 10-23 DNAzyme	102
<b>4.</b>	<b>Conclusion and Outlook</b>	<b>107</b>
<b>4.1</b>	<b>Spin labeling of RNA with a <i>gem</i>-diethyl nitroxide via Click-chemistry</b>	<b>107</b>
<b>4.2</b>	<b>The Guanidine-II Riboswitch</b>	<b>107</b>
<b>4.3</b>	<b>Mn<sup>2+</sup> binding study</b>	<b>109</b>
<b>5.</b>	<b>Material and Methods</b>	<b>110</b>
<b>5.1</b>	<b>RNA sequences</b>	<b>110</b>
<b>5.2</b>	<b>Extinction coefficients</b>	<b>111</b>
5.2.1	Extinction coefficients of the RNA constructs	111
5.2.2	Extinction coefficient of spin label 1*	111
<b>5.3</b>	<b>Concentration determination</b>	<b>112</b>
<b>5.4</b>	<b>Spin labeling</b>	<b>112</b>
<b>5.5</b>	<b>HPLC purifications</b>	<b>113</b>
<b>5.6</b>	<b>Annealing</b>	<b>114</b>
5.6.1	The model RNA	114
5.6.2	Fast Annealing	114
5.6.3	Slow Annealing	114
<b>5.7</b>	<b>Buffers</b>	<b>114</b>
<b>5.8</b>	<b>Rebuffering</b>	<b>115</b>
<b>5.9</b>	<b>LCMS measurements</b>	<b>115</b>
<b>5.10</b>	<b>Gdm<sup>+</sup> concentrations</b>	<b>115</b>
<b>5.11</b>	<b>UV-VIS melting curves</b>	<b>116</b>

5.11.1	Sample preparation	116
5.11.2	Measurement	116
5.11.3	Data analysis	117
<b>5.12</b>	<b>CD spectroscopy</b>	<b>117</b>
5.12.1	Sample preparation	117
5.12.2	Measurement	117
<b>5.13</b>	<b>Native PAGEs</b>	<b>118</b>
<b>5.14</b>	<b>cwEPR spectroscopy</b>	<b>119</b>
5.14.1	Sample preparation	119
5.14.2	Measurement	120
<b>5.15</b>	<b>Pulsed EPR spectroscopy</b>	<b>122</b>
5.15.1	Sample preparation	122
5.15.2	Measurement	123
5.15.3	Analysis	124
<b>5.16</b>	<b>NMR measurements</b>	<b>127</b>
5.16.1	Sample preparation	127
5.16.2	Measurement	127
<b>6.</b>	<b>Appendix</b>	<b>128</b>
<b>6.1</b>	<b>Riboswitch ligands</b>	<b>128</b>
<b>6.2</b>	<b>HPLC spectra</b>	<b>129</b>
<b>6.3</b>	<b>Spin labeling yields</b>	<b>130</b>
<b>6.4</b>	<b>LCMS spectra</b>	<b>131</b>
<b>6.5</b>	<b>Native PAGEs</b>	<b>132</b>
<b>6.6</b>	<b>cwEPR spectra</b>	<b>133</b>
6.6.1	Spin label 1*	133
6.6.2	The Guanidine-II Riboswitch	134
<b>6.7</b>	<b>PeldorFit data</b>	<b>136</b>
6.7.1	Summary of the PeldorFit results	136
6.7.2	PeldorFit configuration files	138
<b>6.8</b>	<b>PELDOR data</b>	<b>147</b>
6.8.1	Offset measurements	147



6.8.2	Summed data	151
6.8.3	Validation	158
6.8.4	In silico models and distances	161
<b>6.9</b>	<b>Data of the linker and hairpin length analysis</b>	<b>163</b>
<b>6.10</b>	<b>List of abbreviations</b>	<b>167</b>
<b>6.11</b>	<b>List of figures</b>	<b>169</b>
<b>6.12</b>	<b>List of tables</b>	<b>185</b>
<b>7.</b>	<b><i>References</i></b>	<b>187</b>



# 1. Introduction

When in March 2020 a disease related to a novel corona virus was declared a global pandemic, the whole world health was threatened.<sup>1</sup> Researchers all over the world worked ever since under pressure to develop a vaccine.<sup>2</sup> In this context, a biomolecule started to raise hope: the mRNA. It is known that cells consist of approximately 70% water and 30% biomolecules and other chemical ingredients (Figure 1). The composition of these non-water molecules is dominated by macromolecules such as proteins and RNA.<sup>3</sup> Since 1958, when Francis H. C. Crick described the *central dogma*, proteins have been considered as the only biomolecules involved in cellular function.<sup>4,5</sup> Deoxyribonucleic acid (DNA) stores the genetic information and is transcribed to messenger ribonucleic acid (mRNA), which is then translated into proteins.<sup>3</sup> This central dogma deems RNA to be a simple messenger.<sup>4,5</sup> Its inaccuracy is shown in the following.

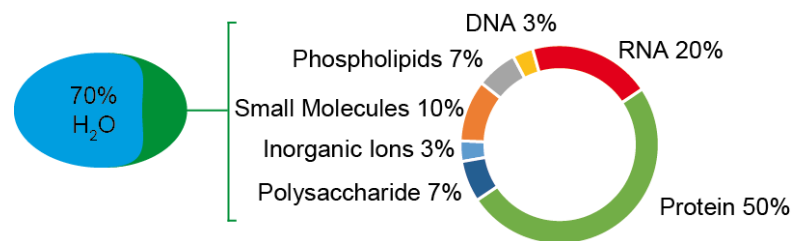


Figure 1. Ingredients of a cell (adapted from reference 3).

## 1.1 Nucleic acids

Nucleic acids i.e., DNA and RNA, are linear polymers made up of nucleotides (nt), which consist of three parts: a phosphate, a sugar and a base (Figure 2A).<sup>3</sup> The canonical bases can be divided in purine bases (adenine and guanine, Figure 2B) and pyrimidine bases (cytosine, thymine and uracil, Figure 2C). Structurally, RNA and DNA differ in two main points: whereas RNA carries a sugar called ribose, DNA is made of deoxyribose (Figure 2A). They share the bases adenine, guanine and cytosine, but RNA contains uracil and DNA instead thymine.<sup>3</sup> Both nucleic acids are able to form three-dimensional structures mainly through Watson-Crick base pairing (adenine with uracil or thymine, guanine with cytosine), Wobble base pairing (commonly guanine with uracil),  $\pi$ -stacking and hydrogen bonds.<sup>6</sup> Whereas DNA dominantly builds stable double-stranded helices to store the genetic information,<sup>3,6</sup> RNA is able to form different tertiary structures,<sup>6,7</sup> which enables the RNA to work as functional biomolecules.<sup>3,6,7</sup> These various functional forms of RNA include e.g., messenger RNA (mRNA), transfer RNA (tRNA), ribosomal

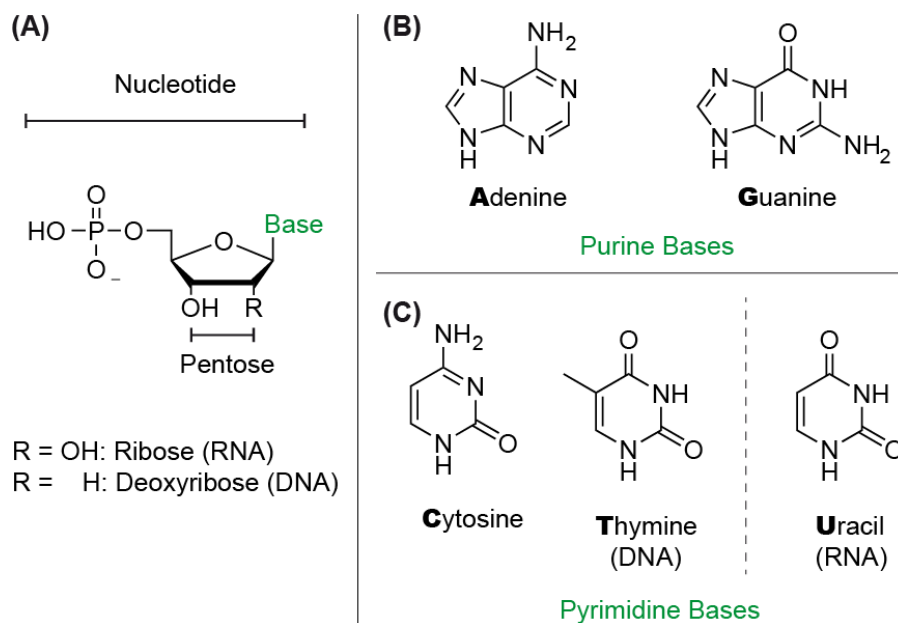


Figure 2. (A) Chemical structure of a nucleotide composed of a phosphate group, a base and the pentose sugar, which is either ribose in the case of RNA or deoxyribose in DNA. (B) Chemical structure of the purine and (C) pyrimidine bases.

RNA (rRNA), micro RNA (miRNA), piwi-interacting RNA (piRNA), short interfering RNA (siRNA), small nuclear RNA (snRNA), small nucleolar RNA (snoRNA), and long noncoding RNA (lncRNA).<sup>8</sup> In the following riboswitches and catalytically active RNAs and DNAs are described in more detail, because these are in the focus of the experimental work of this thesis.

## 1.2 Riboswitches

In the 5' untranslated region of the mRNA, gene regulatory elements, the so-called riboswitches are located, which are found in all three domains of life i.e., bacteria, archaea, and eukaryotes. Their general structure consists of two parts that must partially overlap, an aptamer domain and an expression platform. The aptamer region is a highly conserved section that forms a three-dimensional structure specifically for ligand recognition, whereas the downstream expression platform varies in sequence, structure and mechanism of action. Ligand binding at the aptamer domain alters its structure and induces an interaction with the adjoining expression platform that regulates the subsequent gene expression. The ligand is generally related to the downstream gene. Thus, the genes can be used to predict the ligand, in case it is unknown. Different mechanisms have been validated experimentally or predicted to regulate the gene

expression (Figure 3). The most common ones are translation and transcription control in the way of ON and OFF switches.<sup>9–18</sup>

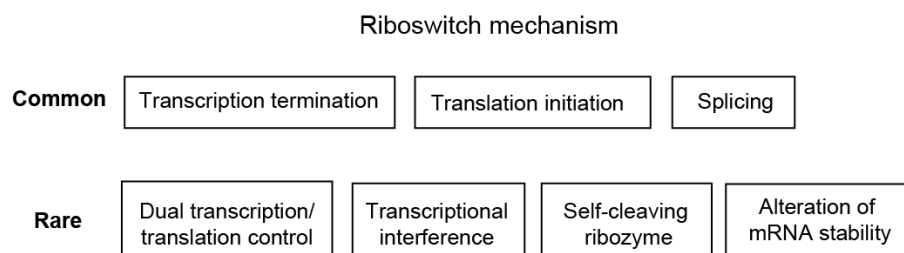


Figure 3. Overview of the riboswitch mechanisms ordered in “common” and “rare” in context of their natural abundance.

### 1.2.1 Transcription control

In the case of transcription control, the expression platform contains an approximately 8 nt long GC-rich sequence that forms a stable hairpin, called terminator (Figure 4A, marked in orange).<sup>19</sup> The terminator causes the RNA polymerase to pause. A poly-uracil region following the terminator stem destabilizes the duplex of DNA and newly transcribed RNA. This causes the RNA polymerase to detach and thus to terminate the transcription.<sup>10,13,15</sup> Such a riboswitch is referred to as transcriptional OFF switch. An riboswitch working opposite is called transcriptional ON switch and is shown in Figure 4A. In this case, ligand binding in the riboswitch aptamer domain induces a destabilization of the terminator stem that enables the RNA polymerase to associate and transcription can proceed.<sup>15</sup>

### 1.2.2 Translation control

In the case of translation control, the riboswitch mechanism involves the Shine-Dalgarno Sequence (SDS),<sup>20</sup> a short purine-rich sequence that base pairs to the pyrimidine rich sequence near the 3' end of the 16S ribosomal RNA (Figure 4B).<sup>21</sup> The SDS is located approximately 7 nt upstream of the AUG initiation codon. Through base pairing with the ribosome, the SDS helps to recruit the ribosome for translation initiation.<sup>21,22</sup> Ligand binding to the aptamer domain in close vicinity to the SDS exposes or sequesters the SDS and/or the start codon. If the SDS is accessible upon ligand binding, the ribosome

binds and translation is initiated (ON switch) or, in the case of an OFF switch, ligand binding causes sequestration of the previously accessible SDS (Figure 4B).<sup>10,14,15</sup>

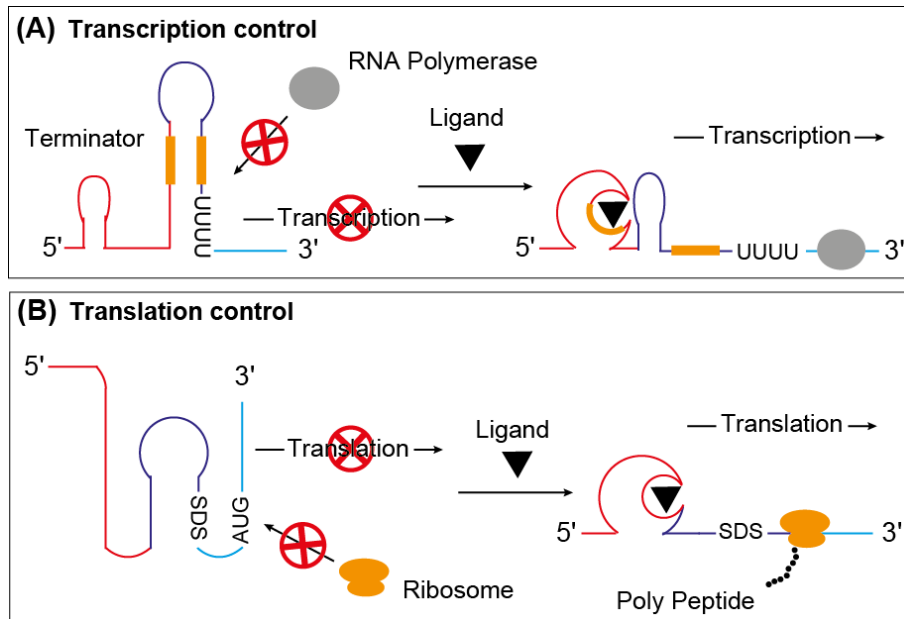


Figure 4. (A) Transcriptional control of a riboswitch. “UUUU” denotes the poly-uracil region. The grey dot represents the RNA polymerase. The orange boxes represent the stable stem of the terminator hairpin. (B) Translational control of a riboswitch. “SDS” denotes the Shine-Dalgarno Sequence and “AUG” the start codon where the ribosome binds. The orange body represents the ribosome that, in case it can bind, expresses polypeptides visualized as black dots.

### 1.2.3 The first riboswitches

The first experimental proof of riboswitches was reported in 2002.<sup>20,23–25</sup> Until that year, cellular metabolites were typically thought to be sensed by regulatory proteins. These proteins were expected to measure the level of a metabolic product and then bind to DNA or RNA to affect the expression of the relevant enzymes.<sup>15</sup> In that regard, extensive effort was made to examine and identify the relevant regulatory element encoding the vitamins B1 (thiamine), B2 (riboflavin) and B12 (cobalamin) genes.<sup>15,26–30</sup> Since no regulatory proteins could be identified within those studies, the aforementioned regulatory role was attributed to specific mRNA regions.<sup>15,30</sup> Later, it was demonstrated that the gene level control of vitamin B1, B2 and B12 is managed by their respective mRNAs, in cases when the mRNA interacts with the three vitamin-derived substances thiamine pyrophosphate (TPP),<sup>23,25</sup> flavin mononucleotide (FMN)<sup>20,23</sup> and adenosylcobalamin (AdoCbl).<sup>24</sup>

### 1.2.4 Overview of riboswitch classes

Today, nearly 40 different classes of riboswitches are known. They are classified in four main groups, according to their ligand type i.e., RNA derivatives, amino acids, ions and “others” (Figure 5, abbreviations are found in the appendix).<sup>10,12,14,16,17,31</sup>

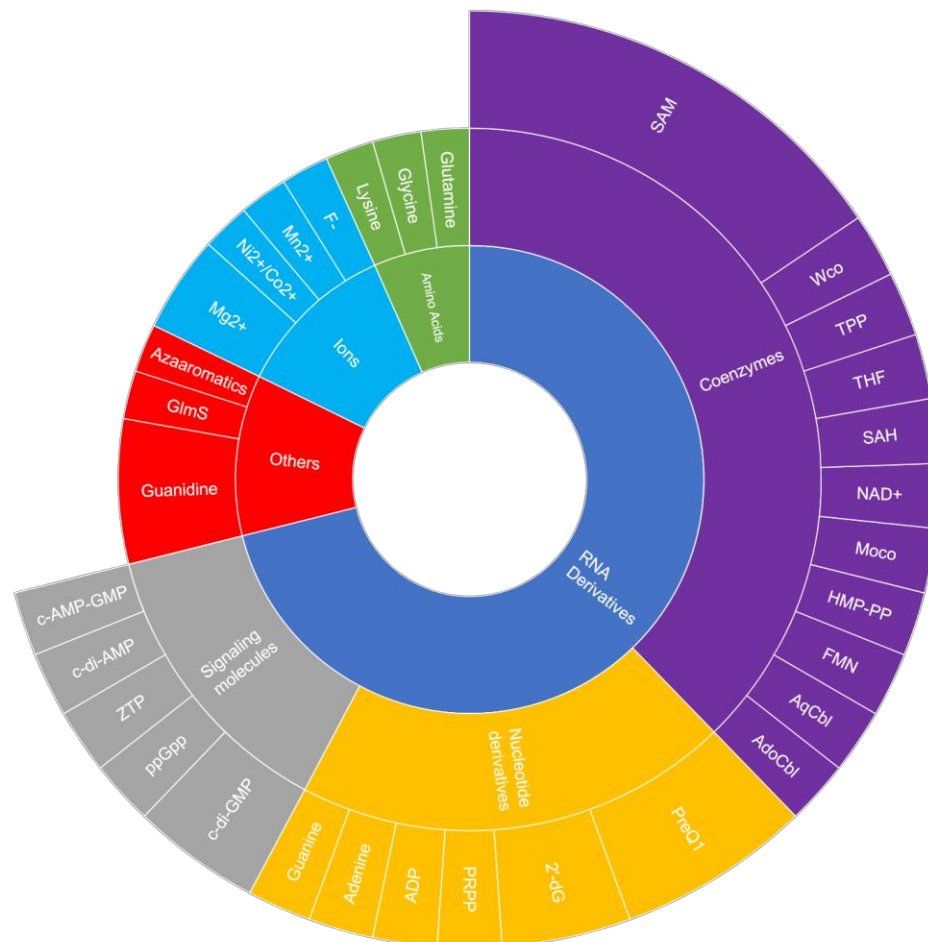


Figure 5. Overview of the riboswitch ligands (adapted from reference 12, 17, and 31, abbreviations are found in the appendix).

The largest number of riboswitches sense ligands derived from RNA nucleotides or their precursors, like nucleotide-like coenzymes, nucleotide derivatives and signaling molecules. It can be pointed out that long time, there was only one riboswitch known occurring in eukaryotes, the TPP riboswitch.<sup>25,32,33</sup> It regulates genes via alternative splicing, wherein TPP binding alters the accessibility of the splicing site of the intron.<sup>34–</sup>

36

Besides the small metabolite molecules derived from RNA biosynthesis, another group of riboswitches senses ions. Three different riboswitch classes respond to cations ( $Mg^{2+}$ ,

Mn<sup>2+</sup>, Ni<sup>2+</sup>, Co<sup>2+</sup>) and another one to the fluoride anion (F<sup>-</sup>).<sup>10,12,14,16</sup> The divalent cations demonstrate two aspects: on the one hand, it implies the importance of metal ions in living organisms as specific gene regulation is activated by their occurrence. On the other hand, it demonstrates the highly specific recognition capability of riboswitches, especially in the context to select a specific divalent metal ion as they are similar in charge and nearly in size. The binding pockets are usually made of highly conserved nucleotides and their selectivity relies on the same recognition strategy: The negative charge of the RNA phosphate backbone is compensated by the metal ion binding, the specificity is based on hydrogen bonding and electrostatic interactions between the metal ion and the RNA.<sup>15</sup> Remarkable is the selective binding pocket for F<sup>-</sup>: The RNA strand carries negatively charged phosphate groups at every nucleotide, but is still able to form a highly selective binding pocket for this anion. The clue is that the F<sup>-</sup> is encapsulated by three Mg<sup>2+</sup>, which are in turn coordinated by the non-bridging oxygens of five phosphate groups (Figure 6).<sup>12,17,37</sup>

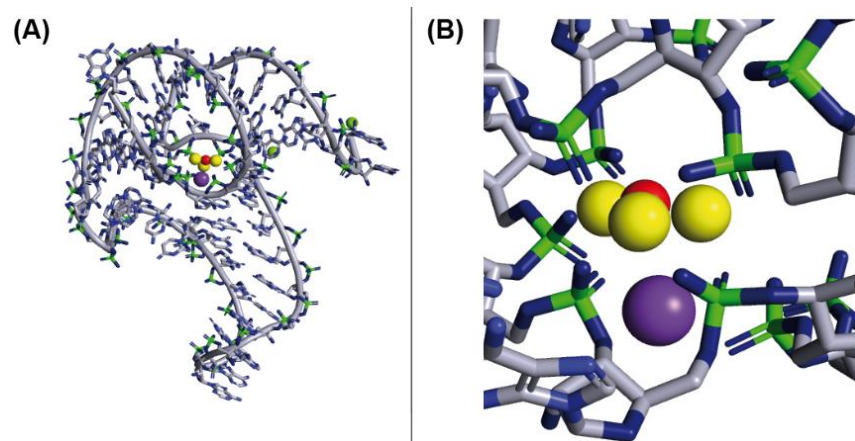


Figure 6. (A) Crystal structure of the F<sup>-</sup> riboswitch with (B) a Zoom-in to the F<sup>-</sup> binding pocket (PDB ID: 4ENC).<sup>37</sup> The F<sup>-</sup> anion (red) is coordinated by three Mg<sup>2+</sup> cations (yellow), which are in turn coordinated by the non-bridging oxygens (blue) of five phosphates (green). In purple an additional K<sup>+</sup> ion is shown.<sup>37</sup>

Another main group of riboswitches responds to amino acids. Until now, only three out of twenty common amino acids are known to be sensed by riboswitches, namely lysine, glycine and glutamine. This permits the assumption that further riboswitches exist, but are still undiscovered.<sup>17</sup>

Only three groups of ligands, which are non-RNA derived metabolites are known. The riboswitches that select ions and amino acids have been presented before. The remaining group is titled “others”. One class of these riboswitches responds to a diverse



collection of multi-ring molecules that can be termed “azaaromatic”. The regulated genes have so far an unknown function.<sup>17</sup> The second class detects the modified sugar compound glucosamine-6-phosphate (GlcN6P). Its selective binding regulates the expression of the *glms* gene. The *glms* riboswitch induces RNA strand scission and causes the associated mRNA to rapidly degrade, thus repressing gene expression.<sup>38,39</sup> Until now, this is the only known metabolite-sensing ribozyme.<sup>12,17</sup> The remaining non-RNA derived ligand is Guanidinium ( $\text{Gdm}^+$ ).<sup>11,12,16,17</sup>

### 1.3 The Guanidine-I riboswitch | The ykkC motif

In 2004, the Breaker lab firstly discovered the ykkC/yxkD element, as a potential riboswitch candidate.<sup>39</sup> It was later called ykkC-I motif or rather Guanidine-I riboswitch.<sup>39,40</sup> This RNA element named after the initial gene of the downstreaming operon in *Bacillus subtilis* was proposed to control genes involved in efflux pumps and detoxification systems, which respond to harmful environmental molecules. While the number of organisms and genes controlled by these riboswitch grew,<sup>41</sup> the ligand was far from being determined.<sup>42</sup> Computational studies identified two further structurally distinct motifs regulating a similar set of genes, which indicated that they bind the same ligand. Accordingly, these elements were named mini-ykkC and ykkC-III.<sup>43,44</sup> While the previously discovered ykkC-I element was expected to be a transcriptional regulator, the latter ones appeared to act as translational controllers. However, the structures of the orphan class seem unrelated.<sup>45</sup>

#### 1.3.1 Challenges of ligand identification

In 2017, the relation between ligand and ykkC-I was finally established.<sup>40</sup> To do so, the aptamer and expression platform of the ykkC-I riboswitch were fused upstream to a  $\beta$ -galactosidase (*lacZ*) reporter gene. Thus, the ON-switched riboswitch induced the expression of *lacZ*. Out of the nearly 2000 conditions tested, only the addition of  $\text{Gdm}^+$  triggered the reporter gene expression. With this finding, the ligand was finally identified.<sup>40</sup> Based on this knowledge, further experiments were conducted on the mini-ykkC and ykkC-III motifs. The biochemical experiments revealed  $\text{Gdm}^+$  as ligand for them, too.<sup>46,47</sup>

## 1.4 The Guanidine-II riboswitch | The mini-ykkC motif

The mini-ykkC motif is predominantly found in bacteria, but also occurs in eukaryotes and archaea (Figure 7). It was firstly discovered in 2007 as one of 22 novel structured RNA motifs disclosed by a computational pipeline.<sup>43</sup> It was named mini-ykkC, because it controls a similar set of genes as ykkC-I and has a simple structure compared to other riboswitches.<sup>43</sup> The proteins expressed after gene controlling are mainly focused on inorganic ion transport and metabolism. Bioinformatic analysis affirmed that operons controlled transcriptionally by ykkC-I were found to contain mini-ykkC, too, that controls the translational set of genes. Controlling on both levels enables tight gene regulation.<sup>46,48</sup> Ten years after its bioinformatical discovery, biochemical experiments revealed that  $\text{Gdm}^+$  is the ligand for the mini-ykkC motif, and it has been referred to as the Guanidine-II riboswitch from that time on.<sup>46</sup>

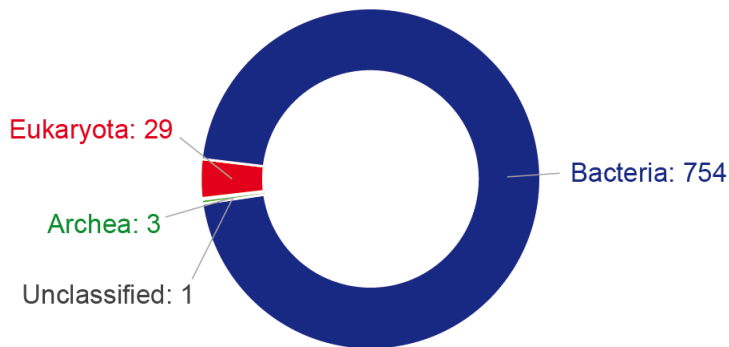


Figure 7. Abundance of the Guanidine-II riboswitch in different organisms.

The structure of the Guanidine-II riboswitch consists of two short hairpins separated by a linker of variable length and sequence of 7-40 nt (Figure 8A).<sup>43,45,46</sup> Each hairpin **P1** and **P2** (marked in yellow and blue in Figure 8A, respectively) is capped by a conserved ACGR tetra loop (R = A or G). Underneath are two conserved G-C base pairs, which are part of the stem.<sup>43,45</sup> Crystal structures of the truncated hairpins show that dimerization of the hairpins occurs, wherein the two hairpins are rotated by 180° against each other (Figure 8B).<sup>48,49</sup> Interaction strictly occurs through the conserved tetra loops and the two G-C base pairs below (Figure 8C-F). In the tetra loops, a binding pocket is created so that each is able to bind one  $\text{Gdm}^+$  (Figure 8B).<sup>48,49</sup> Interestingly, the  $\text{Gdm}^+$  recognition strategy is conserved throughout all Guanidine riboswitches (ykkC-I, mini-ykkC and ykkC-III), but the arrangement of the residues is highly individual.<sup>45</sup> The triangular shape of  $\text{Gdm}^+$  is able to donate six hydrogen bonds in total, two on each amino group. In the Guanidine-II riboswitch,  $\text{Gdm}^+$  donates two hydrogen bonds from one amino group to the Hoogsten face of G5 in the tetra loop (Figure 8C). Additionally, two edges donate three

hydrogen bonds to non-bridging phosphate oxygen atoms (Figure 8C). The negatively charged phosphate groups stabilize  $\text{Gdm}^+$  through ionic effects and select, among others,  $\text{Gdm}^+$  over urea. The sixth potential hydrogen bond is exposed to the solvent.<sup>45,48,49</sup> Thus, the Guanidine-II riboswitch is able to bind  $\text{Gdm}^+$  derivatives such as methyl- and aminoguanidine or diguanidine species linked by a C-chain, as they can stack out of the binding pocket.<sup>49,50</sup> Furthermore,  $\text{Gdm}^+$  is sandwiched between the G2 below the tetra loop and the C4 in the tetra loop (Figure 8C). Through this cation- $\pi$  interaction, ligand discrimination of non-cationic ligands such as urea is enabled.<sup>48,49</sup>

The Guanidine-II riboswitch faces the challenge to discriminate ligands like urea and molecules containing the guanidyl-moiety such as arginine, agmatine, and creatin. With  $\text{Gdm}^+$  binding affinities of  $K_D=50\text{-}300\ \mu\text{M}$ , depending on the species,<sup>46</sup> the full aptamer of the Guanidine-II riboswitch can compete with its structural more complex representatives, the Guanidine-I riboswitch ( $K_D = 60\ \mu\text{M}$ )<sup>40</sup> and the Guanidine-III riboswitch ( $K_D = 60\ \mu\text{M}$ ).<sup>47</sup> Remarkably, an in-line probing experiment found that the aptamer of the Guanidine-II riboswitch binds  $\text{Gdm}^+$  in a cooperative manner,<sup>46</sup> whereas those of Guanidine-I and Guanidine-III do not.<sup>40,47</sup> Based on these experiments, the Breaker lab also proposed that the hairpins of the riboswitch may interact.<sup>46</sup>

Eventually, in 2017, when Strobel and Reiss solved the crystal structure of the **P2** hairpin of the Guanidine-II riboswitch, a switching model was proposed: In the absence of  $\text{Gdm}^+$ , the SDS is expected to be sequestered by base pairing with parts of the linker region and nucleotides at the 5' end of the **P1** helix (Figure 8A). The presence of  $\text{Gdm}^+$  is proposed to induce a kissing hairpin formation of **P1** and **P2**, comparable to the interaction found for the truncated homo hairpins in the crystal structure. This **P1** | **P2** interaction is hypothesized to enforce a structural change that releases the SDS and leads to translation promotion of genes modifying or transporting  $\text{Gdm}^+$ .<sup>48</sup>

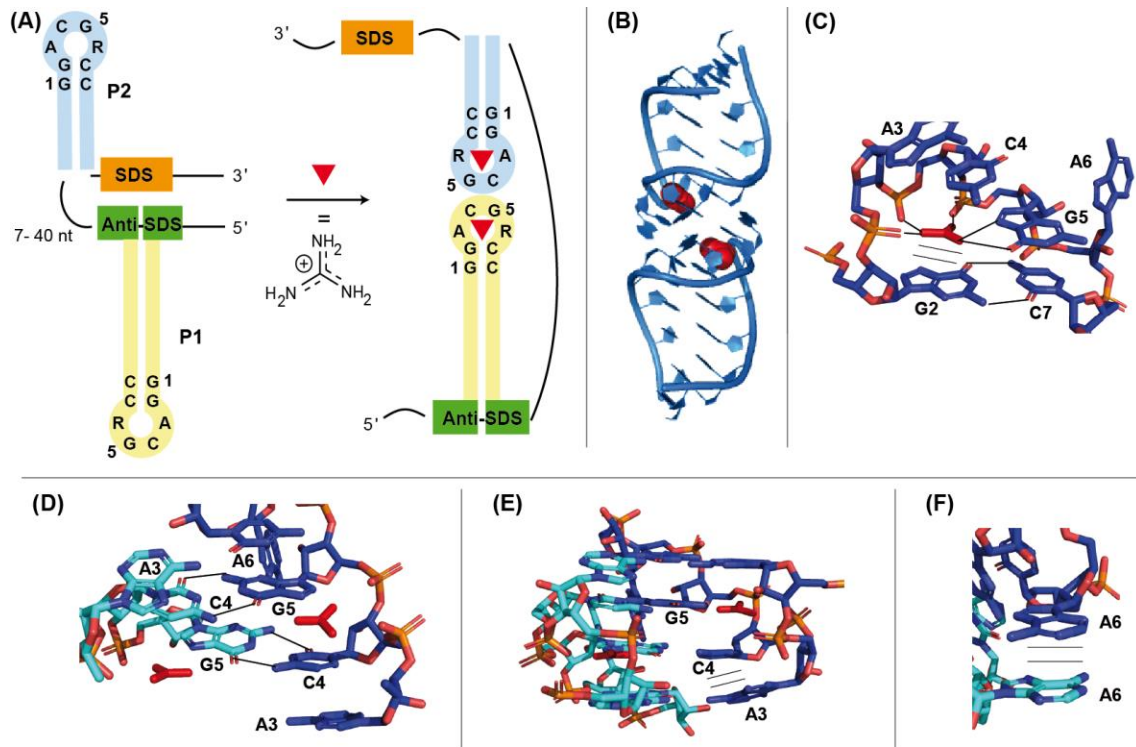


Figure 8. (A) Proposed switching mechanism of the Guanidine-II riboswitch. “SDS” denotes the Shine-Dalgarno Sequence and “Anti-SDS” the complementary Anti-Shine-Dalgarno Sequence. The hairpins **P1** and **P2** are colour coded in yellow and blue, respectively (representation based on reference 48). (B) Crystal structure of **P2** (PDB ID: 5VJ9)<sup>48</sup> with Gdm<sup>+</sup> marked in red. (C)-(F) Visualisation of the interaction of the hairpins and the Gdm<sup>+</sup> binding. The description of the nucleotides follows (A). The dark and the light blue colour marks the two different hairpins. Gdm<sup>+</sup> is coloured in red. Interactions are illustrated with black lines.

## 1.5 Catalytically active RNA and DNA

In 1989, S. Altman and T. Cech have been awarded with the Nobel Prize in Chemistry for their discovery of catalytic active RNA.<sup>51</sup> This discovery questioned the whole understanding of how life on earth began and has developed, because to this date proteins have been considered as only biocatalysts for nearly all chemical reactions taking place in living organisms.<sup>51</sup>

Catalytically active RNA is referred to as ribozyme. The most prominent ribozyme is the ribosome, having the capability to form peptide linkages between amino acids. Though the entire ribosome is a complex arrangement of RNAs and proteins, the catalytic activity is related to an RNA located in a conserved region of the “peptide transferase center”.<sup>52</sup>

Single-RNA ribozymes found so far are capable to participate in phosphoester chemistry i.e., phosphoester hydrolysis or phosphoester transfer reactions.<sup>12,31,53</sup> The most prominent representatives are the self-cleavage hammerhead ribozyme,<sup>54</sup> the hepatitis delta virus<sup>55,56</sup> and the twister ribozyme.<sup>57</sup> Remarkably, only a single ribozyme is known that induces a catalytic reaction and binds a ligand, so that it is additionally a riboswitch: the aforementioned *glms* ribozyme.<sup>58</sup> It is expected that more ligand-dependent ribozymes or even ribozymes catalyzing different reaction will be found.<sup>12,31,59</sup>

Catalytically active DNA is also referred to as DNA catalyst, DNA enzyme, deoxyribozyme or DNAzyme.<sup>60</sup> It has been identified by *in vitro* selection from random DNA libraries and is not encountered to be present in nature.<sup>53,60,61</sup> DNAzymes are able to catalyze different chemical reactions e.g., RNA cleavage<sup>62,63</sup> and ligation,<sup>64</sup> as well as DNA cleavage<sup>65</sup> and ligation,<sup>66</sup> formation of nucleopeptide linkages<sup>67</sup> or formation of carbon-carbon bonds.<sup>68</sup> The most well-characterized DNAzyme is the 10-23 DNAzyme, which is capable to facilitate RNA cleavage.<sup>63</sup> The 10-23 DNAzyme structure consist of a catalytic loop, which is flanked by two substrate binding arms that can be varied in length and sequence to improve RNA substrate specificity.<sup>53,61</sup> The potential to cleave virtually any RNA is emphasized for developing new therapeutics especially for cancer therapy.<sup>69</sup> However, the reaction mechanism is not elucidated so far, which might coincide with the lack of a high-resolution structure.<sup>61</sup>

## 1.6 Structure and dynamic investigation of nucleic acids

In order to understand the function of RNA molecules on a molecular level, methods are needed that provide information on their structures and conformational changes. The first level of RNA structural description is the identification of the base sequence. The second level of organization, the secondary structure, is mainly governed by Watson-Crick and Wobble base pairing, which leads to double-stranded helices interrupted by single-stranded regions in internal or hairpin loops.<sup>6</sup> Nowadays, *in silico* methods are available to predict the secondary structure but research is still ongoing. Due to computational complexity, standard folding programs disregard structural features as pseudoknots, loop-loop interactions or k-way junctions. However, the available *in silico* methods provide a good first insight into the RNA structure. One widely used approach for computational prediction of RNA secondary structure is based on the thermodynamics of the molecule.<sup>70,71</sup> The free energy of the real, native structure is supposed to be the one of the minimum free energy and is computed through thermodynamic parameters via softwares such as Mfold,<sup>72</sup> RNAfold,<sup>73</sup> or RNAstructure.<sup>74</sup> The softwares provide a secondary structure with base pair probabilities and can be used to design experimental measurements or support interpretations. Alternative approaches rely on stochastic models predicting the highest possibility of base pairing or algorithms comparing structural conservations of homologous RNA sequences i.e., sequences of RNAs (tRNA or rRNA) belonging to different organism.<sup>70,71</sup>

A reliable tool to deduce the secondary structure under wet lab conditions is chemical probing. Chemical probing detects single stranded and double stranded elements within RNA strands and allows prediction of the respective secondary structure. The RNA structural elements are characterized either through introduction of chemical adducts or through techniques leading to strand scission. The products can be identified by e.g., direct 5'-labeling with the radioactive <sup>32</sup>P or by reverse transcription. The introduction of chemical adducts is carried out with either base specific reactive alkylation agents or with sequence-independent 2'-hydroxyl acylation reagents. The former can be performed by e.g., dimethylsulfate, kethoxal or carbodiimides. The latter, which is commonly used and the so-called *selective hydroxyl acylation analyzed by primer extension* (SHAPE) method, is carried out with electrophile reagents such as IM7, NAI, or FAI, which are selective for flexible positions within the RNA structure. Ongoing research on novel chemical designs of the aforementioned acylation reagents enable RNA modifications also within cells. The chemical adducts generally block the RNA polymerase so that the truncated RNA strands can be analyzed. Another form of chemical probing relies on

strand scission. The so-called *In-line probing* utilized slightly basic conditions which promotes the intrinsic phosphate backbone cleavage reactivity of the 2' hydroxyl group. The induced 'spontaneous' cleavage reactions are more pronounced on flexible positions within the RNA structure and allow in turn predictions of the RNA structure. Strand scission can also be performed by RNase enzymes cutting at specific binding sites such as singles stranded or double stranded regions within the RNA structure.<sup>75,76</sup> Currently, progress is made to obtain secondary structures via chemical probing *in cell*.<sup>75</sup>

In order to unravel the full three-dimensional structure of RNA molecules additional methods are needed and a selection of them is described in the following.

Since the Nobel prize in chemistry was awarded to J. Dubochet, J. Frank and R. Henderson in 2017, cryo-electron microscopy (cryo-EM) has emerged as a tool to "move biochemistry into a new era".<sup>77,78</sup> Technologic breakthroughs enabled developing a method called single-particle cryo-EM. It is based on an electron beam that is applied to a frozen sample. A large number of 2D images of randomly oriented particles is recorded and computationally combined to a 3D reconstruction. The samples are placed inside a vacuum chamber.<sup>79</sup> To avoid dehydration of the biomolecules in the vacuum, different methods of sample preparation have been developed.<sup>80</sup> Freezing the sample at a specific point in time allowed time-dependent measurements.<sup>81</sup> Thus, a main drawback that cryo-EM cannot detect dynamic motions has been eliminated. Another widely assumed opinion that RNA molecules are too small to achieve an acceptable contrast of individual particles or conformational too heterogeneous to obtain enough images of all sites to reconstruct a model is currently refuted.<sup>79</sup> For example, different RNA molecules, ranging from 119 - 338 nt, from ribozymes to riboswitches, with and without ligands, were successfully resolved.<sup>82</sup>

Nevertheless, the Protein Data Bank,<sup>83</sup> the database for 3D structural data for proteins, nucleic acids and their complexes, is dominated by X-Ray structures (Figure 9).<sup>83</sup> X-Ray crystallography provides detailed atomic information without size restriction from diffraction patterns derived from well-ordered, good quality crystals.<sup>82</sup> It is an excellent method to gain information about rigid proteins and stable complexes. However, obtaining crystals is challenging especially regarding RNA structures that are often highly flexible. In addition, X-Ray crystallography requires pure and

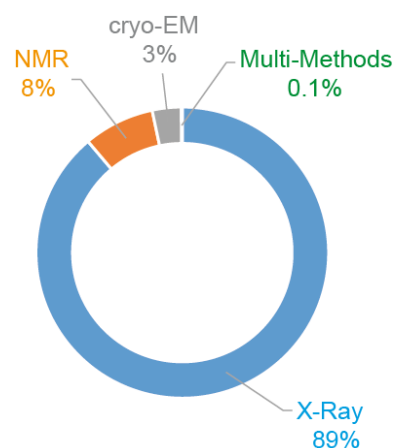


Figure 9. Statistic of the total number of entries available in the Protein Data Bank. Data are obtained from reference 83 on July 9, 2020.

homogeneously folded RNA in large scale.<sup>84</sup> Different crystallization conditions regarding concentration, temperature, precipitant, and salt need to be tested.<sup>85</sup> Besides the difficulties in crystallization, the crystal represents only a static picture of the system. In this regard, X-Ray Free Electron Lasers (XFELs) relying on the “diffraction before destruction” approach, may help.<sup>86</sup> Powerful pulses are applied on a large amount of crystals as small as 0.1-10  $\mu\text{m}$ .<sup>87</sup> Before the radiation damage destroys the crystal, a diffraction pattern is collected. With this approach, four reaction states of the adenine riboswitch with and without ligand binding were obtained.<sup>88</sup> Hence, also dynamics and kinetics are resolvable and methods are currently under development to do so, without the need growing large crystals.<sup>89</sup>

One method that does not require crystals but is still reliant on considerable large amounts of homogeneous RNA, is Nuclear Magnetic Resonance (NMR) spectroscopy. NMR spectroscopy is the main tool to elucidate structure, dynamics and interactions of nucleic acids in solution and on different timescale.<sup>90–92</sup> NMR spectroscopy investigates the interaction of nuclear spins in an applied magnetic field. Due to spectral crowding, NMR measurements are until now restricted to approximately 100 nt.<sup>91–93</sup>

A size unlimited method with respect to the oligonucleotide is Förster Resonance Energy Transfer (FRET). FRET is based on the attachment of two fluorophores to the surface of the biomolecule.<sup>94,95</sup> Due to a broad user application, there are well-studied dyes available with high quantum yields like Alexa Fluor or Atto Dye.<sup>94</sup> Through non-radiative energy transfer between the donor and the acceptor fluorophore, the dipole-dipole interaction allows the determination of distances up to 10 nm.<sup>95,96</sup> Bleaching and stacking of the dyes is a drawback that one needs to bear in mind.<sup>94,95</sup> A concern often raised is related to the large size of the dyes and their long, flexible linkers, which both may have an influence on the biomolecule and the distances measured. However, a recent study of 20 laboratories demonstrated that FRET is a reliable and reproducible method that is applicable on the single-molecule level (smFRET). They showed that a set of DNA duplexes with dyes separated by 11, 15 and 23 nt corresponding to distances between 46 - 84 Å could be measured with total uncertainty of less than 6 Å although different experimental set-ups were used.<sup>94</sup> Also for RNA molecules, several investigations have been published.<sup>97–102</sup> Last but not least, recent studies shown that time-resolved measurements on the picosecond time scale<sup>103–106</sup> as well as *in cell* measurements at room temperature are possible with FRET.<sup>96,104</sup>

Complementary to these methods, electron paramagnetic resonance (EPR) spectroscopy provides insight into the dynamics and structures of biomolecules without



size restriction and in solution.<sup>107–114</sup> In order to apply EPR spectroscopic methods to RNA, the RNA needs to bear one or more unpaired electrons. These electron spin centers can be paramagnetic metal ions or organic radicals, the so-called spin labels. EPR spectroscopic methods enable to measure the dipolar coupling between two or more electron spins that can be translated into distance distributions.<sup>108,110,114–117</sup> Extensive efforts have been made to facilitate measurements under physiological, *in cell* conditions.<sup>118–136</sup> Beyond these distance measurements, EPR-based hyperfine spectroscopy offers the opportunity to unravel the structure of a binding site with atomistic resolution. The number and affinity of metal ion binding sites can be unraveled by means of quantitative continuous wave (cw) EPR measurements, provided that the metal ion is either intrinsically paramagnetic or can be substituted by a paramagnetic one.<sup>108,137–146</sup>

## 1.7 EPR spectroscopy

### 1.7.1 Theoretical background

The EPR theory presented below is described on the example of nitroxides, and gathered from a set of publications.<sup>147–156</sup>

EPR spectroscopy is based on the electron spin  $\vec{s}$ , an intrinsic angular momentum of quantum particles. The electron spin vector length is given by

$$|\vec{s}| = \hbar\sqrt{s(s+1)}. \quad \text{eq. 1}$$

The spin state of an electron is characterized by two quantum numbers, the spin quantum number  $s$ , which is  $\frac{1}{2}$  for one unpaired electron and the magnetic spin quantum number  $m_s$ , which takes on the values  $m_s = \pm\frac{1}{2}$  for  $s = \frac{1}{2}$ . In an applied magnetic field  $B_0$  directed along the z-axis, the spin is aligned parallel or anti-parallel to  $B_0$  yielding for the z-component of the spin vector

$$s_z = m_s\hbar. \quad \text{eq. 2}$$

Due to the Heisenberg uncertainty principle,  $s_x$  and  $s_y$  cannot be determined if  $s_z$  and the magnitude of  $s$  are known. As result of charge and angular momentum, the electron exhibits a magnetic moment  $\vec{\mu}_e$

$$\vec{\mu}_e = -g_e\mu_B\vec{s}, \quad \text{eq. 3}$$

wherein  $\mu_B$  is the Bohr magneton.

The energy corresponding to the two spin states is given by

$$E = -\mu_{e,z}B_0 = g_e\mu_Bm_sB_0. \quad \text{eq. 4}$$

i.e.,

$$E_{(m_s=+\frac{1}{2})} = +\frac{1}{2}g_e\mu_BB_0 \quad \text{eq. 5}$$

$$E_{(m_s=-\frac{1}{2})} = -\frac{1}{2}g_e\mu_BB_0. \quad \text{eq. 6}$$

The energy splitting between the two states is called the electron Zeeman effect (Figure 10). The population of the two energy levels follows the Boltzmann distribution

$$\frac{N_{(m_s=+\frac{1}{2})}}{N_{(m_s=-\frac{1}{2})}} = e^{\frac{-\Delta E}{k_B T}} = e^{\frac{-\frac{1}{2}g_e\mu_BB_0 - \frac{1}{2}g_e\mu_BB_0}{k_B T}} = e^{\frac{-g_e\mu_BB_0}{k_B T}}, \quad \text{eq. 7}$$

wherein  $N$  is the number of spins populating the ground state  $m_s = -\frac{1}{2}$  or the excited state  $m_s = +\frac{1}{2}$ . For typical values of  $T = 300$  K and  $B_0 = 340$  mT, the ratio between ground state and excited state, is 0.999. Thus, the spin population in the ground state is minimally higher compared to the excited state. In EPR spectroscopy, a transition from the ground state to the excited state ( $\Delta E$ ) is triggered with microwave radiation in cases when the resonance condition

$$\Delta E = g_e \mu_B B_0 = h\nu \quad \text{eq. 8}$$

is met. At the point where the resonance condition is met, the absorption of the microwave radiation is detected as a signal (Figure 10). In EPR spectroscopy, microwave frequency is usually kept constant while  $B_0$  is swept.

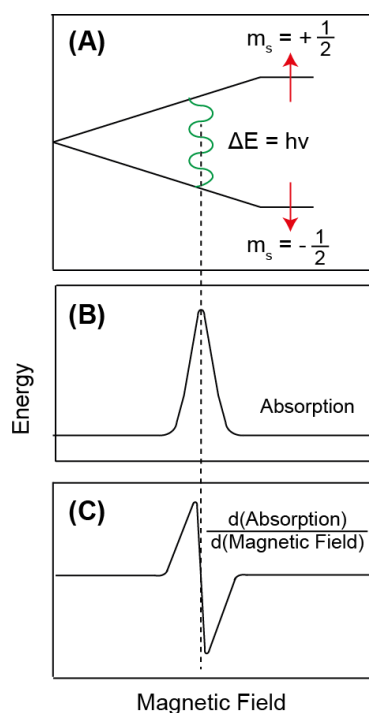


Figure 10. (A) Electron Zeeman splitting for an electron spin in an applied magnetic field  $B_0$ . (B) Absorption line, which is obtained when the resonance condition  $\Delta E = h\nu$  is matched. (C) Resulting cwEPR spectrum obtained as first derivative of the absorption line (Adapted from reference 148).

If the population difference between ground and excited state is increased, the EPR absorption signal increases as well. Eq. 7 demonstrates that this is possible by either decreasing the temperature or by increasing the magnetic field. In cwEPR spectroscopy, the detection is usually done with a Lock-in detector employing an additional, modulated magnetic field, which yields the first derivative of the absorption line (Figure 10 C).

For a free electron this line appears at  $g_e = 2.0023$ . The  $g$ -value is the position of the absorption signal independent of the magnetic field and the microwave frequency (eq. 9)

$$g = \frac{h\nu}{\mu_B B_0} = (7.144775 \times 10^{-2}) \frac{\nu}{B_0} \text{ in } \frac{\text{MHz}}{\text{mT}}. \quad \text{eq. 9}$$

For a nitroxide with  $g \approx 2$  in X-band (9-10 GHz) the resonance occurs at a magnetic field of  $\sim 3,400$  G, whereas it is found at  $\sim 12,000$  G in Q-band (34 GHz). Deviations from  $g_e$  are due to spin orbit coupling and are characteristics of the electron spin state, the bonding situation and the geometry of the particular molecule. It is used to characterize and distinguish different paramagnetic species.

Analogous to the electron Zeeman effect, there exist a nuclear Zeeman effect. Correspondingly, the state of a nucleus is characterized by the nuclear spin quantum number  $I$  and its magnetic spin quantum number  $m_I$ . The energy levels of a nuclear spin state with spin  $I$  is degenerated in  $M = 2I + 1$  e.g.,  $^{14}\text{N}$  nuclei have  $I = 1$ , thus the nuclear ground state splits into three sublevels.

The magnetic moment of the electron spin is coupled to the magnetic moment of nuclei with  $I > 0$ , which causes a splitting of the absorption lines. This interaction is called the hyperfine interaction.

The isotropic hyperfine coupling constant  $A_{\text{iso}}$  depends on  $g_N$  of the nucleus and on the electron spin density in the s-orbital  $|\Psi(r=0)|^2$  at the nucleus (Fermi contact interaction). As both  $g_N$  and  $|\Psi(r=0)|^2$  vary for each atom, an EPR spectrum with resolved hyperfine coupling constant allows statements regarding the structure. In Figure 11, an energy scheme for a nitroxide spin with  $s = \frac{1}{2}$  and  $I = 1$  is given. The three aforementioned interactions, the electron Zeeman interaction, the nuclear Zeeman interaction and the hyperfine interaction, yield six energy levels. Due to the selection rules  $\Delta m_s = \pm 1$  and  $\Delta m_I = 0$ , three transitions are allowed. Thus, a common cwEPR spectrum of a nitroxide spin label freely rotating in liquid solution is detected as three peaks. In such a case, the isotropic g-value is read off at the crossing of the baseline of the central line, and the splitting between the lines is the hyperfine coupling constant (Figure 11F).

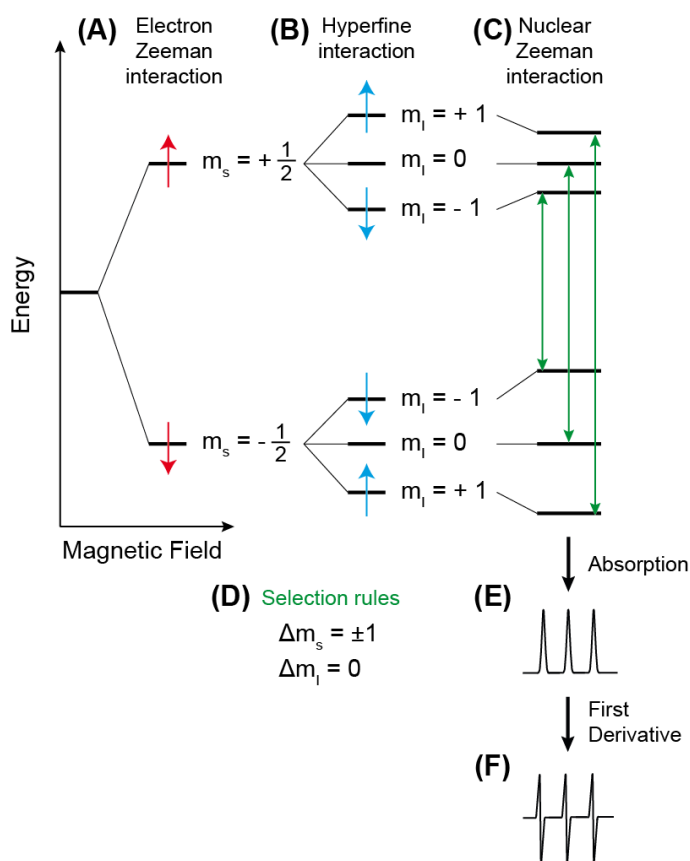


Figure 11. Energy scheme a nitroxide with  $s = \frac{1}{2}$  and  $I = 1$  in an applied magnetic field in the case that the hyperfine interaction exceeded the nuclear Zeeman interaction. (A) The electron Zeeman interaction with the resulting magnetic moments of the electron spins marked as red arrows. (B) The hyperfine interaction yielding the magnetic moments of the nuclear spins marked as blue arrows. (C) The nuclear Zeeman interaction inducing an increase and decrease of the energy levels. (D) The selection rules  $\Delta m_s = \pm 1$  and  $\Delta m_I = 0$  give three allowed transitions indicated as green arrows in (C), which yield (E) the absorption lines and (F) the final cwEPR spectrum as first derivative.

As an example, the cwEPR spectrum of nitroxide  $1^{\bullet}$  in the liquid state is shown in Figure 12 together with the simulation, which was generated with EasySpin.<sup>157</sup> The simulation revealed a hyperfine coupling constant of  $A_{\text{iso}}(^{14}\text{N})$  of 38 MHz and a  $g_{\text{iso}}$  of 2.0036 (see appendix for the simulation script). The weak intensity lines on the low and high field side of each  $^{14}\text{N}$ -line stem from hyperfine coupling to  $^{13}\text{C}$  nuclear spins ( $I = \frac{1}{2}$ ) with  $A_{\text{iso}}(^{13}\text{C})$  of 9 MHz. The low natural abundance of  $^{13}\text{C}$  (1.1%) causes the low intensity. Each of the three  $^{14}\text{N}$  lines would have to be split by ten  $^{13}\text{C}$  nuclei, but the probability that multiple  $^{13}\text{C}$  atoms are found within one molecule is so low that these species do not fully contribute to the spectrum. The hyperfine coupling to the  $^1\text{H}$  nuclei ( $I = \frac{1}{2}$ ) of the *gem*-diethyl groups manifested itself in splitting of the  $^{14}\text{N}$ -lines into multiplets with  $A_{\text{iso}}(^1\text{H})$  of 1 MHz (Figure 12C).

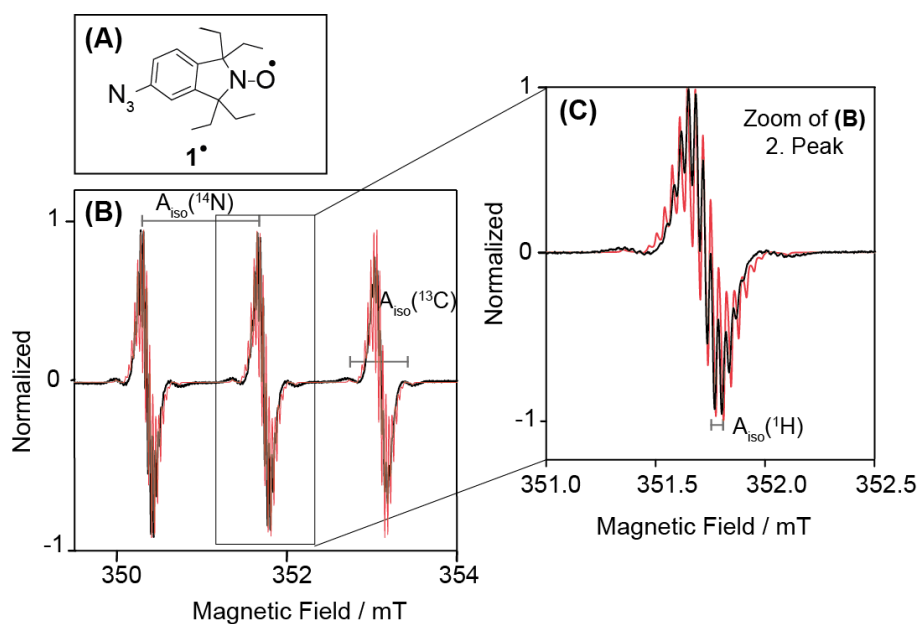


Figure 12. (A) Structure of spin label **1•**. (B) cwEPR spectrum of **1•** in liquid, degassed toluene at room temperature. The hyperfine couplings of  $^{14}\text{N}$  and  $^{13}\text{C}$  are indicated. (C) Zoom of (B) to visualize the  $^1\text{H}$  hyperfine coupling. The simulation is overlaid as red line.

In the solid, may it be a single crystal, a powder, or a frozen solution, one has to consider the anisotropy of the interactions mentioned above. In such cases, the isotropic  $g$ -value turns into a  $3 \times 3$   $\mathbf{g}$ -tensor. In its diagonalized form, its diagonal elements correspond to the canonical  $g_{xx}$ ,  $g_{yy}$ ,  $g_{zz}$ -values. If the molecule is transferred from e.g., the frozen state into the liquid state the three  $g$ -values  $g_{xx}$ ,  $g_{yy}$ ,  $g_{zz}$  are averaged to  $g_{\text{iso}}$ . The same applies to the hyperfine coupling. In the frozen state, the hyperfine coupling has to be described as a  $3 \times 3$   $\mathbf{A}$ -tensor with its diagonal elements corresponding to  $A_{xx}$ ,  $A_{yy}$ ,  $A_{zz}$ . Bringing the molecule from the frozen into the liquid state, also the  $\mathbf{A}$ -tensor will be averaged to an isotropic  $A_{\text{iso}}$  value. In Figure 13 the absorption spectrum of a nitroxide at Q-band in

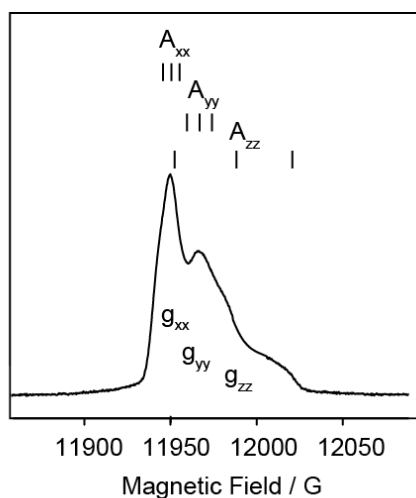


Figure 13. Absorption spectrum of a nitroxide recorded at 50 K at Q-band. The  $g$  anisotropy is resolved yielding  $g_{xx}$ ,  $g_{yy}$ ,  $g_{zz}$ , whereas the components of the  $\mathbf{A}$  anisotropy can be found in different areas of the spectrum (adapted from reference 149).

frozen solution is shown. The elements corresponding to the  $g$  and  $A$  anisotropy are indicated.

Above, the two extreme cases have been described i.e.,  $\mathbf{1}^{\bullet}$  rotating freely in solution (isotropic) or being completely frozen (anisotropic). In cases, where the molecular rotation is comparable slow to the EPR time scale, the  $g$ - and  $A$ -tensors are not fully averaged and the EPR spectrum will depend on the rotation correlation time  $\tau_c$  (Figure 14). This dependence of the shape of the EPR spectrum on  $\tau_c$  can be used to determine  $\tau_c$  from an EPR spectrum. The relation of  $\tau_c$  to the temperature  $T$  and the viscosity  $\eta$  is given by

$$\tau_c = \frac{4\pi\eta r^3}{3k_B T} \quad \text{eq. 10}$$

where  $r$  is the hydrodynamic radius according to Stokes-Einstein and  $k_B$  the Boltzmann constant.

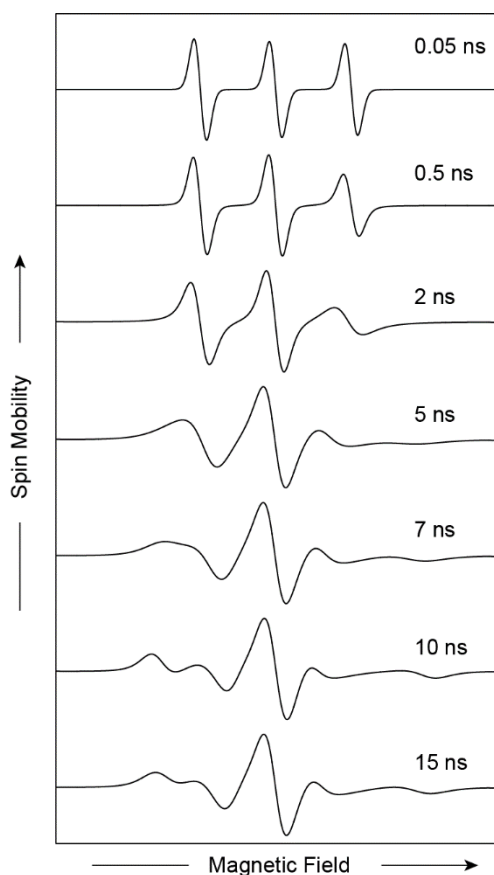


Figure 14. Simulated cwEPR spectra to illustrate the nitroxide spin label dynamic. The program EasySpin<sup>157</sup> was used with the parameters  $g = 2.003, 2.006, 2.008$  and  $A = 20 \text{ MHz}, 20 \text{ MHz}, 90 \text{ MHz}$ .

### 1.7.1.1 Dipolar electron spin electron spin interaction

If the molecule contains two unpaired electrons, e.g. two nitroxides, also the interaction between the magnetic moments of both unpaired electrons has to be considered. The isotropic coupling between these two spins called exchange coupling and is neglected here, because it decays exponentially with the distance. Here, only the dipolar through space contribution to the electron-electron coupling is considered. Within the high field approximation, the electron-electron dipole interaction energy is given by

$$E = \frac{\mu_B g_A g_B \mu_0}{4\pi h} \times \frac{1}{r_{AB}^3} (1 - 3\cos^2\theta). \quad \text{eq. 11}$$

The interaction depends on the distance  $r_{AB}$  between the two spins and the orientation of  $r_{AB}$  with respect to its orientation to  $B_0$ , which is given by the angle  $\theta$  between the interspin distance vector  $r_{AB}$  and the orientation of  $B_0$  (Figure 15A). In a powder, the molecules adopted all angles  $\theta$  with respect to  $B_0$ , meaning that the dipolar spectrum will yield the so-called Pake pattern (Figure 15B). Defining the dipolar coupling constant  $\omega_{AB}$  as

$$\omega_{AB} = \frac{\mu_B g_A g_B \mu_0}{4\pi h} \times \frac{1}{r_{AB}^3} \quad \text{eq. 12}$$

and reading of  $\omega_{AB}$  at  $\theta=90^\circ$  (Figure 15B) shows that  $r_{AB}$  can be calculated according to eq. 12. In eq. 12  $g_A$  and  $g_B$  are the g-values of the two unpaired electrons and  $\mu_0$  is the magnetic constant.

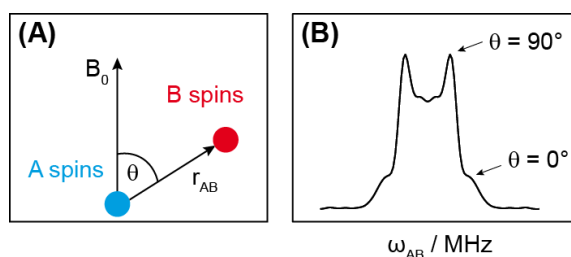


Figure 15. (A) Scheme of the dipole-dipole coupling of two spins (A spins and B spins) that depends on the interspin distance vector  $r_{AB}$  and on the angle  $\theta$ , which is assigned between the magnetic field vector  $B_0$  and the interspin distance vector  $r_{AB}$ . (B) Dipolar spectrum called Pake pattern that is obtained if a spin pair is randomly oriented in a sample and a complete distribution of dipolar frequencies is obtained.



### 1.7.1.2 The spin Hamiltonian concept

All the aforementioned interactions can be described within the spin Hamiltonian concept. In this concept all interactions can be given by one Hamiltonian  $\hat{\mathcal{H}}_0$  as given in eq. 13.

$$\hat{\mathcal{H}}_0 = \hat{\mathcal{H}}_{EZ} + \hat{\mathcal{H}}_{NZ} + \hat{\mathcal{H}}_{HF} + \hat{\mathcal{H}}_{DD} \quad \text{eq. 13}$$

with

$$\hat{\mathcal{H}}_{EZ} = g\mu_B \hat{S} B_0, \quad \text{eq. 14}$$

$$\hat{\mathcal{H}}_{NZ} = g_N \mu_B \hat{I} B_0, \quad \text{eq. 15}$$

$$\hat{\mathcal{H}}_{HF} = \hat{S} \hat{A} \hat{I}, \quad \text{eq. 16}$$

and

$$\hat{\mathcal{H}}_{DD} = \hat{S}_1 \hat{D} \hat{S}_2 \quad \text{eq. 17}$$

The terms given in eq. 13 to eq. 17 describe the electron Zeeman interaction  $\hat{\mathcal{H}}_{EZ}$ , the nuclear Zeeman interaction  $\hat{\mathcal{H}}_{NZ}$ , the hyperfine coupling interaction  $\hat{\mathcal{H}}_{HF}$ , and the dipole-dipole coupling between two electron spins  $\hat{\mathcal{H}}_{DD}$ . This concept is the basis for the programs used to simulate the EPR spectra.

## 1.7.2 Pulsed EPR

With the distribution of the spins over the two electron spin states  $m_s = \pm \frac{1}{2}$  according to the Boltzmann distribution, an ensemble of spins will give rise to a net magnetization  $M_z$  of the sample within the applied magnetic field  $B_0$ . The applied magnetic field  $B_0$  leads to a precession of the electron spins on cones parallel and anti-parallel to  $B_0$ . The frequency at which the electron spin precesses is the Larmor frequency. This gives rise to an oscillating magnetic field to which the oscillating magnetic field of the microwave can couple and thereby flip the spins and thus the magnetization. If the microwave radiation is applied in short time intervals, in EPR usually nanoseconds, one enters the field of pulsed EPR.

In pulsed EPR experiments, usually  $90^\circ$  and  $180^\circ$  pulses are applied. Accordingly, the magnetization is rotated  $90^\circ$  or  $180^\circ$  clockwise to the direction of the pulse. Pulse width and pulse amplitude affect the value of the rotation angle. Thus, a  $180^\circ$  pulse has either twice the length or twofold the power of a  $90^\circ$  pulse. The  $90^\circ$  and  $180^\circ$  pulses are also referred to as  $\frac{\pi}{2}$  and  $\pi$  pulses, respectively.

### 1.7.2.1 The Hahn echo experiment

The Hahn echo experiment corresponds to a simple  $\frac{\pi}{2} - \tau - \pi - \tau - \text{echo}$  pulse sequence (Figure 16A). The  $\frac{\pi}{2}$  pulse rotates the net magnetization  $M_z$  into the +y-direction (Figure 16B and C). This shifts the magnetization out of its thermal equilibrium and induces phase coherence. The spin packets start to dephase during the time  $\tau$  because of the distribution of their Larmor frequencies. A following  $\pi$  pulse flips the spin packets into the -y-direction refocusing their phase maximally after the same time interval  $\tau$  after the  $\pi$  pulse. The magnetization built up in -y-direction can be detected and is referred to as Hahn echo (Figure 16D).

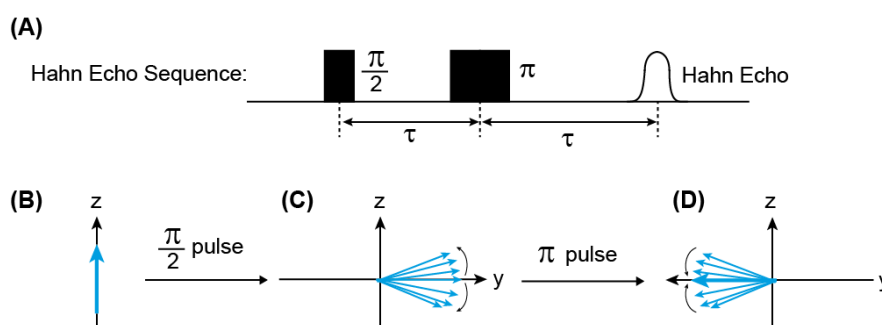


Figure 16. (A) Hahn echo pulse sequence. (B) Illustration of the net spin magnetization in z-direction. (C) Illustration of the dephasing of the spins after applying a  $\frac{\pi}{2}$  pulse. (D) Illustration of the refocusing of the spins after applying a  $\pi$  pulse. The resulting magnetization is detected as Hahn echo.

### 1.7.2.2 Relaxation

After the pulse excitation, the spins will start to relax back to thermal equilibrium. This is driven by two main relaxation processes i.e., the longitudinal ( $T_1$ ) and the transversal ( $T_2$ ) relaxation.

$T_1$  is governed by processes that restore the thermal equilibrium as given by the Boltzmann distribution. The spins dissipate their energy into the surrounding, the lattice, by returning to the z-axis. Accordingly, this process is characterized by an energy transfer between the spin system and the lattice.  $T_1$  dictates the repetition rate of a pulsed EPR experiment that allows the spins to return to equilibrium between two cycles of a pulse sequence. The repetition rate is set to find an optimal signal-to-noise ratio of a pulsed EPR experiment in time. The inverse of  $T_1$  is the relaxation rate constant for the decay process and is temperature dependent. Experimentally,  $T_1$  is assessed through the inversion recovery experiment. This three-pulse experiment consists of a  $\pi$  pulse

applied prior to the variable delay time  $t$  followed by the aforementioned  $\frac{\pi}{2} - \tau - \pi - \tau -$  *echo* sequence. The echo intensity, which recovers towards thermal equilibrium, is measured as function of the time  $t$ . The exponential recovery curve of the echo is fitted, yielding  $T_1$ .

$T_2$  is assigned to relaxation processes in the plane perpendicular to the applied magnetic field, the x,y-plane. The transverse relaxation process is characterized by spin exchange mechanism i.e., spin flip-flops, which destroy the spin coherence. The driving force for this mechanism is the gain in entropy. The relaxation time  $T_2$  can be measured via a two pulse electron spin echo envelope modulation (2PESEEM) experiment (Figure 17). The integrated echo, which is generated by applying a  $\frac{\pi}{2} - \tau - \pi - \tau -$  *echo* sequence, is measured as function of the interpulse delay  $\tau$ . The resulting Hahn echo decay curve is fitted assuming an exponential decay yielding the phase memory time  $T_M$ . In terms of more complicated processes wherein different components are involved, a stretched bi-exponential decay as given in eq. 18 can be used to analyze the components of the phase memory time<sup>158</sup>

$$y(2\tau) = A_1 \times e^{\left(-\frac{2\tau}{T_{M1}}\right)^{x_1}} + A_2 \times e^{\left(-\frac{2\tau}{T_{M2}}\right)^{x_2}} . \quad \text{eq. 18}$$

Since the relaxation process occurs over both periods of  $\tau$  in the Hahn echo sequence, eq. 18 contains  $2\tau$  in the exponent.  $T_{M1}$  and  $T_{M2}$  are the phase memory times, and  $x_1$  and  $x_2$  are the corresponding stretch parameters.  $A_1$  is the pre-exponential weighting factor of the first relaxation component of the Hahn echo decay curve, and the contribution of the second component is given by  $A_2$ , using the restriction  $A_1 + A_2 = 1$ .<sup>158</sup>

The stretch parameters provide insight into the underlying relaxation process that contributes to the respective component of  $T_M$ . If  $x$  is close to 1,  $T_M$  is attributed to instantaneous diffusion. This process occurs when the second pulse of the Hahn echo sequence flips another electron spin in the vicinity of the observed electron spin. In this way, the observed electron spin cannot fully refocus because it is moved out of resonance due to dipolar coupling between both spins. The extent of the contribution of the instantaneous diffusion is influenced by the pulse lengths and the local spin

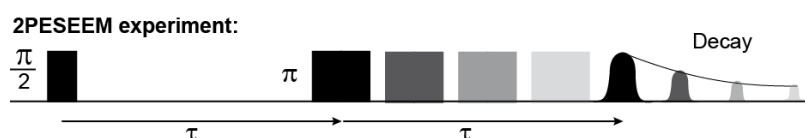


Figure 17. 2PESEEM sequence. The integrated echo is measured as function between the two pulses. The observed decay is analyzed as function of  $T_M$ .

concentration.<sup>150,151,158</sup>

Another main contributor to  $T_M$  is nuclear spin diffusion. If  $x$  is 2 - 2.5,  $T_M$  is dominated by this process. Nuclear spin diffusion includes all processes where nuclear spin flips modulate the electron-nuclear dipolar coupling. The electron spins lose their coherence in the  $x, y$  - plane and thereby dephases. The larger the magnetic moment of the dipolar coupled nuclear spin is, the greater the impact. Thus, the smaller magnetic moment of  $^2\text{H}$  compared to  $^1\text{H}$  decreases the impact of the nuclear spin flip on the electron and lengthen  $T_M$ . Hence, using deuterated buffers or placing the spin label into an aprotic environment can lead to a longer  $T_M$ .<sup>151,159-161</sup> Not only solvent protons, but also those of the biomolecule<sup>151,159,160,162-164</sup> or the spin label himself influence  $T_M$ .<sup>151,165,166</sup> Thus,  $T_M$  can be used to characterize the spin label environment, especially regarding polar and non-polar biomolecule surfaces.<sup>151,159,160</sup> It further indicates the influence of the *gem*-substituents of the spin label and thus the design strategy of a spin label. Classical rotation of *gem*-dimethyl groups is responsible for a shortened  $T_M$  because the averaged inequivalent coupling of nuclear spins influences the electron spin dephasing.<sup>150,151,165,166</sup>

### 1.7.2.3 The pulsed electron-electron double resonance experiment

In the work reported here, pulsed electron-electron double resonance (PELDOR), also called double electron-electron resonance (DEER), is employed to determine distances between two nitroxide spin labels on RNA strands. The four-pulse PELDOR sequence used is depicted in Figure 18A and consists of four microwave pulses applied at two different microwave frequencies, the detection frequency ( $\nu_{\text{det}}$ ) and the pump frequency ( $\nu_{\text{pump}}$ ). The three microwave pulses applied at the detection frequency  $\nu_{\text{det}}$  excite only those spins in resonance with the detection frequency, referred to as the A spins. Likewise, the microwave pulse generated at the pump frequency  $\nu_{\text{pump}}$  excites only those spins in resonance with the pump frequency, designated as the B spins. The first two detection pulses separated by the delay  $\tau_1$  create a Hahn echo of the A spins after the time  $\tau_1$  after the first  $\pi$  - pulse. The second  $\pi$  - pulse applied at a time  $\tau_2$  after the Hahn echo refocuses the spin echo after another time delay  $\tau_2$  after this pulse. The introduction of the  $\pi$ -pump pulse, applied between the second and third detection pulse, flips the magnetization of the B spins. Due to dipole-dipole coupling between A and B spins, the local magnetic field at the A spins changes so that the Larmor frequencies of the A spins are shifted. The echo intensity of the A spins recorded as function of the time  $t$  yields the PELDOR time trace (Figure 18B), where the echo intensity oscillates with  $\cos(\omega_{AB}t)$ . To obtain reliable data, at least 1.5 full oscillation periods have to be recorded.

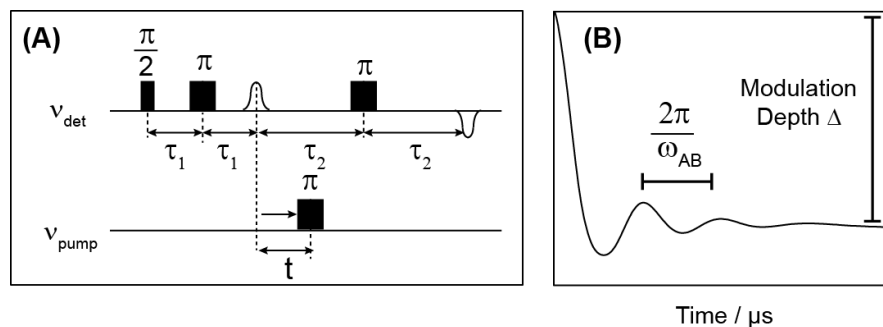


Figure 18. (A) Four-pulse PELDOR sequence. (B) PELDOR time trace. The modulation depth  $\Delta$  and a fully oscillation are indicated.

Besides the oscillation frequency, the PELDOR time trace is characterized by the modulation depth  $\Delta$ , which depends on the efficiency of the pump pulse excitation and on the fraction of coupled spins (Figure 18B). For two coupled nitroxide spin labels under the usual Q-band measurement conditions the expected modulation depth is approximately 35%. The dipolar spectrum, the Pake pattern, is obtained by Fourier transformation of the PELDOR time trace.

Chapter 1.7.1.1 showed that the dipole-dipole interaction provides in addition to the interspin distance the possibility to obtain the relative orientation ( $\theta$ ) of two spin labels providing the spin labels have a fixed orientation to  $B_0$ . This is the case for rigid spin labels. The non-random detection of  $\theta$  leads to an incomplete Pake pattern. Orientation-selective measurements can be analyzed to determine the spatial orientation of the spin labels e.g., with PeldorFit,<sup>167</sup> or by summing up a set of orientation selective time traces recorded at different pump and probe frequencies.<sup>168–170</sup>

## 1.8 Site directed spin labeling

In order to make RNA accessible to EPR spectroscopic methods, the RNA has to be labeled in a site directed way. The design and bioconjugation of spin labels to RNA is thus an important task. Since the beginning of the 21st century, the development of spin labels for nucleic acids has made enormous progress. Several different methods have been published and a few examples are summarized in the following.<sup>114–117,171,172</sup> In general, spin labels are attached to all three subunits of the RNA: the phosphate group, the sugar and the base. The main strategies of site directed spin labeling (SDSL) of RNA are either based on spin label introduction during the nucleic acid synthesis, mainly in the form of modified phosphoramidites, or post-synthetically at a pre-functionalized position. New, unconventional strategies involve e.g., non-covalently bound spin labels or the modified genetic alphabet for spin label introduction.<sup>114–117,171–176</sup>

### 1.8.1 3' and 5' spin labeling

SDSL/EPR on RNA found its beginning in the spin labeling of 3' and 5'-termini due to their good accessibility and the minimal structural perturbations that their labeling exhibits. However, the spin label at the specific site has high rotational freedom, which hinders a precise mobility analysis of the RNA in cw X-band EPR measurements and broadens the distance distributions from PELDOR.

3' labeling was already conducted on tRNA in 1976.<sup>177</sup> To do so, a 3' terminal adenosine of a natural occurring, unfractionated tRNA from *E.coli* was subjected to oxidative cleavage with sodium periodate. Subsequent closure to a 6-membered ring via reductive amination with the spin label 4-amino-TEMPO using sodium borohydride afforded the spin labeled product (Figure 19A).<sup>177</sup> Nearly ten years later, this approach was extended to obtain information about initiator and elongator tRNA.<sup>178</sup>

A 5' labeling approach published in 1999 achieved substantial improvement compared

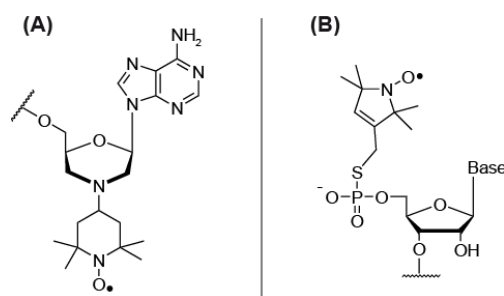


Figure 19. (A) 3' termini spin label and (B) 5' termini spin label.

to the 3' labeling because it did not need such harsh reaction conditions. 5' labeling was conducted on a guanosine monophosphorothioate (GMPs), which was introduced during transcription. Subsequently, an  $S_N$ -reaction with a thiol-functionalized nitroxide spin label yielded the labeled product. Thereby, cwEPR measurements were recorded on an HIV Rev peptide and its Rev response element RNA.<sup>179</sup> An analogous strategy uses the transfer of the  $\gamma$ -phosphorothioate group of adenosine-5'-O-(3-thiotriphosphate) (ATP $\gamma$ S) to the 5'-termini, utilizing the same aforementioned  $S_N$ -reaction (Figure 19B).<sup>180</sup>

## 1.8.2 Phosphate spin labeling

Spin labeling of the RNA phosphate group has the advantage to be sequence independent. However, the covalently bound spin label removes the negative charge from the phosphate group, which can result in misfolding of the RNA. This SDSL approach was firstly conducted with an iodo-carrying nitroxide spin label via  $S_N$ -reaction to phosphorothioate (Figure 20A).<sup>181–183</sup> cwEPR spectra were recorded of a glycine riboswitch labeled at three different sites within the leader-linker region. In this way, the backbone dynamic of this specific region was investigated by monitoring the glycine riboswitch conformational change in dependence of KCl, MgCl<sub>2</sub>, and glycine. The SDSL approach was improved by attaching the spin label at two neighboring phosphate groups (Figure 20B).<sup>184</sup> As a result the spin label has no flexible freedom and the mobility information within the EPR measurement can directly be translated into the RNA mobility.<sup>184</sup>

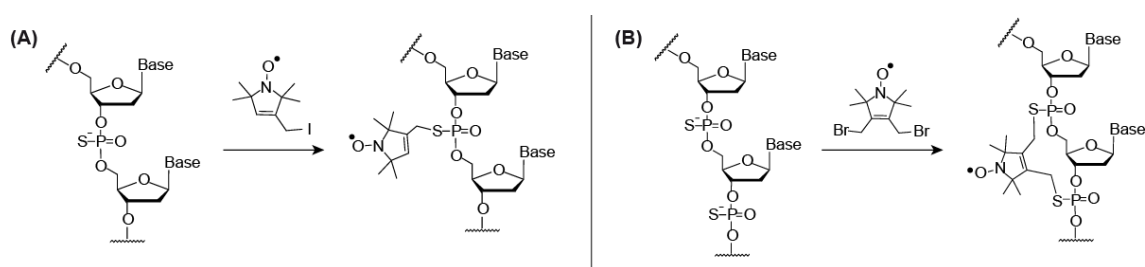


Figure 20. Spin labeling reactions performed on the phosphate group.

### 1.8.3 Ribose spin labeling

2'-amino modified nucleotides have been employed for post-synthetic spin labeling. This approach has the advantage to be applicable to commercially available phosphoramidites. Several biological applications, especially regarding the trans-activation responsive region (TAR) of HIV RNA were published and demonstrated the performance of this SDSL strategy in combination with a TEMPO-derived nitroxide spin label with an isocyanate linker (Figure 21A).<sup>185–191</sup> A major drawback of the used spin label is the high reactivity of the isocyanate group, which promotes hydrolysis of the RNA. Consequently, the isocyanate was substituted to the less reactive isothiocyanate. Further modifications resulted in two isothiocyanate carrying isoindoline nitroxide spin labels (Figure 21B).<sup>192</sup> The isoindoline based spin labels display a limited mobility and are, therefore, promising candidates for distance measurements.<sup>192</sup> Additionally, *gem*-diethyl isoindoline nitroxides exhibit a high stability towards reducing agents, making them auspicious for *in cell* measurements.<sup>125,192–196</sup>

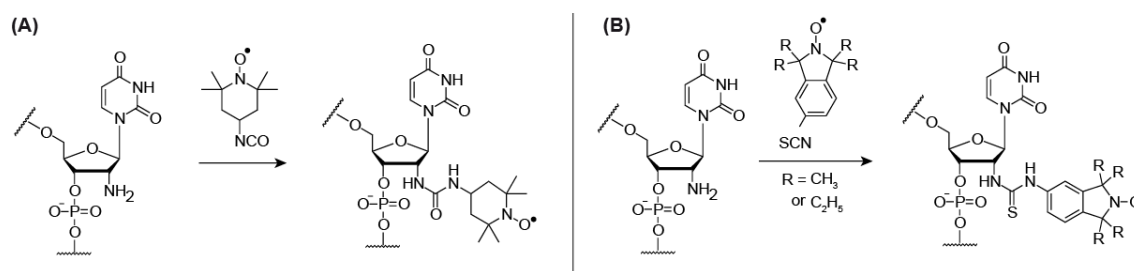


Figure 21. Spin labeling reactions performed on the ribose.

### 1.8.4 Nucleobase spin labeling

Nucleobase spin labeling has been applied to pyrimidine and purine bases, but labeling of the pyrimidine bases is more common. One early approach was published in 1970. 4-thiouridine, a naturally occurring non-canonical nucleobase in tRNA, was bioconjugated to a bromide carrying nitroxide spin label via  $S_N$ -reaction (Figure 22A). cwEPR spectra were used to monitor the mobility of the spin labels in different tRNAs. Differences were detected and local base interactions were deduced.<sup>197</sup>



Commercial availability of 4-thiouridine containing RNA strands renewed the interest in this labeling strategy. The introduction of 4-thiouridine at specific positions in RNA strands enabled  $S_N$ -reactions with three different nitroxide spin labels that exhibited a methanethiosulfonate linker. In this way, cwEPR measurements were executed reporting on RNA local structure and dynamics.<sup>198</sup>

A further nucleobase labeling strategy utilizes RNA strands with 5-ethynyl-2'-deoxyuridine bases at specific sites. The modified positions in combination with an azido-carrying spin label allow  $Cu^I$  catalyzed [3+2] azide-alkyne cycloaddition (CuAAC Click-reaction),<sup>199,200</sup> which has been used extensively to modify oligonucleotides.<sup>201–207</sup> Obeying the principle of Click-chemistry, the CuAAC reaction enables high yields under mild and simple reaction conditions, it tolerates a diverse range of functional groups and the aromatic triazole unit is extremely stable and non-toxic.<sup>199,200,202,207,208</sup> To conduct EPR spectroscopic measurements, CuAAC was used to attach an azido-carrying *gem*-dimethyl isoindoline spin label. The spin label was discovered to not perturb the native RNA structure. Furthermore, it exhibited hindered rotational mobility and in turn ensured orientation selectivity enabling resolution of angular and distance information of two spin labels by PELDOR measurements.<sup>209–211</sup>

Another spin labeling strategy relies on the palladium(0) catalyzed *Sonogashira-Hagihara* cross-coupling reaction that is used to attach the 3-ethenyl-2,2,5,5-tetramethyl-pyrrolin-1-yloxy (TPA) to iodo-modified bases i.e., 5-iodo-uridine, 5-iodo-cytidine, and 2-iodo-adenosine (Figure 22C).<sup>212–215</sup> The spin label excels through its restricted mobility caused by the short and rigid linker resulting in narrow distance

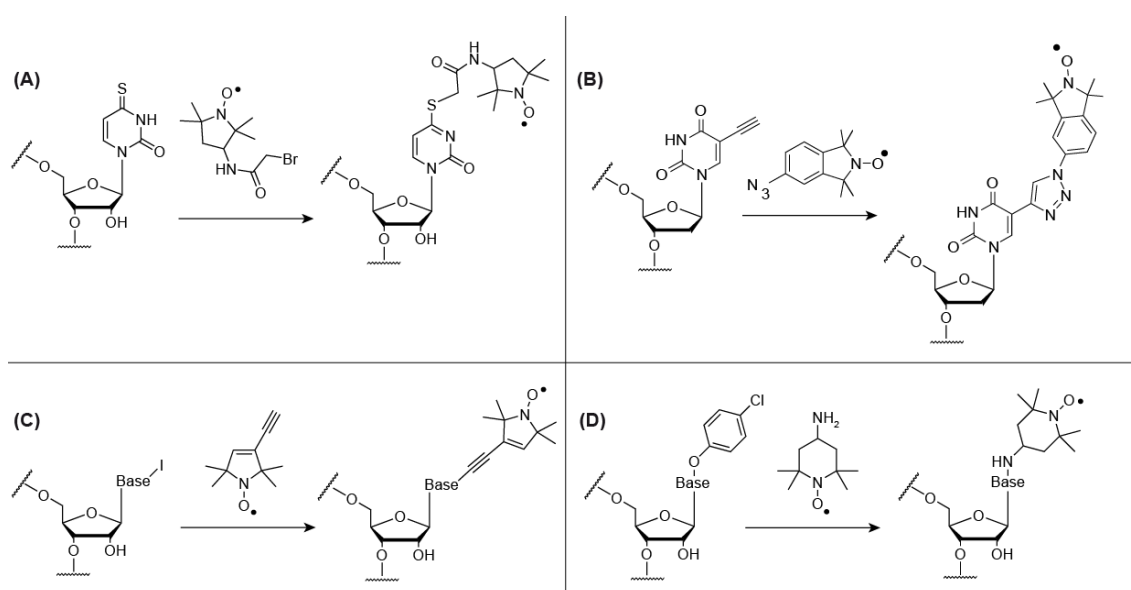


Figure 22. Spin labeling reactions performed on the nucleotide base.

distributions. The spin labeling reaction is carried out during the solid phase synthesis of the RNA as “on-column reaction”. Pausing the solid phase synthesis, spin labeling and reinstallation of the spin labeled RNA strand onto the synthesizer allows introduction of the spin label at any sequence position of the RNA.<sup>212</sup> However, the spin label is in this procedure exposed to the harsh conditions of the solid phase synthesis and might be partially reduced. A newly investigated 2'-hydroxy protection group, the 2'-bis(acetoxyethoxy)methyl ether (ACE), enabled mild removal from the 2'-hydroxy group and thus significantly lowered the amounts of reduced nitroxide. In this way, the incorporation of TPA through *Sonogashira-Hagihara* cross coupling provides good labeling efficiencies.<sup>214,215</sup>

Another nucleobase spin labeling approach utilizes convertible nucleosides, commercially available phosphoramidites modified with leaving groups, which can be post-synthetically displaced by nitroxide spin labels (Figure 22D). In this way, adenine, cytosine, and guanine were converted into nitroxide carrying nucleobases. This SDSL approach was used to generate a set of RNA duplexes. The secondary structure of the duplexes was analyzed by UV spectroscopy and PELDOR measurements and yielded a low structural perturbation of the RNA structure by the spin labels.<sup>216</sup>

A further nucleobase spin labeling approach builds on the rigid spin label  $\zeta m$  (Figure 23A). The great advantage of  $\zeta m$  introduced into an RNA structure is that distance distributions and the spatial orientation between two spin labels can be accessed by PELDOR measurements. Its minor degree of perturbation of the RNA structure and its high output of structural information were tested on hairpins, duplexes and dumbbells.<sup>217,218</sup> Recently,  $\zeta m$  was employed to investigate the tetracycline aptamer. The tetracycline aptamer conformational flexibility was tested in dependence of  $Mg^{2+}$  monitoring the distance change of two  $\zeta m$  spin labels by PELDOR measurements.<sup>219</sup> However, the nitroxide-carrying phosphoramidite  $\zeta m$  is commercially not available and needs to be synthesized in eight steps starting from 2'-O-methyluridine. To avoid reduction of the nitroxide center during the RNA synthesis, it was concealed as a benzoyl hydroxylamine. The benzoyl group is stable towards the conditions of RNA synthesis on the solid-support and is removed under the standard RNA deprotection conditions yielding a hydroxylamine, which is oxidized *in situ* to the desired nitroxide. Thereby, high yielded spin-labeled RNA can be obtained.<sup>220</sup> Further, the spin label design itself was improved by substitution of the *gem*-dimethyl groups towards *gem*-diethyl groups. This new spin label, which was referred to as  $E\zeta m$  (Figure 23B), demonstrated high resistance towards reducing environment,<sup>196</sup> making the spin label an overall promising

candidate for *in cell* measurements with the possibility of precise analysis of angles and distances.

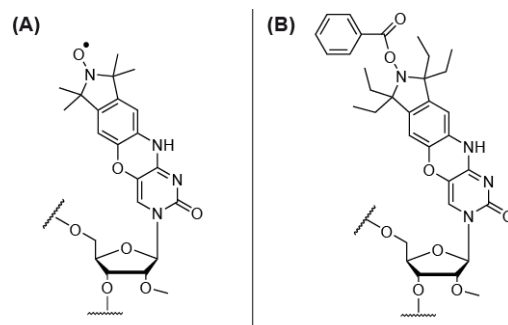


Figure 23. Rigid spin labels.

### 1.8.5 Non-covalent spin label

Another spin labeling approach takes advantage of abasic sites. These naturally occurring apurine / apyrimidine sites in nucleic acids give the opportunity to introduce a spin label at the exact position in which it is fixed through hydrogen bonding and  $\pi$ -stacking. The binding affinities of ten spin labels towards an abasic site in a RNA duplex were tested by cwEPR spectroscopy but were only obtained in a low binding regime.<sup>221</sup> However, in 2016, the spin label  $\dot{G}$  was synthesized in a simple one-step reaction starting from commercially available materials (Figure 24)<sup>222</sup> and exhibited high specificity in a model RNA duplex<sup>223</sup> and also in a triplex.<sup>224</sup> Furthermore, orientation selectivity was detected in a PELDOR experiment that yielded additional structural information.<sup>174</sup>

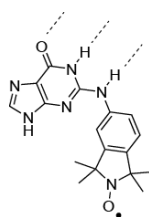


Figure 24. Non-covalent spin labels with the ability to build hydrogen-bonds for base pairing shown as dotted lines.

### 1.8.6 Spin labeling of long RNA strands

The accessibility of long RNA strands i.e., with modified positions, is primarily hindered by the synthetic capability of the solid-phase method. Different attempts have been performed to overcome this limitation. One strategy is the ligation approach that relies on the linkage of a 3' hydroxy RNA strand, which is referred to as acceptor and a 5' phosphate RNA strand, named the donor.<sup>225,226</sup> The phosphodiester bonding reaction can be catalyzed by e.g., the enzymes T4 RNA ligase (Figure 25A),<sup>225,227</sup> T4 RNA ligase 2<sup>228</sup> and T4 DNA ligase (Figure 25B),<sup>210,227,229–231</sup> or by DNAzymes (Figure 25C).<sup>60,232</sup> Lebars et al. used the T4 RNA ligase 2 for RNA ligation. This ligating enzyme requires double stranded ligation complexes. For this reason, a DNA splint was used, which was complementary to the pre-ligated RNA sequence. The RNA donor strand was pre-functionalized at a specific position with a thio-modified nucleotide enabling a  $S_N$ -reaction with the 3-(2-Iodacetamido)-proxyl spin label subsequent to the ligation. In that way, a singly labeled 55 nt long RNA strand was achieved.<sup>228</sup>

Duss et al. applied the T4 DNA Ligase approach at the 72 nt non-coding RNA RsmZ to investigate the 70 kDa protein-RNA complex. In contrast to the previously described method, they found that post-labeling did not yield spin labeled product. Still, spin labeling and subsequent ligation yielded 20-40% of the ligated and spin labeled RNA.<sup>230,231</sup>

The lab of Höbartner compared the T4 DNA ligase approach with their DNAzyme catalyzed strategy. The RNA substrate was ligated with the DNAzyme 9DB1\* and afterwards spin labeled using convertible nucleotides. In that way, a spin labeled 53 nt SAM-III and a 118 nt SAM-I riboswitch were synthesized with better yields compared to the T4 DNA Ligase strategy.<sup>60,232</sup>

A differing attempt to achieve long spin labeled RNA was made by Babaylova et al. The key step of their method adopted a modified complementary DNA sequence carrying a 4-[*N*-(2-Chloroethyl)-*N*-methylamino]benzyl moiety (Figure 26A). The formation of a complex between this modified DNA and the substrate RNA was promoted by a helper

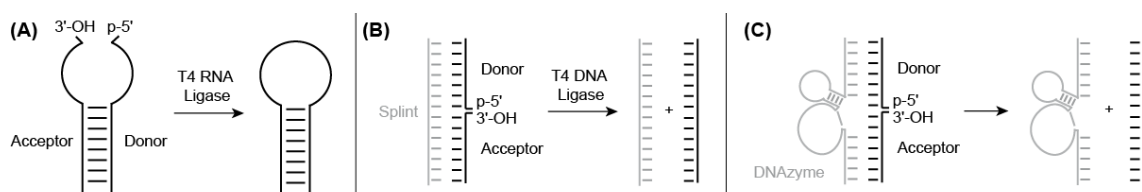


Figure 25. Ligation strategies utilizing the (A) T4 RNA Ligase, (B) the T4 DNA Ligase, and (C) a DNAzyme.

DNA that interrupted the tertiary structure of the RNA at the specific region and facilitated complex formation. RNA alkylation followed by hydrolysis (Figure 26B and C), released a covalently bound amino group on the RNA that reacted with a nitroxide spin label (Figure 26D).<sup>233</sup> Following this complementary-addressed SDSL approach, a 341 nt long Hepatitis C Virus (HCV) RNA *internal Ribosome entry site* (IRES) was successfully spin labeled.<sup>234</sup>

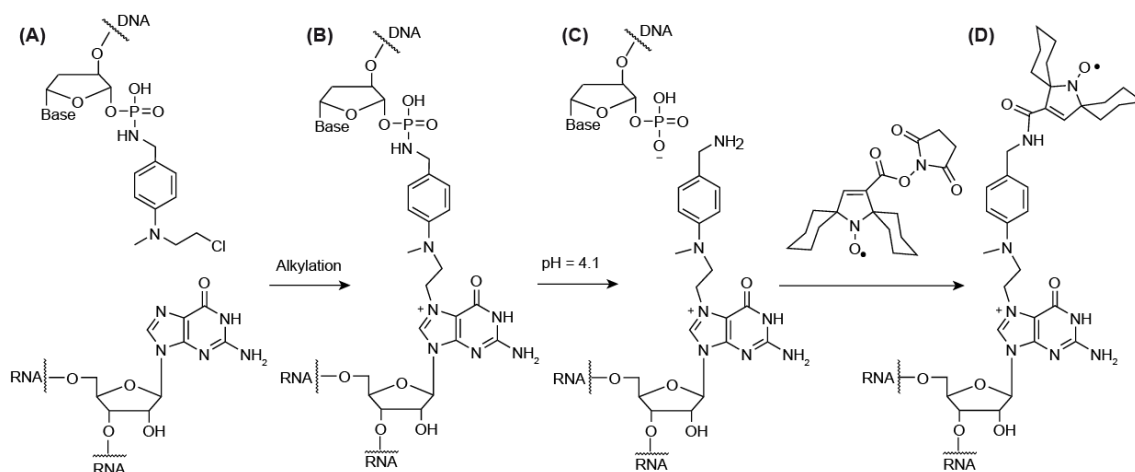


Figure 26. Spin labeling reaction based on the site directed complementary addressed approach.

Recently, another novel strategy for SDSL of long RNAs was published. This method makes use of a novel nitroxide carrying RNA triphosphate (Figure 27A) that is introduced through in vitro transcription using an expanded genetic alphabet (Figure 27B). Domnick et al. successfully labeled RNA duplexes, a 185 nt long glmS ribozyme as well as a 377 nt long non-coding RNA XIST.<sup>175</sup> Shortly after the publication, a nearly identical approach was published.<sup>176</sup>

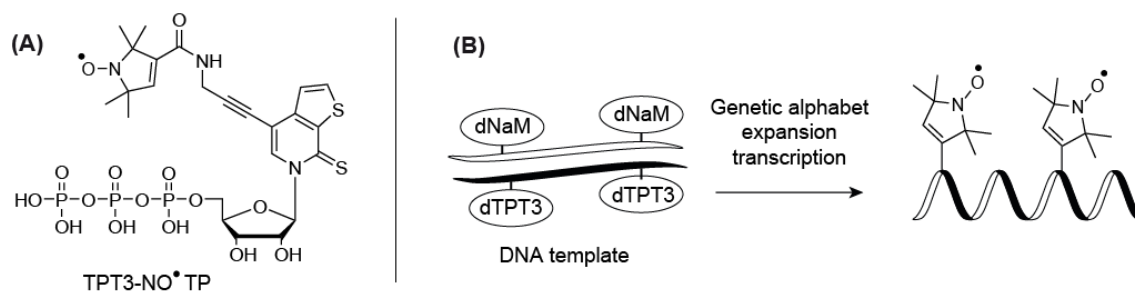


Figure 27. (A) Novel nitroxide carrying RNA triphosphate (TPT3-NO<sup>\*</sup> TP). (B) RNA labeling strategy using the DNA template constructed with two additional nucleotides (dNAM and dTPT3). The genetic alphabet expansion transcription introduces TPT3-NO<sup>\*</sup> TP at specific positions.

### 1.8.7 Trityl spin labeling

The ultimate goal of SDSL in combination with EPR spectroscopy is the measurement of biological relevant RNA at physiological temperature within cells. Promising spin label candidates for this are derivatives of the Finland radical (Figure 28A). The Finland radical was first published in patents in the 1990s and is used as contrast agent in Overhauser magnetic resonance imaging.<sup>235–238</sup> In EPR context, derivatives of the Finland radical also referred to as Trityl radicals have emerged as promising spin labels because of their sensitivity,<sup>239</sup> their comparatively long relaxation time at room temperature,<sup>120,240</sup> and their resistance to *in cell* conditions.<sup>118,119,122</sup> By now, SDSL approaches with Trityl radicals have only been established for proteins and DNA, whereas RNA labeling is still lacking.

The first attempt of SDSL of DNA was conducted on the 5' termini of a model DNA duplex by substitution of the 5' hydroxy group by a piperazine moiety and subsequent esterification with a Trityl radical ester (Figure 28B).<sup>121</sup> MD simulation revealed that the spin label does not perturb the DNA structure.<sup>241</sup> Aiming to improve the accuracy of the distance measurement, a shorter linker was developed (Figure 28C).<sup>242</sup> Comparison of

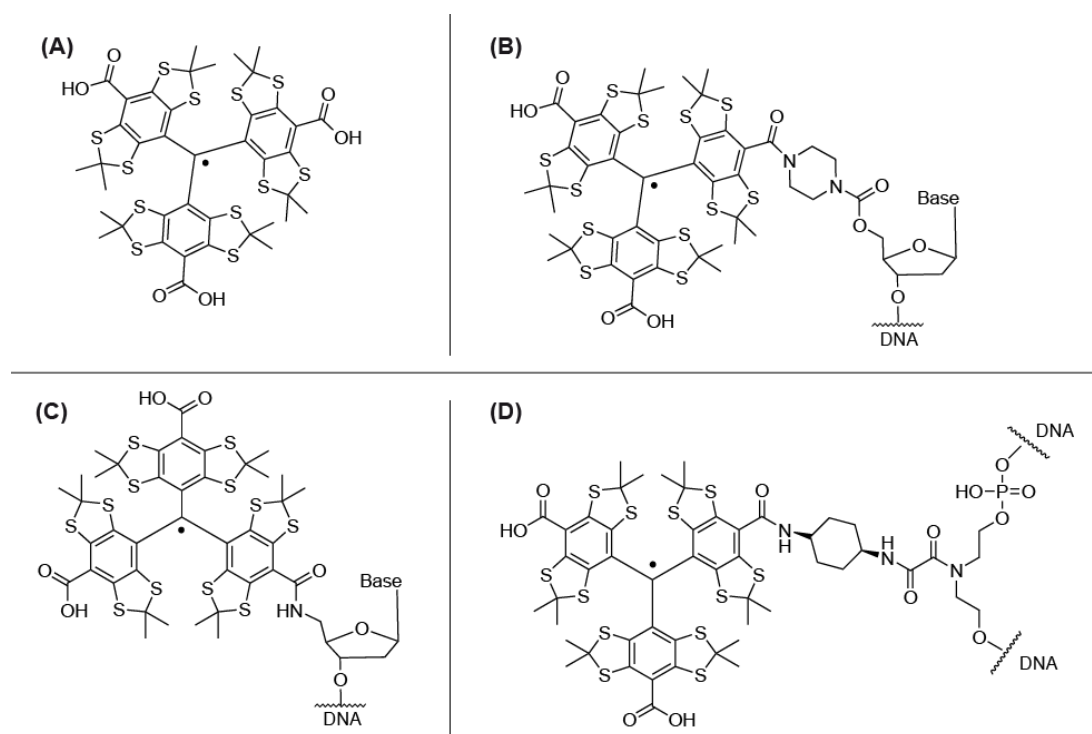


Figure 28. (A) Finland Trityl. (B) First spin labeling approach using a Trityl radical on the 5' termini of a DNA duplex. (C) Improved spin labeling strategy using a shorter linker. (D) Internal spin labeling approach with a non-nucleotide phosphoramidite.

the performance of the both Trityls demonstrated that the distance distributions were comparable in accuracy and width. Additionally, the MD simulations indicated that both Trityl spin labels tend to cap the DNA at the termini.<sup>242</sup> Conflicting results were obtained regarding their orientation selectivity. Whereas the Trityl labeled DNA with the shorter linker did not exhibit an orientation selectivity, the piperazine linked Trityl demonstrated this selectivity at 50 K in W-band.<sup>243</sup> But at higher frequency, none of them showed an orientation selectivity.<sup>244</sup>

Further measurements with the piperazine linked Trityl were conducted at room temperature on immobilized DNA using modified silica gel<sup>121</sup> and different saccharides.<sup>245</sup> Internal spin labeling was performed with non-nucleotide phosphoramidites with subsequent esterification of the Trityl spin label (Figure 28D).<sup>246</sup> However, due to the high conformational flexibility,<sup>246</sup> there is still a need for development of new strategies for internal labeling and especially RNA spin labeling with Trityl radicals.

### 1.8.8 Gd<sup>3+</sup> and Cu<sup>2+</sup> spin labeling

Spin labeling approaches were also established for gadolinium (Gd<sup>3+</sup>) and copper (Cu<sup>2+</sup>) complexes. In comparison to nitroxides, Gd<sup>3+</sup> provides increased sensitivity in high-field EPR experiments (>30 GHz),<sup>247,248</sup> as well as higher stability for *in cell* measurements.<sup>123,124,128,249–254</sup> Though, one drawback of Gd<sup>3+</sup> is the need of attachment via chelate complexes. These complexes exhibit often a very bulky structure, which may interrupt the biomolecule structure. Furthermore, the binding of Gd<sup>3+</sup> needs to be very

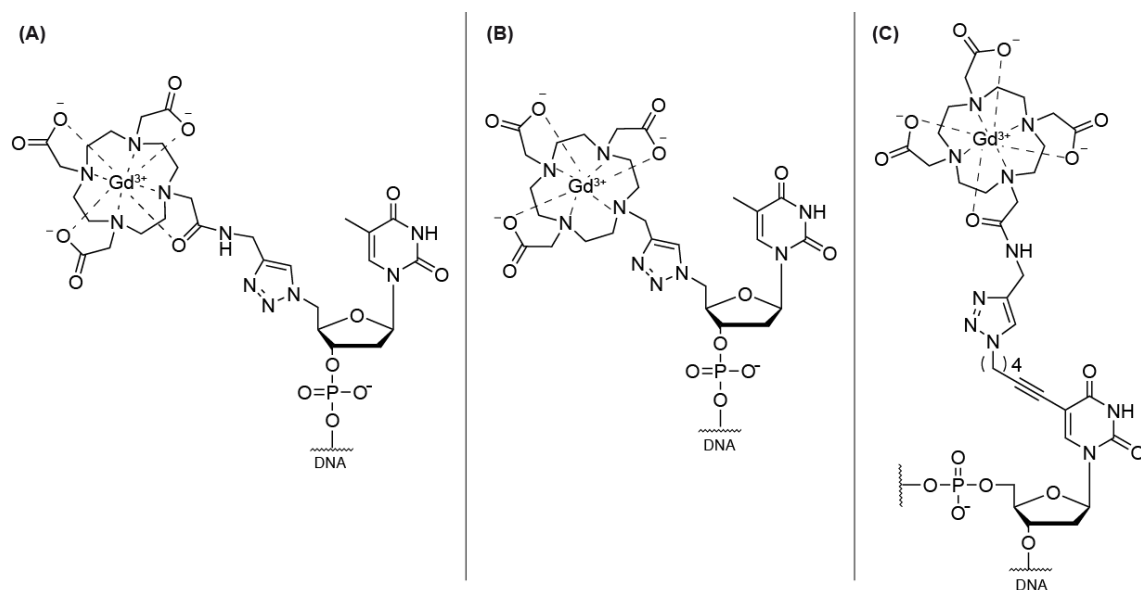


Figure 29. Gd<sup>3+</sup> spin labeling strategies.

strong to promise tight binding. The free  $Gd^{3+}$  in solution does otherwise show background signals, which are difficult to analyze.<sup>248</sup> Until today, only a few attempts were made to incorporate  $Gd^{3+}$  in DNA. The first one made in 2011 allows the attachment of  $Gd^{3+}$  tags with two different flexible linkers to the 5' termini with the aid of a DOTA ligand and Click-chemistry (Figure 29A and B). Distance measurements on a 14 nt long DNA duplex was conducted but exhibited high spin tag mobility.<sup>255</sup> In 2015, another spin label was introduced that enabled internal spin labeling (Figure 29C) of DNA duplexes followed by distance measurements within cells.<sup>251</sup>

$Cu^{2+}$  spin labeling has yet only been established for DNA. In analogy to the aforementioned  $Gd^{3+}$  spin labeling strategies,  $Cu^{2+}$  needs strong chelating complexes to be attached to oligonucleotides. A hand full of different complexes have been tested so far. In 2010, complexation of  $Cu^{2+}$  ions with salen ligands inside a DNA helix was accomplished (Figure 30A). Analysis of the electron-electron spin-spin exchange coupling yielded short range distances between two  $Cu^{2+}$  ions.<sup>256</sup> Another approach utilizes ligands coordinating  $Cu^{2+}$  in a square-planar fashion made of porphyrine based ligands (Figure 30B). These  $Cu^{2+}$ -porphyrins were found to bind to guanine quadruplexes. Stacking them on top and bottom of guanine quadruplexes enabled distance measurements via EPR and disclosed that increasing the number of quartet units within the quadruplex increases the  $Cu^{2+}$ - $Cu^{2+}$  distance.<sup>257</sup> Another approach of  $Cu^{2+}$  spin labeling is the covalent attachment of pyridine to the DNA termini. In this way, an extensive investigation of DNA quadruplexes was performed (Figure 30C).<sup>258,259</sup> Furthermore, a labeling strategy was made by introducing the commercially available 2,2'-dipicolylamine phosphoramidite (DPA) during solid phase synthesis opposite to an

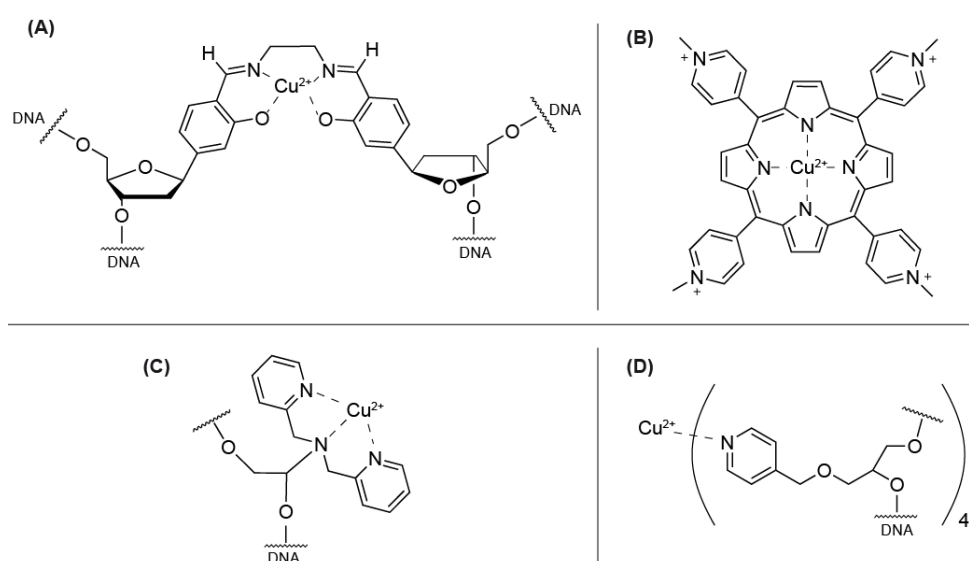


Figure 30.  $Cu^{2+}$  based spin labeling.



abasic site into a DNA duplex (Figure 30D). Chelation of the  $\text{Cu}^{2+}$  from the DPA allowed structure and nucleotide independent distance measurements.<sup>260–262</sup>

## 2. Aim of the Study

RNA is involved in many cellular processes and it is evident that not all functions have been revealed, yet. Based on the notion that function and structure are highly interwoven, for an understanding of RNA function on a molecular level, it is thus important to unravel the structures of RNAs.<sup>8,9,12,15,18,53,263–265</sup> The toolbox of structural biology and biophysics provides various methods to obtain these structures. One of these is electron paramagnetic resonance (EPR) spectroscopy, which is the main method used in this thesis, because it has no size restriction and the nucleic acid can be studied in solution.<sup>108–110,114,150,151,266,267</sup> In order to make the intrinsically diamagnetic RNA accessible for EPR methods, the RNA has to be spin labeled. The first aim of this thesis was to establish a labeling strategy for a new *gem*-diethyl nitroxide that can be easily and reproducibly performed. For the spin label attached to RNA, the EPR and *in cell* properties were to be determined. In a second step, the developed labeling methodology was to be used in combination with PELDOR to test experimentally the switching mechanism of the Guanidine-II riboswitch.<sup>48</sup> Last but not least, a reliable protocol was to be established for quantifying Mn<sup>2+</sup> binding sites in oligonucleotides by means of cw X-band EPR spectroscopy. This protocol is intended to be used to quantify the number and affinity of Mn<sup>2+</sup> binding sites in the 10-23 DNAzyme.

### 3. Results and Discussion

#### 3.1 Spin labeling of RNA with a *gem*-diethyl nitroxide via Click-chemistry

##### 3.1.1 The spin labeling reaction

In this section, it was the aim to establish an easy, reliable and reproducible labeling strategy for RNA with a *gem*-diethyl nitroxide. In this regard, Click-chemistry seemed most appropriate especially, since alkyne functionalized phosphoramidites are commercially available and the synthesis of the azido-functionalized *gem*-diethyl isoindoline **1\*** (Figure 31A) has been described in the literature.<sup>268</sup> In addition, the labeling of the *gem*-dimethyl analogue **2\*** on the 5-ethynyl-2'-deoxyuridine has been described before.<sup>209–211</sup> Here, this protocol was transferred to the *gem*-diethyl derivate.

Parts of this section was done under my supervision by Dominik Brajtenbach<sup>269</sup>, Simon Blume<sup>270</sup>, Felix Schmidt<sup>271</sup> in the context of their Bachelor theses and by Florian Haege<sup>272</sup> in context of his Master thesis.

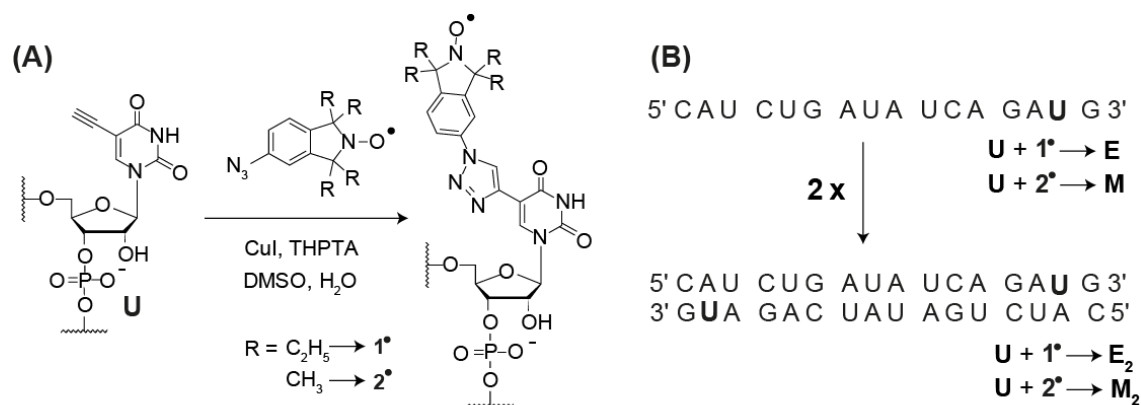


Figure 31. (A) Spin labeling reaction based on the CuAAC Click-reaction introducing **1\*** and **2\*** into RNA strands. (B) Sequence of the single strand RNA and the annealed duplex. "U" corresponds to the labeling positions. In the following, the RNA single strand labeled with **1\*** is referred to as **E**, while the one labeled with **2\*** is titled **M**. The spin labeled single stranded RNAs **E** and **M** were annealed to obtain duplexes **E<sub>2</sub>** and **M<sub>2</sub>**, respectively.

As the model system, the self-complementary 16-mer RNA in Figure 31B was chosen. Spin label **1**<sup>\*</sup> attached to the single strand is referred to as **E**, while annealed to the duplex it is called **E**<sub>2</sub>. In analogy, spin label **2**<sup>\*</sup> conjugated to the single strand is called **M** and assembled to the duplex **M**<sub>2</sub>. Inconclusive results were obtained regarding the spin labeling yields following the previously published protocol.<sup>210</sup> To achieve reliable yields, the spin labeling procedure was modified. Initially, the spin labeling reaction was carried out in a water bath at 37 °C for 20-30 minutes. In order to compensate temperature fluctuations occurring therein, the more temperature stable Thermomixer was used at 300 rpm. Furthermore, the temperature was increased to 60 °C and the reaction time was kept constant at 30 minutes. Additionally, the catalytically active solution was scaled up to a 10-fold excess, because the previously used small volumes were difficult to handle. These modifications of the protocol result in reproducible high ratios of labeled versus unlabeled RNA and isolated yields of 50 % with respect to the starting amount of RNA. The purification of the spin labeled RNA was performed with reverse phase high performance liquid chromatography (RP HPLC, Figure 32A).

The success of the labeling reaction and purification was confirmed by liquid chromatography mass spectrometry (LCMS, Figure 32B-E), showing in each case one peak at the expected mass. Spin counting by means of cw X-band EPR spectroscopy

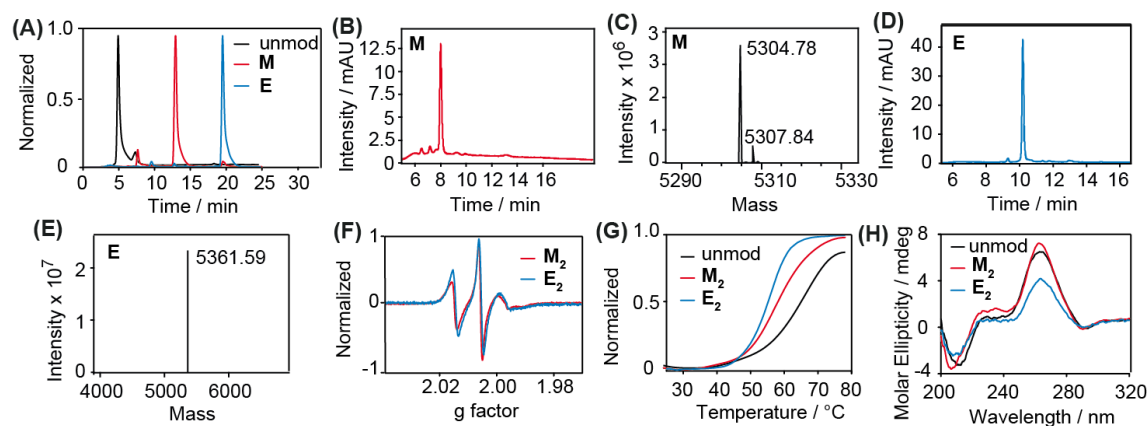


Figure 32. (A) Overlay of the HPLC runs of the unmodified (black line) and labeled RNAs **M** (red line) and **E** (blue line). (B) LCMS UV chromatogram and (C) deconvoluted mass of **M** (calculated mass 5305.03, found mass 5304.78). (D) LCMS UV chromatogram and (E) deconvoluted mass of **E** (calculated mass 5361.03, found mass 5361.59). (F) Experimental cwEPR spectra of 35  $\mu$ M **M**<sub>2</sub> (red line) and 35  $\mu$ M **E**<sub>2</sub> (blue line). The measured spin concentrations using the spin counting tool are 32  $\mu$ M for **M**<sub>2</sub> and 31  $\mu$ M for **E**<sub>2</sub>. (G) Temperature dependent UV VIS curves of the unmodified (black line,  $T_m = 66$  °C) and labeled RNAs **M**<sub>2</sub> (red line,  $T_m = 58$  °C) and **E**<sub>2</sub> (blue line,  $T_m = 55$  °C). (H) CD spectra of the unmodified (black line) and labeled RNAs **M**<sub>2</sub> (red line) and **E**<sub>2</sub> (blue line).

highlighted that each RNA strand carried a nitroxide i.e., the labeling was quantitative, and that no free label was present in the solution (Figure 32F).

### 3.1.2 Test for structural perturbation

The degree of perturbation of the native RNA structure is always an issue when introducing a modification such as a spin label. Especially, because the *gem*-diethyl isoindoline spin label is sterically more demanding than its *gem*-dimethyl analogue. Two methods were employed to test for the degree of structural perturbation, namely UV-VIS based melting studies and CD spectroscopy.

UV-VIS based melting curves were facilitated by measuring the absorbance at 260 nm in dependence of the temperature and setting the inflection point of the resulting curve equal to the melting temperature  $T_m$ . The  $T_m$  values of the unmodified and spin labeled RNAs were compared to access the influence of the spin label. For **M<sub>2</sub>**, a decrease was found for  $T_m$  by 4.0 °C per spin label in comparison to the unmodified duplex. For **E<sub>2</sub>**, the decrease for  $T_m$  was 5.5 °C per spin label (Figure 32G). Both values are in the usual range reported for these spin labels.<sup>209,210</sup>

CD spectroscopy is a light absorption spectroscopy measuring the difference between right- and left circularly polarized light. It has been shown that CD spectra are sensitive for different structures, thus structural perturbations should be visible.<sup>209,210,214,273,274</sup> Compared to the unmodified RNA, the CD spectra of **M<sub>2</sub>** and **E<sub>2</sub>** display only minor changes in the amplitude and the same characteristics of the negative and positive molar ellipticity at 210 and 270 nm (Figure 32H). Taking both results i.e., UV-VIS melting temperatures and CD-studies together, **1\*** was assessed to have only a minor local influence on the structure of the duplex RNA.

### 3.1.3 EPR characteristics

The relaxation time is an important characteristic of the spin labeled system, because it sets the upper limit of the accessible distance range within the PELDOR measurement. Therefore, 2PESEEM experiments were performed on  $\mathbf{M}_2$  and  $\mathbf{E}_2$  in the temperature range  $T = 10 - 120$  K and in dependence of the water content. Additionally, the suitable inversion recovery time was investigated finding a value for the optimal shot-repetition time of the PELDOR experiment.

#### 3.1.3.1 Temperature-dependent 2PESEEM measurements

The obtained 2PESEEM traces in the temperature range  $T = 10 - 120$  K are shown in Figure 33 and were fitted by a stretched bi-exponential decay given by eq. 18. The fitting parameters are listed in Table 1 and plotted against the temperature in Figure 34. The relaxation of  $\mathbf{M}_2$  and  $\mathbf{E}_2$  was found to consist of two components,  $T_{M1}$  and  $T_{M2}$  (Figure 34A), where the first-mentioned was dominated by nuclear spin diffusion ( $x_1 \sim 2$ ) and the latter by instantaneous diffusion ( $x_2 \sim 1$ ) (Figure 34B).<sup>158</sup>  $T_{M1}$  was assigned to a slower

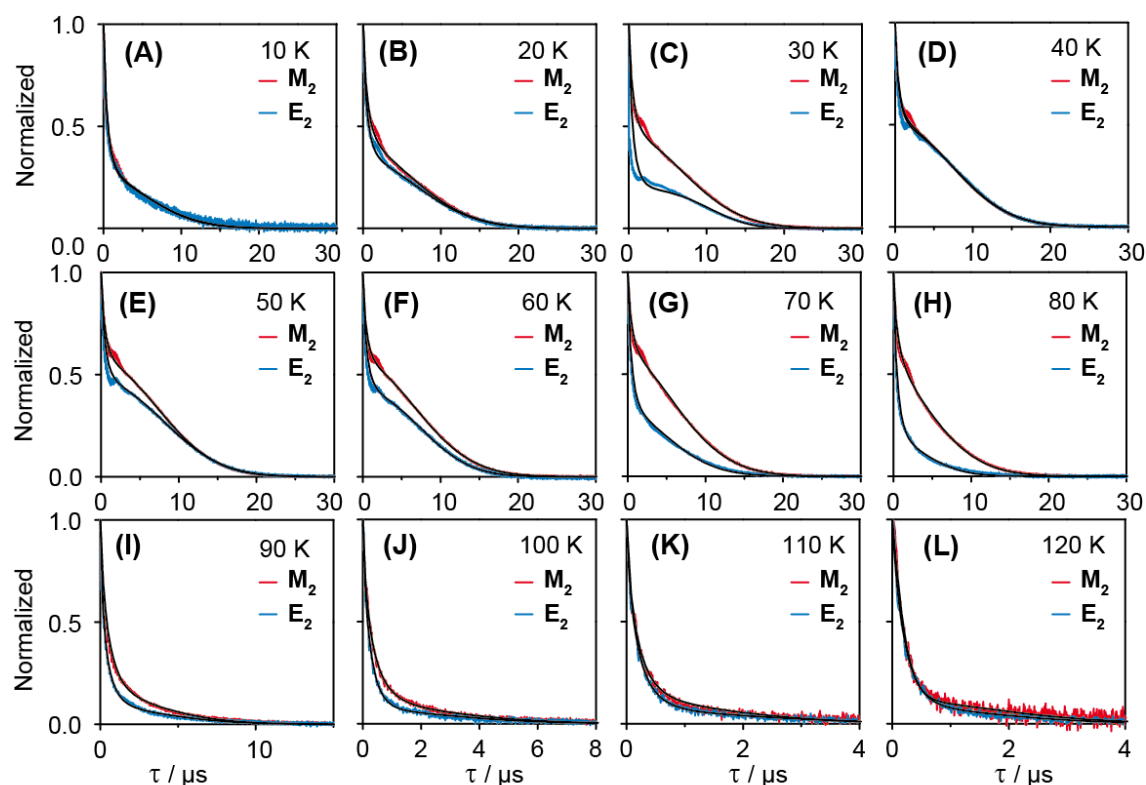


Figure 33. 2PESEEM traces of  $\mathbf{M}_2$  (red line) and  $\mathbf{E}_2$  (blue line) at temperatures between 10 K – 120 K overlaid with their fits (black line). The fit data are listed in Table 1.

relaxing process. The contributions of  $T_{M1}$  and  $T_{M2}$  are given by  $A_1$  and  $A_2$ , respectively (Figure 34C).

Table 1. Fitted parameters of the 2PESEEM traces of  $M_2$  and  $E_2$  in dependence of the temperature.

T / K	$M_2$						$E_2$					
	$A_1$	$T_{M1} / \mu\text{s}$	$x_1$	$A_2$	$T_{M2} / \mu\text{s}$	$x_2$	$A_1$	$T_{M1} / \mu\text{s}$	$x_1$	$A_2$	$T_{M2} / \mu\text{s}$	$x_2$
10	0.24	17.1	1.8	0.76	1.0	0.8	0.26	16.5	1.8	0.74	1.0	0.8
20	0.39	19.4	1.8	0.61	1.2	0.8	0.33	20.4	1.9	0.67	1.0	0.8
30	0.44	20.4	1.9	0.56	1.1	0.8	0.19	23.7	2.9	0.81	1.0	0.8
40	0.50	20.4	2.0	0.50	1.0	0.8	0.48	21.1	2.0	0.52	1.0	0.8
50	0.55	20.7	2.0	0.45	1.1	0.8	0.46	22.1	2.1	0.54	1.0	0.8
60	0.54	19.9	1.9	0.46	1.0	0.8	0.41	19.9	2.2	0.59	1.0	0.8
70	0.57	18.1	1.8	0.43	1.1	0.8	0.30	15.9	1.8	0.70	1.0	0.8
80	0.45	15.8	1.7	0.55	1.5	0.7	0.16	13.0	1.8	0.84	1.0	0.8
90	0.13	11.1	1.8	0.87	1.0	0.8	0.08	11.9	1.8	0.92	0.6	0.7
100	0.09	8.6	1.8	0.91	0.6	0.8	0.07	8.4	1.8	0.93	0.5	0.8
110	0.10	5.0	1.8	0.90	0.4	0.8	0.06	6.0	1.8	0.94	0.4	0.8
120	0.11	5.0	1.8	0.89	0.4	1.2	0.08	4.7	1.8	0.92	0.4	0.9

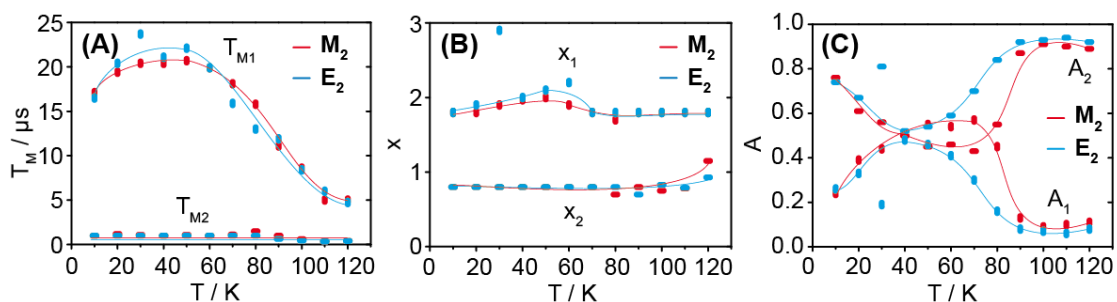


Figure 34. Plot of the fitted phase memory time relaxation parameters of  $M_2$  (red) and  $E_2$  (blue). The vertical line symbol displays the parameter with the subscript “1”, whereas the horizontal line symbol displays the parameter with the subscript “2”. (A) shows the variation of the phase memory times components  $T_{M1}$  and  $T_{M2}$  in dependence of the temperature, (B) the stretched exponents  $x_1$  and  $x_2$  and (C) the weighting factors  $A_1$  and  $A_2$ . Lines are shown as eye guidance in the same color code. For  $E_2$  at 30 K an outlier is suspected, so that this data point is excluded from the discussion.

At low temperatures (10 – 40 K), the 2PESEEM shapes of **M**<sub>2</sub> and **E**<sub>2</sub> were clearly dominated by instantaneous diffusion e.g.,  $A_2 = 0.7-0.8$  and  $x_2 = 0.8$  at 10 K, which is in agreement with the literature.<sup>151</sup> This implied that in this temperature regime, the rotation of the methyl and ethyl substituents was frozen.

The longest phase memory time was found at 50 K with values for **M**<sub>2</sub> of  $A_1 = 0.55$  and  $T_{M1} = 20.7 \mu\text{s}$  and for **E**<sub>2</sub> of  $A_1 = 0.46$  and  $T_{M1} = 22.1 \mu\text{s}$ . Accordingly, the phase memory times at this temperature point were composed of almost 50% nuclear spin diffusion and 50% instantaneous diffusion indicating an increased rotation of the methyl and ethyl substituents.

Interestingly, the 2PESEEM trace of **M**<sub>2</sub> exhibited a slightly longer  $T_M$  compared to **E**<sub>2</sub> (Figure 33). Since, the *gem*-substituents were the only difference between the spin labels, the ethyl for methyl exchange seems to slightly shorten the phase memory time. This is in agreement with the literature, as the shortening of the phase memory time due to additional protons was already published before.<sup>151,159,160,162–166</sup>

At entering higher temperatures i.e.,  $T = 60 - 120 \text{ K}$ , the phase memory time and the contribution of nuclear spin diffusion decreased (smaller  $T_{M1}$  and  $A_1$ ). This might be related to a promoted rotation of the *gem*-substituents. For **E**<sub>2</sub>, the fast-relaxing component gradually increased with rising temperature, whereas for **M**<sub>2</sub> an abrupt rise was observed at 80 K. The rotation of methyl groups is normally restricted to the temperature range of 80 - 250 K.<sup>161</sup> It seems likely that the ethyl groups exhibited a different rotation behavior than the methyl analogues.

At 120 K, the phase memory times of **M**<sub>2</sub> and **E**<sub>2</sub> matched and were dominated by a very fast ( $T_{M2} = 0.4 \mu\text{s}$ ) component that mainly arises from instantaneous diffusion ( $x_2 \sim 1$ ).

As pointed out above, the longest phase memory time of  $\sim 21 \mu\text{s}$  was observed at 50 K, which is the temperature at which PELDOR measurements are usually performed.<sup>147,149–</sup>

<sup>151</sup>

### 3.1.3.2 Solvent-dependent 2PESEEM measurements

In order to test if the newly introduced ethyl groups shield the unpaired electron from spin diffusion processes arising from the solvent, 2PESEEM measurements were conducted at 50 K in pure D<sub>2</sub>O and with 17% water content (Figure 35 and Table 2).

For **E**<sub>2</sub>, it can easily be seen, that the 2PESEEM decay curves significantly changes in dependence of the amount of deuterons (Figure 35A), and that there is only a minor difference between **M**<sub>2</sub> and **E**<sub>2</sub> (Figure 35B). The former effect was attributed to the nuclear spin diffusion process and can be explained by the larger magnetic moment of



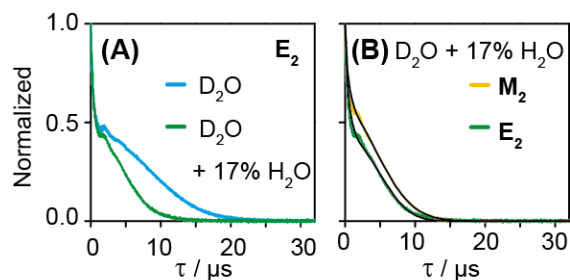


Figure 35. (A) 2PESEEM decay curves of **E<sub>2</sub>** in deuterated buffer (blue line) and in deuterated buffer with 17% additional water content (green line) both obtained at 50 K. (B) Comparison of the 2PESEEM traces of **M<sub>2</sub>** (yellow line) and **E<sub>2</sub>** (green line) in deuterated buffer with additional 17 % water recorded at 50 K.

Table 2. Fitting parameters of the 2PESEEM decay curves of **M<sub>2</sub>** and **E<sub>2</sub>** in dependence of the solvent.

	<b>M<sub>2</sub></b>						<b>E<sub>2</sub></b>					
	A <sub>1</sub>	T <sub>M1</sub> / μs	x <sub>1</sub>	A <sub>2</sub>	T <sub>M2</sub> / μs	x <sub>2</sub>	A <sub>1</sub>	T <sub>M1</sub> / μs	x <sub>1</sub>	A <sub>2</sub>	T <sub>M2</sub> / μs	x <sub>2</sub>
D <sub>2</sub> O	0.55	20.7	2.0	0.45	1.1	0.8	0.46	22.1	2.1	0.54	1.0	0.8
D <sub>2</sub> O + 17% H <sub>2</sub> O	0.54	13.7	2.0	0.46	1.0	0.8	0.40	13.3	2.3	0.60	1.0	0.8

protons compared to deuterons. The electron-proton dipolar coupling is thus larger than the electron-deuteron dipolar coupling.<sup>159,160</sup> Therefore, the spin flip of neighboring protons was expected to have a greater impact on the phase memory time. As can be seen from the fitting parameters in Table 2, the T<sub>M</sub> relaxation of **M<sub>2</sub>** and **E<sub>2</sub>** is dominated by T<sub>M1</sub> of 20-22 μs in pure D<sub>2</sub>O. T<sub>M1</sub> significantly shortened to a value of ~13 μs upon addition of H<sub>2</sub>O. Such a behavior has been reported before in the literature and is attributed to nuclear spin diffusion.<sup>151,159,160,162,163,165,166</sup> In contrast, T<sub>M2</sub> did not alter. Thus, the ethyl for methyl substitution has only a minor effect on T<sub>M</sub>, but the effect of deuteration is significant.

Indeed, such long phase memory times were reported before in the context of nitroxide radicals for deuterated proteins.<sup>162-164</sup> It was found that if the spin center is surrounded by deuterons within a critical range of < 1 nm, T<sub>M</sub> is significantly lengthened.<sup>161</sup> In cases of **1'** and **2'** the NO group has a distance of 0.7-1 nm to the backbone of the RNA, which does not contain protons (Figure 36). In addition, most protons in the RNA are exchangeable for deuterons just by exchanging the buffer. Thus tremendously reducing the number of protons in the critical range of the NO group.

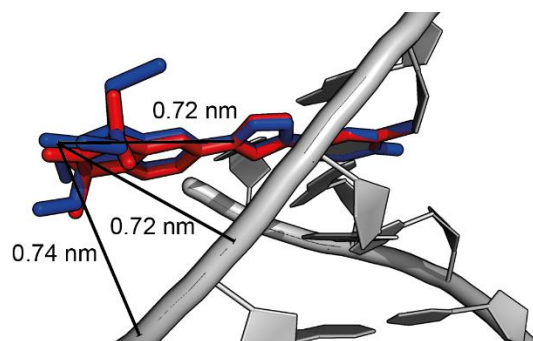


Figure 36. Illustration of the critical range of spin label 1\* (blue) and 2\* (red) attached to the RNA. The RNA model generation is explained in the appendix.

### 3.1.3.3 Magnetic field-dependent 2PESEEM measurements

In order to investigate if  $T_M$  is anisotropic i.e., depends on the magnetic field position, Hahn echo decay curves were recorded in the range of 11940 - 12056 G. Figure 37 shows that the maximal phase memory time can be achieved by recording the spectra on the maximum of the spectrum.

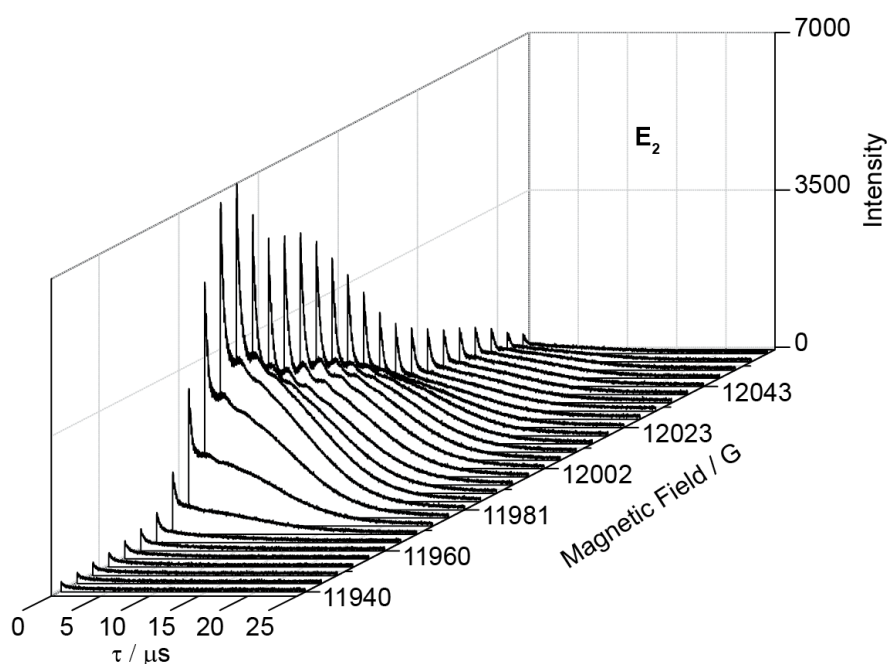


Figure 37. 2PESEEM measurements of  $E_2$  in dependence of the magnetic field recorded at 50 K.

### 3.1.3.4 Inversion recovery measurement

$T_1$  sets the lower limit for the shot-repetition time (SRT) of the PELDOR measurements in order to avoid saturation of the spin system. Since a faster SRT leads to more acquired PELDOR time traces per time, it is common to operate under partial saturation.<sup>150</sup> In Figure 38 the inversion recovery measurement of  $\mathbf{E}_2$  at 50 K is shown. The SRT for the following PELDOR measurements was set to 3 ms reflecting the time after which 70 % of the net magnetization has relaxed back to its thermal equilibrium.

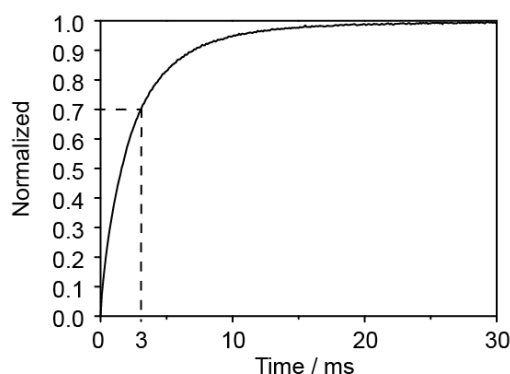


Figure 38. Inversion recovery measurement of  $\mathbf{E}_2$  recorded at 50 K. The marked data point reflects the SRT of 3 ms that is in the partially saturated region of the trace.

Summarizing the results from the relaxation study, the 2PESEEM measurements showed that PELDOR measurements should be recorded at 50 K in deuterated buffer and on the maximum of the EPR spectrum. Furthermore, the inversion recovery experiment at this temperature showed that a SRT of approximately 3 ms is suitable.

### 3.1.4 PELDOR measurements

A previous published study showed that **2'** is fairly rigid yielding orientation selectivity in PELDOR and thus access to angular information.<sup>209</sup> Here it was tested, whether this is also the case for **1'**. To this end, PELDOR measurements were conducted on different positions of the echo detected field-swept EPR spectrum (EDFS, Figure 39 and Table 3). As can be seen by eye, the PELDOR time traces do indeed oscillated with different dipolar frequencies and exhibited different modulation depths at different magnetic fields, thus indicating orientation selectivity (Figure 42A and B).<sup>107,150,169,170</sup>

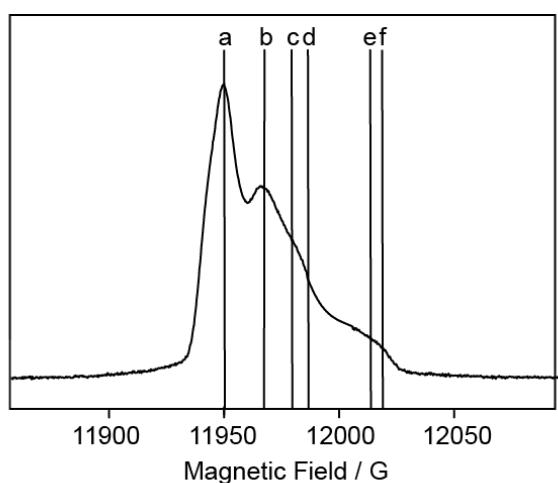


Table 3. Notation of the frequency offsets shown in Figure 39.

Pump Position	Detection Position	Frequency Offset/MHz
a	b	60
a	c	80
a	d	100
b	e	120
a	f	180

Figure 39. Echo detected field sweep (EDFS) of **E<sub>2</sub>** recorded at 50 K with the different pump and detection positions indicated as lines.

One way to reduce orientation selectivity is by summing the individual time traces and analyzing the summed time traces<sup>168–170</sup> with DeerAnalysis.<sup>275</sup> This yields the distance distribution in Figure 40 with the most probable distance of 4.69 nm for **M<sub>2</sub>** and 4.76 nm for **E<sub>2</sub>** and a distribution width of 1.30 nm and 1.33 nm, respectively.

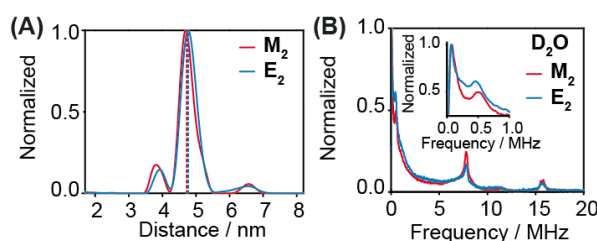


Figure 40. (A) Comparison of the generated distance distributions received from the sum of the time traces of **M<sub>2</sub>** (red line) and **E<sub>2</sub>** (blue line), and the distances calculated from the dipolar coupling frequency of the 2PESEEM pattern of **M<sub>2</sub>** (dotted red line) and **E<sub>2</sub>** (dotted blue line) indicated as dotted lines. (B) Frequency domain 2PESEEM spectrum of **M<sub>2</sub>** (red line) and **E<sub>2</sub>** (blue line). The inset is a Zoom-in for the frequency range 0-1 MHz. The dipolar coupling frequency of ~0.49 MHz is translated into the distance in (A).

Interestingly, the Fourier transformed 2PESEEM traces already encode the distance information. In Figure 40B the frequency spectra of  $\mathbf{M}_2$  and  $\mathbf{E}_2$  depict peaks at  $\sim 0.49$  MHz, 7.8 MHz and 15.6 MHz. Whereas the latter two were assigned to the Larmor frequency of  $^2\text{H}$  and its second harmonic, the first value is related to the dipolar coupling frequency. For  $\mathbf{M}_2$ , a value of 0.496 MHz was measured, which was transformed into a distance of 4.72 nm; for  $\mathbf{E}_2$ , a value of 0.482 MHz was observed, which resulted in a distance of 4.77 nm. Comparison with the distances received from DeerAnalysis<sup>275</sup> showed an excellent agreement (Figure 40A). However, it should be noted that cases in which the dipolar coupling is observed in 2PESEEM spectrum are very rare.<sup>162,163,276</sup>

A second way to analyze orientation selective time traces is by fitting each of them in a global approach. Here this is done by means of the program PeldorFit.<sup>167</sup>

PeldorFit uses a simple geometric model as given in Figure 41 assuming two spins, spin A and spin B, which are separated by a distance vector  $r$  and defined by the angles  $\xi$ ,  $\varphi$ ,  $\alpha$ ,  $\beta$ , and  $\gamma$ . The background-corrected PELDOR time traces and spectroscopic parameters were used as input to PeldorFit. The program fits the time traces using a genetic algorithm until a minimal root-mean-square deviation (RMSD) between the experimental and simulated data is achieved. The values are outputted together with a calculated error plot.<sup>167</sup>

In Figure 42, the best fits to the PELDOR time traces of  $\mathbf{M}_2$  and  $\mathbf{E}_2$  as well as the corresponding error plots for the distance and angular distributions are shown. The best values for each fitting parameter are collected in Table 4. The geometric parameters for  $\mathbf{M}_2$  and  $\mathbf{E}_2$  were best defined for the distance  $r$  and the angles  $\xi$  and  $\beta$  and were assessed to be very similar. Comparison with the distances received by the analysis of the summed PELDOR time traces and of the 2PESEEM spectrum revealed excellent agreement (Table 5).

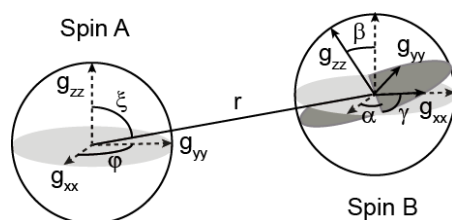


Figure 41. Geometric model used by PeldorFit.<sup>167</sup>

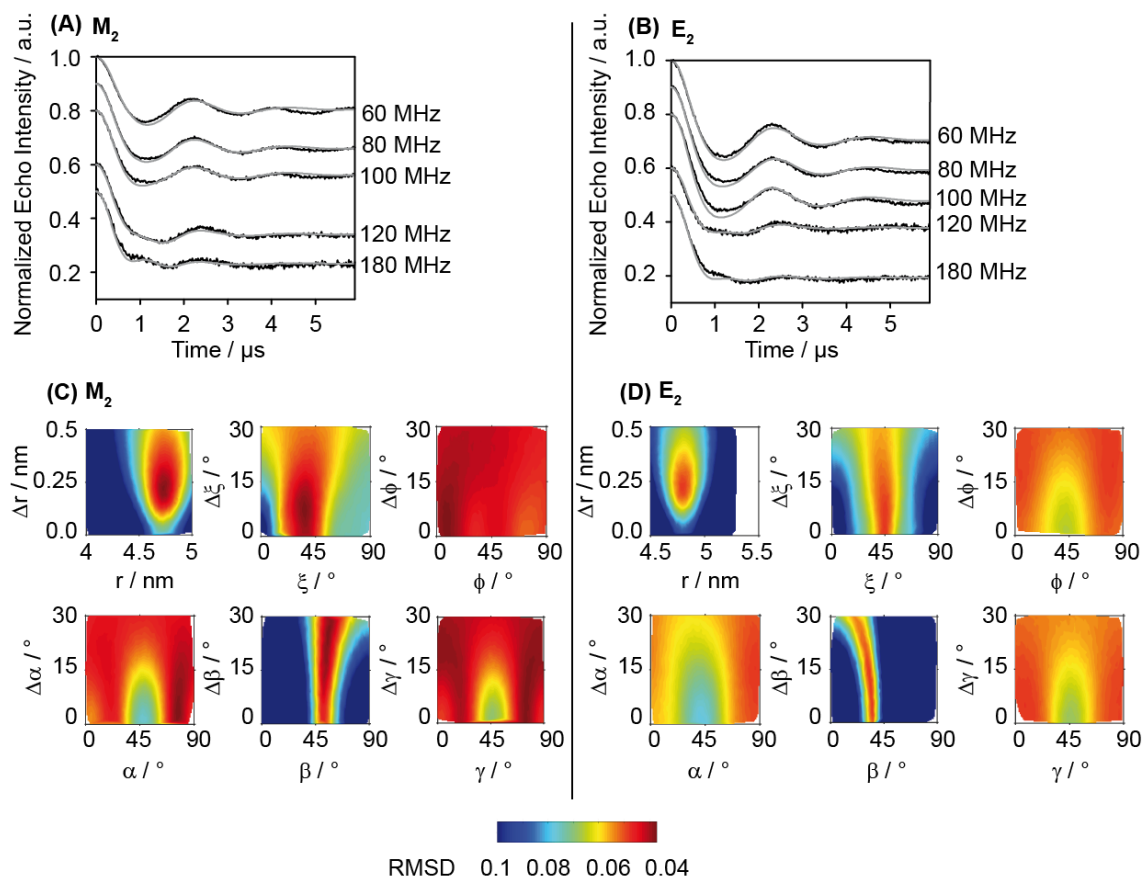


Figure 42. Background corrected Q-band PELDOR time traces acquired at different offsets (black lines) are overlaid with their PeldorFit<sup>167</sup> simulations (grey lines) for (A)  $\mathbf{M}_2$  and (B)  $\mathbf{E}_2$ . RMSD between experimental and simulated PELDOR time traces as a function of the geometric parameter of PeldorFit<sup>167</sup> for (C)  $\mathbf{M}_2$  and (D)  $\mathbf{E}_2$ .

Table 4. Geometric parameters of the PeldorFit<sup>167</sup> analysis of  $\mathbf{M}_2$  and  $\mathbf{E}_2$ .

Parameter			$\mathbf{M}_2$ <sup>[a]</sup>		$\mathbf{E}_2$ <sup>[a]</sup>	
$r$	$\Delta r$	/ nm	4.74 (0.06)	0.22 (0.07)	4.80 (0.06)	0.22 (0.08)
$\xi$	$\Delta\xi$	/ $^\circ$	37/143 (10)	7 (10)	44/136 (10)	4 (15)
$\beta$	$\Delta\beta$	/ $^\circ$	56/124 (5)	25 (15)	34/146 (5)	10 (15)

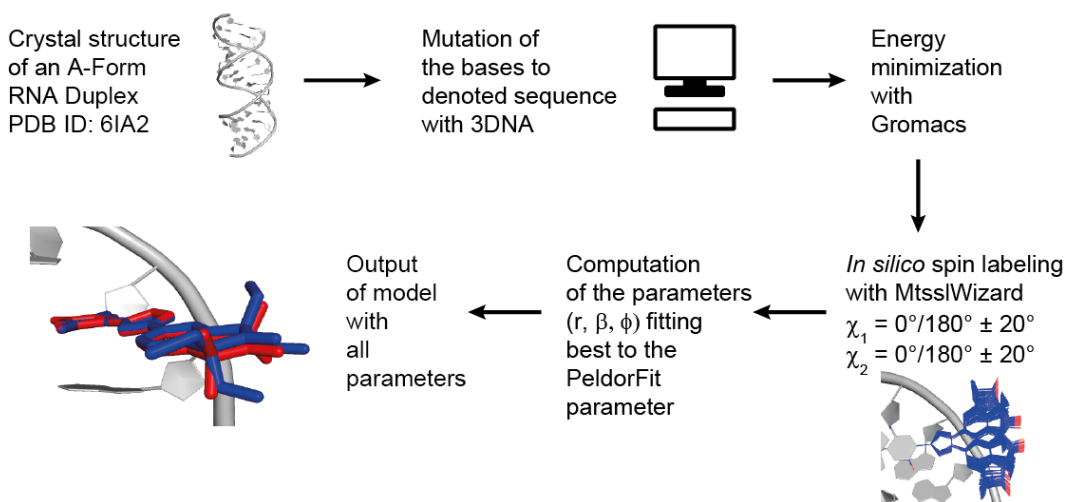
[a] The value in round brackets is in each case the error of this parameter. The error was determined as the parameter ranges in which 110% of the minimal RMSD were reached.

Table 5. Comparison of the three methods receiving the interspin distance of the two spin labels for **M<sub>2</sub>** and **E<sub>2</sub>** i.e., the analysis with DeerAnalysis<sup>275</sup> of the summed PELDOR time traces, the translation of the dipolar coupling frequency obtained in the 2PESEEM spectrum, and the analysis with PeldorFit.<sup>167</sup>

r / nm obtained by the	<b>M<sub>2</sub></b>	<b>E<sub>2</sub></b>
<b>summed</b> time traces analyzed with DeerAnalysis, <sup>275</sup>	4.69	4.76
translation of the dipolar coupling frequency observed in the <b>2PESEEM</b> spectrum, and the <b>PeldorFit</b> analysis. <sup>167</sup>	4.72	4.77
	4.74	4.80

### 3.1.5 Conversion of distance and angular distributions into label conformers

In order to translate the distances and angles into label conformations and to compare if **1\*** was aligned in the RNA in the same way as **2\***, an *in silico* model of the RNA duplex was generated (Scheme 1). Therein, the focus was on the angles  $\chi_1$  and  $\chi_2$  (Figure 43) as previous DFT calculations done on **M<sub>2</sub>** revealed that  $\chi_1$  has a single energy minimum at 0 ° and  $\chi_2$  two energetically equal minima at 0 ° and 180 °.<sup>209</sup> For the model generation, the crystal structure of an A-form RNA duplex (PDB ID: 6IA2) was used.<sup>277</sup> The base sequence was mutated *in silico* to the used sequence (Figure 31) with the program 3DNA<sup>278</sup> prior to energy minimization with Gromacs<sup>279–282</sup> using the CHARMM 36 all atom force field (version January 2018)<sup>283,284</sup> and conducted by Prof. Dr. Stephanie Kath-Schorr. Afterwards, the RNA was *in silico* spin labeled either with **1\*** or **2\*** within



Scheme 1. Illustration of the model generation. An A-Form RNA duplex (PDB ID: 6IA2)<sup>277</sup> was subjected to 3DNA<sup>278</sup> mutating the base sequence. Energy minimization was performed with Gromacs<sup>279–282</sup> using the CHARMM 36 all atom force field.<sup>283,284</sup> *In silico* model generation was executed with MtsslWizard<sup>285–287</sup> prior to comparison of the geometrical parameters of the model with the ones of PeldorFit.<sup>167</sup>

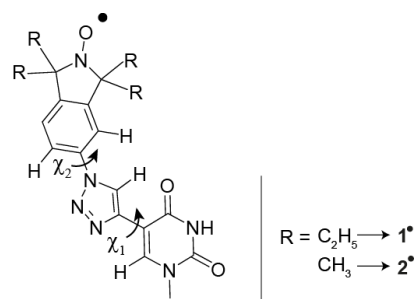


Figure 43. Spin label attached to the base with the denoted angles  $\chi_1$  and  $\chi_2$ .

MtsslWizard<sup>285–287</sup> with  $\chi_1$  and  $\chi_2$  both set to  $0^\circ \pm 20^\circ$  and  $180^\circ \pm 20^\circ$ . The values were chosen based on the results of the previous DFT calculations.<sup>209</sup> This generated 1000 different spin label conformers. A home-written python script provided by Dr. Dinar Abdullin was then used to determine the values of  $\chi_1$  and  $\chi_2$  that match the experimental results of  $r$ ,  $\xi$  and  $\beta$  best. The best scores for **M<sub>2</sub>** and **E<sub>2</sub>** are listed in Table 6. For both, **M<sub>2</sub>** and **E<sub>2</sub>** very similar  $\chi_1$  values of  $17^\circ$  and  $9^\circ$ , respectively and  $\chi_2$  of  $169^\circ$  and  $179^\circ$ , respectively, were obtained, which are in perfect agreement with the DFT calculations.<sup>209</sup> Thus, the results are in agreement with the CD and UV-VIS measurements indicating that **1\*** aligned comparable in the RNA as **2\***.

Table 6. Comparison of the PeldorFit<sup>167</sup> data for **M<sub>2</sub>** and **E<sub>2</sub>** with the parameters from their *in silico* generated models.

Parameter			<b>M<sub>2</sub></b>		Model <b>M<sub>2</sub></b>	<b>E<sub>2</sub></b>		Model <b>E<sub>2</sub></b>
$r$	$\Delta r$	/ nm	4.74	0.22	4.73	4.80	0.22	4.79
$\xi$	$\Delta \xi$	/ °	37/143	7	46	44/136	4	48
$\beta$	$\Delta \beta$	/ °	56/124	25	154	34/146	10	159
$\chi_1$		/ °			17			9
$\chi_2$		/ °			169			179



### 3.1.6 Implication of the long phase memory time

The longer the relaxation time  $T_M$ , the longer the time evolution window  $T$  can be chosen in a PELDOR experiment. In order to test, which time window is maximal feasible with  $\mathbf{1}^*$ , a PELDOR time trace with a 20  $\mu\text{s}$  dipolar evolution time window was recorded. After 24 h acquisition time, the time trace exhibited a clear oscillation and a reasonable signal-to-noise ratio (Figure 44A). The corresponding distance distribution yields a most probable distance of 4.73 nm, which is in perfect agreement with the distance data obtained above (Figure 44B). According to the plot in Figure 45, such a long time window does enable to measure distances of up to 8 nm.<sup>267</sup>

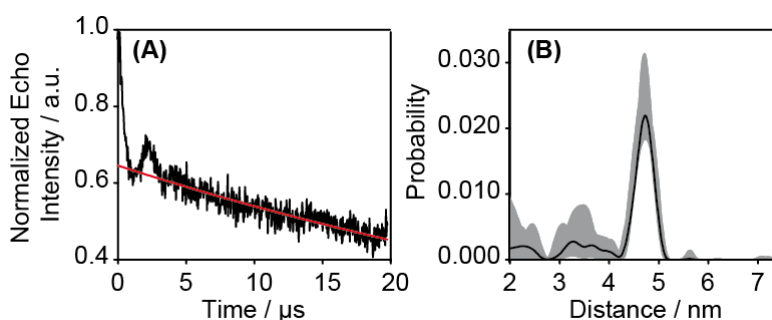


Figure 44. (A) PELDOR time trace of  $\mathbf{E}_2$  with an 80 MHz offset in deuterated buffer at 50 K and (B) the corresponding distance distribution.

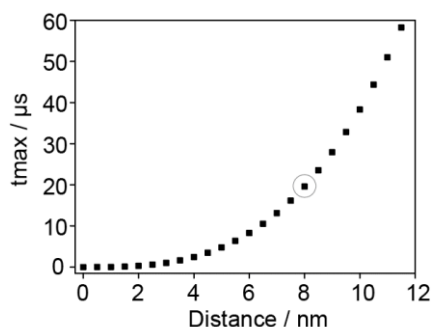


Figure 45. Plot of the maximum dipolar evolution time required for a reliable distance  $r$  (Adapted from Reference 267). The marked data point corresponds to the maximal phase memory time of  $\sim 21 \mu\text{s}$  obtained for  $\mathbf{E}_2$ .

### 3.1.7 Investigation of the spin label stability

*Gem*-diethyl isoindoline spin labels are said to be more stable under the reducing *in cell* conditions than their dimethyl analogues.<sup>192–196</sup> This was tested by Florian Haege in the context of his Master thesis, which I supervised.<sup>272</sup> Due to solubility issues,  $\mathbf{1}^*$  was coupled to DNA using the labeling protocol for RNA, which provided that the established labeling protocol is transferable to DNA. Figure 46 shows the obtained decay curves of

the cwEPR signal. One can easily see that  $1^{\bullet}$  has a considerable higher resistance towards reduction than MTSL. This is in agreement reported on other nitroxide spin labels with *gem*-diethyl groups and makes  $1^{\bullet}$  a promising candidate for *in cell* measurements.<sup>192–196</sup>

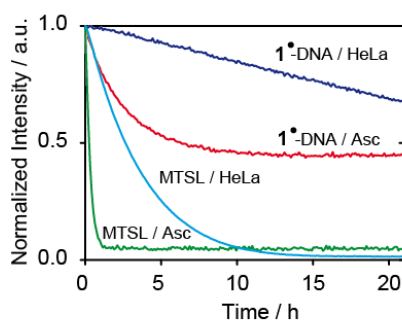


Figure 46. Stability decay curves of MTSL in ascorbate (green line) and HeLa extract (blue line), and  $1^{\bullet}$  attached to DNA in ascorbate (red line) and HeLa extract (purple line).

### 3.1.8 Analysis of *in cell* measurements

In the context of his Bachelor thesis that I supervised, Felix Schmidt attached  $1^{\bullet}$  to a DNA duplex with the aim of measuring *in cell* distances.<sup>271</sup> A test in MBS buffer verified that the spin labeling procedure was successful and that precise distance distributions can be obtained (Figure 47). However, the cwEPR X-band measurements on the labeled DNA injected into *Xenopus laevis* oocytes showed no nitroxide signal. Different obstacles were disclosed during the experimental *in cell* set-up. Beside the injection procedure itself, incubation times were evaluated as issue. It has to be ensure that the spin labeled sample had enough time to diffuse and thereby prevent spin clusters. But the injection time should not last too long to prevent that the spin label is fully reduced and thus no signal will be recorded. So far, the *in cell* measurements were not repeated but remain subject of ongoing studies.

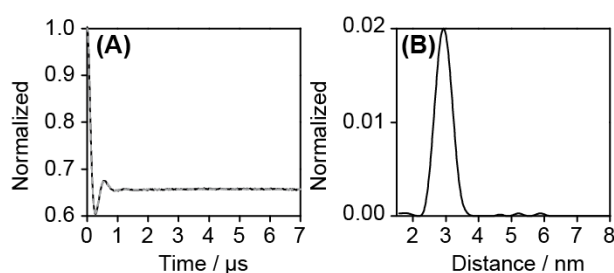


Figure 47. (A) Background corrected PELDOR time traces of  $1^{\bullet}$  attached to the DNA duplex at 50 K in MBS buffer and (B) the corresponding distance distribution.

## 3.2 The Guanidine-II Riboswitch

### 3.2.1 Analysis of the truncated hairpin $P_2^{U14}$

In 2017, the crystal structure of the truncated **P2** hairpin of the Guanidine-II riboswitch from *Pseudomonas aeruginosa* revealed a homo dimerization of the hairpins.<sup>48</sup> The kissing hairpin interaction is facilitated through the conserved ACGR sequence, which houses a Gdm<sup>+</sup> in each tetra loop site. To test if the kissing hairpin interaction can be found in solution, the truncated hairpin **P2** was singly spin labeled and analyzed by PELDOR measurements.

Parts of the work described in this section was done under my supervision by Maria F. Vicino in the context of her Master thesis.<sup>288</sup>

#### 3.2.1.1 Spin labeling

**1\*** was incorporated into the **P2** RNA sequence through CuAAC following the procedure above (Figure 48A). The labeled **P2** is now described as  $P_2^{U14}$ . The subscript denotes the hairpin, here **P2**, and the superscript the labeling position, here nucleotide U14. Separation of unlabeled ( $P_2^{\text{unmod}}$ ) and labeled RNA ( $P_2^{U14}$ ) was executed by RP HPLC.  $P_2^{\text{unmod}}$  was recognized to fold at room temperature into various conformations, resulting in four main peaks in the HPLC elugram (Figure 48B). This hinted towards the ability of **P2** to adopt different three-dimensional structures. In order to disrupt the tertiary structures and homogenize the RNA, the HPLC purification was performed at a column temperature of 60 °C. In this way, a defined peak was accomplished. Accordingly,  $P_2^{\text{unmod}}$  and  $P_2^{U14}$  were separated at a column temperature of 60 °C (Figure 48C). After desalting the desired HPLC fractions,  $P_2^{U14}$  was obtained with 60% yield with respect to the starting amount. The successful bioconjugation as well as purification was proven by LCMS (Figure 48D). A modification such as a spin label introduced into a RNA might always induces a structural disruption. The influence of the spin label on the RNA fold was assessed in the same way as for the model RNA by CD and UV-VIS based measurements (Figure 48E and F). The CD spectra of  $P_2^{\text{unmod}}$  and  $P_2^{U14}$  detected a very similar negative molar ellipticity at 210 nm and a positive one at 270 nm. The melting temperature decreased by 7 °C upon labeling, which is in the same range as reported in the literature before.<sup>209,210</sup> Based on these results, the influence of the spin label was substantiated as being insignificant and only local (Figure 48).

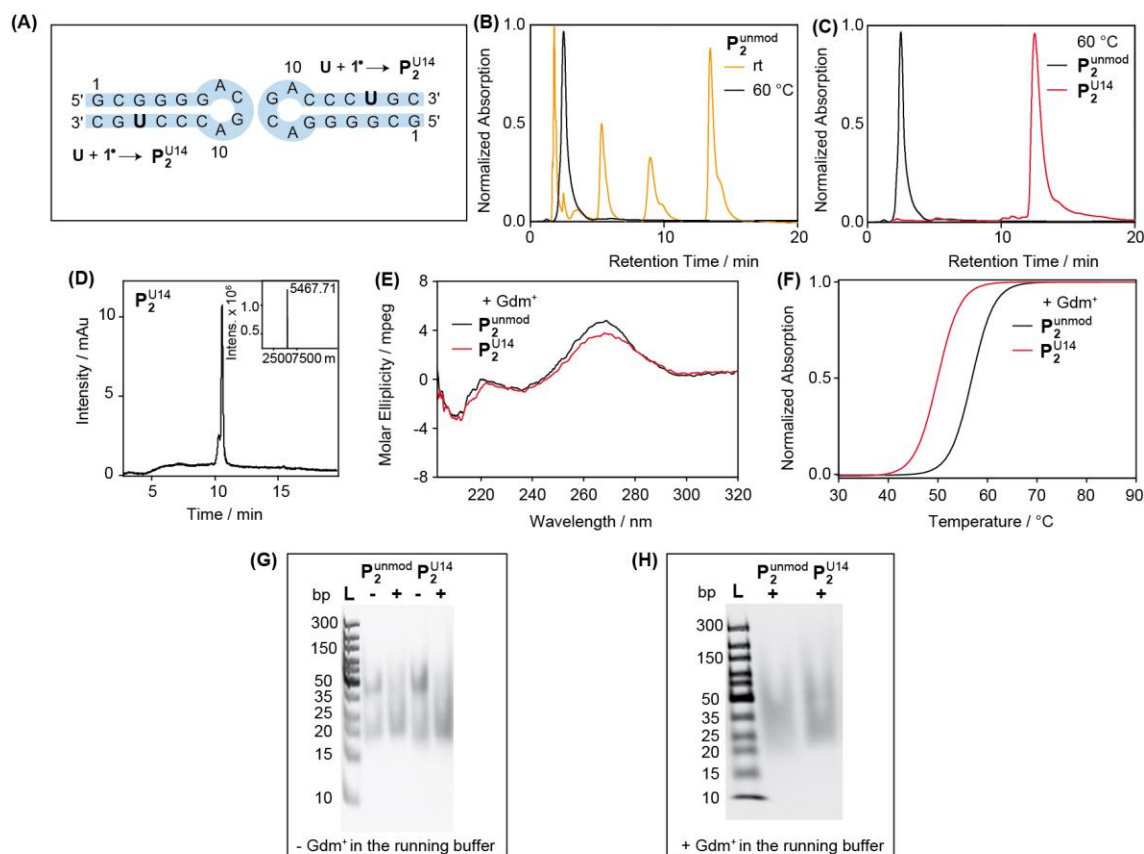


Figure 48. (A) RNA sequence of  $P_2$ . Introduction of spin label  $1^*$  at the position marked with the bold “U” leads the spin labeled construct referred to as  $P_2^{U14}$ . (B) HPLC run of the unmodified RNA performed at room temperature (orange line) and with the column heated to  $60\text{ }^\circ\text{C}$  (black line). (C) HPLC run of the unmodified RNA (black line) and labeled RNA (red line) performed at  $60\text{ }^\circ\text{C}$  column temperature. (D) LCMS UV chromatogram at  $254\text{ nm}$  and the deconvoluted ESI-mass shown as inset of  $P_2^{U14}$ . The calculated mass  $M_{\text{calc}}(P_2^{U14}) = 5443.10$  matched the found mass  $M_{\text{found}}(P_2^{U14}) = 5467.71$ , which was assigned to  $[M+^{23}\text{Na}]^+$ . (E) CD spectra and (F) UV-VIS melting curves of the unmodified  $P_2^{\text{unmod}}$  (black line) and labeled  $P_2^{U14}$  (red line) in the presence of  $\text{Gdm}^+$ .  $T_m(P_2^{\text{unmod}}) = 56.9\text{ }^\circ\text{C}$  and  $T_m(P_2^{\text{labeled}}) = 50.0\text{ }^\circ\text{C}$ . (G) 15 % native PAGE analysis of  $P_2^{\text{unmod}}$  and  $P_2^{U14}$  prepared in the absence (-) and presence (+) of  $\text{Gdm}^+$  during the fast annealing, and without  $\text{Gdm}^+$  in the running buffer. (H) 15 % native PAGE analysis of  $P_2^{\text{unmod}}$  and  $P_2^{U14}$  prepared in the absence (-) and presence (+) of  $\text{Gdm}^+$  during the fast annealing, and with  $\text{Gdm}^+$  in the running buffer. “L” depicts the GeneRuler ultra low range DNA ladder (ThermoFisher) with the base pair sizes on the left.

These results were further complemented by native PAGE (polyacrylamide gel electrophoresis) experiments. The native RNA is placed in a polyacrylamide gel and an electrophoresis power is supplied. The electrophoretic mobility depends on many factors such as the charge of the RNA, the RNA structural conformation, the RNA length, the interaction between RNA and ions in the gel running buffer, and the temperature. Consequently, the absolute electrophoretic mobility is difficult to predict, but the presence of different conformations can be visualized.<sup>289</sup>

15 % native PAGEs were prepared in the absence and presence of  $\text{Gdm}^+$  and with a fast

annealing (Figure 48G), which implies heating the sample at 95 °C and quickly cooling on ice. Standard staining procedures with ethidium bromide did not yield analyzable bands, probably because the short hairpins prevented intercalation. A post-staining procedure with GelRed generated better visible bands.

The native PAGE revealed two main bands running at the same height for  $P_2^{\text{unmod}}$  and  $P_2^{\text{U14}}$  at ~20 bp and ~50 bp (Figure 48G). A shift in the bands could be observed upon addition of  $\text{Gdm}^+$  yielding one main band at ~20 bp. Thus, the spin label does not perturb the structure. It is worth noting to say that the bands in presence of  $\text{Gdm}^+$  migrated faster than the ones in absence of  $\text{Gdm}^+$ . This indicated that dominantly a smaller RNA conformation was generated in the presence of  $\text{Gdm}^+$ , which was assigned to the monomer hairpin. To prove if  $\text{Gdm}^+$  ran out of the kissing hairpin structures and leaves monomer hairpins, native PAGEs were repeated in presence of  $\text{Gdm}^+$  during the sample preparation and additional in the running buffer (Figure 48H). All samples presented a smeared band at ~40 bp, which is higher than without  $\text{Gdm}^+$  in the running buffer. Thus, the running conditions clearly influenced the conformation of the samples. The proposed dominant conformations were: in the absence of  $\text{Gdm}^+$  during the sample preparation and in the absence of  $\text{Gdm}^+$  in the running buffer monomer hairpin and duplex; in the presence of  $\text{Gdm}^+$  during the sample preparation and in the absence of  $\text{Gdm}^+$  in the running buffer the monomer hairpin; in the presence of  $\text{Gdm}^+$  during the sample preparation and in the presence of  $\text{Gdm}^+$  in the running buffer the kissing hairpin. Nevertheless, the native PAGEs verified that the unmodified and labeled RNA captured comparable conformations that responded similar to  $\text{Gdm}^+$ .

### 3.2.1.2 PELDOR measurements

Due to the pronounced orientation selectivity induced by  $1^*$ , the measurements were repeated at various positions on the nitroxide EPR spectrum (Figure 49A), the orientation selective time traces summed up, and subsequent analyzed with DeerAnalysis.<sup>275</sup> The offset measurements, the summed data and the validated data of all measurements are listed in the appendix. An example of a set of orientation selective measurements is shown in Figure 49B.

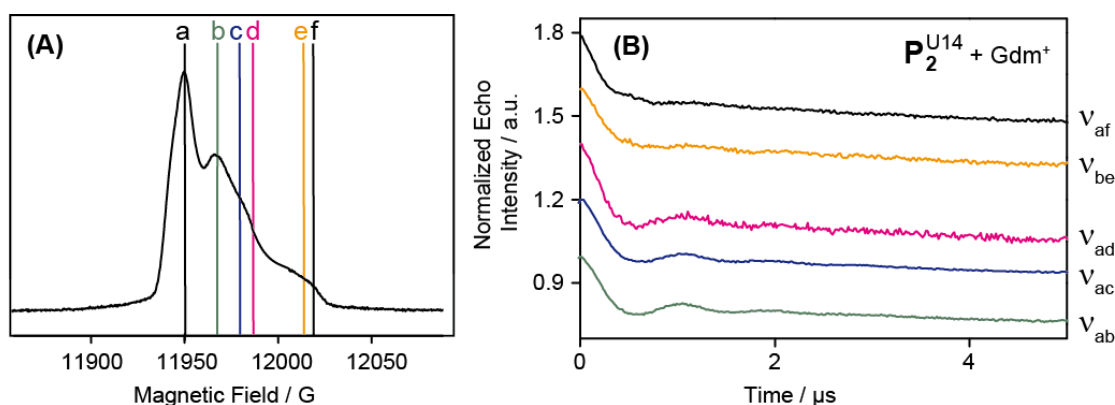


Figure 49. (A) EDFS with assigned pump and detection position. (B) Offset measurements of  $P_2^{U14}$  in the presence of 40 mM  $\text{Gdm}^+$  with the offsets measurements marked in (A), where  $v_{ab} = 60$  MHz,  $v_{ac} = 80$  MHz,  $v_{ad} = 100$  MHz,  $v_{be} = 120$  MHz,  $v_{af} = 180$  MHz.

In the absence of  $\text{Gdm}^+$ , the PELDOR time trace showed a low modulation depth of 8% and almost no oscillations (Figure 50A and B). For a pure two-spin system, a modulation depth of  $\sim 35\%$  indicates that all spins are coupled to each other; deviations indicate that either some spins have been reduced or that the RNA does not form a dimer of single strands. The former can be excluded due to the LCMS and cwEPR data (see above). Based on the modulation depth, the sample was thus assigned to be populated by 77% monomer hairpins. Consequently, only 23% of the solution was occupied by some sort

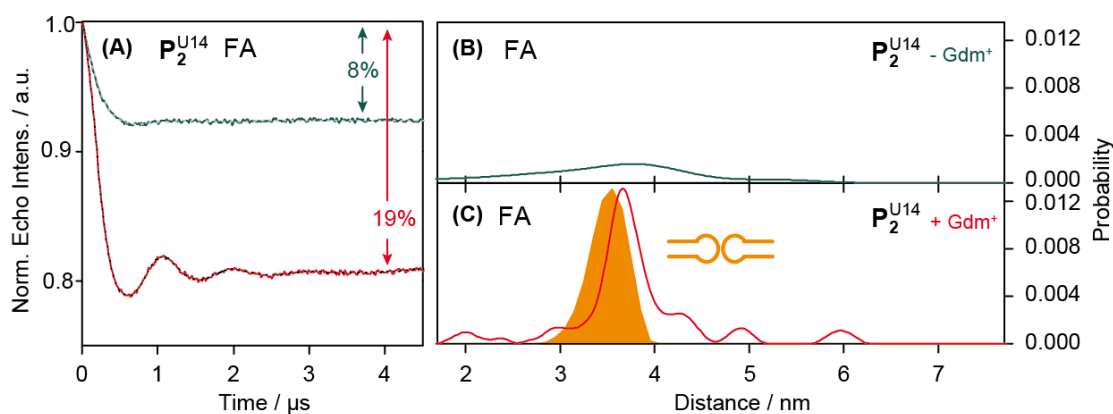


Figure 50. (A) Background corrected PELDOR time traces of  $P_2^{U14}$  in the absence (dark green line) and presence (red line) of  $\text{Gdm}^+$  and prepared with the Fast Annealing (FA). The fits are overlaid as grey or black dotted line, respectively. The modulation depths are indicated in percentages. (B) and (C) The corresponding distance distributions to the time traces in (A) shown as solid lines following the same color code as in (A). The *in silico* generated distance distribution is shown in orange. The structure used in MtsslWizard assigned to the distribution is shown next to it.

of dimer structures, which ones cannot be assigned as the corresponding distance distribution is too broad.

Adding 0.4 mM Gdm<sup>+</sup>, which corresponds to the 2- to 8-fold the K<sub>D</sub> of the full-length construct,<sup>46</sup> altered the shape of the dipolar trace (Figure 50A). The modulation depth increased to 19% and a clear oscillation was visible. The probability function yielded a main distance peak at 3.7 nm (Figure 50C). To assign if this distance peak arose from kissing hairpin formation, the crystal structure (PDB ID: 5VJ9)<sup>48</sup> was *in silico* spin labeled with MtssIWizard.<sup>285–287</sup> The theoretical obtained distance distribution matched the experimental data (Figure 50C). Accordingly, Gdm<sup>+</sup> led to the formation of the kissing hairpin that populate to 54% of the solution. To receive additionally angular information, PeldorFit was employed on the PELDOR data of the sample containing Gdm<sup>+</sup>.<sup>167</sup> Several attempts were undertaken but the experimental time traces could not be resembled by PeldorFit.<sup>167</sup> Thus, in the following, only the sum of the offset data were analyzed and exclusively distance distributions were obtained from the PELDOR data.

### 3.2.1.3 EPR analysis of fast versus slow annealed P<sub>2</sub><sup>U14</sup>

Maria F. Vicino examined in her Master thesis that the structural arrangement of **P2** can be influenced through the annealing procedure and that, besides the monomer and kissing hairpin, the duplex can be obtained.<sup>288</sup> The two annealing procedures employed are called Fast Annealing (FA) and Slow Annealing (SA). The first procedure implied that the sample is heated to 95 °C and quickly cooled on ice, whereas the latter followed the temperature program: heating to 95 °C for 5 min, cooling with 1 °C/min to 60 °C, resting at 60 °C for 3 min, cooling with 1 °C/min to 50 °C, resting at 50 °C for 3 min, cooling to 5 °C with 1 °C/min. The FA procedure was used for the native PAGEs and PELDOR measurements described above. The influence of the SA procedure is studied now.

cw X-band EPR spectroscopic measurements on the SA and FA sample revealed only minor differences, which could not be transformed into structural information (Figure 51). Adding Gdm<sup>+</sup> to both samples, FA and SA, did not change the cwEPR spectra. This indicated that the cwEPR spectra reflect only the local mobility and not the overall RNA structure.

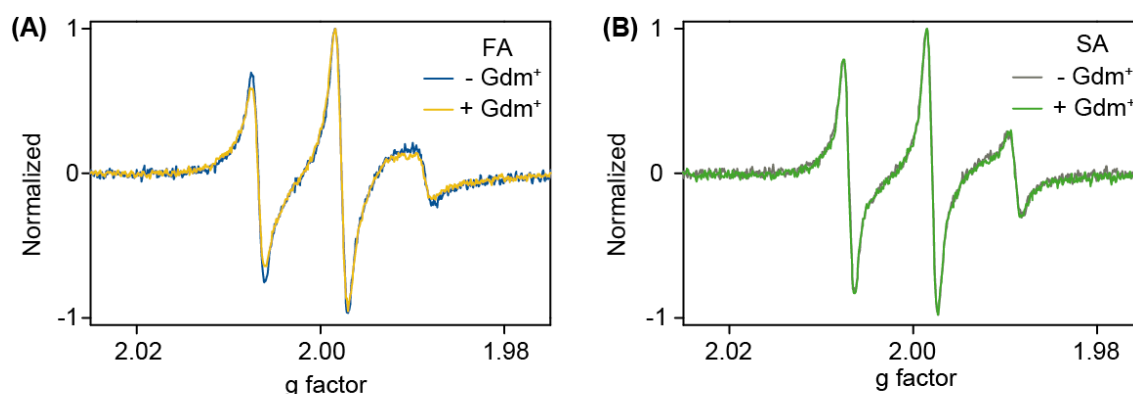


Figure 51. 25  $\mu\text{M}$  cwEPR measurements of  $\text{P}_2^{\text{U14}}$ . (A) The Fast Annealed (FA) RNA in the absence (-  $\text{Gdm}^+$ , blue line) and presence (+  $\text{Gdm}^+$ , yellow line) of  $\text{Gdm}^+$  and (B) the Slow Annealed (SA) RNA in the absence (-  $\text{Gdm}^+$ , grey line) and presence (+  $\text{Gdm}^+$ , green line) of  $\text{Gdm}^+$ . Spin counting revealed the following concentrations: FA:  $c(-\text{Gdm}^+) = 23 \mu\text{M}$  and  $c(+\text{Gdm}^+) = 27 \mu\text{M}$ . SA:  $c(-\text{Gdm}^+) = 23 \mu\text{M}$  and  $c(+\text{Gdm}^+) = 24 \mu\text{M}$ .

With PELDOR clear differences can be resolved. In the absence of  $\text{Gdm}^+$ , the dipolar trace of the SA sample of P2 exhibited a modulation depth of 13% (Figure 52A). The observed most probable distance is 4.0 nm (Figure 52B). To identify the structure, an A-Form RNA duplex was generated within 3DNA<sup>278</sup> and *in silico* spin labeled with MtssIWizard.<sup>285–287</sup> The theoretically obtained distance differed by only 0.25 nm from the experimental one, and was thus within the error of MtssIWizard.<sup>285–287</sup> Accordingly, the found structure was assigned to an A-form RNA duplex. Adding  $\text{Gdm}^+$  to the SA sample

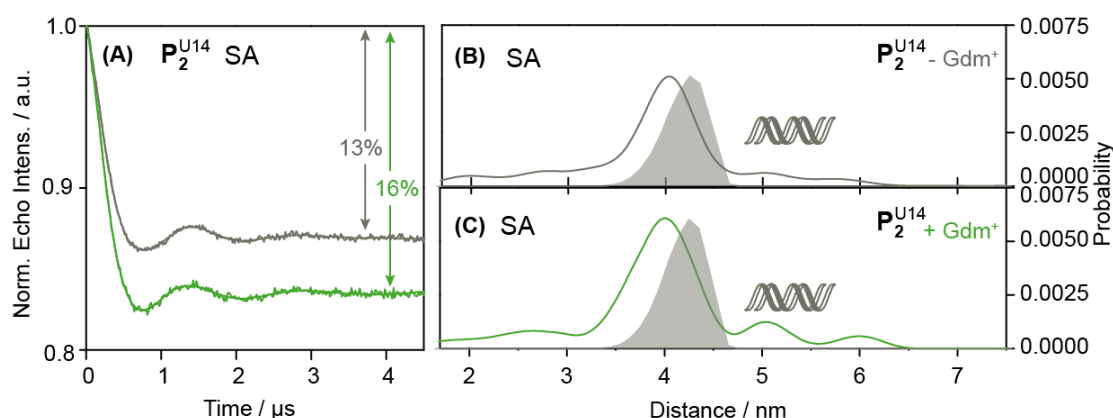


Figure 52. (A) Background corrected PELDOR time traces for the slowly annealed  $\text{P}_2^{\text{U14}}$  in the absence (dark green line) and presence (red line) of  $\text{Gdm}^+$ . The fits are overlaid as grey or black dotted line, respectively. The modulation depths are indicated in percentages. (B) and (C) show the corresponding distance distributions to the time traces in (A) shown as solid lines following the same color code as in (A). The *in silico* generated distance distribution is shown in grey. The structure used in MtssIWizard assigned to the distribution is shown next to it.



slightly increased the modulation depth to 16%, but did not change the distance distribution (Figure 52C). This indicates that  $\text{Gdm}^+$  cannot transform the duplex into the kissing hairpin structure. In contrast, the FA procedure yielded mainly the monomer hairpin in the absence of  $\text{Gdm}^+$ , which can be converted into the kissing hairpin dimer upon addition of  $\text{Gdm}^+$ .

### 3.2.1.4 Other methods to investigate fast versus slow annealed P2

This result was complemented by native PAGE experiments. The differently annealed samples were electrophoresed on a 15% native PAGE at 16 °C in the absence and presence of  $\text{Gdm}^+$  (Figure 53). Concentrations of RNA and  $\text{Gdm}^+$  were chosen comparable to the PELDOR measurements to avoid a concentration effect. In the absence of  $\text{Gdm}^+$ , two bands are obtained for both annealing procedures (I and III). Addition of  $\text{Gdm}^+$  lead to only one band also independent of the annealing protocol (II and IV). Thus, native PAGE was able to detect a structural change induced by  $\text{Gdm}^+$ . However, the native PAGE could not resolve the different structures due to the different annealing protocols, which might be due to the high temperature of the gel during the electrophoreses.

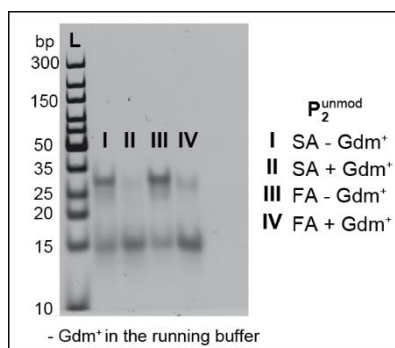


Figure 53. 15 % native PAGE of the unmodified P2 RNA with the different annealings in absence and presence of  $\text{Gdm}^+$ . The native PAGE was facilitated without  $\text{Gdm}^+$  in the running buffer.

Furthermore, CD spectroscopy was performed to see if the different structures lead to characteristic changes in the CD spectra. The concentrations of RNA and  $\text{Gdm}^+$  were chosen comparable to the PELDOR measurements to avoid effects resulting from the concentration. The experimental CD spectra showed the same minima at approximately 210 nm and 235 nm and a maximum at ~270 nm for the FA and SA as well as in the absence or presence of  $\text{Gdm}^+$  (Figure 54). Hence, CD spectroscopy is rather insensitive to these structural changes.

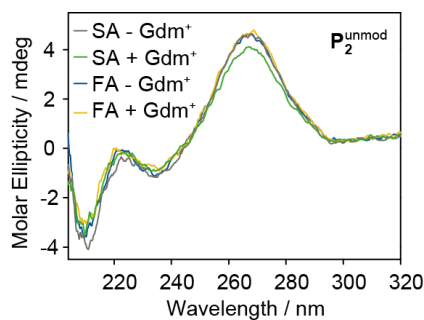


Figure 54. 25  $\mu\text{M}$  circular dichroism spectroscopic measurements of the different annealed unmodified **P2** in absence and presence of  $\text{Gdm}^+$ .

Finally, NMR spectroscopy was utilized to evaluate duplex, monomer and kissing hairpin structures. NMR spectroscopy is a reliable tool for RNA dynamic investigation in solution.<sup>90,91,93</sup> For this short RNA strand, imino proton resonance was assumed to yield enough information to verify the structural models.<sup>290–292</sup> The signals of the imino protons of guanine and uracil residues tend to appear between 10–15 ppm. They contain valuable information about base pairing in the RNA molecule, as only imino protons protected from exchange with the solvated water are observable.<sup>92,93,293</sup>

In Figure 55, the secondary structure of the kissing hairpin and the duplex of the **P2** hairpin are shown. Counting only the Watson-Crick base pairs and attribute each a separated peak, five peaks were suggested for the monomer hairpin, seven peaks for the kissing hairpin and six peaks for the duplex structure. The experimental  $^1\text{H}$ -NMR spectra of the differently annealed samples in absence and presence of  $\text{Gdm}^+$  are presented in Figure 55C–F. The FA sample in the absence of  $\text{Gdm}^+$  leads to an  $^1\text{H}$ -NMR spectrum with the expected five peaks for the hairpin. Adding  $^{14}\text{N}$ - $\text{Gdm}^+$  resulted in the occurrence of three additional peaks at 9.2, 12.9 and 13.0 ppm. Two additional peaks were expected upon formation of the kissing hairpin dimer and the third peak at 9.2 ppm might be due to the protons of the  $\text{Gdm}^+$  bound within the tetra loop but arises at a region untypically for imino protons. In order to test this, the  $\text{Gdm}^+$  was labeled with  $^{15}\text{N}$  and the  $^{15}\text{N}$ - $\text{Gdm}^+$  added to the FA sample. The  $^1\text{H}$ -NMR revealed that the peak at 9.2 ppm did not change (Figure 56), but instead a splitting of the peak at 6.5 ppm was observed (Figure 57). This splitting can be assigned to the free  $^{15}\text{N}$ - $\text{Gdm}^+$ , as this peak increased by adding  $^{15}\text{N}$ - $\text{Gdm}^+$  and showed a drastic higher intensity than the imino proton signals. However, the assignment of the peaks to the imino protons and the RNA structures is shaky. The SA procedure yielded six peaks and the spectrum did also not change upon addition of  $\text{Gdm}^+$  as expected from the PELDOR measurements. The absence of the

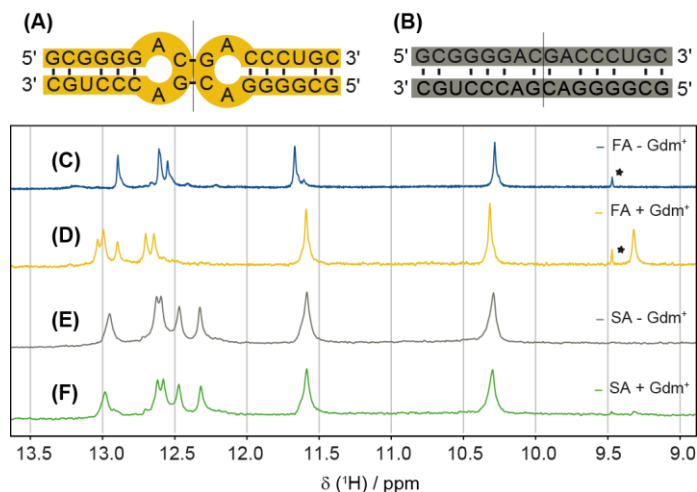


Figure 55. Secondary structure of (A) the **P2** kissing hairpin and (B) the **P2** duplex. The point symmetric plane is visualized as grey line. (C)-(F) <sup>1</sup>H NMR spectra of the iminio region of the differently annealed samples in the absence and presence of Gdm<sup>+</sup>. The asterisk indicates an impurity of the NMR tube.

peak at around 9.2ppm, maybe due to Gdm<sup>+</sup> not being able to bind in a tetra loop. Interestingly, the <sup>1</sup>H-NMR spectrum of the sample prepared with the SA procedure containing Gdm<sup>+</sup> but reannealed in the NMR spectrometer resemble the one of the FA containing Gdm<sup>+</sup> (Figure 58). However, without 2D experiments, it is difficult to assign the spectra and draw solid conclusions about the structures present. Yet, for such 2D NMR experiments, it was not enough RNA available.

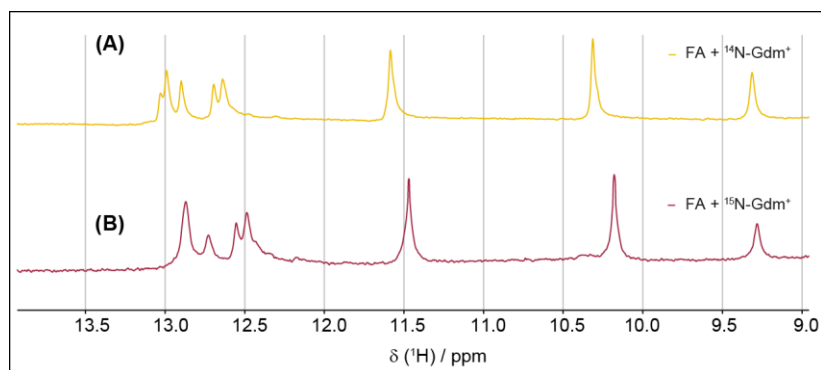


Figure 56. **P2** <sup>1</sup>H NMR spectra of (A) the Fast annealed sample subsequent to <sup>14</sup>N-Gdm<sup>+</sup> addition and (B) of the Fast annealed sample subsequent to <sup>15</sup>N-Gdm<sup>+</sup> addition.

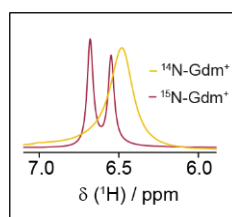


Figure 57. Comparison of the <sup>1</sup>H NMR spectra of the <sup>14</sup>N-Gdm<sup>+</sup> (yellow line) and <sup>15</sup>N-Gdm<sup>+</sup> (red line) free in solution.

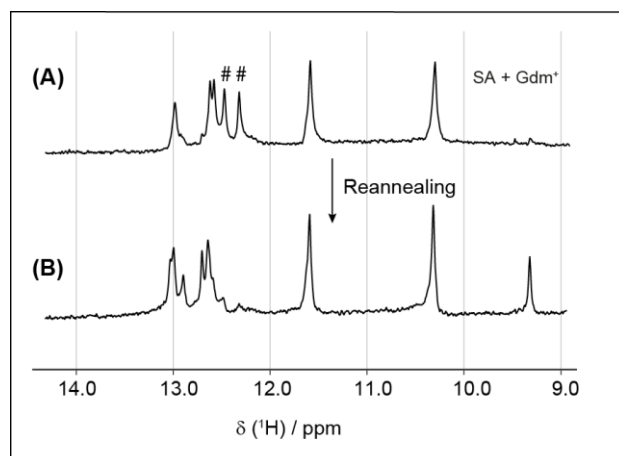


Figure 58. P2 <sup>1</sup>H NMR spectra of (A) the SA sample after addition of Gdm<sup>+</sup> and (B) of the reannealed sample.

### 3.2.2 Analysis of the truncated hairpin $P_1^{U18}$

In 2007, Weinberg et al. published base sequences of the Guanidine-II riboswitch from different species resulting from a bioinformatic genome analysis. They found that the hairpins **P1** and **P2** share their conserved ACGR tetra loop, but the stem length is variable.<sup>43</sup> A closer look at the characters of the hairpins showed that the **P1** stem length mainly exceeds the **P2** stem length (Figure 59). In this chapter, the hairpin with the longer stem **P1** was analyzed. Parts of this chapter were included in the Bachelor thesis of Marcel Mueller<sup>294</sup>, which I supervised.

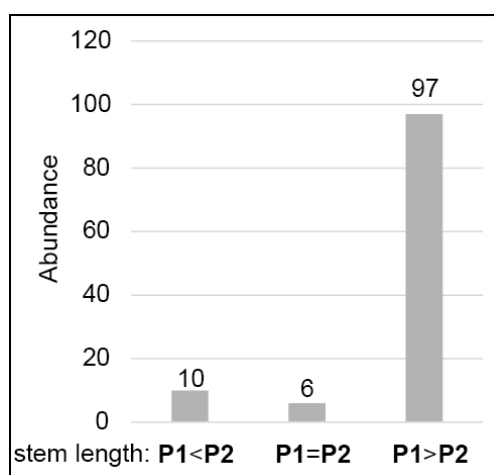


Figure 59. Comparison of the abundance of the events that the **P1** stem length is shorter (**P1<P2**), has the same length (**P1=P2**) or exceeds the **P2** stem length (**P1>P2**).

#### 3.2.2.1 Spin labeling

The spin labeling position in **P1** was chosen to be approximately at the same position as in **P2**, and approximately 3-4 nt below the tetra loop to avoid that the binding property is perturbed, and further at a natural occurring uridine residue. Thus, the uridine U18 was spin labeled yielding the spin labeled RNA referred to as  $P_1^{U18}$  (Figure 60A).

Introduction of  $1^*$  in the 22 nt long **P1** RNA strand was executed with the protocol established above. HPLC purification was directly performed at 60 °C to guarantee a homogeneous sample with respect to the tertiary fold (Figure 60B). The successful isolation of the spin labeled product was proven by LCMS, showing one peak at the expected mass (Figure 60C). Spin counting by means of cwEPR X-band measurements indicated that each **P1** strand carried a nitroxide i.e., the labeling was quantitative and

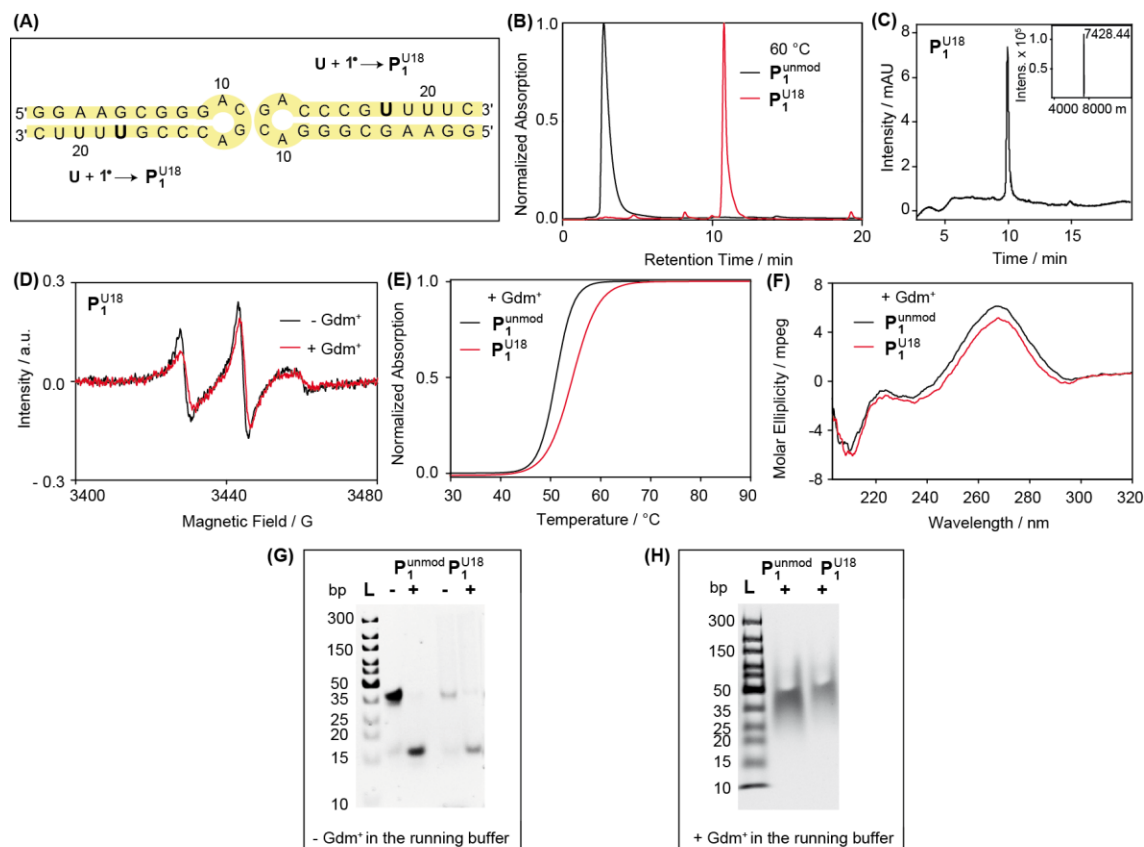


Figure 60. (A) RNA sequence of **P1**. Introduction of spin label **1\*** at the position marked with a bold “**U**” leads to the spin labeled construct referred to as  $P_1^{U18}$ . (B) HPLC run of the unmodified RNA ( $P_1^{\text{unmod}}$ ) (black line) and the labeled RNA ( $P_1^{U18}$ ) (red line) performed at 60 °C column temperature. (C) LCMS UV chromatogram and the deconvoluted ESI-mass of the labeled RNA shown as inset. The calculated mass  $M_{\text{calc}}(P_1^{U18}) = 7365.23$  matched the found mass  $M_{\text{found}}(P_1^{U18}) = 7428.44$ , which was assigned to  $[M+^{23}\text{Na}+^{39}\text{K}]^+$ . (D) 25  $\mu\text{M}$  cwEPR spectra in the absence (black line) and presence (red line) of  $\text{Gdm}^+$ . Spin counting revealed the following concentrations:  $c(-\text{Gdm}^+) = 26 \mu\text{M}$  and  $c(+\text{Gdm}^+) = 21 \mu\text{M}$ . (E) UV-VIS melting curve of  $P_1^{\text{unmod}}$  (black line) and  $P_1^{U18}$  (red line) RNA in the presence of  $\text{Gdm}^+$ .  $T_m(P_1^{\text{unmod}}) = 51.0 \text{ }^\circ\text{C}$  and  $T_m(P_1^{U18}) = 54.4 \text{ }^\circ\text{C}$ . (F) CD spectra of  $P_1^{\text{unmod}}$  (black line) and  $P_1^{U18}$  (red line) in the presence of  $\text{Gdm}^+$ . (G) 15 % native PAGE analysis of  $P_1^{\text{unmod}}$  and  $P_1^{U18}$  prepared in the absence (-) and presence (+) of  $\text{Gdm}^+$  during the fast annealing, and without  $\text{Gdm}^+$  in the running buffer. (H) 15 % native PAGE analysis of  $P_1^{\text{unmod}}$  and  $P_1^{U18}$  prepared in the absence (-) and presence (+) of  $\text{Gdm}^+$  during the fast annealing, and with  $\text{Gdm}^+$  in the running buffer. “L” depicts the GeneRuler ultra low range DNA ladder (ThermoFisher) with the base pair sizes on the left.

no free spin label is present in the solution (Figure 60D). Isolated yields of 72 % with respect to the starting amount of RNA were obtained.

The degree of the structural perturbation in **P1** induced by **1\*** was tested in the same way as for **P2** and found to be comparable. The melting temperature  $T_m$  is reduced by 3 °C per spin label and the CD spectra of modified and unmodified RNA is superimposable (Figure 60E and F). Therefore, the spin label influence was assessed as being minor

and local.

Additionally, the native PAGE showed that unmodified and labeled RNA captured comparable conformations as response to  $\text{Gdm}^+$  (Figure 60G and H)

### 3.2.2.2 PELDOR measurements

PELDOR measurements were performed on samples of **P1** prepared with the Fast annealing (FA), because this protocol yielded the hairpins in the case of **P2**. In the absence of  $\text{Gdm}^+$ , the PELDOR time trace of  $\text{P}_1^{\text{U18}}$  exhibited a pronounced oscillation (Figure 61A). The modulation depth of 27% implied that 77% of the RNA populates a dimer structure. The corresponding distance distribution showed a maximum at 4.8 nm (Figure 61B). Since this distance did not match the theoretically expected distance of the kissing hairpin of 4.1 nm,<sup>49,285–287</sup> an A-Form duplex was generated<sup>278</sup> and subjected to *in silico* spin labeling.<sup>285–287</sup> The experimental found distance fit to this nearly self-complementary duplex. A crystal structure of **P1** was already solved in the absence of  $\text{Gdm}^+$  in the context of a Dissertation. It viewed a duplex as well.<sup>295</sup>

Adding 0.4 mM  $\text{Gdm}^+$ , which was sufficient for the kissing hairpin formation of  $\text{P}_2^{\text{U14}}$ , did not induce a conformational change. Increasing the  $\text{Gdm}^+$  concentration to 40 mM, led to an increase of the modulation depth to 32% (Figure 61A). This indicates that the solution now contains almost 100% dimers. The corresponding distance distribution

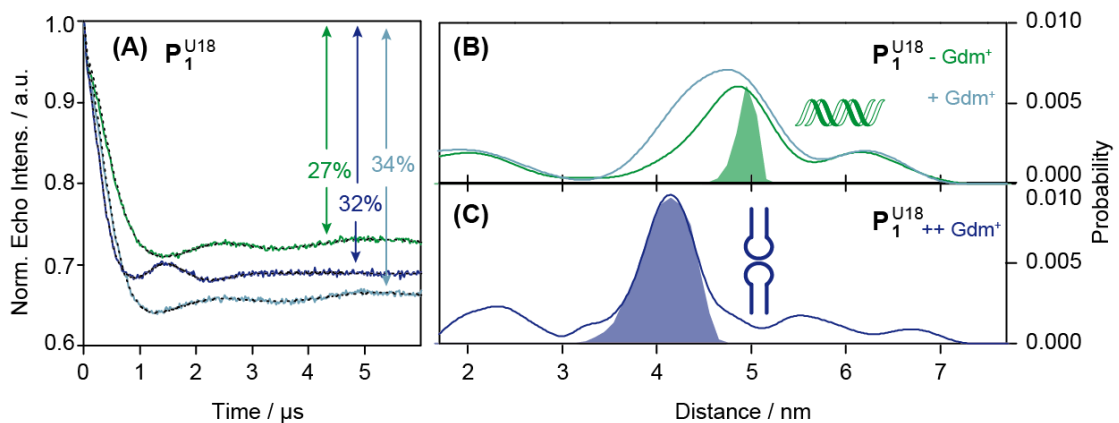


Figure 61. (A) Background corrected PELDOR time traces for  $\text{P}_1^{\text{U18}}$  in the absence (green line) and presence of 0.4 mM (blue line) and 40 mM (purple line)  $\text{Gdm}^+$ . The fits are overlaid as black dotted lines, respectively. The modulation depths are indicated in percentages. (B) and (C) The corresponding distance distributions to the time traces in (A) shown as solid lines following the same color code as in (A). The *in silico* generated distance distributions are shown as green and purple areas, respectively. The structure used in MtssWizard assigned to the distribution is shown next to it.

revealed that the most probable distance is now shifted from 4.8 nm to 4.1 nm, matching perfectly the *in silico* predicted distance of the kissing hairpin dimer of **P1** (Figure 61C).

The distance distribution of the sample with 0.4 mM Gdm<sup>+</sup> deserved a closer inspection. It was tested if the experimental obtained distance distribution is a superposition of the peaks corresponding to the duplex and the kissing hairpin structure. The assigned distance distributions were normalized and fitted by Gaussians (Figure 62) through

$$y = y_0 + \left( \frac{A}{\sqrt{2\pi w^2}} \right) \times e^{-\frac{(x-x_c)^2}{2w^2}} \quad \text{eq. 19}$$

wherein  $y_0$  is the offset,  $x_c$  is the center,  $A$  the amplitude and  $w$  the width of the Gaussian peak. The superposition showed that the 0.4 mM sample is indeed a mixture of 68% duplex and 32% kissing hairpin.

Interestingly, for the hairpins with the shorter stems **P<sub>2</sub><sup>U14</sup>** 0.4 mM Gdm<sup>+</sup> were sufficient to form the kissing hairpins. In contrast, for **P<sub>1</sub><sup>U18</sup>**, higher concentrations were needed. The longer stem of **P1** is probably the cause of this. With more G-C base pairs, the additional hydrogen bonds favor the formation of a stable duplex and it maybe that only higher amounts of Gdm<sup>+</sup> can induce the switch to the kissing hairpin.

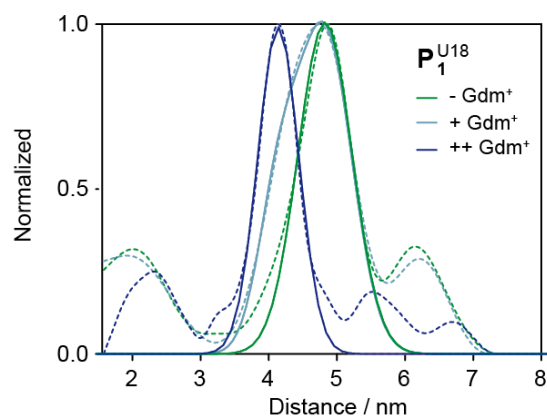


Figure 62. Gaussian fits of the normalized distance distributions corresponding to the PELDOR measurements of **P<sub>1</sub><sup>U18</sup>** (solid lines) overlaid with the experimental measurements (dotted lines).



### 3.2.2.3 $^1\text{H-NMR}$ measurements

In Figure 63 the secondary structure of the kissing hairpin and the duplex of the **P1** hairpin are shown. Counting the Watson-Crick base pairs and attribute each a separated peak, seven peaks were suggested for the monomer hairpin, nine peaks for the kissing hairpin and eight peaks for the duplex structure. Samples of **P1** prepared with FA and SA procedure yielded in the absence and presence of  $\text{Gdm}^+$  the  $^1\text{H-NMR}$  spectra in Figure 63. With the FA in the absence of  $\text{Gdm}^+$ , it can be clearly seen that broad peaks were obtained, which hindered counting of the peaks. The presence of  $\text{Gdm}^+$  leads to a structure from which sharper peaks were obtained. There maybe nine imino peaks, which would correspond to the number of peaks expected for the kissing hairpin. Interestingly, the peak at 9.2 ppm arose here as well in the presence of  $\text{Gdm}^+$ . For the SA sample nine imino peaks were observed in the absence of  $\text{Gdm}^+$ , which does not match to the expected eight imino peaks for the duplex structure. Addition of  $\text{Gdm}^+$  did not change the spectrum as expected for the duplex. However, for an assignment 2D NMR experiments are required, for which was not enough RNA available.

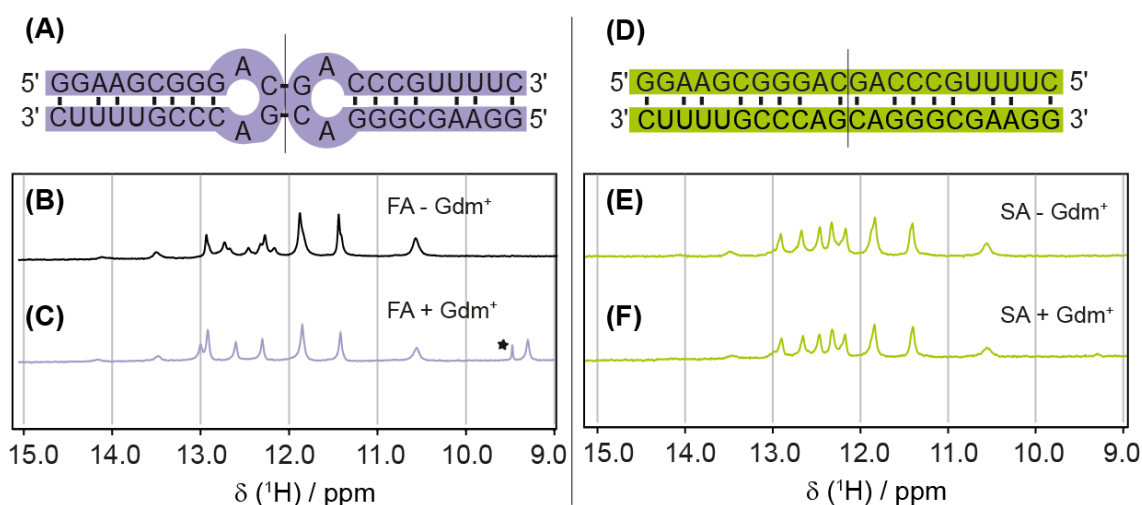


Figure 63. (A) Secondary structure of **P1** forming the kissing hairpin.  $^1\text{H}$  NMR spectra of the imino region (B) upon FA in the absence of  $\text{Gdm}^+$  and (C) in the presence of  $\text{Gdm}^+$ . (D) Secondary structure of the **P1** duplex.  $^1\text{H}$  NMR spectra of the imino region (E) upon SA in the absence of  $\text{Gdm}^+$  and (F) after addition of  $\text{Gdm}^+$ . The asterisk indicates an impurity signal of the NMR tube.

### 3.2.3 Analysis of the hetero hairpin mixture $P_1^{U18} | P_2^{U14}$

The proposed switching model of the Guanidine-II riboswitch is based on the kissing hairpin interaction between **P1** and **P2**.<sup>48</sup> Up to this chapter, only the homo dimers **P2 | P2** and **P1 | P1** were analyzed. Therefore, the next step was to mix the hairpins and investigate if the hetero kissing hairpin dimer **P1 | P2** can be detected.

#### 3.2.3.1 PELDOR measurements

Mixing  $P_2^{U14}$  and  $P_1^{U18}$  in equal amounts yielded the PELDOR time traces and distance distributions shown in Figure 64. In the absence of  $Gdm^+$ , a time trace with 21% modulation depth was obtained, which yielded a broad distance distribution. This matches the expectation, since a mixture of RNA structures was expected, due to the results from the measurements on pure  $P_2^{U14}$  and  $P_1^{U18}$ . Adding  $Gdm^+$  increased the modulation depth to 30% indicating that 86% of the sample is some kind of dimer. The corresponding distance distribution presented a maximum at 4.0 nm. Whether the homo dimers  $P_1^{U18} | P_1^{U18}$  and  $P_2^{U14} | P_2^{U14}$  and/or the hetero dimer  $P_1^{U18} | P_2^{U14}$  were formed was not distinguishable because the *in silico* derived distances are with 4.1 nm, 3.7 nm and 3.5 nm too close to each other.

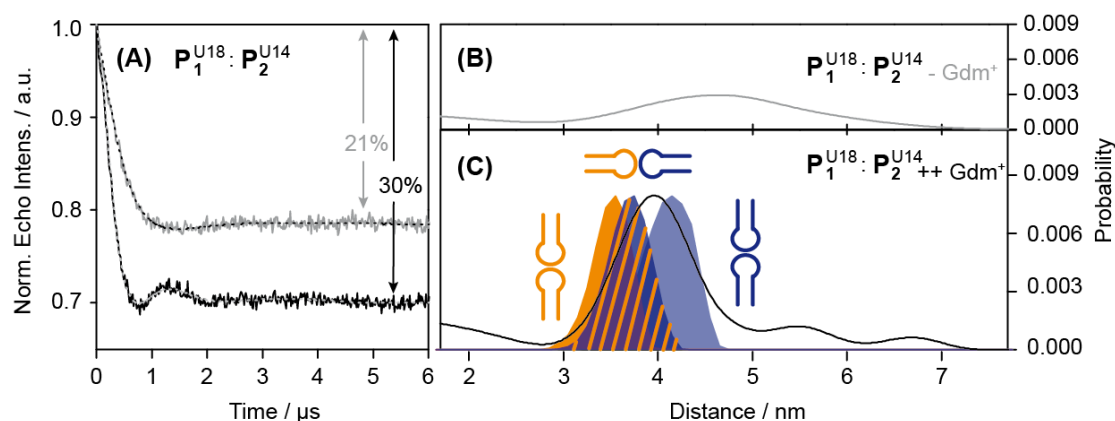


Figure 64. (A) Background corrected PELDOR time traces for  $P_2^{U14}$  mixed equivalently with  $P_1^{U18}$  in the absence (light grey line) and presence of 40 mM (black line)  $Gdm^+$ . The fits are overlaid as black or grey dotted lines, respectively. The modulation depths are indicated in percentages. (B) and (C) show the corresponding distance distributions to the time traces in (A) as solid lines following the same color code as in (A). The *in silico* generated distance distributions are shown as filled areas and follow the same color code as in Figure 50 and Figure 61. The structure used in MtssWizard assigned to the respective distribution is shown next to it.

### 3.2.4 Analysis of the truncated hairpin $P_1^{U20}$

In order to overcome this obstacle and to assign the distance peaks to structures, a new labeling position was introduced, namely position U20 for the hairpin **P1** (Figure 65A).

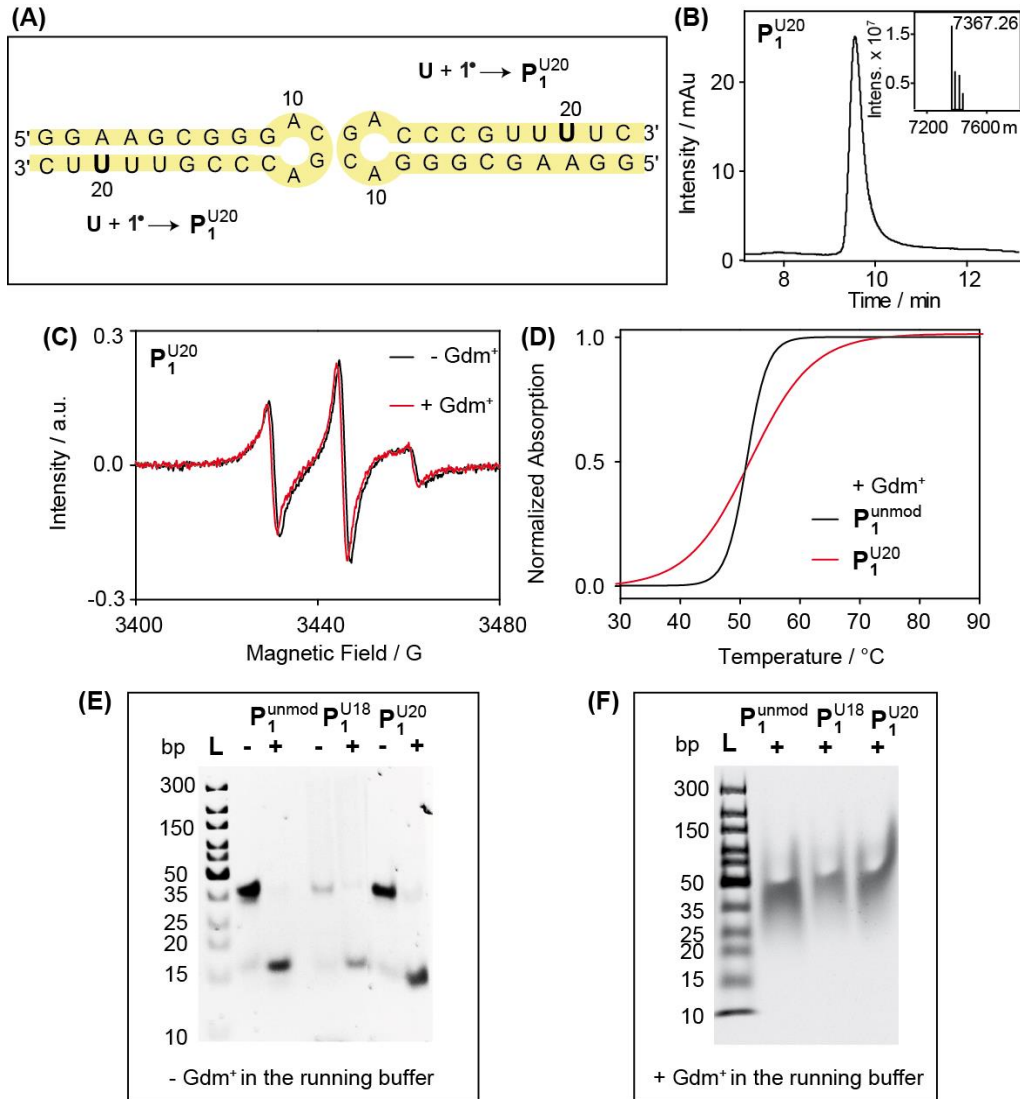


Figure 65. (A) RNA sequence of **P1**. Introduction of spin label  $1^*$  at the position marked with a bold “U” leads to the spin labeled construct referred to as  $P_1^{U20}$ . (B) LCMS UV chromatogram and the deconvoluted ESI-mass of the labeled RNA shown as inset. The calculated mass  $M_{\text{calc}}(P_1^{U20}) = 7365.23$  matched the found mass  $M_{\text{found}}(P_1^{U20}) = 7367.26$ , which was assigned to  $[M+1H]^+$ . (C) 25  $\mu\text{M}$  cwEPR spectra in the absence (black line) and presence (red line) of  $\text{Gdm}^+$ . Spin counting revealed the following concentrations:  $c(-\text{Gdm}^+) = 25\ \mu\text{M}$  and  $c(+\text{Gdm}^+) = 22\ \mu\text{M}$ . (D) UV-VIS melting curve of the unmodified (black line) and labeled (red line) RNA in the presence of  $\text{Gdm}^+$ .  $T_m(P_1^{\text{unmod}}) = 51.0^\circ\text{C}$  and  $T_m(P_1^{U20}) = 51.7^\circ\text{C}$ . (E) 15% native PAGE analysis for  $P_1^{\text{unmod}}$ ,  $P_1^{U18}$  and  $P_1^{U20}$  prepared in the absence (-) and presence (+) of  $\text{Gdm}^+$  during the fast annealing, and without  $\text{Gdm}^+$  in the running buffer. (F) 15% native PAGE analysis for  $P_1^{\text{unmod}}$ ,  $P_1^{U18}$  and  $P_1^{U20}$  prepared in the absence (-) and presence (+) of  $\text{Gdm}^+$  during the fast annealing, and with  $\text{Gdm}^+$  in the running buffer. “L” depicts the GeneRuler ultra low range DNA ladder (ThermoFisher) with the base pair sizes on the left.

The distances computed *in silico* were 5.6 nm for the homo dimer  $P_1^{U20} | P_1^{U20}$  and 4.5 nm for the hetero dimer  $P_1^{U20} | P_2^{U14}$ , whereas the homo dimer  $P_2^{U14} | P_2^{U14}$  stayed at 3.5 nm. Consequently, the new labeling site was assumed to enable separation and assignment of the distances to structures.

#### 3.2.4.1 Spin labeling

Attachment of  $1^*$  was facilitated through CuAAC following the protocol from above. Successful spin labeling and purification was confirmed by LCMS measurement and through spin counting of the respective cwEPR spectra (Figure 65B and C). Due to limited amount on RNA, CD spectra were not recorded. However, the spin label on  $P_1^{U18}$  was already shown to have a negligible effect, and the melting temperature of  $P_1^{U20}$  was found to vary only about 1 °C from  $P_1^{unmod}$  (Figure 65D). Thus, the influence of  $1^*$  was here as well judged as being minor. Comparable to  $P_1^{U18}$ , the native PAGEs verified that  $P_1^{unmod}$  and  $P_1^{U20}$  captured comparable conformations that responded similar to  $Gdm^+$  (Figure 65E and F)

#### 3.2.4.2 PELDOR measurements

Distance derived measurements by means of PELDOR were firstly conducted on the homo dimer  $P_1^{U20} | P_1^{U20}$  (Figure 66). In the absence of  $Gdm^+$ , a well-defined distance distribution was obtained with a main peak at 5.2 nm and the time trace had a modulation depth of 15 %. In the presence of  $Gdm^+$ , the most probable distance was found at 5.7 nm and a modulation depth of 20 % was detected. Unfortunately, the new position did not allow to distinguish between the duplex and the kissing hairpin, as both yielded a most probable distance of 5.6 nm in the *in silico* prediction. Thus, an assignment to the experimental data was difficult. However, based on the results presented for  $P_1^{U18}$  before, the structure obtained in the absence of  $Gdm^+$  was assumed to belong to the duplex, which can be converted to the kissing hairpin dimer upon addition of  $Gdm^+$ .

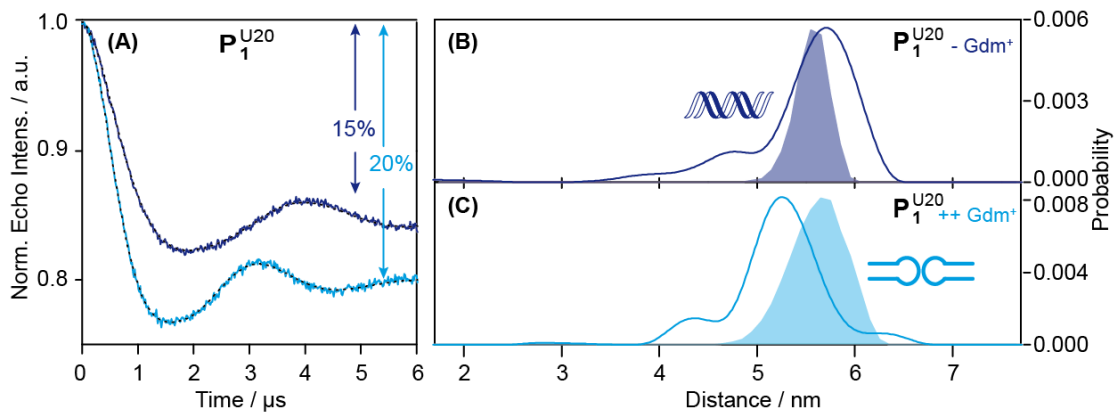


Figure 66. (A) Background corrected PELDOR time traces for  $P_1^{U20}$  in the absence (purple line) and presence (blue line) of  $Gdm^+$ . The fits are overlaid as black dotted lines. The modulation depths are indicated in percentages. (B) and (C) show the distance distributions corresponding to the time traces in (A) as solid lines following the same color code as in (A). The fully shaded shapes are the distance distributions derived from MtssIWizard. The structure assigned to the distribution is shown next to it.

### 3.2.5 Analysis of the hetero hairpin mixture $P_1^{U20} | P_2^{U14}$

However, the new spin labeling position was chosen to study the hetero dimer interaction.

#### 3.2.5.1 PELDOR measurements

Therefore,  $P_1^{U20}$  and  $P_2^{U14}$  were mixed in equivalent amounts. PELDOR measurements were executed in the absence and presence of  $Gdm^+$  (Figure 67). In the absence of  $Gdm^+$ , a modulation depth of 13% was obtained with a time trace corresponding to a distance distribution peaking at 4.2 nm and 5.6 nm. The two maxima were supposed to be a superposition of the  $P_1^{U20}$  duplex, the  $P_2^{U14}$  monomer hairpin, that decreases the modulation depth, and already formed  $P_1^{U20} | P_2^{U14}$  kissing hairpin. The latter was generated *in silico* with a maximum at 4.5 nm. Adding  $Gdm^+$  caused the dimer population to increase from 36% to 66%. The corresponding distance distribution exhibited three maxima at 3.6 nm, 4.4 nm and 5.2 nm. They nicely matched the distances arising from the two homo dimers  $P_2^{U14} | P_2^{U14}$  (3.6 nm) and  $P_1^{U20} | P_1^{U20}$  (5.2 nm), and to the hetero dimer  $P_1^{U20} | P_2^{U14}$  (4.4 nm). Thus, the experimental distance distribution of the hetero

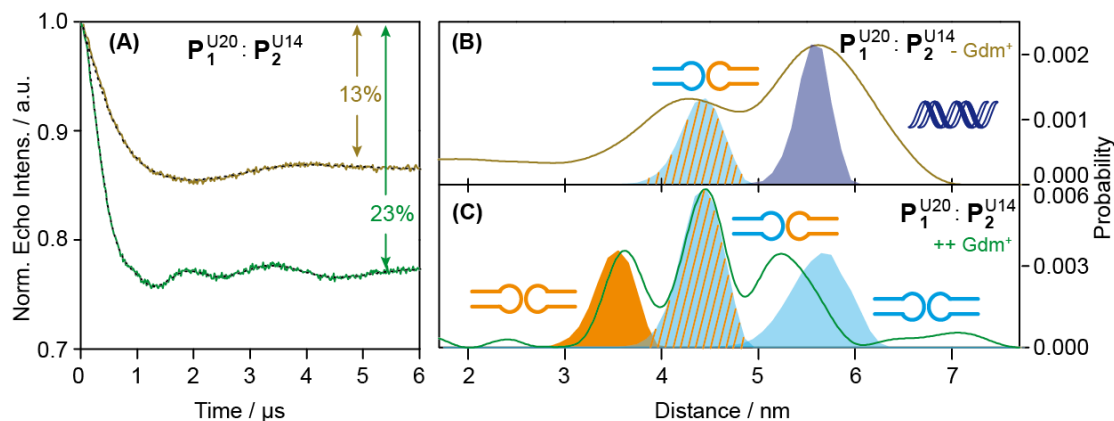


Figure 67. (A) Background corrected PELDOR time traces for the 1:1 mixture of  $P_1^{U20} | P_2^{U14}$  in the absence (olive line) and presence (green line) of Gdm<sup>+</sup>. The fits are overlaid as black dotted lines. The modulation depths are indicated in percentages. (B) and (C) show the distance distributions corresponding to the time traces in (A) as solid lines following the same color code as in (A). The fully shaded shapes are the distance distributions derived from MtsslWizard. The structure assigned to the distribution is shown next to it.

hairpin mixture in the presence of Gdm<sup>+</sup> implied the formation of the hetero dimers **P1 | P2** next to the two homo dimers **P1 | P1** and **P2 | P2**. The ratio of the three compounds were analyzed by comparing the amplitudes (Table 7), and the areas. The areas were analyzed with Gaussian Fits of the distance distributions according to eq. 19 (Table 8 and Figure 68). A statistically driven ratio of 1:2:1 was obtained with both methods. Thus, the hetero kissing hairpin dimer as proposed for the switching mechanism of the riboswitch was found.

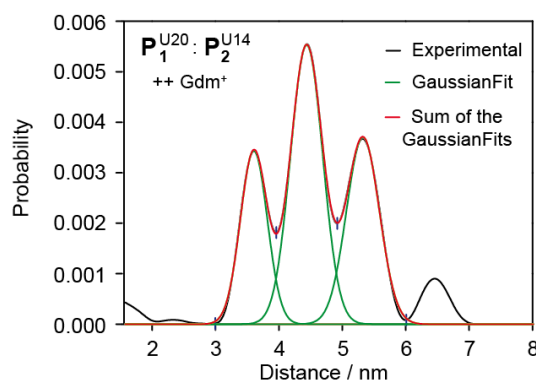


Figure 68. Gaussian fitted peaks corresponding to the distance distribution obtained of  $P_1^{U20} | P_2^{U14}$  in presence of Gdm<sup>+</sup>.

Table 7. Results of the amplitude based analysis corresponding to the distance distribution obtained of  $P_1^{U20} | P_2^{U14}$  in presence of Gdm<sup>+</sup>.

Center of the peak / nm	Height of the amplitude	Statistic
3.6	0.00346	1.3
4.4	0.00554	2.0
5.2	0.00371	1.3

Table 8. Results of the Gaussian Fit based analysis corresponding to the distance distribution obtained of  $P_1^{U20} | P_2^{U14}$  in presence of Gdm<sup>+</sup>.

Center of the peak / nm	Area of the Gaussian Fit	Statistic
3.6	0.00183	1.0
4.4	0.00352	2.0
5.2	0.00776	1.3

### 3.2.6 Analysis of the singly labeled full-length riboswitch

While the **P1 | P2** interaction has been observed for the truncated hairpins, this interaction remains to be proven for the full-length riboswitch. The challenge being, that this **P1 | P2** interaction can occur within the same strand, which is the wanted intrastrand interaction, but also between **P1** and **P2** from two different strands so an interstrand interaction. For the studies on the full-length riboswitch the 59 nt full-length construct derived from *P. aeruginosa* was used.<sup>43</sup> The spin labeling positions were chosen to be the same as used for the truncated hairpins (Figure 69). The abbreviations of the RNA constructs were chosen such that the subscript “1” or “2” denotes if the labeling positions is located in the hairpin **P1** and/or **P2**. The subscript “Full” shows that it is the full-length riboswitch. Furthermore, the superscript denotes the respective labeled nucleobase in hairpin **P1** and/or **P2**.

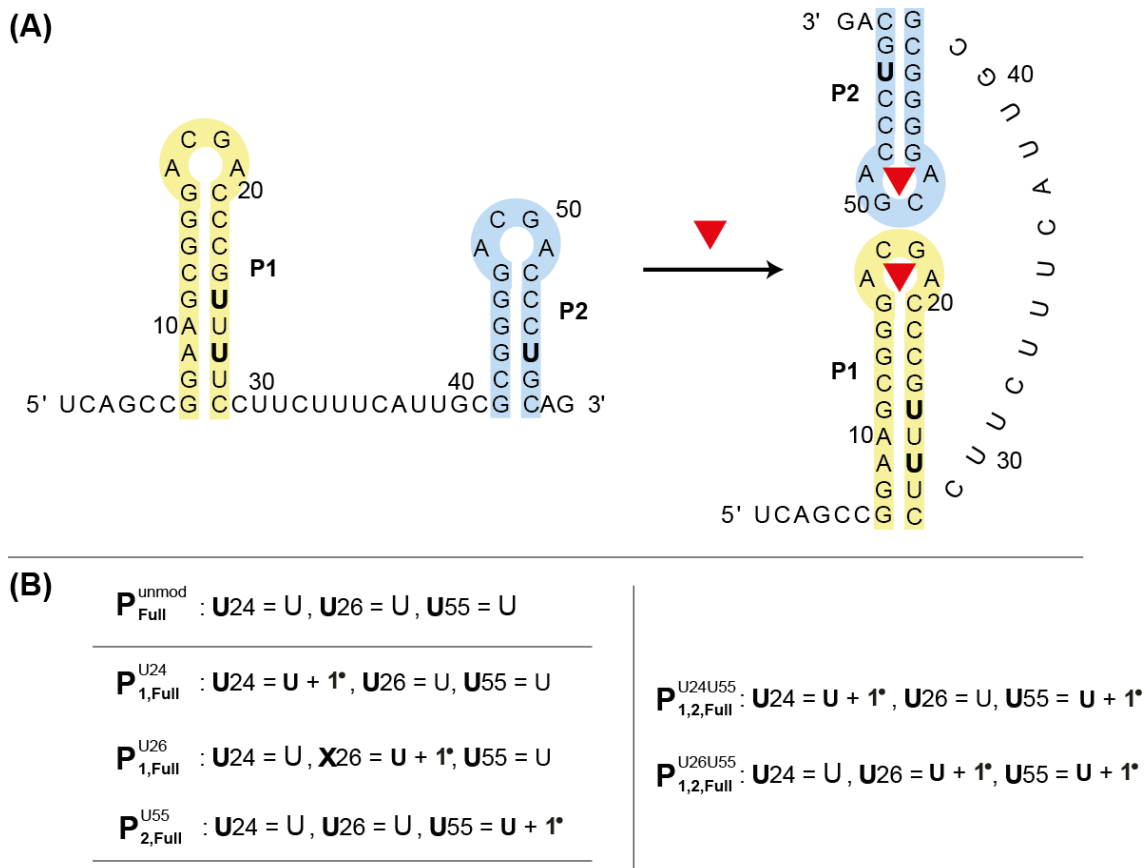


Figure 69. (A) Proposed switching mechanism of the Guanidinium-II riboswitch with the base sequence used in this analysis (the representation is based on reference 48). (B) Overview of the modifications and the corresponding abbreviations of the RNA sequences. If it reads “unmod”, the strand is not labeled. The subscripts “1” or “2” denotes if the spin labeled position is in hairpin **P1** and/or **P2**. The subscript “Full” shows that it is the full-length construct. The superscript denotes the base that is spin labeled. If it is “UX = U”, the designated base is a natural uridine. If it is “UX = U + 1\*”, the mentioned base was spin labeled with 1\*.



### 3.2.6.1 Spin labeling

**1\*** was bioconjugated to the 59 nt long RNA strand following the established protocol from above. The HPLC purification was slightly modified, because it was expected that due to the lengthened RNA strand, the retention time differ from the truncated hairpins. Owing to that, a semi-preparative reverse phase column was used at 60 °C with an adjusted solvent gradient. The LCMS and cwEPR spectra of the purified constructs  $P_{1,Full}^{U24}$ ,  $P_{1,Full}^{U26}$  and  $P_{2,Full}^{U55}$  are shown in Figure 70. The LCMS data of  $P_{1,Full}^{U24}$  and  $P_{2,Full}^{U55}$  depicted a single peak in the UV-VIS trace and a single peak in the deconvoluted mass. The deconvoluted mass matched the calculated mass. However, it was not possible to detect a single peak in the deconvoluted mass for  $P_{1,Full}^{U26}$ , although the UV-VIS trace clearly demonstrated that a pure substance was loaded (Figure 70B). Since ESI<sup>-</sup> was not suitable for these construct, MALDI TOF<sup>+</sup> was tried. Because MALDI TOF<sup>+</sup> measurements on RNA are not routine measurements for the *Zentralanalytik Universität Bonn*, the performance and accuracy were tested first on the unmodified full-length construct. A concentration range from 100  $\mu$ M to 1  $\mu$ M was employed to test the concentration needed for reliable data. Identically spectra were observed for 100  $\mu$ M and 1  $\mu$ M with respect to the main peaks indicating that each concentration in this range is suitable (Figure 71A and B). The found mass  $M_{found}(P_{Full}^{unmod})$ :  $[M]^+ = 18882.6$  differed in

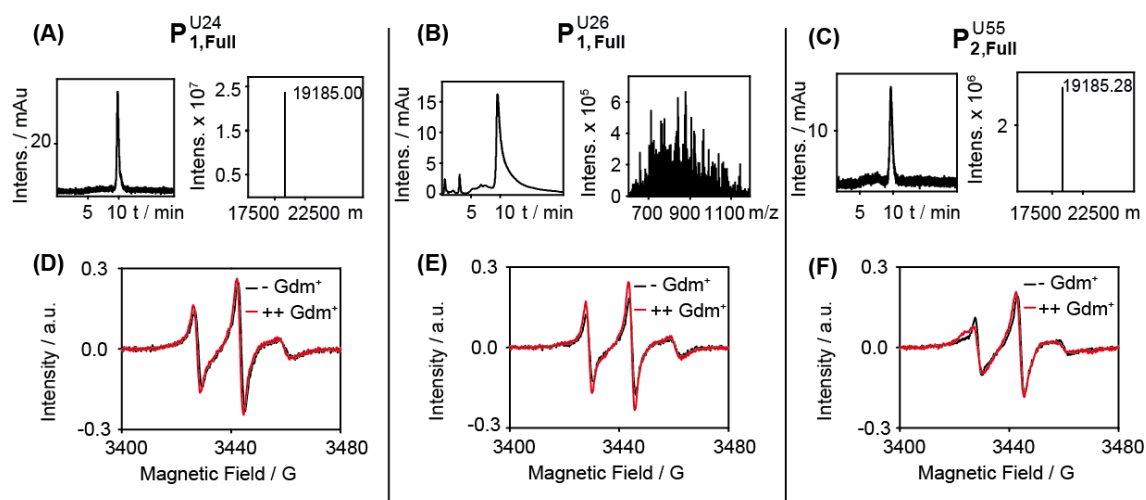


Figure 70. Characterization of the singly labeled full-length constructs. **Top part left panel:** UV-VIS chromatograms. **Top part right panel:** Deconvoluted masses. **Bottom part:** cwEPR spectra in the absence (red line) and in the presence of Gdm<sup>+</sup> (black line). (A) and (D)  $P_{1,Full}^{U24}$ , (B) and (E)  $P_{1,Full}^{U26}$  and (C) and (F)  $P_{2,Full}^{U55}$ . It was not possible to obtain a deconvoluted mass for  $P_{1,Full}^{U26}$ , thus the raw spectrum is shown. For the discussion, see the text. The calculated mass is  $M_{calc}(P_{X,Full}^{UX}) = 19186.28$ . Spin counting concentrations are given in Table 9.

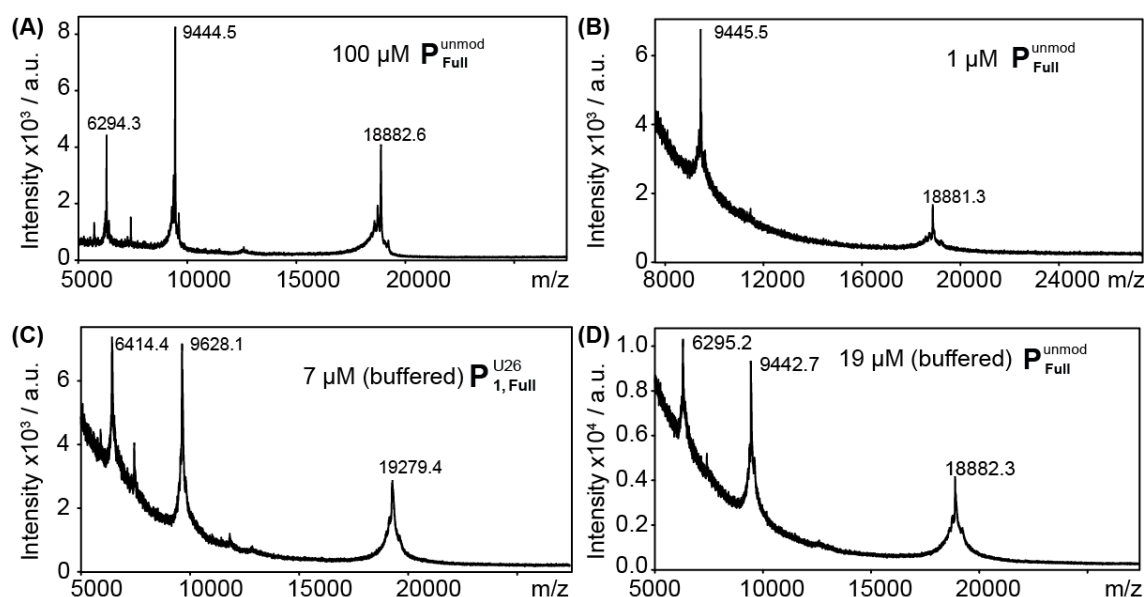


Figure 71. MALDI TOF<sup>+</sup> spectra. (A) 100  $\mu\text{M}$   $\text{P}_{\text{Full}}^{\text{unmod}}$  in  $\text{H}_2\text{O}$ . (B) 1  $\mu\text{M}$   $\text{P}_{\text{Full}}^{\text{unmod}}$  in  $\text{H}_2\text{O}$ . (C) 7  $\mu\text{M}$   $\text{P}_{1,\text{Full}}^{\text{U26}}$  in Folding Buffer. (D) 19  $\mu\text{M}$   $\text{P}_{\text{Full}}^{\text{unmod}}$  in Folding Buffer.  $M_{\text{calc}}(\text{P}_{\text{Full}}^{\text{unmod}})$ :  $[\text{M}]^+ = 18892.36$ .  $M_{\text{found}}(\text{P}_{\text{Full}}^{\text{unmod}})$ :  $[\text{M}]^+ = 18882.6$ ,  $[\text{M}]^{2+} = 9444.5$ ,  $[\text{M}]^{3+} = 6294.3$ .  $M_{\text{calc}}(\text{P}_{1,\text{Full}}^{\text{U26}})$ :  $[\text{M}]^+ = 19186.28$ .

approximately 10 m/z from the calculated one  $M_{\text{calc}}(\text{P}_{\text{Full}}^{\text{unmod}})$ :  $[\text{M}]^+ = 18892.4$ . Additional peaks from the twofold and threefold ionized product were obtained. The mass of the product was in the correct mass range and depicted the correct ionization behavior. Thus, the difference towards the calculated mass was proposed to arise from calibration troubles. The calibration was performed with a protein of similar size, and improvements are recommended on this issue.

Afterwards, a 7  $\mu\text{M}$  solution of  $\text{P}_{1,\text{Full}}^{\text{U26}}$  was measured with MALDI TOF<sup>+</sup> (Figure 71C). While no peak was detected at the calculated mass of  $M_{\text{calc}}(\text{P}_{1,\text{Full}}^{\text{U26}})$ :  $[\text{M}]^+ = 19186.28$ , a peak at  $M_{\text{found}}(\text{P}_{1,\text{Full}}^{\text{U26}}) = 19279.4$  could be obtained, which may correspond to  $[\text{M}+2\times^{23}\text{Na}+^{39}\text{K}]^+ = 19271.36$ ,  $[\text{M}+4\times^{23}\text{Na}]^+ = 19274.19$ , or  $[\text{M}+^{23}\text{Na}+2\times^{39}\text{K}]^+ = 19287.47$ . The mass of additional ions in the MALDI TOF<sup>+</sup> spectrum maybe related to the buffer used ( $\text{P}_{1,\text{Full}}^{\text{U26}}$  was stored in folding buffer, whereas  $\text{P}_{\text{Full}}^{\text{unmod}}$  was stored in water, only). To test this,  $\text{P}_{\text{Full}}^{\text{unmod}}$  was rebuffed and measured again (Figure 71D). With a found mass of  $M_{\text{found}}(\text{P}_{\text{Full}}^{\text{unmod}})$ :  $[\text{M}]^+ = 18882.3$ , the mass of additional ions was not obtained. The found mass of  $M_{\text{found}}(\text{P}_{1,\text{Full}}^{\text{U26}}) = 19279.4$  could therefore not clearly assigned to a product. However, it can be excluded that the labeling had not worked, because the unlabeled RNA has a mass of 18901.3. In addition, the cwEPR spectra of  $\text{P}_{1,\text{Full}}^{\text{U26}}$  in Figure 70E showed anisotropy, which is caused by an immobilized  $1^{\bullet}$ . Consequently,  $1^{\bullet}$  was assumed to be attached to the RNA. Furthermore, the spin counting revealed for all

singly labeled constructs quantitatively labeled RNA as the set and measured spin concentration matched (Table 9).

Table 9. Spin concentrations of the singly labeled full-length constructs.

Construct		c(- Gdm <sup>+</sup> ) / $\mu$ M	c(++ Gdm <sup>+</sup> ) / $\mu$ M
<b>P</b> <sub>1,Full</sub> <sup>U24</sup>	set	25	25
	measured	27	31
<b>P</b> <sub>1,Full</sub> <sup>U26</sup>	set	21	21
	measured	19	20
<b>P</b> <sub>2,Full</sub> <sup>U55</sup>	set	25	25
	measured	29	31

### 3.2.6.2 Test for structural perturbation

The previously data of the model RNA and the truncated hairpins had shown that the **1**<sup>\*</sup> did not alter the RNA fold. Nevertheless, CD spectra and temperature dependent UV-VIS spectra were recorded for **P**<sub>1,Full</sub><sup>U24</sup> and **P**<sub>2,Full</sub><sup>U55</sup>, to evaluate the influence of the spin label on the full-length construct. The CD spectra of unmodified and singly labeled full-length riboswitch depicted minor changes in the amplitude but very similar negative molar ellipticity at 210 nm and positive at 270 nm (Figure 72A). However, previously data of **P2** had demonstrated that CD spectroscopy was not suitable if different conformations were present in the solution. Supplementary, the UV-VIS based measurements resulted in inconclusive data. The best ones are shown in Figure 72B. Heterogeneous folded

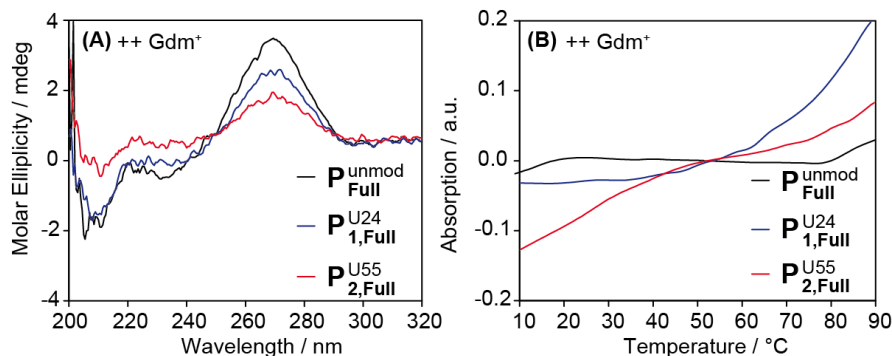


Figure 72. (A) CD spectra of **P**<sub>Full</sub><sup>unmod</sup> (black line), **P**<sub>1,Full</sub><sup>U24</sup> (blue line) and **P**<sub>2,Full</sub><sup>U55</sup> (red line) in presence of 40 mM Gdm<sup>+</sup>. (B) UV-VIS melting curves with the same color code as shown in (A) in presence of 40 mM Gdm<sup>+</sup>.

conformations were expected to occlude differences between unmodified and labeled RNA.

Another approach to assess if unlabeled and labeled RNA capture comparable conformations, was the analysis on a native PAGE (Figure 73). In absence of  $Gdm^+$ , different conformations were visible as various bands in particular for  $P_{Full}^{unmod}$  and  $P_{1,Full}^{U24}$ . Upon addition of  $Gdm^+$ , one dominant band was visible for all samples, unlabeled and labeled at ~75 bp but also lightly bands at 200 bp and 30 bp. Thus, for the singly labeled full-length the native PAGE indicated that the unmodified and labeled RNAs fold and respond to  $Gdm^+$  similarly.

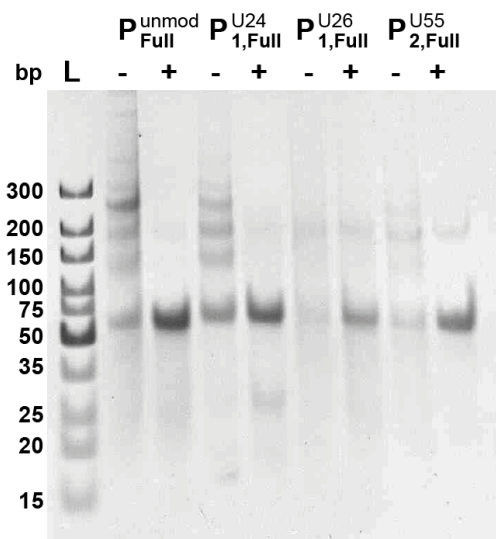


Figure 73. 15% Native PAGE analysis of the singly labeled full-length constructs without  $Gdm^+$  in the running buffer in the absence (-) and presence (+) of 40 mM  $Gdm^+$  "L" depicts the GeneRuler ultra low range DNA ladder (ThermoFisher) with the base pair sizes on the left.

### 3.2.6.3 PELDOR measurements

The modulation depth in the PELDOR time trace arises from dipolar coupled spins. If the switching mechanism of the Guanidine-II riboswitch is correct, the intrastrand kissing hairpins (Figure 74A) of the singly labeled constructs  $P_{1,Full}^{U24}$ ,  $P_{1,Full}^{U26}$  and  $P_{2,Full}^{U55}$  was assumed to demonstrate a modulation depth of nearly 0%.

However, the modulation depth in the PELDOR measurement for all constructs varied between 11-16% (Figure 75A, C, E). Thus, the solution was occupied by 31-46% of oligomeric RNA structures. Some of the possible interaction that were expected are illustrated in Figure 74. It is worth noting to say that the distance distribution of  $P_{1,Full}^{U24}$  and  $P_{1,Full}^{U26}$  demonstrated a similar broad distance distributions in absence and presence of  $Gdm^+$ , whereas the native PAGE indicated that at least in the presence of  $Gdm^+$  a cominant conformation was presented. In contrast, the distance distribution of  $P_{2,Full}^{U55}$  did alter upon addition of  $Gdm^+$ . Beside the broad distance distribution that is detected in the absence and presence of  $Gdm^+$ , an additional peak arose at 3.6 nm in response of  $Gdm^+$  (Figure 75F). The peak was assigned to the homo dimer interaction based on the previous obtained results from the truncated hairpin **P2**. This interaction was referred to the interstrand kissing hairpins illustrated in Figure 74C or F. Decreasing the RNA concentration was executed to demonstrate that in this way the intrastrand kissing hairpin also decreased (Figure 76). And indeed, the modulation depth of the time trace as well as the probability of the peak at 3.6 nm diminished indicating a reduced intramolecular **P2 | P2** interaction. However, the experimental sample preparation was done by thawing, dilution and refreezing the RNA due to a limited amount of sample, and cannot provide that the RNA folding is influenced through this procedure. Thus, additional dilution was not carried out.

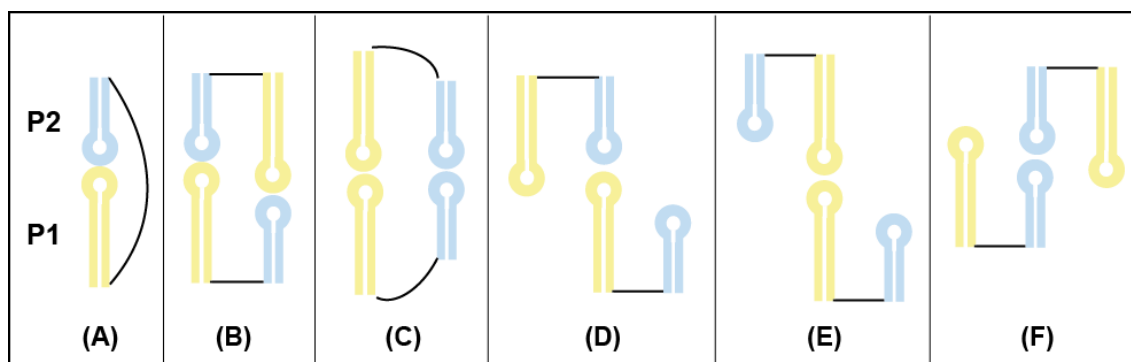


Figure 74. Illustration of the (A) intrastrand and (B)-(F) potential interstrand interactions of the Guanidine-II riboswitch.

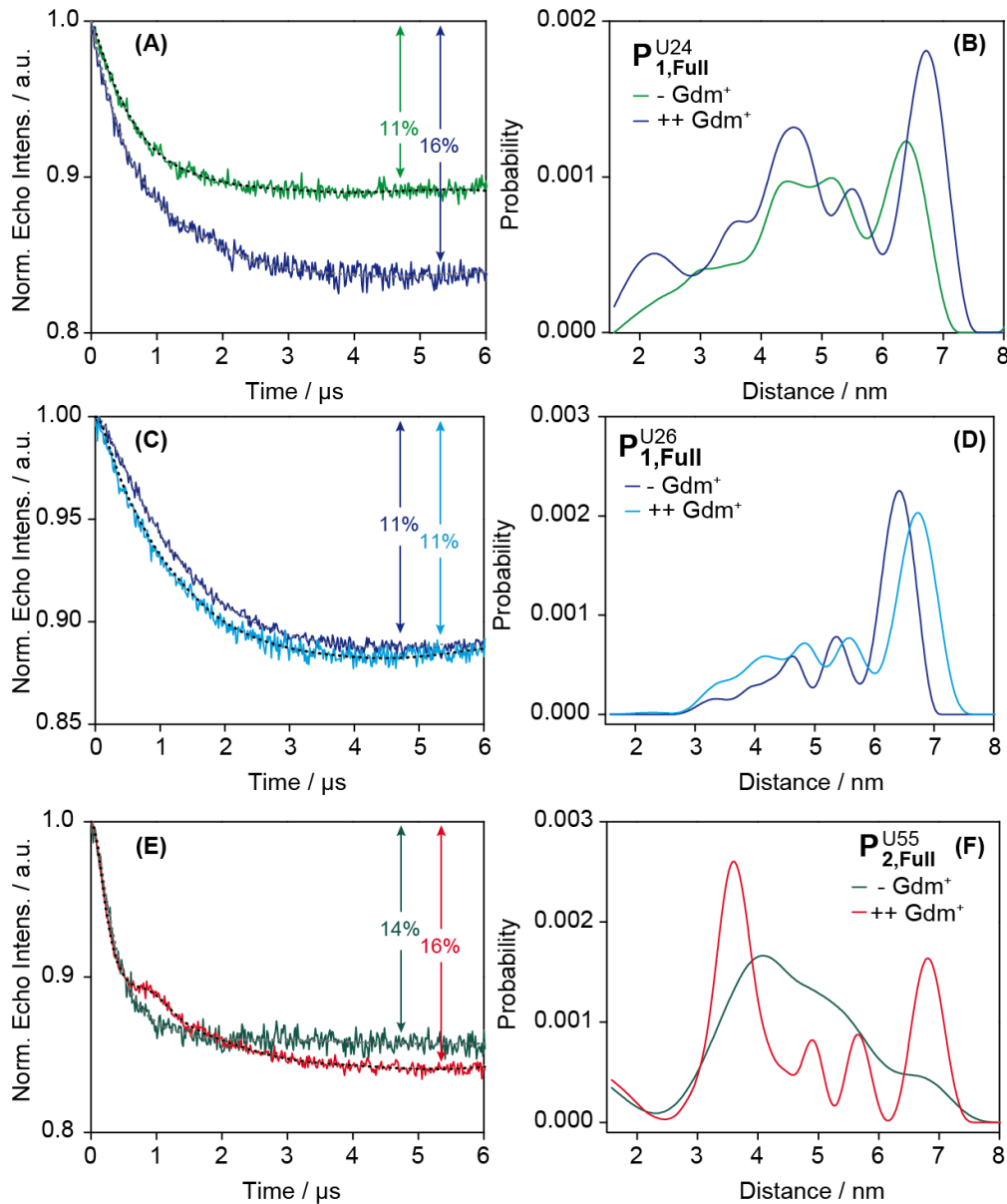


Figure 75. **Left panel** PELDOR time traces and **right panel** distance distributions for (A) and (B)  $P_{1,Full}^{U24}$ , (C) and (D)  $P_{1,Full}^{U26}$  and (E) and (F)  $P_{2,Full}^{U55}$ . **Top panel:** (A) Background corrected PELDOR time traces for  $P_{1,Full}^{U24}$  in the absence (green line) and presence (dark blue line) of  $Gdm^+$ . The fits are overlaid as black dotted lines. The modulation depths are indicated in percentages. (B) shows the distance distributions corresponding to the time traces in (A) as solid lines following the same color code as in (A). **Middle panel:** (C) Background corrected PELDOR time traces for  $P_{1,Full}^{U26}$  in the absence (light blue line) and presence (blue line) of  $Gdm^+$ . The fits are overlaid as black dotted lines. The modulation depths are indicated in percentages. (D) shows the distance distributions corresponding to the time traces in (C) as solid lines following the same color code as in (C). **Bottom Panel:** (E) Background corrected PELDOR time traces for  $P_{2,Full}^{U55}$  in the absence (dark green line) and presence (red line) of  $Gdm^+$ . The fits are overlaid as black dotted lines. The modulation depths are indicated in percentages. (F) shows the distance distributions corresponding to the time traces in (E) as solid lines following the same color code as in (E).

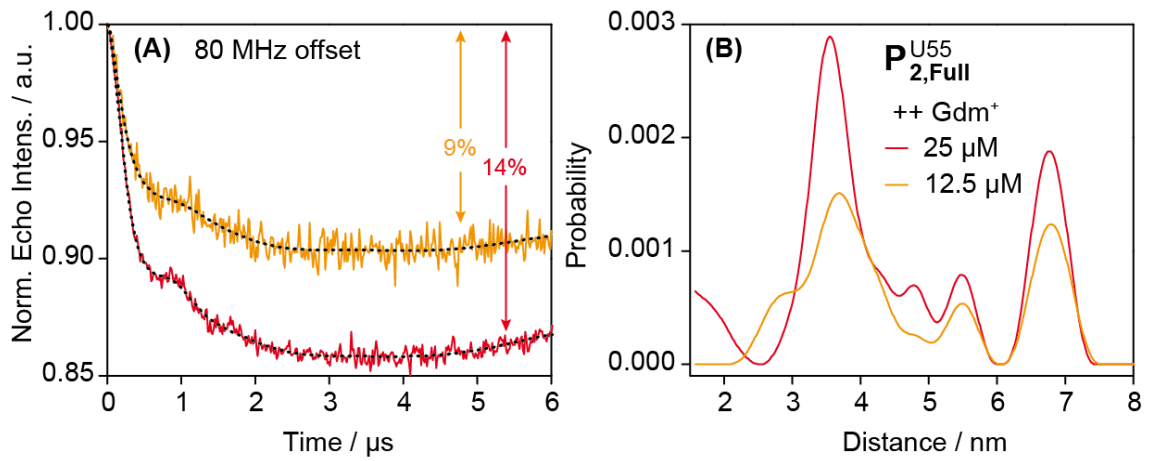


Figure 76. (A) Background corrected PELDOR time traces for the 80 MHz offset of 25  $\mu$ M (red line) and 12.5  $\mu$ M (yellow line)  $P_{2,Full}^{U55}$  in the presence of  $Gdm^+$ . The fits are overlaid as black dotted lines. The modulation depths are indicated in percentages. (B) shows the distance distributions corresponding to the time traces in (A) as solid lines following the same color code as in (A).

### 3.2.7 Analysis of the doubly labeled full-length riboswitch

#### 3.2.7.1 Spin labeling

The SDSL/PELDOR approach was further extended to two doubly labeled full-length constructs, namely  $P_{1,2,Full}^{U24,U55}$  and  $P_{1,2,Full}^{U26,U55}$ . The spin labeling positions were chosen comparable to the truncated hairpins and the singly labeled full-length constructs. An overview about the positions is given in Figure 69. The spin labeling procedure and purification was performed analogue as described above. Prior,  $1^*$  was used in a 80-fold excess. For the doubly labeled construct, the 50-fold excess in relation to the labeling sites was considered to be adequate. LCMS characterization subsequent to the HPLC purification was suitable for  $P_{1,2,Full}^{U24,U55}$ , showing one peak at the expected mass (Figure 77A). The LCMS UV-VIS trace of  $P_{1,2,Full}^{U26,U55}$  presented a distinct, but much broader peak compared to  $P_{1,2,Full}^{U24,U55}$  (Figure 77B). A deconvoluted mass of the respective ESI<sup>-</sup> spectrum could not be observed for  $P_{1,2,Full}^{U26,U55}$ . MALDI TOF<sup>+</sup> was also not applicable. However, the cwEPR spectra of both constructs indicated that  $1^*$  was immobilized and free spin label was separated (Figure 77C and D). The spin counting revealed that the following measurements were done with quantitatively spin labeled RNA, as the set and measured spin concentrations matched (Table 10).

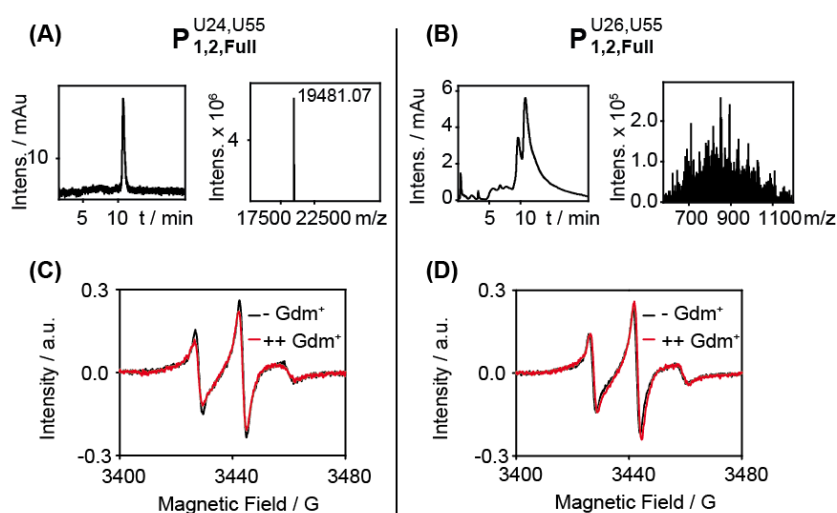


Figure 77. Characterization of the doubly labeled full-length constructs. **Top part left panel:** UV-VIS chromatograms. **Top part right panel:** Deconvoluted masses. **Bottom part:** cwEPR spectra in the absence (red line) and in the presence of Gdm<sup>+</sup> (black line). (A) and (C)  $P_{1,2,Full}^{U24,U55}$ , (B) and (D)  $P_{1,2,Full}^{U26,U55}$ . It was not possible to obtain a deconvoluted mass for  $P_{1,2,Full}^{U26,U55}$ , thus the raw spectrum is shown. For the discussion, see the text. The calculated masses are  $M_{calc}(P_{1,2,Full}^{U24,U55}) = M_{calc}(P_{1,2,Full}^{U26,U55}) = 19480.20$ . Spin counting concentrations are given in Table 10.



Table 10. Spin concentrations of the doubly labeled full-length constructs.

Construct		c(- Gdm <sup>+</sup> ) / $\mu$ M	c(++ Gdm <sup>+</sup> ) / $\mu$ M
<b>P</b> <sup>U24,U55</sup> <sub>1,2,Full</sub>	set	34	33
	measured	29	26
<b>P</b> <sup>U26,U55</sup> <sub>1,Full</sub>	set	35	34
	measured	29	31

### 3.2.7.2 Test for structural perturbation

Native PAGE was performed to assess if **1**<sup>\*</sup> influences the RNA fold and the conformational change, and if a conformational change is present (Figure 78). The band shifts of the unlabeled, singly and doubly labeled full-length construct showed the same pattern: In the absence of Gdm<sup>+</sup> various bands in turn thus various conformations were observed. Whereas in the presence of Gdm<sup>+</sup>, a dominant band at ~75 bp was visible. Thus, a conformational change was detected upon adding Gdm<sup>+</sup>, and the unmodified and labeled RNA captured comparable conformations.

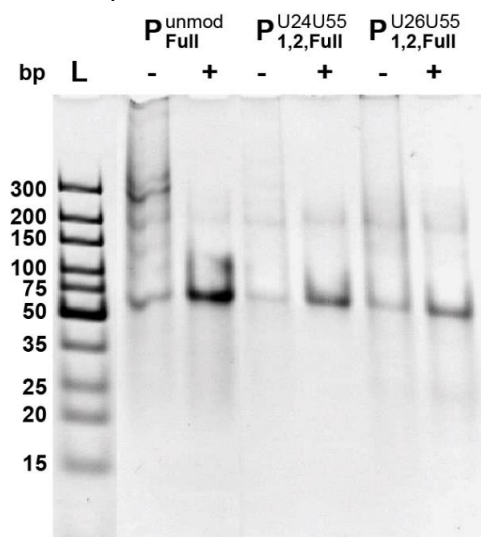


Figure 78. 15% Native PAGE analysis of the doubly labeled full-length constructs without Gdm<sup>+</sup> in the running buffer in the absence (-) and presence (+) of 40 mM Gdm<sup>+</sup> "L" depicts the GeneRuler ultra low range DNA ladder (ThermoFisher) with the base pair sizes on the left.

### 3.2.7.3 PELDOR measurements

PELDOR measurements were conducted in the absence and presence of  $\text{Gdm}^+$  on  $\text{P}_{1,2,\text{Full}}^{\text{U24U55}}$  and  $\text{P}_{1,2,\text{Full}}^{\text{U26U55}}$ . It was not known to that time, that position U24 was unfavorable due to the close homo- and hetero-kissing hairpins distances as shown for the truncated hairpins before. Nevertheless, the PELDOR measurements of  $\text{P}_{1,2,\text{Full}}^{\text{U24U55}}$  yielded important information. In the absence of  $\text{Gdm}^+$ , a modulation depth of 36% was obtained for  $\text{P}_{1,2,\text{Full}}^{\text{U24U55}}$  that yielded a broad distance distribution (Figure 79). In the presence of  $\text{Gdm}^+$ , the modulation depth increased to 49% and the corresponding distance distribution showed a distinct peak at 3.7 nm. Both the modulation depths exceed  $\sim 35\%$  that is expected for a pure dimer. Thus, interstrand kissing hairpins were built here. Dilution of the sample to decrease the intermolecular interaction, yielded nearly the identical distance distribution with a corresponding time trace with 44% modulation depth (Figure 80). While preparing the diluted sample that was done comparable to  $\text{P}_{2,\text{Full}}^{\text{U55}}$ , white particles were observed in the solution, which may be related to the RNA being insoluble after drying in the speed vac during the labeling procedure. Therefore, the full-length constructs were not dried anymore but rebuffered in the respective buffer. The measurements conducted on  $\text{P}_{1,2,\text{Full}}^{\text{U24U55}}$  prepared by drying in the speed vac and by rebuffering are judged to be reliable, because the results in presence of  $\text{Gdm}^+$  were identically and shown in the appendix.

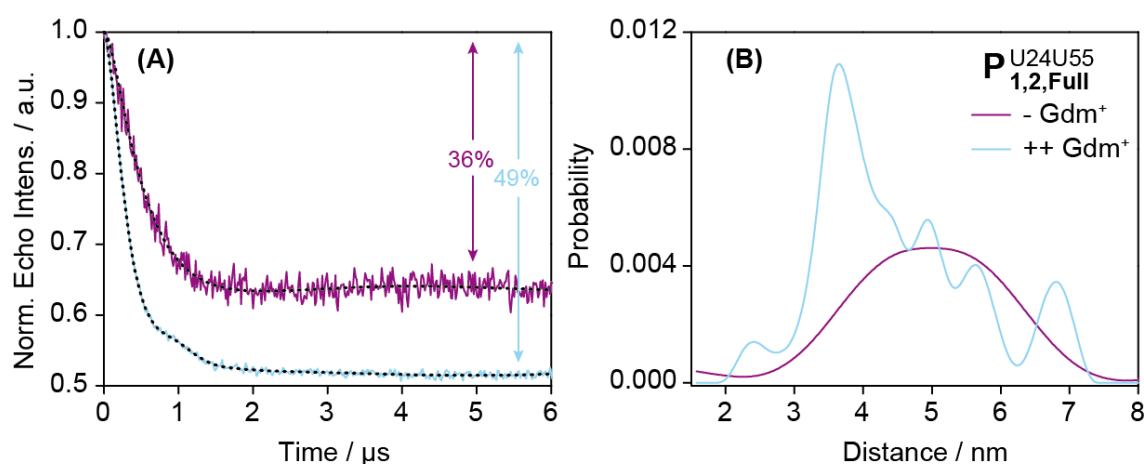


Figure 79. (A) Background corrected PELDOR time traces for  $\text{P}_{1,2,\text{Full}}^{\text{U24U55}}$  in the absence (purple line) and presence (light blue line) of  $\text{Gdm}^+$ . The fits are overlaid as black dotted lines. The modulation depths are indicated in percentages. (B) shows the distance distributions corresponding to the time traces in (A) as solid lines following the same color code as in (A).

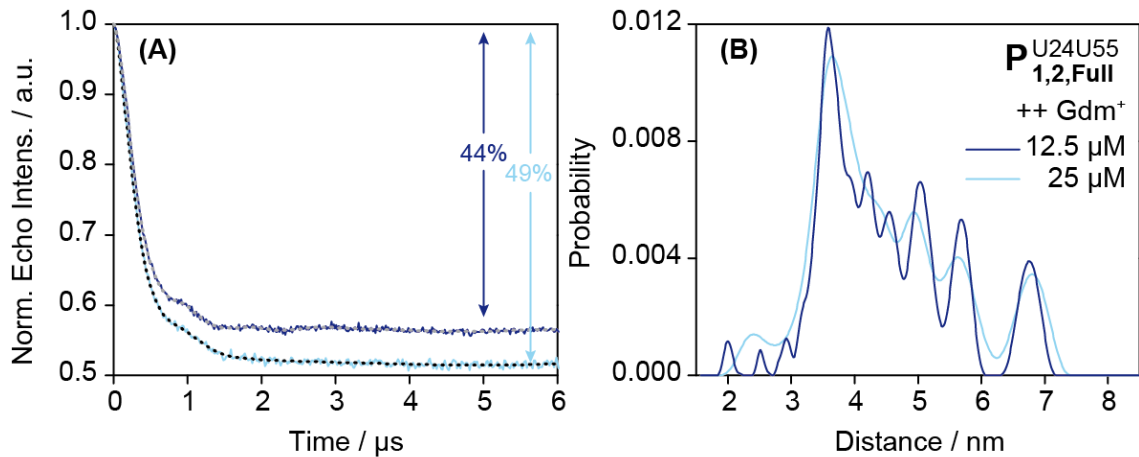


Figure 80. (A) Background corrected PELDOR time traces for  $P_{1,2,Full}^{U24U55}$  of 25  $\mu\text{M}$  (light blue line) and 12.5  $\mu\text{M}$  (dark blue line) in the presence of  $\text{Gdm}^+$ . The fits are overlaid as black and grey dotted lines, respectively. The modulation depths are indicated in percentages. (B) shows the distance distributions corresponding to the time traces in (A) as solid lines following the same color code as in (A).

The labeling position U26 was more useful to address the question if hetero- or homo dimers form in solution. The PELDOR data in the absence and presence of  $\text{Gdm}^+$  of  $P_{1,2,Full}^{U26U55}$  are shown in Figure 81. In the absence of  $\text{Gdm}^+$ , the time trace indicated 27% modulation depth corresponding to a broad distance distribution, which cannot be related to specific structures. The addition of  $\text{Gdm}^+$  caused 49% modulation depth and more pronounced peaks at 3.6 nm, 4.3 nm, 4.7 nm, 5.5 nm, and 6.5 nm. Thus, besides the expected distances of the homo dimers and the hetero dimer at 3.6 nm, 4.4 nm and 5.2 nm, additional distance peaks were obtained. To exclude distances arising from

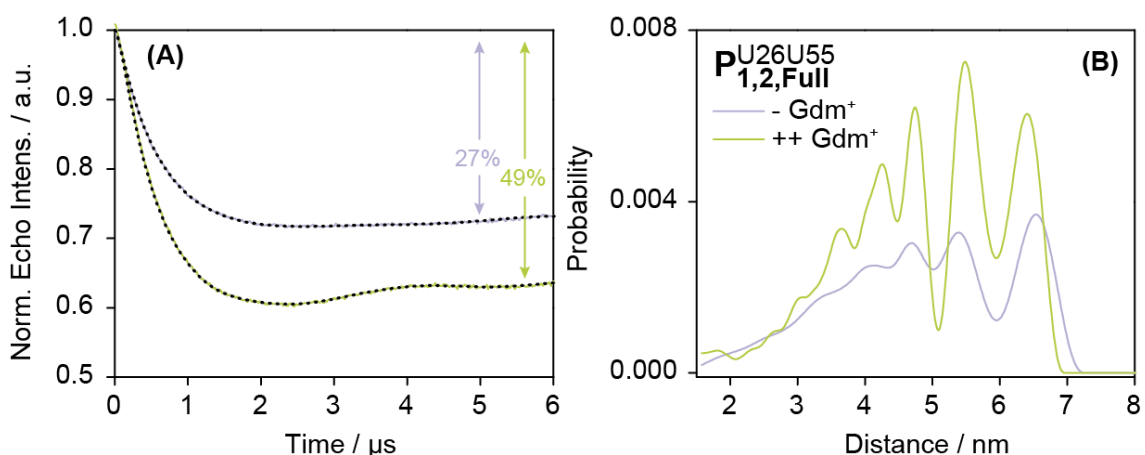


Figure 81. (A) Background corrected PELDOR time traces for  $P_{1,2,Full}^{U26U55}$  in the absence (light purple line) and presence (light green line) of  $\text{Gdm}^+$ . The fits are overlaid as black dotted lines. The modulation depths are indicated in percentages. (B) shows the distance distributions corresponding to the time traces in (A) as solid lines following the same color code as in (A).

multispin effects, DeerAnalysis<sup>275</sup> offers the ghost-suppression tool, that can be used if more than two spins are present.<sup>296</sup> However, the distance distribution did not alter by applying the ghost-peak suppression. In addition, the validated data did not exclude peaks that arose from the background correction (see appendix).

The modulation depth exceeded ~35%, indicating that interstrand kissing hairpins had formed. To decrease the intermolecular interactions, the spin concentration was decreased from 36  $\mu\text{M}$  to 13  $\mu\text{M}$  and subsequent to 2  $\mu\text{M}$  and subjected to PELDOR measurements again (Figure 82). The modulation depth decreased from 37% to 33% to 31%, respectively. However, due to the observed homo dimer distances of 3.6 nm and 5.5 nm, it was clear that interstrand interactions contributed to the modulation depth. The hetero kissing hairpin was assumed to induce a distance at 4.5 nm. The distances at 4.3 nm and 4.7 nm were expected to arise from the hetero kissing hairpins, because in the 2  $\mu\text{M}$  measurement it seemed like they merged towards the 4.7 nm peak. However, it can not be said whether the **P1 | P2** formation is based on an intra- or interstrand interaction.

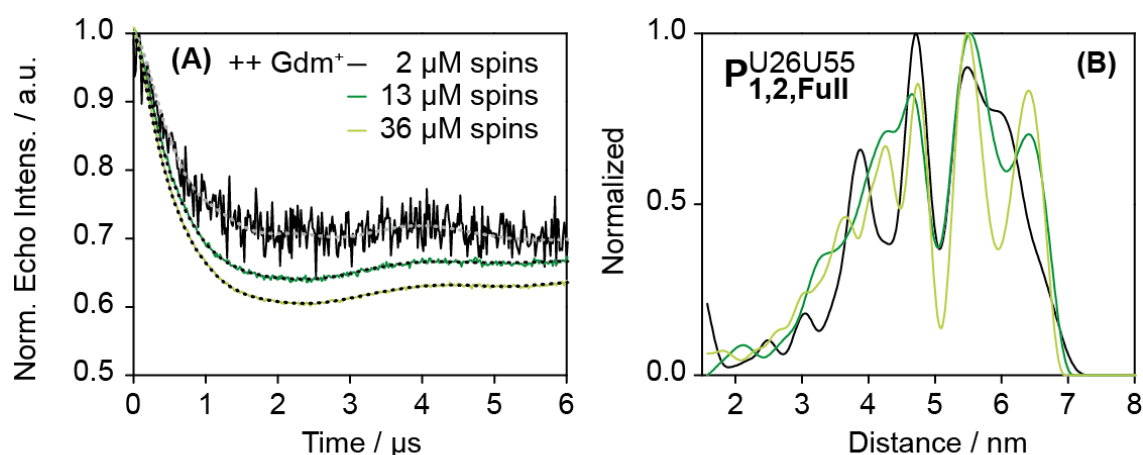


Figure 82. (A) Background corrected PELDOR time traces for  $\text{P}_{1,2,\text{Full}}^{\text{U26U55}}$  of 36  $\mu\text{M}$  (light green line), 13  $\mu\text{M}$  (green line) and 2  $\mu\text{M}$  (black line) in the presence of  $\text{Gdm}^+$ . The fits are overlaid as black or grey dotted lines, respectively. (B) shows the distance distributions corresponding to the time traces in (A) as solid lines following the same color code as in (A).

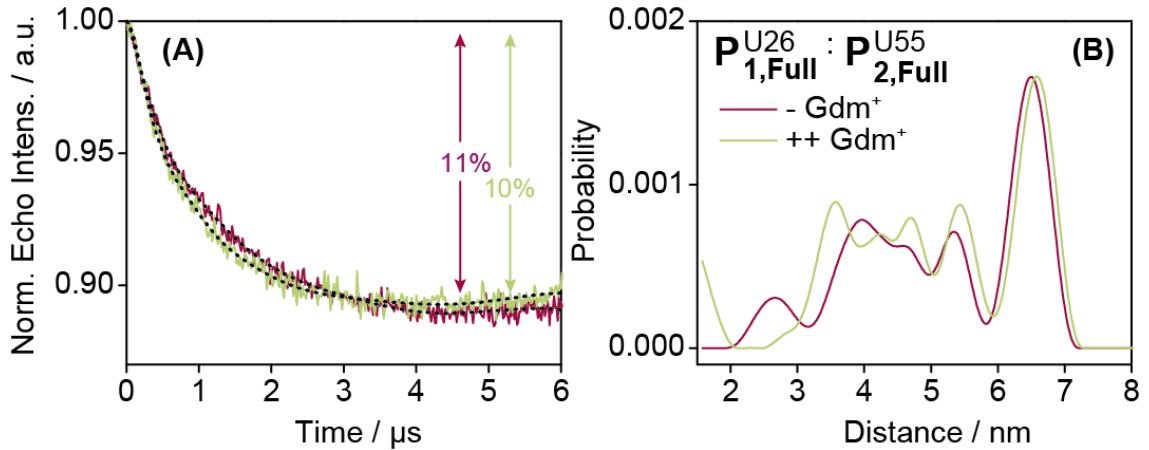


Figure 83. (A) Background corrected PELDOR time traces for  $P_{1,Full}^{U26}$  mixed equivalently with  $P_{2,Full}^{U55}$  in the absence (dark red line) and presence of 40 mM (light green line) Gdm<sup>+</sup>. The fits are overlaid as black dotted lines. The modulation depths are indicated in percentages. (B) shows the corresponding distance distributions to the time traces in (A) as solid lines following the same color code as in (A).

To check if mainly interstrand kissing hairpins were observable, another experiment was set up. The singly labeled full-length constructs  $P_{1,Full}^{U26}$  and  $P_{2,Full}^{U55}$  were mixed equivalently and measured in the absence and presence of Gdm<sup>+</sup> (Figure 83). In agreement with the measurements performed solely on the homo singly labeled full-length constructs, ~10% modulation depth was obtained that matched to almost 28% unspecific intermolecular interactions. A broad distance distribution was detected with no hint of a promoted hetero kissing hairpin interaction.

A peak at ~6.5 nm was discernable. However, this peak is in a region where the distances are not reliable and could result from background corrections. Cross interactions visualized in Figure 84 were supposed to contribute to this distance. But the experimental set up did not allow to draw a conclusion about that.

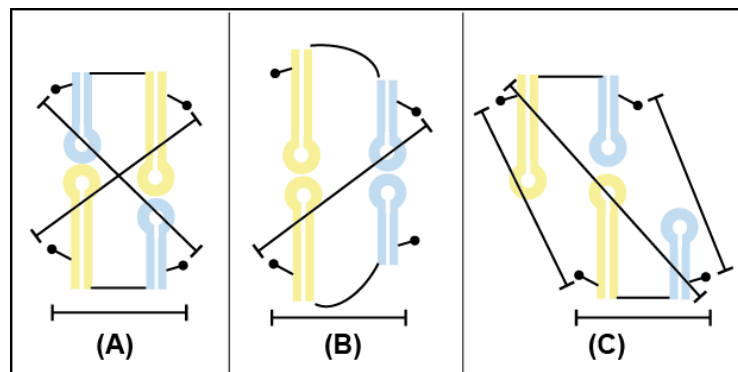


Figure 84. Cross interactions, which might contribute to the PELDOR measurement.

Summarizing the results, the PELDOR measurements on the full-length construct could not show that the intramolecular hetero kissing hairpins build in a promoted way. Nor did they allow to distinguish if the distance belonging to the hetero kissing hairpins is relatable to intra- or interstrand interaction. The question arose whether the linker between the hairpins was long enough to enclose the kissing hairpin formation, or whether the linker length may inhibit the intramolecular kissing hairpin formation.

#### 3.2.7.4 Analysis of the linker length

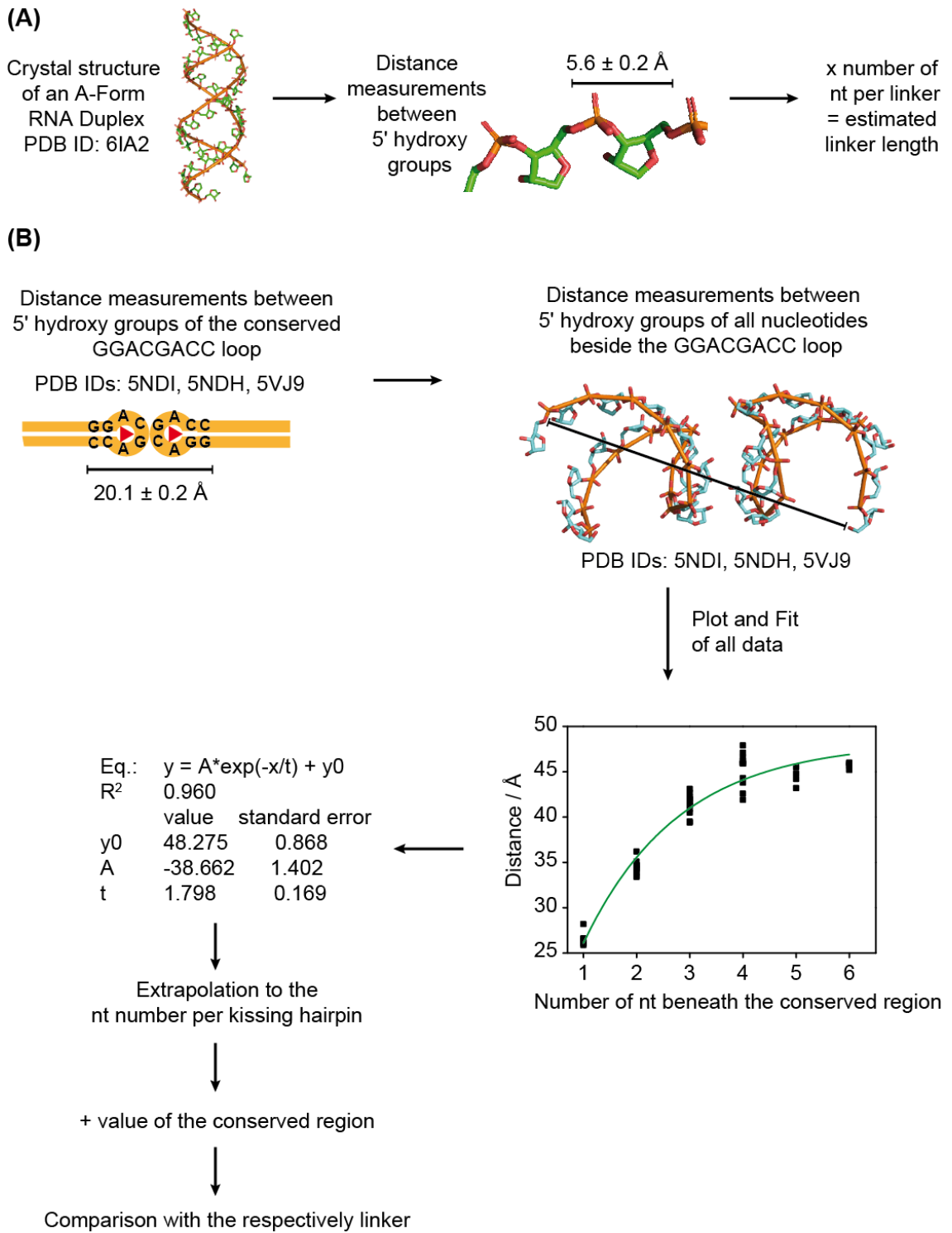
To answer this question, the Guanidine-II riboswitch RNA sequence used in this thesis and the 112 other RNA sequences derived from other species reported by Weinberg et al.<sup>43</sup> were analyzed. All raw data are listed in the appendix.

To test whether the linker length enables the intrastrand kissing hairpin interaction, the number of nt per linker was transformed into a distance. Subsequently, the length of the kissing hairpins was estimated and compared to the former one. The general approach is visualized in Scheme 2. At first the linker length was considered (Scheme 2A). An overview about the number of nt per linker is given in Table 11. The linker length in general varies between 8 and 39 nt, with its median at 14 nt.

Table 11. Overview of the number of nt per linker.

Number of nt	Minimum	Median	Maximum
Linker	8	14	39

To translate the number of nt into a distance, the size of one nt was evaluated. To do so, distances between the 5' hydroxy groups of an A-Form RNA duplex (PDB ID: 6IA2)<sup>277</sup> were measured. The median distance of 5.6 Å (Table 12) was multiplied with the number of nt per linker to estimate the linker length. The smallest distance the shortest linker of 8 nt is able to encompass was received with 45 Å. Whereas, the greatest linker of 39 nt was found to be able to enclose a distance of 218 Å (Table 13).



Scheme 2. Visualization of the approach to obtain (A) the linker length and (B) the kissing hairpin length.

Table 12. Overview of the measured 5' hydroxy distance of the duplex.

Distance / Å	Minimum	Median	Maximum
Duplex	5.4	5.6	5.9

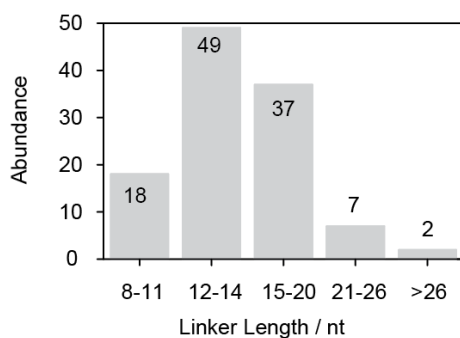


Figure 85. Overview of the abundance of a certain linker length in nt.

Table 13. Overview of the estimated linker length.

Estimated linker length / Å	Minimum	Median	Maximum
Linker	44.8	78.4	218.4

### 3.2.7.5 Analysis of the kissing hairpin length

Afterwards, the distance the linker needed to enclose was predicted, that is to say the kissing hairpin length (Scheme 2B). The stem length of **P1** was mostly found to exceed the length of **P2** with median values of **P1** = 8 nt and **P2** = 5 nt (Table 14 and Figure 85).

 Table 14. Overview of the number of nt per **P1** and **P2** stem.

Number of nt	Minimum	Median	Maximum
<b>P1</b>	3	8	14
<b>P2</b>	4	5	7

All available crystal structures containing  $\text{Gdm}^+$  as ligand showed a conserved GG ACGA CC region (PDB ID: 5NDI<sup>49</sup>, 5NDH<sup>49</sup> and 5VJ9<sup>48</sup>). The distance stretched between



the conserved region delivered similar results with a median of 20.1 Å (Table 15).

Table 15. Overview of the measured distance stretched by the conserved GG ACGA CC binding pocket region.

Measured distance / Å	Minimum	Median	Maximum
conserved region	19.7	20.1	20.5

The stem of the hairpins vary between 3 – 14 nt (Table 14). However, the maximum length of a stem in a solved crystal structure is only 6 nt (PDB ID: 5NDI)<sup>49</sup>. Therefore, a mathematical model was used to describe the length of the stem exceeding 6 nt. To do so, the distances between the 5' hydroxy groups of the nt above the conserved region were measured and fitted according to an exponential curve (Scheme 2B). The stem sizes exceeding 6 nt were subsequently estimated with the exponential fit. The whole kissing hairpin size was afterwards calculated by addition of the length of the conserved region to the stem length. Eventually, the size of the kissing hairpin were compared to the respective linker (Figure 86).

The results indicated that in 80%, the linker is long enough to enclose the kissing hairpin and thereby enable the kissing hairpin formation.

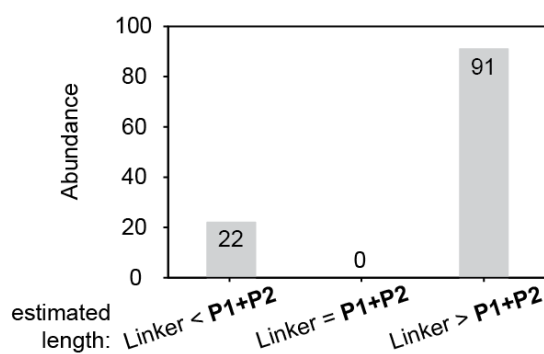


Figure 86. Overview about the abundance that the estimated linker length is either smaller (Linker<P1+P2), has the same size (Linker=P1+P2) or exceed the estimated length of the kissing hairpin (Linker>P1+P2).

In this thesis, the stem of **P1** was assigned to 9 nt, the stem of **P2** to 6 nt and the linker to 13 nt (Table 16). The estimated distance of the kissing hairpin exceeded the one of the linker by 1 Å. Due to uncertainties of this approach, this hinted towards the possibility

that the linker could not enclose the kissing hairpin, and could explain why mainly interstrand kissing hairpins were found.

Table 16. Overview of the distance estimation connected to the specific sequence used in this study.

Number of nt			Estimated Distance / Å		
<b>P1</b>	<b>P2</b>	Linker	Kissing Hairpins	Linker	Linker - Kissing Hairpins
9	6	12	68.3	67.2	-1.1

The distance estimation was based on several assumptions that might bias the reliability. The linker geometry was related to the one of a duplex. Unfortunately, there exist no crystal structure or other measurement revealing the linker length. Thus, the linker could have a different length, but a duplex was a good starting point. Additionally, the hairpin approach relied on only three crystal structures, which are generated under different conditions. Na<sup>+</sup>, K<sup>+</sup>, Mg<sup>2+</sup>, sulfate and spermine<sup>48,49</sup> were found in the crystals, which might alter nucleotide arrangements. This was especially visible by comparing the variance of the distance of the hairpins 4 nt apart of the conserved region. Through all crystal structures, it varied between 41.9 and 47.9 Å. However, the fitting curve to estimate the stem length resembled the experimental data with an R<sup>2</sup> = 0.96. Thus, the extrapolation was a good way to go.

### 3.2.8 Analysis of the doubly labeled full-length riboswitch with additional SDS

In the absence of  $\text{Gdm}^+$ , the mechanistically proposed about the Guanidine-II riboswitch assumes a pairing of the Anti-SDS located in the linker and the 5' end of the **P1** stem with the SDS (Figure 87).<sup>48</sup> To test this, two spin label were introduced in the Guanidine-II riboswitch that included the SDS.

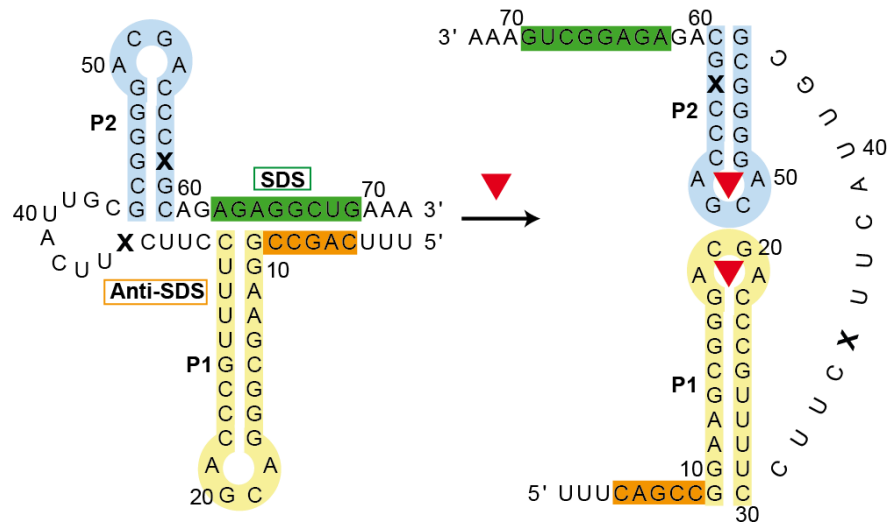


Figure 87. Proposed switching mechanism of the Guanidine-II riboswitch with the base sequence used in this study and additional SDS (the representation is based on reference 48). The bold "X" represents the spin labeling position.

#### 3.2.8.1 Spin labeling reaction

The spin labeling positions were chosen in the proven position in the **P2** stem and in the connecting linker between the hairpins (Figure 87). Based on the proposed mechanism,<sup>48</sup> the spin labels were suggested to be in close vicinity and that addition of  $\text{Gdm}^+$  should alter the distance of the spin label.

Absorption measurements of the stock solution of the RNA, meaning the purchased RNA diluted in water gave evidently wrong values. Request by the provider revealed that their concentration determination relies on absorption measurements in cuvettes with high concentrations and they advised not using the NanoDrop for that purpose. By reason that only a small amount of RNA was on hand, concentration determination in cuvettes were not an option. Thus, the RNA concentration was estimated and approximately 2.5 nm aliquots for the spin labeling reaction were prepared.

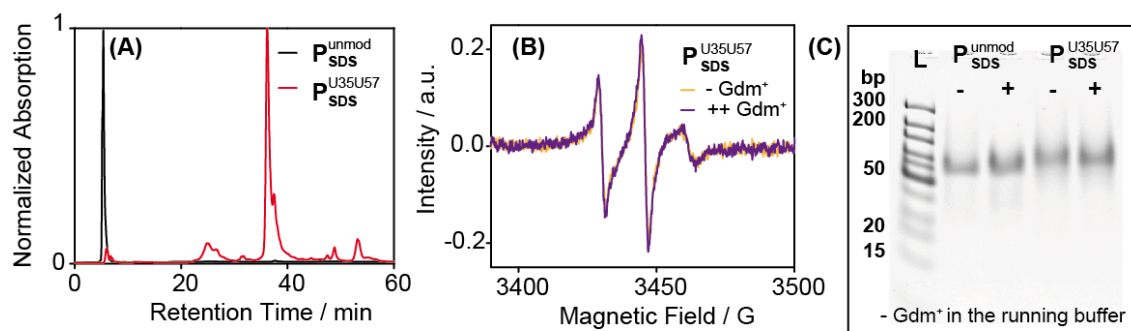


Figure 88. (A) HPLC Run of the unmodified RNA (black line) and labeled RNA (red line) performed at 60 °C column temperature. (B) cwEPR spectrum of  $P_{SDS}^{U35U57}$  in the absence (yellow line) and presence (purple line) of  $Gdm^+$ . (C) 15% native PAGE analysis without  $Gdm^+$  in the running buffer in the absence (-) and presence (+) of  $Gdm^+$  for  $P_{SDS}^{unmod}$  and  $P_{SDS}^{U35U57}$ . "L" depicts the GeneRuler ultra low range DNA ladder (ThermoFisher) with the base pair sizes on the left.

The spin labeling procedure was conducted as described above. The purification of the spin labeled product on the HPLC presented a distinct shift from unmodified to labeled RNA. Thus, the general spin labeling procedure was proposed to be directly transmittable to long RNA strands (Figure 88A).

cwEPR measurements confirmed the successful spin labeling and separation of free spin label (Figure 88B).

To prove if the spin label, especially the newly introduced one in the linker, interrupted the folding of the RNA, native PAGE were performed in absence and presence of  $Gdm^+$ . Comparison of unmodified and labeled RNA did not yield any different. In the absence and presence of  $Gdm^+$ , one defined band was observed, which argued for a good defined conformation. Furthermore, the native PAGE verified that the RNA fold in comparable conformations evaluating the influence of the spin label as minor (Figure 88C).

### 3.2.8.2 PELDOR measurements

The PELDOR time trace and the corresponding distance distributions are shown in Figure 89 in the absence (yellow line) and presence (purple line) of  $Gdm^+$ . The modulation depth of 34% indicated that mainly intramolecular interactions were obtained. However, the distance distributions was broad and detected no change by addition of  $Gdm^+$ . Moreover, the broad distance distribution was received with the peak at 6.5 nm that could result from background corrections and is thus unreliable. So, it might be that the construct adopted a conformation where the spin labels were too far away to observe their dipolar coupling. Due to the native PAGE, it seemed likely that it folds into a specific

conformation. But unfortunately, this conformation can not be assigned to a structure with the PELDOR data.

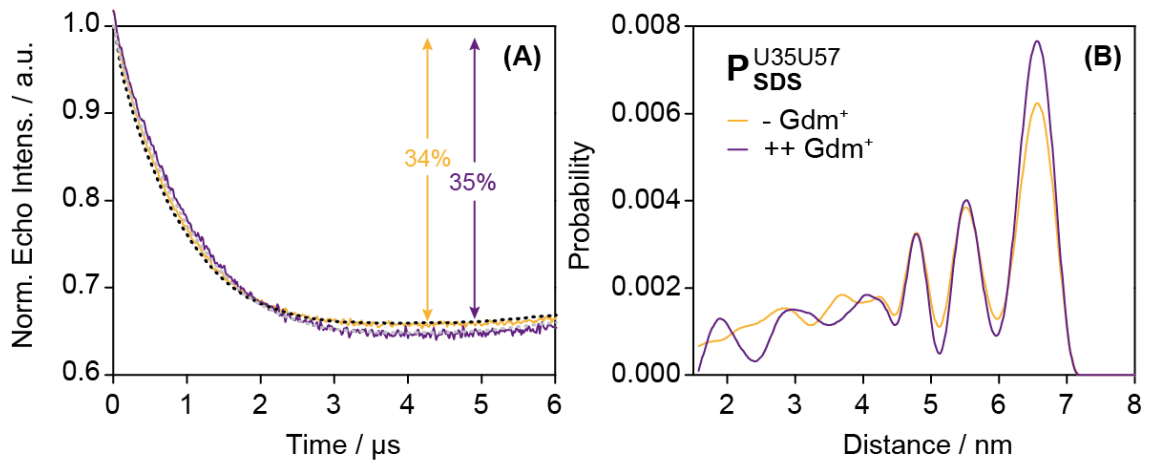


Figure 89. (A) Background corrected PELDOR time traces for  $P_{\text{SDS}}^{\text{U35U57}}$  in the absence (yellow line) and presence (purple line) of  $\text{Gdm}^+$ . The fits are overlaid as black or grey dotted lines, respectively. The modulation depths are indicated in percentages. (B) shows the distance distributions corresponding to the time traces in (A) as solid lines following the same color code as in (A).

### 3.3 Mn<sup>2+</sup> binding study

DNAzymes are functional DNA molecules, that are able to form three-dimensional structures and catalyze different reactions as cleavage or ligation of RNA and DNA strands. Its function is proposed to be metal ion dependent.<sup>61,297,298</sup> Here, the binding of Mn<sup>2+</sup> to the 10-23 DNAzyme was investigated. The 10-23 DNAzyme analysis was done as a collaboration with the Span and Etzkorn lab and the spectra were recorded with Julian Victor and Hannah Rosenbach. The DNAzyme:RNA complexes used in this study were stabilized and thus prevented to perform its cleavage reaction by introducing a 2'-fluoro RNA substrate. To determine if the metal ion dependent cleavage activity goes hand in hand with specific metal ion binding sites, Mn<sup>2+</sup> binding studies were conducted.

At room temperature, the cwEPR X-band signal of the high spin Mn<sup>2+</sup> consists of six lines as a result of the coupling of the electron spin  $s = \frac{5}{2}$  to the nuclear spin  $I(^{55}\text{Mn}) = +\frac{5}{2}$ . With an electron spin of  $s = \frac{5}{2}$ , Mn<sup>2+</sup> has zero-field splitting (ZFS). In a high symmetric ligand field as the Mn<sup>2+</sup> exhibit in aqueous conditions, the six lines in the cwEPR spectrum are sharp (Figure 90). Increasing the asymmetry of the ligand field by binding of Mn<sup>2+</sup> to a biomolecule increases the ZFS. Additionally, the large size of the biomolecule induces a slower molecular tumbling. The effects together lead to a strong line broadening so that the amplitude of the EPR signal vanished. The diminution of the signal compared to a Mn<sup>2+</sup> reference in aqueous condition is used to quantify the bound Mn<sup>2+</sup>. Thus comparing cwEPR spectra of oligonucleotide containing sample with a reference, discloses the number and affinity of bound Mn<sup>2+</sup>.<sup>108,137–146</sup>

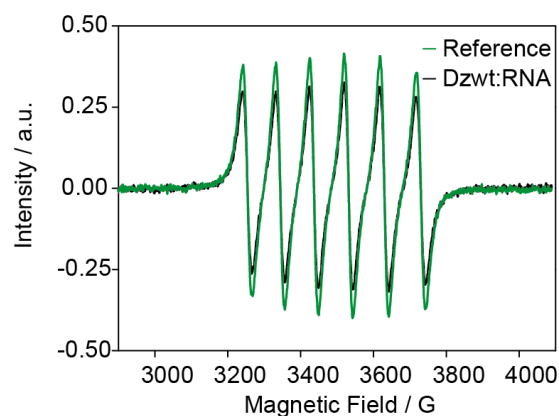


Figure 90. cwEPR spectrum of a reference Mn<sup>2+</sup> measurement (green line) and the same concentrated Mn<sup>2+</sup> binding to the Dzwt:RNA complex (black line).

Quantitative measurements are difficult to perform and previously approaches were done under my supervision by Max Stockmeier and Moritz Wittig in context of their Bachelor thesis.<sup>299,300</sup>

### 3.3.1 Protocol for the cwEPR Mn<sup>2+</sup>-titration

Titration was conducted in a special flat cell with a volume of 500  $\mu\text{L}$ . The cell has a comparable large volume. High volumes of aqueous solutions are difficult to measure in EPR spectroscopy due to the high dielectric constant. Therefore, the flat cell in combination with the resonator ER 4103TM (Bruker) was used, which provide high Q values, thus good data quality. The resonator allows to place the sample in a minimum of the electric field, but in the maximum of the magnetic field.<sup>301</sup> The precise alignment in exactly this position was difficult to perform and is part of the tuning procedure. The tuning has the aim to achieve an optimal absorption of the EPR signal. It manifests itself in a dip. The dip should be as narrow and deep as possible. Tuning was performed at 20 dB. If no dip is visible, the most common reason is that the flat cell is not positioned correctly. Moving the cell carefully up and down and also rotation might help to find the correct field position. It is crucial for the measurement, that the tuning is processed meticulous. When the dip was found, the flat cell position, the iris and the frequency was optimized. Auto Tuning was possible and is strongly recommended to be done. Afterwards, measurement of the Q-value was performed. This enable comparable properties, which are essential for quantitative measurements.

The spectrometer was switched into the Operate modus at 60 dB for at least one hour before starting the measurements. This promoted that the spectrometer had enough time to warm up. Otherwise, the dip was found to be unstable. Normally, the Tune modus is used for that issue, but after a while the spectrometer was found to switch in the Standby modus then.

Titration was performed by adding 2  $\mu\text{L}$  Mn<sup>2+</sup> stock solution directly into 500  $\mu\text{L}$  buffer or buffered oligonucleotide solution into the flat cell with a 10  $\mu\text{L}$  Microloader tip (Eppendorf). To avoid chelation of the metal ions, a non-chelating buffer was used e.g., tris(hydroxymethyl)aminomethane (*Tris*). Subsequent to addition of Mn<sup>2+</sup>, the solution was mixed. Prior tests with a visualizer, here Bromphenol blue, demonstrated that reliable mixing is difficult to perform in the flat cell itself. The flat cell does not allow to inject a standard pipette. Thus normal “up-and-down”-pipetting cannot be performed. Furthermore, the solution cannot be filled into e.g., an Eppendorf tube for the mixing-

issue because the pipette cannot be injected into the solution. Besides there would be small sample loss by transferring into another tube. A home-build syringe was utilized to that mixing-issue. The construction allowed injection of the solution in the flat cell and enabled collection of the whole solution. The home-build syringe was prepared by cutting approximately 4 mm of the groove of a Microloader tip (Eppendorf) with a sterile scalpel and shortly flamed the cutting site to enable a smooth surface. The tip was introduced into a 1 mL Tuberculin syringe (NORM-JECT) and leak-proven with buffer. In this way, the whole solution was collectable. By putting on a vortexer, the solution could be mixed. The homogenate solution was reinjected into the flat cell.

### 3.3.2 Data analysis and measurements conducted on the 10-23 DNAzyme

Measurements were conducted on I) the 10-23 DNAzyme, now called Dzwt, in the absence of the monovalent NaCl, in the presence of 100 mM NaCl and in the presence of 1 M NaCl, and on II) the 10-23 DNAzyme wherein one nucleotide in the catalytic core is mutated, referred to as Dz<sup>5C</sup>. At first, the general data analysis is described on the example of the Dzwt, followed by the results for both DNAzyme constructs.

The cwEPR spectrum of free Mn<sup>2+</sup> in a reference measurement showed six lines. Comparison with the Dzwt:RNA complex at the same Mn<sup>2+</sup> concentration nicely demonstrated, that binding to the biomolecule induced a spectrum alteration (Figure 90). Precise analysis of this signal difference was adopted to predict the bound fraction of Mn<sup>2+</sup>.

The cwEPR data analysis is visualized in Figure 91. Spectra especially at low Mn<sup>2+</sup> concentrations (< 100 μM) were challenging to analyze. Single integration, followed by baseline correction of a third order polynomial and subsequent single integration resulted in reliable data. The double integrals (*Double Integral*) were corrected taking the Q-value (*Q Value*) and the microwave power (*Power*) into account. The values of the corrected double integral (*Double Integral<sub>corr</sub>*) were calculated by

$$Double\ Integral_{corr} = \frac{Double\ Integral}{Q\ Value \times \sqrt{Power}} \quad eq. 20$$



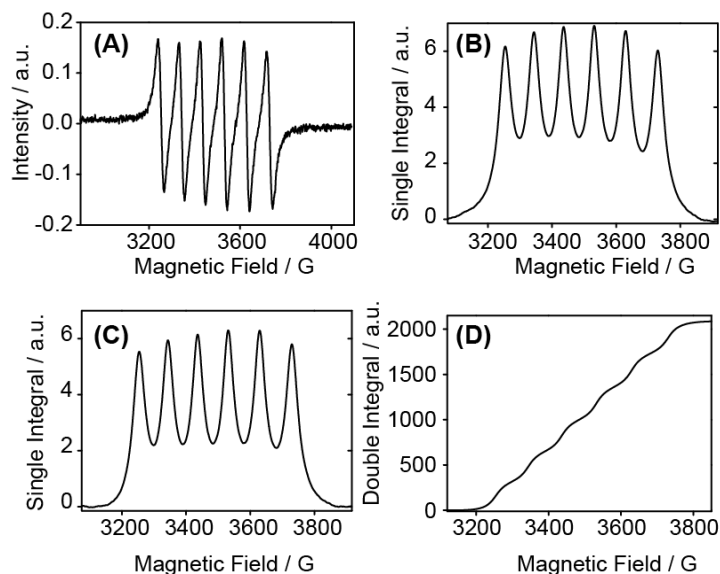


Figure 91. cwEPR Mn<sup>2+</sup> titration data analysis. (A) Raw spectrum. (B) Single integrated spectrum. (C) Baseline corrected single integrated spectrum. (D) Double integrated spectrum.

A Graph in which the  $Double\ Integral_{corr}$  was plotted against the titrated Mn<sup>2+</sup> concentration gave a first hint about the binding properties (Figure 92). The data points of the oligonucleotide containing sample (Dzwt:RNA) showed lower  $Double\ Integral_{corr}$  compared to reference. Thus, Mn<sup>2+</sup> was expected to bound to the oligonucleotide. To obtain the specific binding number and affinity, binding isotherms were prepared. The  $Double\ Integral_{corr}$  of the reference ( $Double\ Integral_{corr,reference}$ ) and the one of the oligonucleotide containing sample ( $Double\ Integral_{corr,oligo}$ ) were used to calculate the concentration of free Mn<sup>2+</sup> in the oligonucleotide containing sample ( $[Mn_{free,oligo}^{2+}]$ ). To do so, the slope of the reference measurement in Figure 92 was predicted ( $slope_{reference}$ ).  $slope_{reference}$  contains the information how the  $Double\ Integral_{corr}$

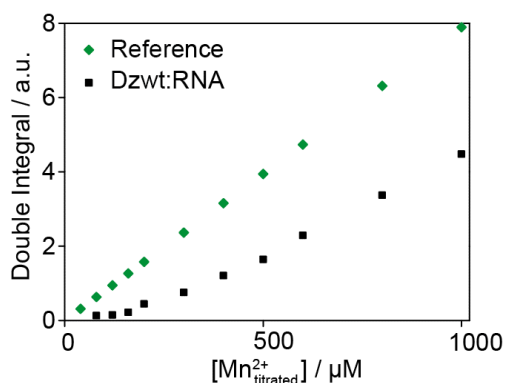


Figure 92. Plot of the corrected double integral against the titrated Mn<sup>2+</sup> of a reference solution (green line) and an exemplary DNAzyme:RNA complex (black line).

changes upon increased concentration of free  $Mn^{2+}$ . Thus, comparison with  $Double\ Integral_{corr,oligo}$  yielded  $[Mn^{2+}_{free,oligo}]$ .  $[Mn^{2+}_{free,oligo}]$  was consequently determined by

$$[Mn^{2+}_{free,oligo}] = \frac{Double\ Integral_{corr,oligo}}{slope_{reference}} \quad eq. 21$$

The bound fraction of  $Mn^{2+}$   $[Mn^{2+}_{bound,oligo}]$  was calculated by subtracting  $[Mn^{2+}_{free,oligo}]$  from the titrated  $Mn^{2+}$  concentration  $[Mn^{2+}_{titrated,oligo}]$ .

$$[Mn^{2+}_{bound,oligo}] = [Mn^{2+}_{titrated,oligo}] - [Mn^{2+}_{free,oligo}] \quad eq. 22$$

Binding isotherms were received by plotting the ratio between  $[Mn^{2+}_{bound,oligo}]$  and the oligo concentration  $[oligo]$ , that was in this study 40  $\mu M$ , against the concentration of  $[Mn^{2+}_{free,oligo}]$ .

The binding isotherms for the Dzwt:RNA complex obtained with different NaCl concentrations are shown in Figure 93. Fitting the data yielded the  $Mn^{2+}$  binding number and affinity. The data in the absence of NaCl (Figure 93A) were best described by assuming one non-cooperative binding site with

$$\frac{[Mn^{2+}_{bound}]}{[oligo]} = \frac{n \times [Mn^{2+}_{free,oligo}]}{K_D + [Mn^{2+}_{free,oligo}]} \quad eq. 23$$

wherein each bound  $Mn^{2+}$  ion had an affinity constant of  $K_D$ . One specific binding site with a  $K_D = 111 \pm 20 \mu M$  was found in the absence of NaCl.

The data in the presence of 100 mM (Figure 93B) and 1000 mM NaCl (Figure 93C) were best fitted by a cooperative binding with

$$\frac{[Mn^{2+}_{bound}]}{[oligo]} = \frac{[Mn^{2+}_{free,oligo}]^n}{(K_D + [Mn^{2+}_{free,oligo}])^n} \quad eq. 24$$

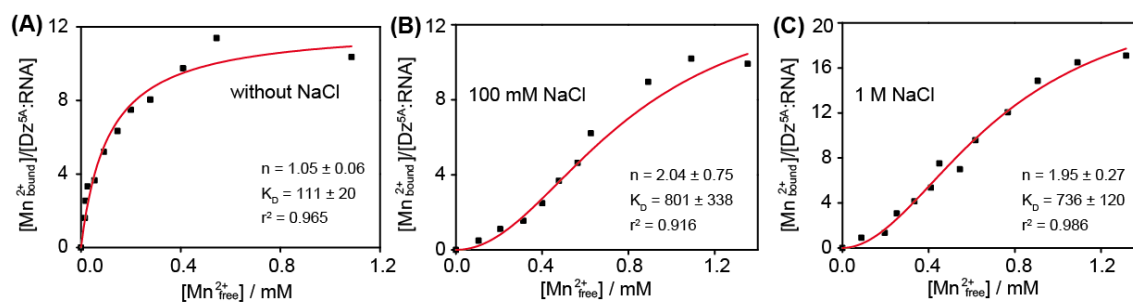


Figure 93.  $Mn^{2+}$  binding isotherms for 40  $\mu M$  Dzwt:RNA complex (A) in the absence of NaCl, (B) in the presence of 100 mM NaCl and (C) in the presence of 1000 mM NaCl.

In the error width, two identical binding sites were observed with a  $K_D \sim 750 \mu\text{M}$ . Thus, in the presence of NaCl, it seemed like the high specific binding site was already occupied by Na<sup>+</sup> ions and two Mn<sup>2+</sup> ions bound with lower affinity.

Binding studies were also conducted on the 10-23 DNAzyme where an A was mutated to a C into the catalytic core and which is now called Dz<sup>5C</sup>. A binding isotherm was recorded in the presence of 100 mM NaCl in 20% D<sub>2</sub>O to be comparable to measurements done in an NMR experiment.

The binding isotherms were fitted with the non-cooperative and cooperative model in the concentration range of  $[Mn_{free}^{2+}]$  of 0-0.5 mM and 0-6.5 mM (Figure 94). The non-cooperative model did not fit the data, whereas the cooperative model matched. The data in the concentration range of  $[Mn_{free}^{2+}]$  of 0-0.5 mM was fitted with eq. 24. The result indicated two cooperative binding sites with a  $K_D = 362 \pm 83 \mu\text{M}$ . The best fit of the experimental data of the larger concentration range was obtained assuming a cooperative binding with three different binding sites with

$$\frac{[Mn_{bound}^{2+}]}{[oligo]} = \frac{[Mn_{free,oligo}^{2+}]^{n_1}}{(K_{D1} + [Mn_{free,oligo}^{2+}])^{n_1}} + \frac{[Mn_{free,oligo}^{2+}]^{n_2}}{(K_{D2} + [Mn_{free,oligo}^{2+}])^{n_2}} + \frac{[Mn_{free,oligo}^{2+}]^{n_3}}{(K_{D3} + [Mn_{free,oligo}^{2+}])^{n_3}} \quad \text{eq. 25}$$

The results detected two specific binding sites with a  $K_D = 173 \pm 109 \mu\text{M}$  and several non-specific sites. Nevertheless, both fits, in the small and the large concentration range,

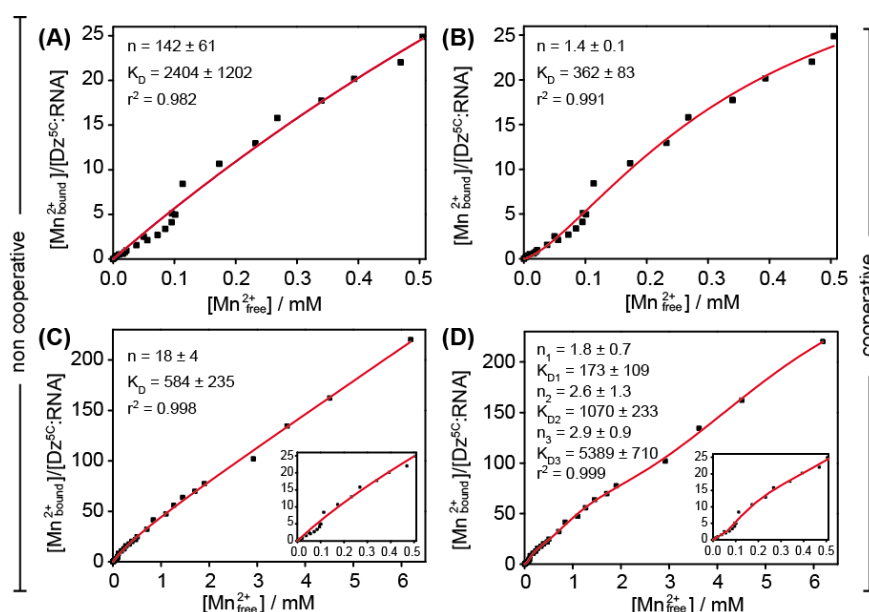


Figure 94. Mn<sup>2+</sup> binding isotherms for 40 μM Dz<sup>5C</sup>:RNA complex in the presence of 100 mM NaCl analyzed with **left panel**: the non-cooperative fit and **right panel**: a cooperative fit in the concentration range of (A) and (B) 0-0.5 mM, and (C) and (D) 0-6.5 mM of free Mn<sup>2+</sup>.

detected two cooperative binding sites. Thus the results are nicely in agreement with the wildtype DNAzyme in the presence of 100 mM NaCl.

Furthermore, the  $Dz^{5C}$ :RNA complex was prepared in 100 mM NaCl and 600  $\mu\text{M}$   $\text{Mn}^{2+}$ . The divalent binding sites was assumed to be occupied by  $\text{Mn}^{2+}$  ions under these conditions.  $\text{Mg}^{2+}$  was added to investigate the exchange. In Figure 95 is shown that the double integral did not change. Thus, two conclusions can be drawn: either,  $\text{Mn}^{2+}$  bound with higher affinity to the complex and was thus not substituted from  $\text{Mg}^{2+}$ , or  $\text{Mn}^{2+}$  bound at different sites.

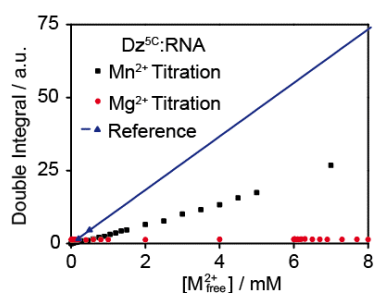


Figure 95 Double Integral vs concentration of the respective divalent metal ion. In black the sample of (A) containing 40  $\mu\text{M}$   $Dz^{5C}$ :RNA complex and 100 mM NaCl titrated with  $\text{Mn}^{2+}$ , in blue the reference  $\text{Mn}^{2+}$  measurement, and in red the sample containing 40  $\mu\text{M}$   $Dz^{5C}$ :RNA complex, 100 mM NaCl, 600  $\mu\text{M}$   $\text{Mn}^{2+}$  titrated with  $\text{Mg}^{2+}$ .

## 4. Conclusion and Outlook

### 4.1 Spin labeling of RNA with a *gem*-diethyl nitroxide via Click-chemistry

For the azide functionalized *gem*-diethyl isoindoline nitroxide spin label **1\***, a protocol was established to successfully bioconjugate it via Click-chemistry to RNA. Through temperature dependent UV-VIS measurements and CD spectroscopy, the degree of RNA structure perturbation was assessed to be minor and comparable to its *gem*-dimethyl analogue **2\***. A detailed study on the  $T_M$  relaxation revealed that the phase memory times of **1\*** and **2\*** consist of two contributors, the instantaneous spin diffusion and the nuclear spin diffusion. It can be highlighted that both phase memory times were found in the range of 21  $\mu$ s at 50 K in deuterated buffer. This relaxation time is fairly long compared to proteins, which is attributed to the spin label design and the meticulous sample preparation.

The rigidity of the spin labels was affirmed in a PELDOR experiment, as the orientation selectivity could be resolved. Subsequent data analysis with PeldorFit<sup>167</sup> predicted similar spatial orientations and interspin distances for **1\*** and **2\***, providing evidence for the assumption that both spin labels adopted comparable conformations within the RNA structure.

In order to approach *in cell* EPR distance measurements, the reduction stability of **1\*** was assessed in reducing environments. Given the lacking water-solubility of **1\***, a model DNA construct was spin labeled, highlighting that the SDSL is applicable to both nucleic acids. The spin labeled DNA was found to be more resistant compared to the commonly used MTSL towards reducing conditions mimicking cellular environment. However, distance measurements within intact cells have not been carried out.

### 4.2 The Guanidine-II Riboswitch

The developed SDSL approach in combination with PELDOR measurements was further applied to the Guanidine-II riboswitch to validate its switching mechanism that is proposed to base on the interaction of the hairpins **P1** and **P2**.<sup>48</sup>

Accordingly, SDSL was performed on singly and doubly modified RNA strands varying in length from 16 to 72 nt. The singly spin labeled, truncated hairpins **P1** (22 nt) and **P2** (16 nt) of the Guanidine-II riboswitch revealed the **P1 | P2** interaction was present alongside the homodimers if  $Gdm^+$  was added (Figure 96). This study also showed that

the RNA strands can adopt duplex and monomer hairpin structures in the absence of  $\text{Gdm}^+$ .

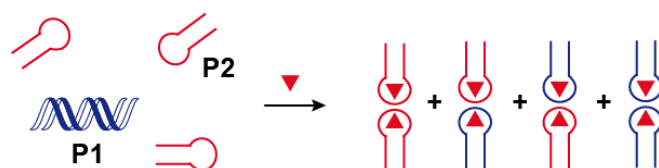


Figure 96. Conclusion regarding the truncated hairpins **P1** and **P2**. Binding of  $\text{Gdm}^+$  (red triangle) was found to form hetero kissing hairpins alongside of homo kissing hairpins in a statistical 1:2:1 fashion.

Ultimately, the investigation was extended to the full-length riboswitch construct consisting of the truncated hairpins connected via a 13 nt long linker. To do so, three singly spin labeled and two doubly labeled full-length riboswitch constructs were prepared. The EPR based measurements on the aforementioned constructs revealed that the Guanidine-II riboswitch forms both intrastrand and interstrand kissing hairpins (Figure 97). Even though, the PELDOR measurements detected hetero kissing hairpins, this method did not allow to distinguishing between intra- or interstrand interaction (Figure 97). However, the size of complexes arising from both kind of interaction should differ remarkably. Therefore, alternative methods as dynamic light scattering or the NMR based diffusion ordered spectroscopy (DOSY) might provide future insights into the composition of the formed kissing hairpins. Nevertheless, the comparable high RNA concentrations necessary for these methods might impede generation of the native structure.

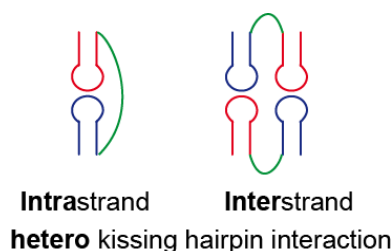


Figure 97. Conclusion regarding the full-length Guanidine-II riboswitch. Intrastrand and interstrand interaction of the hetero kissing hairpins could not be distinguished.

An approach was made to evaluate if the linker in general and especially the one used in this study is long enough to enclose the hetero kissing hairpins and allow their interaction. The results disclosed that out of 113 Guanidine-II riboswitch sequences found by Weinberg et al. in different species,<sup>43</sup> 80% should be able to form intrastrand kissing hairpins. However, the RNA sequence used in this thesis might actually belong to the ones where the linker could not enclose the hetero kissing hairpins.

### 4.3 Mn<sup>2+</sup> binding study

A protocol for quantitative Mn<sup>2+</sup> cwEPR measurements was established to assess the number and affinity of Mn<sup>2+</sup> ion binding sites in two 10-23 DNAzymes. Application of it to the wildtype Dzwt:RNA complex, revealed that the Mn<sup>2+</sup> ions compete with Na<sup>+</sup> ions for the binding site. In the absence of Na<sup>+</sup> ions, one high specific binding site of  $K_D \sim 111 \mu\text{M}$  for Mn<sup>2+</sup> was found. In the presence of NaCl (100 mM and 1M), it seems like Na<sup>+</sup> occupies the high specific binding site revealing two cooperative Mn<sup>2+</sup> binding sites with lower affinity of  $K_D \sim 750 \mu\text{M}$ . The EPR based binding curves of the Dz<sup>5C</sup>:RNA complex prepared under the conditions used for external NMR measurements (100 mM NaCl in 20% D<sub>2</sub>O), showed a more complex binding behavior compared to the wildtype. However and in agreement to the wildtype, two cooperative binding sites were found. Furthermore, a Mg<sup>2+</sup> exchange experiment with the Dz<sup>5C</sup>:RNA complex prepared in 100 mM NaCl and 600  $\mu\text{M}$  Mn<sup>2+</sup> indicated that either Mn<sup>2+</sup> bound with higher affinity to the Dz<sup>5C</sup>:RNA complex compared to Mg<sup>2+</sup>, or that Mn<sup>2+</sup> bound at different binding sites than Mg<sup>2+</sup>. Nevertheless, the results showed that the DNAzyme:RNA complexes specifically bind metal ions, supporting the structural/catalytic importance of these ions for this DNAzyme.

## 5. Material and Methods

Before starting work, the bench was purified with RNase Away (Thermo Scientific). Exclusively autoclaved pipette tips and glass bottles were used.

### 5.1 RNA sequences

RNA constructs were purchased from metabion international AG (Planegg, Germany) with the denoted sequences.

Table 17. List of the RNA constructs used in this study. The marked **X** depicted the 5-deoxy-2'-ethynyl-Uridine, thus the spin labeling position.

Construct	Sequence 5' to 3'
model RNA <sup>unmod</sup>	CAU CUG AUA UCA GAU G
model RNA <sup>U15</sup>	CAU CUG AUA UCA GAX G
<b>P</b> <sub>1</sub> <sup>unmod</sup>	GGA AGC GGG ACG ACC CGU UUU C
<b>P</b> <sub>1</sub> <sup>U18</sup>	GGA AGC GGG ACG ACC CGX UUU C
<b>P</b> <sub>1</sub> <sup>U20</sup>	GGA AGC GGG ACG ACC CGU UXU C
<b>P</b> <sub>2</sub> <sup>unmod</sup>	GCG GGG ACG ACC CUG C
<b>P</b> <sub>2</sub> <sup>U14</sup>	GCG GGG ACG ACC CXG C
<b>P</b> <sub>Full</sub> <sup>unmod</sup>	UCA GCC GGA AGC GGG ACG ACC CGU UUU CCU UCU UUC AUU GCG CGG GGA CGA CCC UGC AG
<b>P</b> <sub>1,Full</sub> <sup>U24</sup>	UCA GCC GGA AGC GGG ACG ACC CGX UUU CCU UCU UUC AUU GCG CGG GGA CGA CCC UGC AG
<b>P</b> <sub>1,Full</sub> <sup>U26</sup>	UCA GCC GGA AGC GGG ACG ACC CGU UXU CCU UCU UUC AUU GCG CGG GGA CGA CCC UGC AG
<b>P</b> <sub>2,Full</sub> <sup>U55</sup>	UCA GCC GGA AGC GGG ACG ACC CGU UUU CCU UCU UUC AUU GCG CGG GGA CGA CCC XGC AG
<b>P</b> <sub>1,2,Full</sub> <sup>U24,U55</sup>	UCA GCC GGA AGC GGG ACG ACC CGX UUU CCU UCU UUC AUU GCG CGG GGA CGA CCC XGC AG
<b>P</b> <sub>1,Full</sub> <sup>U26,U55</sup>	UCA GCC GGA AGC GGG ACG ACC CGU UXU CCU UCU UUC AUU GCG CGG GGA CGA CCC XGC AG



$P_{SDS}^{U35U57}$

UUU CAG CCG GAA GCG GGA CGA CCC GUU UUC CUU CXU UCA UUG CGC  
GGG GAC GAC CCX GCA GAG AGG CUG AAA

## 5.2 Extinction coefficients

### 5.2.1 Extinction coefficients of the RNA constructs

Extinction coefficients were provided by metabion international AG (Planegg, Germany) as listed in Table 18.

Table 18. Extinction coefficients of the RNA constructs.

Construct	Extinction coefficient / mol L <sup>-1</sup> cm <sup>-1</sup>
model RNA <sup>unmod</sup> , model RNA <sup>U15</sup>	168,000
$P_2^{unmod}$ , $P_2^{U14}$	147,000
$P_1^{unmod}$ , $P_1^{U18}$ , $P_1^{U20}$	216,000
$P_{Full}^{unmod}$ , $P_{1,Full}^{U24}$ , $P_{1,Full}^{U26}$ , $P_{1,Full}^{U55}$ , $P_{2,Full}^{U55}$ , $P_{1,2,Full}^{U24,U55}$ , $P_{1,Full}^{U26,U55}$	561,000
$P_{SDS}^{U35U57}$	704,000

### 5.2.2 Extinction coefficient of spin label 1\*

The extinction coefficient of 1\* was measured as dilution series using the NanoDrop Spectrophotometer (Thermo Scientific) in the range of 220-350 nm. Due to the solubility

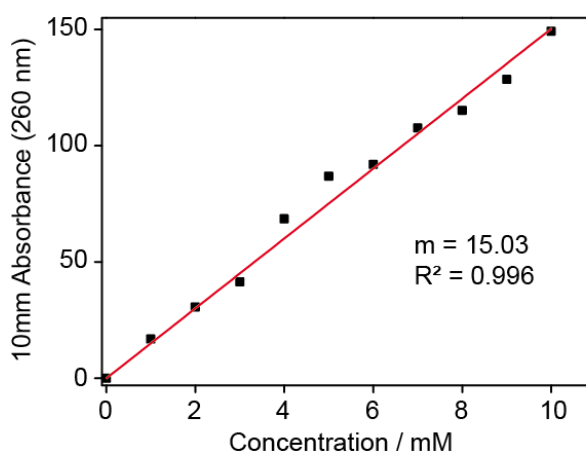


Figure 98. Linear regression of the absorbance at 260 nm of spin label 1\* plotted against the respective concentration.

of the spin label, it was measured in DMSO (Carl Roth) and was therefore not directly comparable to the measurements of RNA in buffered solution, but was used to get an idea of its influence on the RNA concentration determination. The regression line of the measurements in context of the absorbance at 260 nm is shown in Figure 98 and resulted in an extinction coefficient of  $15.03 \text{ mM cm}^{-1}$ . As it is small compared to the extinction coefficients of the RNA, it is neglected when calculating the RNA concentration.

### 5.3 Concentration determination

Nucleic acid concentrations were determined by measuring the absorbance of ultraviolet light using the NanoDrop Spectrophotometer (Thermo Scientific) in the range of 220-350 nm. The ratio of absorbance at 260 nm and 280 nm was used to verify the purity of the RNA. A ratio of  $\sim 2.0$  is generally accepted as “pure” RNA. Furthermore, the ratio 260/230 nm was adopted as secondary proof of RNA purity, commonly ranging between 2.0-2.2.<sup>302,303</sup>  $1^\bullet$  absorbed at 260 nm and induced a little change in the real absorbance profile of the RNA. Additionally, double stranded and single stranded RNA strands altered the absorbance. Thus, values of the RNA concentration noted in the study were only taken as guide values. The concentrations were derived from the Lambert-Beer law, taking the amount of light absorption at 260 nm proportional to the concentration of RNA in solution with respect to the extinction coefficients provided by metabion international AG (Planegg, Germany).

### 5.4 Spin labeling

The purchased dried, modified RNA was dissolved in DEPC (Carl Roth) treated water, now called DEPC water, to obtain a  $100 \mu\text{M}$  stock solution. The concentration was confirmed by measuring the absorption at 260 nm.  $2.5 \text{ nmol}$  aliquots were prepared and dried at the Concentrator plus (Eppendorf). The dried RNA was dissolved in  $4.4 \mu\text{L}$  of DEPC water. Then,  $8 \mu\text{L}$  of a  $250 \text{ mM}$  solution of THPTA (Sigma–Aldrich) in DMSO (Carl Roth) were mixed with  $8 \mu\text{L}$  of a freshly prepared  $50 \text{ mM}$  solution of  $\text{CuI}$  (Carl Roth) in DMSO.  $20 \mu\text{L}$  of DMSO were added and the mixture was incubated for 5 min at room temperature. Then,  $3.6 \mu\text{L}$  of the catalytic solution and  $2 \mu\text{L}$  of  $100 \text{ mM}$  either  $1^\bullet$  or  $2^\bullet$  in DMSO were added to the RNA solution. The reaction solution was mixed and incubated for 30 min at  $60^\circ\text{C}$  and 300 rpm (Thermomixer comfort, Eppendorf, Hamburg, Germany). Via adding of  $480 \mu\text{L}$  DEPC water, the reaction was quenched and

transferred to an Amicon® ultra 3K column (Merck). The desalted products were finally purified via reverse-phase high-performance liquid chromatography (RP HPLC). The relevant fractions were desalted or rebuffered using an Amicon® ultra 3K column (Merck) or an illustra™ NAP™ Column (GE Healthcare).

## 5.5 HPLC purifications

The RNA constructs were purified through RP HPLC with an Agilent 1200 Series HPLC System (Agilent Technology, Santa Clara, CA, USA) in combination with the listed columns. The different RNA constructs were purified at 60 °C with different eluents denoted in the following table.

Table 19. HPLC Methods.

Construct	Time	Acetonitrile / %	0.1 M TEAA / %	Flow / ml per min	Column (Agilent Technologies, Santa Clara, CA, USA)
<b>M, E</b> <sup>[a]</sup>	0	8	92	1.0	Zorbax 300SB-C18, 4.6x150mm
	20	25	75		
<b>P</b> <sup>U18, U14</sup> , <b>P</b> <sup>U20</sup> , <b>P</b> <sup>U14</sup>	0	8	92	1.5	Zorbax 300SB-C18, 4.6x150mm
	20	25	75		
<b>P</b> <sup>U24</sup> , <b>P</b> <sup>U55</sup> , <b>P</b> <sup>U24, U55</sup> , <b>P</b> <sup>U24, U55</sup> , <b>P</b> <sup>U24, U55</sup>	0	8	92	2.0	Zorbax 300SB-C18, 9.4x250mm
	10	8	92	2.0	
	65	23	77		
<b>P</b> <sup>U26</sup> , <b>P</b> <sup>U26, U55</sup> , <b>P</b> <sup>U26, U55</sup> , <b>P</b> <sup>U26, U55</sup>	0	8	92	2.0	Zorbax 300SB-C18, 9.4x250mm
	10	8	92	2.0	
	65	23	77		
<b>P</b> <sup>U35, U57</sup> , <b>P</b> <sup>SDS</sup>	0	12	88	2.0	Zorbax 300SB-C18, 9.4x250mm
	10	12	88	2.0	
	65	25	75		

<sup>[a]</sup>The model RNA<sup>U15</sup> single strand labeled with **1**' is called **E**, while the one labeled with **2**' is titled **M**.

## 5.6 Annealing

### 5.6.1 The model RNA

The model RNA was annealed in Phosphate buffer by heating to 70 °C for 1 min and then cooling to 5 °C with a rate of 1 °C/min in a PCR Thermocycler (Mastercycler nexus, Eppendorf).

### 5.6.2 Fast Annealing

The samples were annealed in a Thermomixer (Thermomixer comfort, Eppendorf) in Folding buffer in the absence or presence of Gdm<sup>+</sup>, respectively, by incubating at 95 °C for 5 min and rapid cooling on ice for at least 10 min.

### 5.6.3 Slow Annealing

The samples were annealed in Folding buffer in absence or presence of Gdm<sup>+</sup>, respectively, in a PCR Thermocycler (Mastercycler nexus, Eppendorf). They were heated to 95°C and hold at this temperature for 3 min. Afterwards, the samples were slowly cooled with 1°C/min, rested at 60°C for 3 min, cooled with 1°C/min and rested again at 50°C for 3min. Lastly, the samples were cooled to 5°C with a rate of 1°C/min.

## 5.7 Buffers

Table 20. List of buffers.

Buffer	Components
Phosphate Buffer	145 mM NaCl (Carl Roth)
	10 mM NaH <sub>2</sub> PO <sub>4</sub> / Na <sub>2</sub> HPO <sub>4</sub> (Carl Roth) pH 7.0
Folding Buffer	10 mM KCl
	10 mM MgCl <sub>2</sub>
	10 mM HEPES pH 7.5
10 x TB Buffer	890 mM Tris-Base
	890 mM Boric Acid
	250 mM NaCl

Loading Buffer	2 x TB Buffer
	50% glycerol
	Bromophenol Blue, Xylencyanol
MBS Buffer	88 mM NaCl
	1 mM KCl
	0.4 mM CaCl <sub>2</sub>
	0.33 mM Ca(NO <sub>3</sub> ) <sub>2</sub>
	0.8 mM MgSO <sub>4</sub>
	5 mM Tris-HCl
	2.4 mM NaHCO <sub>3</sub>

## 5.8 Rebuffering

RNA samples were rebuffered by transferring the sample into an Amicon Ultra-0.5 mL Centrifugal Filter with an 3 K cut-off (Merck). The filter was washed three times with 500  $\mu$ L of the desired buffer by centrifugation for 30 minutes at 14,000 rcf each time. The sample was regained by flipping the column upside down into a second tube and centrifugation for 2 minutes at 2,000 rcf.

## 5.9 LCMS measurements

LCMS measurements were performed on an HTC esquire (Bruker Daltonik) in combination with an Agilent 1100 Series HPLC system (Agilent Technologies) using a Zorbax Narrow Bore SB C18 (2.1 $\times$ 50 mm, 5  $\mu$ m) column (Agilent Technologies). As solvent A 10 mM triethylamine/100 mM hexafluoroisopropanol was adopted with a gradient of 5  $\rightarrow$  20 % B in 20 minutes. As solvent B acetonitrile (MeCN) was used.

## 5.10 Gdm<sup>+</sup> concentrations

The Gdm<sup>+</sup> concentration was set with 0.4 mM or 40 mM Gdm<sup>+</sup> depending on the experiment. Figure captions denote the respective concentration, wherein -Gdm<sup>+</sup> means the absence of Gdm<sup>+</sup>, +Gdm<sup>+</sup> 0.4 mM and ++Gdm<sup>+</sup> 40 mM Gdm<sup>+</sup>.

## 5.11 UV-VIS melting curves

### 5.11.1 Sample preparation

#### a) The model RNA

100 pmol labeled RNA were dried (Centrifuge Concentrator, Concentrator plus, Eppendorf) and resuspended in 100  $\mu$ M aqueous Phosphate buffer. The samples were transferred into cuvettes (Sub-Micro Cell, Quartz, 10 mm, 80  $\mu$ L, Agilent Technologies) and covered with 30  $\mu$ L mineral oil (Carl Roth) to avoid evaporation.

#### b) The Guanidine-II Riboswitch

2.5 nmol of the constructs  $P_2^{U14}$  and  $P_2^{unmod}$ , 400 pmol of  $P_1^{U18}$ ,  $P_1^{U20}$ , and  $P_1^{unmod}$ , and 100 pmol of  $P_{1,Full}^{U24}$ ,  $P_{2,Full}^{U55}$ ,  $P_{1,2,Full}^{U24,U55}$ ,  $P_{Full}^{unmod}$  were dried (Centrifuge Concentrator, Concentrator plus, Eppendorf) and resuspended in 100  $\mu$ L aqueous Folding Buffer. 40 mM Gdm<sup>+</sup> was added and the respective annealing procedure was employed. The samples were filled into cuvettes (Sub-Micro Cell, Quartz, 10 mm, 80  $\mu$ L, Agilent Technologies) and covered with 30  $\mu$ L mineral oil (Carl Roth) to avoid evaporation.

The designated cuvettes were prior to the measurement cooled down to 7 °C. This prevent warming up the RNA before starting the measurement.

### 5.11.2 Measurement

The absorbance measurements were recorded on a Cary 100 UV-Vis spectrophotometer (Agilent Technologies, Santa Clara, CA, USA). Before starting the temperature dependent measurement, an absorbance scan was conducted. The absorbance between 200-400 nm were recorded in 1 nm steps to obtain if the specific RNA absorbance is obtained at 260 nm. The UV melting curves were afterwards recorded at a wavelength of 260 nm. The temperature of the sample was increased with a heating rate of 1 °C/min from 20 °C to 95 °C.

### 5.11.3 Data analysis

The raw UV melting curves were baseline corrected according to the literature.<sup>302</sup> To do so, an upper ( $A_{up}(T)$ ) and lower baseline ( $A_{low}(T)$ ) were generated. The baselines were assigned to the regime where the raw absorbance ( $A_{raw}(T)$ ) adopt almost linearity. The corrected absorption ( $A_{corr}(T)$ ) was obtained by

$$A_{corr}(T) = \frac{A_{raw}(T) - A_{low}(T)}{A_{up}(T) - A_{low}(T)}$$

The melting temperature was obtained by fitting the corrected absorption curve with the *Boltzmann function* in *OriginLab* (OriginPro, Version 8G, OriginLab Corporation, Northampton, MA, USA).

## 5.12 CD spectroscopy

### 5.12.1 Sample preparation

#### a) The model RNA

2 nmol labeled RNA were dried (Centrifuge Concentrator, Concentrator plus, Eppendorf) and resuspended in 200  $\mu$ L Phosphate buffer. After annealing, the samples were transferred into the cuvette (QS High Precision Cell, Art.No 110-1-40, Light Path 1mm, HellmaAnalytics).

#### b) The Guanidine-II Riboswitch

2 nmol  $P_2^{U14}$ ,  $P_2^{unmod}$ ,  $P_1^{U18}$ ,  $P_1^{U20}$ , and  $P_1^{unmod}$ , and 400 pmol  $P_{1,Full}^{U24}$ ,  $P_{2,Full}^{U55}$ ,  $P_{1,2,Full}^{U24,U55}$ ,  $P_{Full}^{unmod}$  were dried (Centrifuge Concentrator, Concentrator plus, Eppendorf) and afterwards diluted in 200  $\mu$ L Folding buffer, which contained 40 mM Gdm<sup>+</sup>, if stated in the figure caption. After annealing, the samples were transferred into the cuvette (QS High Precision Cell, Art.No 110-1-40, Light Path 1mm, HellmaAnalytics).

### 5.12.2 Measurement

CD-spectra were recorded on a JASCO J-810 spectropolarimeter at room temperature. The sensitivity was adjusted to "Standard", which corresponded to 100 mdeg. The

scanning speed was set to 100 nm/min and the spectral range to 200 - 320 nm. The response was adjusted to 1 sec and the bandwidth to 1 nm. 15 scans were averaged.

### 5.13 Native PAGEs

5 mL Acylamide mix (Rotiphorese® Gel 30, 37,5:1, Carl Roth), 4 mL H<sub>2</sub>O and 1 mL TB buffer were mixed. 80 µL 10 % ammonium persulfate solution (APS) and 4 µL tetramethylethylenediamine (TEMED) were added and the gel prepared. The native PAGE gel was pre-runed without sample at least 30 minutes. Native PAGE analysis were carried out on the amount of RNA as denoted in Table 21. The RNA was dried (Centrifuge Concentrator, Concentrator plus, Eppendorf) and resuspended in Folding buffer to obtained a concentration of 25 µM. Equally volume Loading Buffer was added. The Gel was runned within 1x TB at 100 V in an iced cooled water bath. The bands of Bromphenol Blue and Xylencyanol was indicated as visualizer. The Gel was runned until a clear separation of the two bands was obtained and the Bromphenol Blue band reached the downer part of the gel. Post-staining was conducted as denoted in Table 21.

Table 21. Amounts of RNA and staining procedure employed for the native PAGE analysis.

PAGE	RNA / pmol	staining
$P_2^{U14}$ , $P_2^{unmod}$ , $P_1^{U18}$ , $P_1^{U20}$ , $P_1^{unmod}$	90 <sup>[a]</sup>	GelRed 1:10000
$P_{1,Full}^{U24}$ , $P_{1,Full}^{U26}$ , $P_{2,Full}^{U55}$ , $P_{1,2,Full}^{U24,U55}$ , $P_{1,2,Full}^{U26,U55}$ , $P_{Full}^{unmod}$	45	Ethidium Bromide 1:10000
$P_{SDS}^{U35,U57}$ , $P_{SDS}^{unmod}$	50	Ethidium Bromide 1:10000
$P_{Full}^{unmod}$ <sup>[b]</sup>	100	Ethidium Bromide 1:10000

[a] The hetero mixed samples were prepared with 45 pmol of each RNA.

[b] Native PAGEs were exclusively conducted on the unmodified RNA to prove which Gdm<sup>+</sup> concentration is sufficient to convert the RNA into a specific conformation. The Gels are shown in the appendix.



## 5.14 cwEPR spectroscopy

### 5.14.1 Sample preparation

#### a) The model RNA

The HPLC purified RNAs were rebuffered in deuterated Phosphat buffer. The resulting 35  $\mu$ M samples were annealed and filled into 10  $\mu$ L capillaries.

#### b) The Guanidine-II Riboswitch

250 pmol of the labeled RNA constructs  $P_1^{U18}$ ,  $P_1^{U20}$ ,  $P_2^{U14}$ ,  $P_{1,Full}^{U24}$ , and  $P_{2,Full}^{U55}$  were dried (Centrifuge Concentrator, Concentrator plus, Eppendorf) and resuspended in aqueous Folding Buffer. Then, the respective annealing procedure in presence or absence of  $Gdm^+$  was employed. The samples were filled into 10  $\mu$ L capillaries with a diameter of 0.6 mm, resulting the concentrations listed in Table 22.

The RNA constructs  $P_{1,Full}^{U26}$ ,  $P_{1,2,Full}^{U24,U55}$ ,  $P_{1,2,Full}^{U26,U55}$ , and  $P_{SDS}^{U35,U57}$  were rebuffered after HPLC purification in aqueous Folding Buffer, resulting in the concentrations listed in Table 22. Annealing was performed in absence of  $Gdm^+$  or after addition of 40 mM  $Gdm^+$ . The samples were afterwards filled into 10  $\mu$ L capillaries with a diameter of 0.6 mm.

Table 22. RNA concentrations for the cwEPR measurements of the Guanidine-II constructs.

Construct	c(without $Gdm^+$ ) / $\mu$ M	c(with $Gdm^+$ ) / $\mu$ M
$P_1^{U18}$	25	25
$P_1^{U20}$	25	25
$P_2^{U14}$	25	25
$P_{1,Full}^{U24}$	25	25
$P_{1,Full}^{U26}$	21	21
$P_{2,Full}^{U55}$	25	25
$P_{1,2,Full}^{U24,U55}$	17	17
$P_{1,2,Full}^{U26,U55}$	17	17
$P_{SDS}^{U35,U57}$	6	6

### **c) The DNAzyme**

The cwEPR titrations were done in a 500  $\mu\text{L}$  flat cell (Rototec-Spintec) with samples containing 40  $\mu\text{M}$  of the DNAzyme:RNA complex that was annealed following the literature and provided by the lab's of Etzkorn and Span.<sup>304</sup> The construct Dz5A:RNA was measured a) in the absence of NaCl, b) with 100 mM NaCl and c) with 1 M NaCl, in 50 mM Tris-HCl pH 7.5. The measurements on construct Dz5C:RNA were conducted with a) 100 mM NaCl and b) 100 mM NaCl and 600  $\mu\text{M}$   $\text{Mn}^{2+}$  both in 50 mM Tris-HCL pH 7.5 and 20%  $\text{D}_2\text{O}$ . For each data point, 2  $\mu\text{L}$  either  $\text{Mn}^{2+}$  or  $\text{Mg}^{2+}$  stock solution was added into the 500  $\mu\text{L}$  of the initial sample. The  $\text{Mg}^{2+}$  titration was conducted on the sample containing initially 600  $\mu\text{M}$   $\text{Mn}^{2+}$ .

## **5.14.2 Measurement**

### **a) The model RNA**

The cwEPR spectra of the 35  $\mu\text{M}$  model RNAs were recorded at room temperature at X-band frequencies on an EMXnano spectrometer (Bruker BioSpin, Rheinstetten, Germany) with a microwave power of 10 mW, a modulation frequency of 100 kHz, a modulation amplitude of 1.0 G, a microwave frequency of 9.6 GHz, and 1300 points in the field interval 337.9–350.9 mT.

### **b) The Guanidine-II Riboswitch**

All samples belonging to the Guanidine-II riboswitch were recorded at room temperature at X-band frequencies on an EMXnano spectrometer (Bruker BioSpin). The spectra were measured with a microwave power of 1.995 mW, a modulation frequency of 100 kHz, a modulation amplitude of 1.0 G, a microwave frequency of 9.6 GHz, and 1300 points in the field interval 337.9–350.9 mT.

### **c) The DNAzyme**

The cwEPR spectroscopic measurements were recorded at X-band frequency on a Bruker EMX micro spectrometer (Bruker BioSpin) equipped with an ER 4103TM resonator (Bruker BioSpin). The spectra were measured at room temperature with a modulation frequency of 100 kHz, a modulation amplitude of 5.0 G, a microwave frequency of 9.79 GHz, and 1440 points in the field interval of 2890-4090 G. The

resulting  $\text{Mn}^{2+}$  EPR signals were baseline corrected (polynomial of third order) and doubly integrated (DI). The DI was corrected ( $\text{DI}_{\text{corr}}$ ) taking the individual Q-values (Q) and microwave powers (P) into account employing the following equation

$$\text{DI}_{\text{corr}} = \frac{\text{DI}}{Q \times \sqrt{P}}$$

Where  $\text{DI}_{\text{corr}}$  = corrected double integral, DI = initial double integral of the EPR signal, Q = calculated Q-value from the spectrometer, and P = microwave power.<sup>301</sup>

Binding isotherms were constructed by plotting the concentration of bound  $\text{Mn}^{2+}$  divided by the concentration of the complex versus the free  $\text{Mn}^{2+}$ . The concentration of bound  $\text{Mn}^{2+}$  was determined by comparison of the EPR double integral of the sample containing the complex and  $\text{Mn}^{2+}$  with the EPR double integral of  $\text{Mn}^{2+}$  free in solution. The reference samples of  $\text{Mn}^{2+}$  free in solution were measured on each day of data collection freshly prepared from a stock solution ( $\text{MnCl}_2$ , 1 M, 10x1 mL, Sigma Aldrich).

## 5.15 Pulsed EPR spectroscopy

### 5.15.1 Sample preparation

#### a) The model RNA

The HPLC purified RNA samples were rebuffed in deuterated Phosphate buffer to yield concentrations of 35  $\mu$ M. The RNAs were annealed and 20 %  $d_6$ -ethylene glycol (Deutero) was added. Afterwards the samples were transferred into Q-band tubes and frozen in liquid nitrogen.

#### b) The Guanidine-II Riboswitch

The labeled RNA constructs  $P_1^{U18}$ ,  $P_1^{U20}$ ,  $P_2^{U14}$ ,  $P_{1,Full}^{U24}$ ,  $P_{2,Full}^{U55}$ , and  $P_{1,2,Full}^{U24,U55}$  were dried (Centrifuge Concentrator, Concentrator plus, Eppendorf) and resuspended in aqueous Folding Buffer.  $Gdm^+$  was added, if stated in the figure caption, and the annealing procedure was employed. The resulting concentrations are listed in Table 23. The samples were proceeded a second drying process and resuspended in a 4:1 mixture of  $D_2O$  (Deutero) and  $d_6$ -ethylene glycol (Deutero). Afterwards the samples were transferred into Q-band tubes and frozen in liquid nitrogen.

The RNA constructs  $P_{1,Full}^{U26}$ ,  $P_{1,2,Full}^{U24,U55}$ ,  $P_{1,2,Full}^{U26,U55}$ , and  $P_{SDS}^{U35,U57}$  were rebuffed after HPLC purification in deuterated Folding Buffer that already contains  $Gdm^+$ , if necessary for the measurement. The resulting concentrations are listed in Table 23. The RNAs were annealed and 20 %  $d_6$ -ethylene glycol (Deutero) was added. Afterwards the samples were transferred into Q-band tubes and frozen in liquid nitrogen.

Table 23. PELDOR spin concentrations of the Guanidine-II constructs.

Construct	c(without Gdm <sup>+</sup> ) / $\mu\text{M}^{\text{[a]}}$	c(with Gdm <sup>+</sup> ) / $\mu\text{M}^{\text{[a]}}$
$\text{P}_1^{\text{U18}}$	25	25
$\text{P}_1^{\text{U20}}$	25	25
$\text{P}_2^{\text{U14}}$	25	25
$\text{P}_1^{\text{U24}}:\text{P}_2^{\text{U55}}$	25	25
$\text{P}_1^{\text{U26}}:\text{P}_2^{\text{U55}}$	25	25
$\text{P}_{1,\text{Full}}^{\text{U24}}$	25	25
$\text{P}_{1,\text{Full}}^{\text{U26}}$	12	12
$\text{P}_{2,\text{Full}}^{\text{U55}}$	25	25
$\text{P}_{1,2,\text{Full}}^{\text{U24,U55}}$	25 <sup>[b]</sup>	25 <sup>[b]</sup>
$\text{P}_{1,2,\text{Full}}^{\text{U26,U55}}$	36	36
$\text{P}_{\text{SDS}}^{\text{U35,U57}}$	32	32

[a] Some measurements were conducted on a diluted sample made out of the denoted one.

[b] The samples prepared by drying and rebuffering had both a concentration of 25  $\mu\text{M}$ .

### 5.15.2 Measurement

The pulsed EPR measurements were conducted at Q-band frequencies on a Bruker ELEXSYS 580 EPR spectrometer (Bruker BioSpin, Rheinstetten, Germany) equipped with an ER 5106QT-II resonator and a 150 W TWT-amplifier (Applied System Engineering, Fort Worth, TX, USA). The temperature was adjusted to the appropriate value using a CF935 helium gas-flow cryostat (Oxford Instruments, Abingdon, UK) in conjugation with an Oxford Instruments ITC 502 temperature controller.

The 2PESEEM spectra were recorded using a standard two-pulse Hahn echo sequence with pulse lengths of 12 ns and 24 ns for the  $\pi$  and  $\pi/2$  pulses, respectively, an initial  $\tau$  of 200 ns, and with increments of  $\tau$  of 8 ns.

The PELDOR experiments were performed at Q-band with the standard four-pulse sequence. The frequency of the pumping pulse was set at the maximum intensity of the nitroxide signal. The offset between pump and detection frequencies was varied as depicted in Figure 39 and Figure 49. Optimal  $\pi/2$  and  $\pi$  pulse lengths were used. For the  $\pi/2$  pulse, a two-step phase cycle was executed. The pump pulse length was optimized. The initial  $\tau$  was set to 260 ns. Deuterium modulation was suppressed by addition of 8 time traces with an increment of 16 ns for  $\tau$ . The detection window with a width of 40 ns was set to the maximum of the echo. The PELDOR signal was recorded with a shot repetition time of 3 ms. To achieve an acceptable SNR, the signal was averaged for 3 to 24 h, depending on the offset.

### 5.15.3 Analysis

#### a) PeldorFit<sup>167</sup>

PeldorFit was used to analyze the orientation selectivity of the model RNA. The configuration file contains three main blocks:

1. Experimental data of each offset measurement.
  - Pump pulse length
  - Pump frequency
  - Observer pulse length
  - Observer frequency
  - Magnetic field.

The experimental data were provided in the respective DSC data file.

2. Spectroscopic parameters of the involved spins.
  - g-factor and -strain
  - Number of nuclei
  - Nuclear spin
  - Hyperfine coupling constant and strain
  - Peak-to-peak linewidth.

The spectroscopic parameters were validated by simulating the experimental Q-band spectrum obtained at 50 K with EasySpin.<sup>157</sup> The spectrometric parameter for the fit are denoted in the Table 24.

Table 24. Spectroscopic parameters used for PeldorFit.

Parameter	50 K
g-tensor	2.0095 2.0076 2.0034
A-tensor / MHz	19 18 100
Line width / MHz	20.4

### 3. Geometric parameter $r$ , $\xi$ , $\varphi$ , $\alpha$ , $\beta$ , and $\gamma$ .

The parameter of Table 25 were employed as fitting parameter. Rhombic magnetic tensors for the spins were supposed.

Table 25. Geometric parameters used for PeldorFit.

Parameter	Mean	Width
$r$ / nm	4-5	0-1
$\xi$ / °	0-90	0-30
$\varphi$ / °	0-180	0-60
$\alpha$ / °	0-180	0-60
$\beta$ / °	0-90	0-30
$\gamma$ / °	0-180	0-60

PeldorFit fits the orientation selective PELDOR time traces by means of a genetic algorithm and assuming a simplified geometric model. It yields the geometric parameter  $r$ ,  $\xi$ ,  $\varphi$ ,  $\alpha$ ,  $\beta$ , and  $\gamma$  and their distributions. The genetic algorithm was set to a maximal number of generations of 200 and a generation size of 192. The geometric parameters are optimized until the corresponding RSMD reaches its minima. PeldorFit outputted 16 symmetry-related sets of parameters due to the invariance of the g- and A-tensor towards inversion of their axes.<sup>167</sup> The results ordered by their RMSD are listed in Table 29 and Table 30 and the original configuration files are presented in the appendix.

### **b) Model Generation – Model RNA**

The structural model of the 16mer RNA duplex was constructed based on the duplex RNA crystal structure with PDB ID 6IA2.<sup>277</sup> The type of bases were changed within the program 3DNA<sup>278</sup> to yield the sequence 5' CAU CUG AUA UCA GAU G 3' used herein. Then, energy minimization was performed by Prof. Dr. Stephanie Kath-Schorr in Gromacs 2018 using the CHARMM 36 all atom force field (version January 2018).<sup>279–281,283</sup> The structure was placed in a cubic box (7.378 nm<sup>3</sup>) solvated with 12561 TIP3P water molecules and 30 Na<sup>+</sup> counterions. The system was energy minimized applying the steepest descent gradient until convergence to machine precision. The RNA was then in silico spin labeled with the program mtsslWizard<sup>285–287</sup> using a cut-off of 2.5 Å and setting the allowed clashes value to 5. The spin label rotamers were configured in the painstaking mode and the spin labels were set to rotate about the angles  $\chi_1$  and  $\chi_2$  in the range of 0° and 180° ± 20° each. This generates 1000 spin label conformers, which were analyzed using a homebuilt python script from Dr. Dinar Abdullin that determined the best values of  $\chi_1$  and  $\chi_2$  that match the experimental results of  $r$ ,  $\xi$  and  $\beta$ .

### **c) Translation time to frequency domain – 2PESEEM**

The experimental obtained 2PESEEM time domain was translated into frequency domain by discrete Fourier transformation following the literature<sup>150</sup> To do so, the signal was background corrected using an exponential decay. A Hamming window was apodized followed by “zero filling”. Zero filling was conducted by adding zeroes at the end of the time trace. Afterwards a discrete Fourier transformation was performed that yielded the frequency domained spectrum. Data processing was conducted with the ELEXSYS Series: Xepr Software (Bruker).

### **d) DeerAnalysis**

DeerAnalysis2016<sup>275</sup> was employed to process the PELDOR data. The last  $\mu$ s of the time traces were removed to ensure no artefacts were present. The zero times were set to the maximum of the time trace before fitting the homogenous background decay function. Tikhonov Regularization was then used to extract the probability function for the distance distribution using the L-curve as a criterion for determining the optimum regularization parameter. The summed PELDOR data were further analyzed by employing the Validation tool.



### e) Model Generation – Guanidine-II Riboswitch

In silico predicted distances were generated within mtssWizard<sup>285–287</sup> by **1\*** to the uridine base in the respective structure. In this way, nitroxide rotamers were generated and interspin distances were measured. For **P2**, the crystal structure of PDB ID: 5VJ9 was used.<sup>48</sup> For **P1**, the crystal structure of PDB ID: 5NDI was adopted.<sup>49</sup> An uridine was mutated in the crystal structure of **P1**, because the crystal was generated from a construct derived from E.coli. Herein the construct of P. aeruginosa was analyzed. Thus the sequences did not match completely. The desired RNA sequence was mutated with 3DNA.<sup>278</sup> To determine the distance of the hetero dimers, the desired positions were also mutated within 3DNA.<sup>278</sup> Each crystal structure contains two kissing hairpins in each unit cell.<sup>48,49</sup> Thus, two in silico generated distance distributions were obtained, each. The final distance distribution were validated as average. The A-Form RNA duplexes were generated with 3DNA.<sup>278</sup>

## 5.16 NMR measurements

### 5.16.1 Sample preparation

30 nmol unmodified RNA were dried (Centrifuge Concentrator, Concentrator plus, Eppendorf) and diluted in 280  $\mu$ L aqueous Folding Buffer. After annealing in aqueous buffer, the sample was lyophilized (Freeze dryer, Alpha 3-4 LSC basic, Martin Christ GmbH) and resuspended in 280  $\mu$ L of a 1:9 mixture of D<sub>2</sub>O (Deutero) and H<sub>2</sub>O. To obtain a pure spectrum, in two Eppendorf Tubes 15 nmol RNA was prepared in 140 mL Folding buffer and 460  $\mu$ L H<sub>2</sub>O to obtain a 25  $\mu$ M concentration each. The samples were heated 10 minutes at 95 °C and shocked in 800  $\mu$ L iced water. The RNA was lyophilized (Freeze dryer, Alpha 3-4 LSC basic, Martin Christ GmbH) and together resuspended in 280  $\mu$ L of a 1:9 mixture of D<sub>2</sub>O (Deutero) and H<sub>2</sub>O. The ~100  $\mu$ M sample was transferred into a Shigemmi NMR tube (BMS-005B). 5  $\mu$ L Gdm<sup>+</sup> was added until at least a concentration of 100 mM Gdm<sup>+</sup> was reached.

### 5.16.2 Measurement

The NMR measurements were supervised by Dr. Senada Nozinovic. <sup>1</sup>H NMR spectra were acquired on a *Bruker Avance III Sirius 700 MHz Cryo NMR spectrometer* using a He-CP 700 QCI H-P/C/N probehead at room temperature. 512 scans were averaged.

## 6. Appendix

### 6.1 Riboswitch ligands

Table 26. Overview of the riboswitch ligands and their abbreviations utilized in Figure 5.

Ligand group	Ligand abbreviation	Ligand
Coenzymes	SAM	S-Adenosylmethionine
Coenzymes	Wco	Tungsten cofactor
Coenzymes	TPP	Thiamine pyrophosphate (Vitamin B1)
Coenzymes	THF	Tetrahydrofolate
Coenzymes	SAH	S-Adenosylhomocysteine
Coenzymes	NAD <sup>+</sup>	Nicotinamide adenine dinucleotide
Coenzymes	Moco	Molybdenum cofactor
Coenzymes	HMP-PP	4-amino-5-hydroxymethyl-2-methylpyrimidine pyrophosphate
Coenzymes	FMN	Flavin mononucleotide (Vitamin B2)
Coenzymes	AqCbl	Aquacobalamin
Coenzymes	AdoCbl	Adenosylcobalamin (Vitamin B12)
Nucleotide derivatives	PreQ1	Prequeuosine-1
Nucleotide derivatives	2'-dG	2'-Deoxyguanosine
Nucleotide derivatives	PRPP	Phosphoribosylpyrophosphate
Nucleotide derivatives	ADP	Adenosinediphosphate
Nucleotide derivatives	Adenine	Adenine
Nucleotide derivatives	Guanine	Guanine
Signaling molecules	c-di-GMP	3'-5'-cyclic di-guanosine-monophosphate
Signaling molecules	ppGpp	Guanosine 3',5'-bispyrophosphate
Signaling molecules	ZTP	5-Amino 4-imidazole carboxamide riboside 5'-triphosphate
Signaling molecules	c-di-AMP	3'-5'-cyclic di-adenosine-monophosphate
Signaling molecules	c-AMP-GMP	3'-5'-cyclic adenosine-monophosphate guanosine-monophosphate
Others	Guanidine	Guanidine
Others	GlmS	Glucosamine-6-phosphate
Others	Azaaromatic	Azaaromatic
Ions	Mg <sup>2+</sup>	Magnesium ions
Ions	Ni <sup>2+</sup> /Co <sup>2+</sup>	Nickel or cobalt ions
Ions	Mn <sup>2+</sup>	Manganese ions
Ions	F <sup>-</sup>	Fluoride ions
Amino Acids	Lysine	L-Lysine
Amino Acids	Glycine	L-Glycine
Amino Acids	Glutamine	L-Glutamine

The color code corresponds to Figure 5.

## 6.2 HPLC spectra

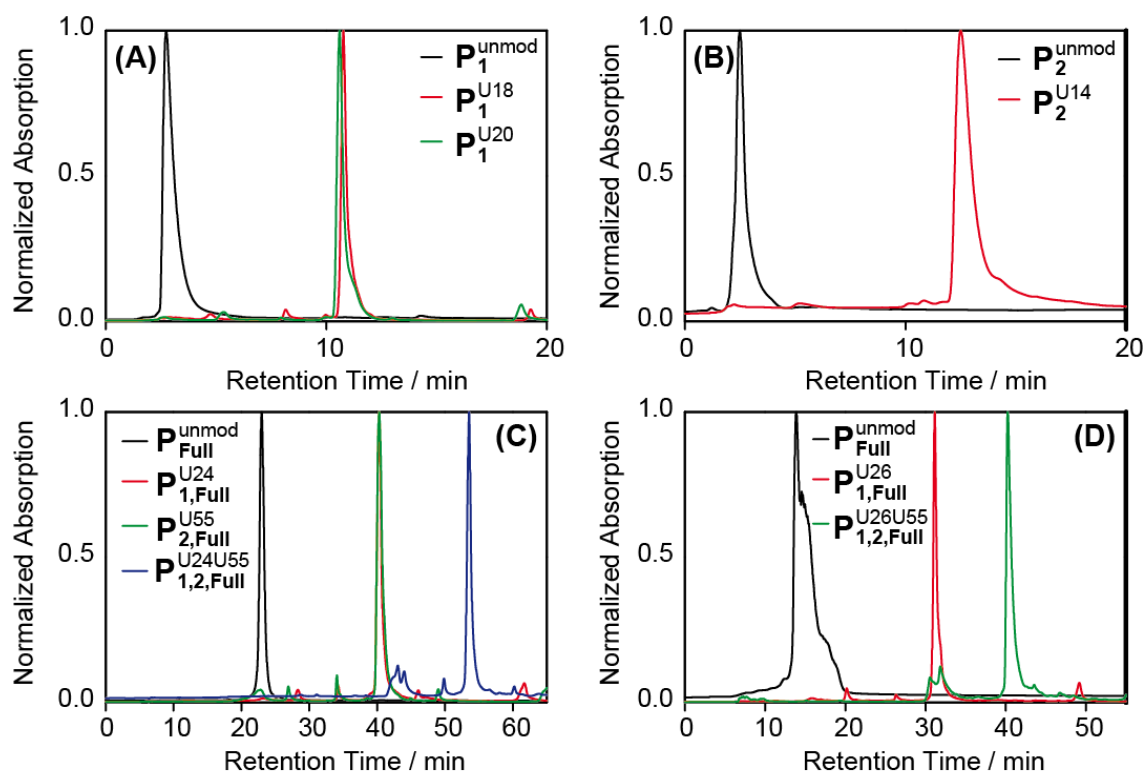


Figure 99. HPLC spectra of the Guanidine-II riboswitch constructs.

### 6.3 Spin labeling yields

Table 27. Spin labeling yields.

Construct	Yield / %
model RNA <sup>U15</sup>	50
<b>P</b> <sub>1</sub> <sup>U18</sup>	72
<b>P</b> <sub>1</sub> <sup>U20</sup>	60
<b>P</b> <sub>2</sub> <sup>U14</sup>	60
<b>P</b> <sub>1,Full</sub> <sup>U24</sup>	64
<b>P</b> <sub>1,Full</sub> <sup>U26</sup>	40
<b>P</b> <sub>2,Full</sub> <sup>U55</sup>	48
<b>P</b> <sub>1,2,Full</sub> <sup>U24,U55</sup>	52
<b>P</b> <sub>1,Full</sub> <sup>U26,U55</sup>	36
<b>P</b> <sub>SDS</sub> <sup>U35U57</sup>	38

## 6.4 LCMS spectra

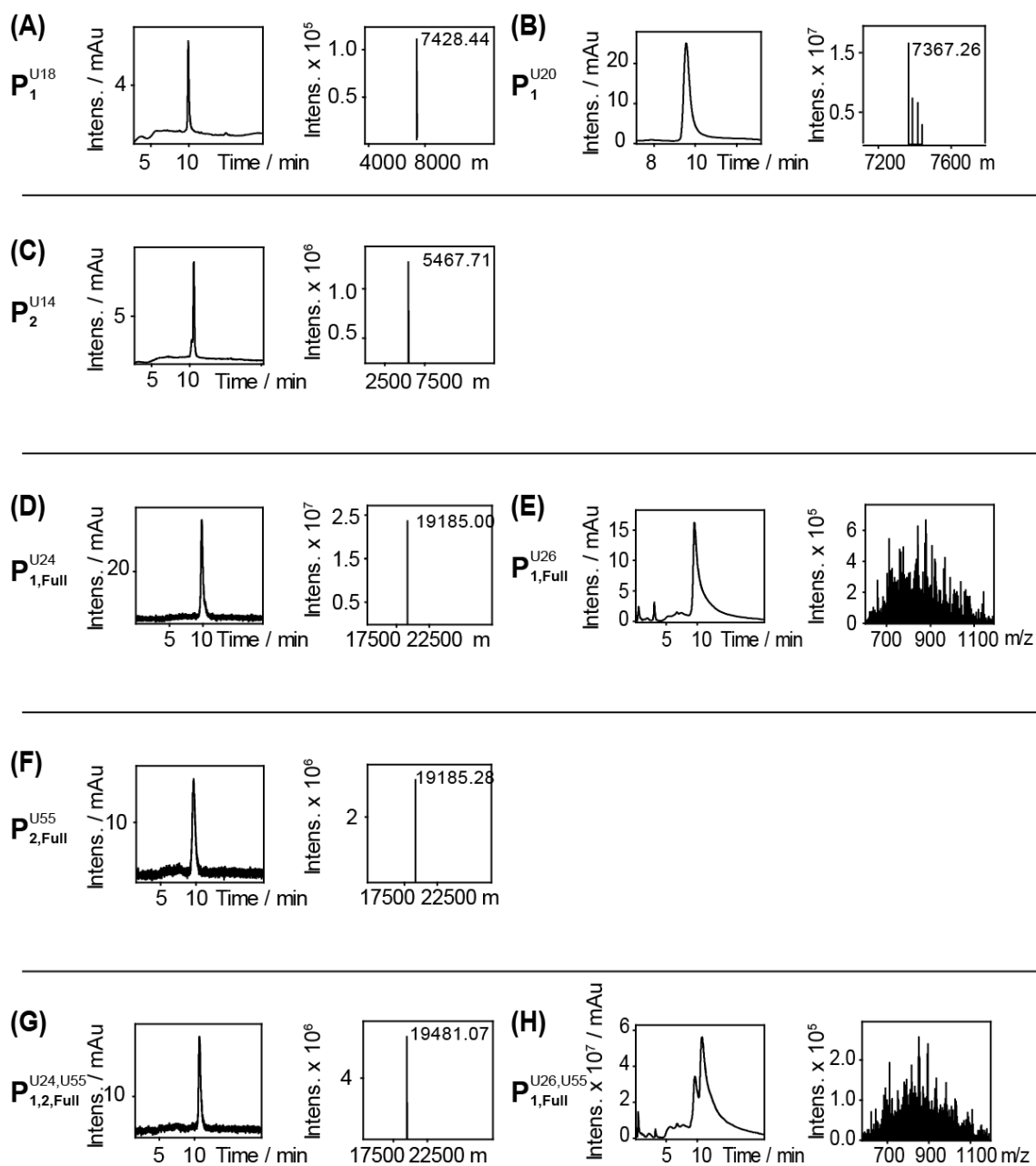


Figure 100. LCMS spectra of the Guanine-II riboswitch constructs.

## 6.5 Native PAGEs

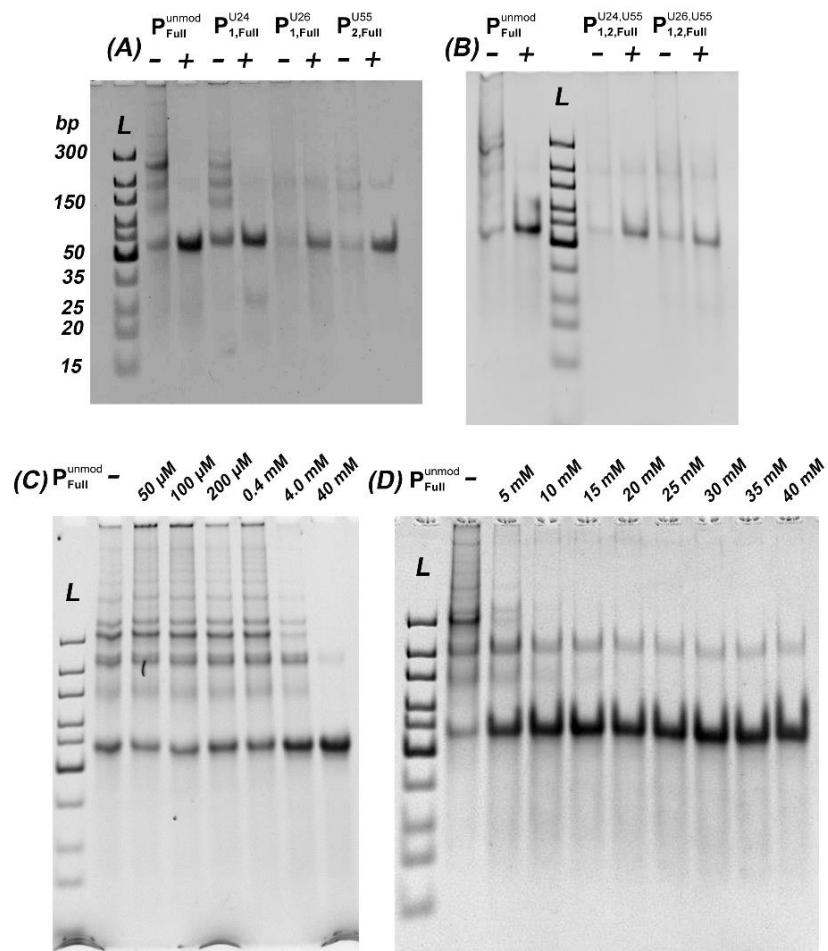


Figure 101. 15% Native PAGEs of the full-length constructs in the absence (-) or presence of 40 mM (+)  $Gdm^+$ . The ladder is denoted as "L". The respective band sizes are shown in (A). In (C) and (D) the  $Gdm^+$  concentrations is varied as depicted.

## 6.6 cwEPR spectra

### 6.6.1 Spin label 1\*

The spectrum of 1\* in Figure 12 was simulated using EasySpin and the script listed below.<sup>157</sup>

```
Exp.mwFreq = 9.8636;  
Exp.Range = [347 357];  
Exp.ModAmp = 0.1;  
Exp.nPoints = 10000;  
  
Sys.g = 2.003600;  
Sys.Nucs = '14N,1H,1H';  
Sys.n = [1 8 12];  
Sys.A = [13.715 0.349 0.349]*2.802;  
Sys.lw = [0.005,0.01]*1;  
Sys.weight = 1  
  
Sys1.g = 2.003600;  
Sys1.Nucs = '14N,13C' ;  
Sys1.n = [1 2 ] ;  
Sys1.A = [13.715 3.3 ]*2.802;  
Sys1.lw = [0.010,0.01]*1;  
Sys1.weight = 0.01  
  
[x,y] = garlic({Sys,Sys1},Exp);
```

## 6.6.2 The Guanidine-II Riboswitch

Table 28. List of the spin countings of the cwEPR spectra of the Guanidine-II riboswitch constructs.

Construct		c(without Gdm <sup>+</sup> ) / $\mu$ M	c(with Gdm <sup>+</sup> ) / $\mu$ M
<b>P<sub>1</sub><sup>U18</sup></b>	set	25	25
	measured	26	21
<b>P<sub>1</sub><sup>U20</sup></b>	set	25	25
	measured	25	22
<b>P<sub>2</sub><sup>U14</sup></b>	set	25	25
	measured	24	24
<b>P<sub>1,Full</sub><sup>U24</sup></b>	set	25	25
	measured	27	31
<b>P<sub>1,Full</sub><sup>U26</sup></b>	set	21	21
	measured	19	20
<b>P<sub>2,Full</sub><sup>U55</sup></b>	set	25	25
	measured	29	31
<b>P<sub>1,2,Full</sub><sup>U24,U55</sup></b>	set	34	33
	measured	29	26
<b>P<sub>1,2,Full</sub><sup>U26,U55</sup></b>	set	35	34
	measured	29	31
<b>P<sub>SDS</sub><sup>U35,U57</sup></b>	set	12	12
	measured	12	18



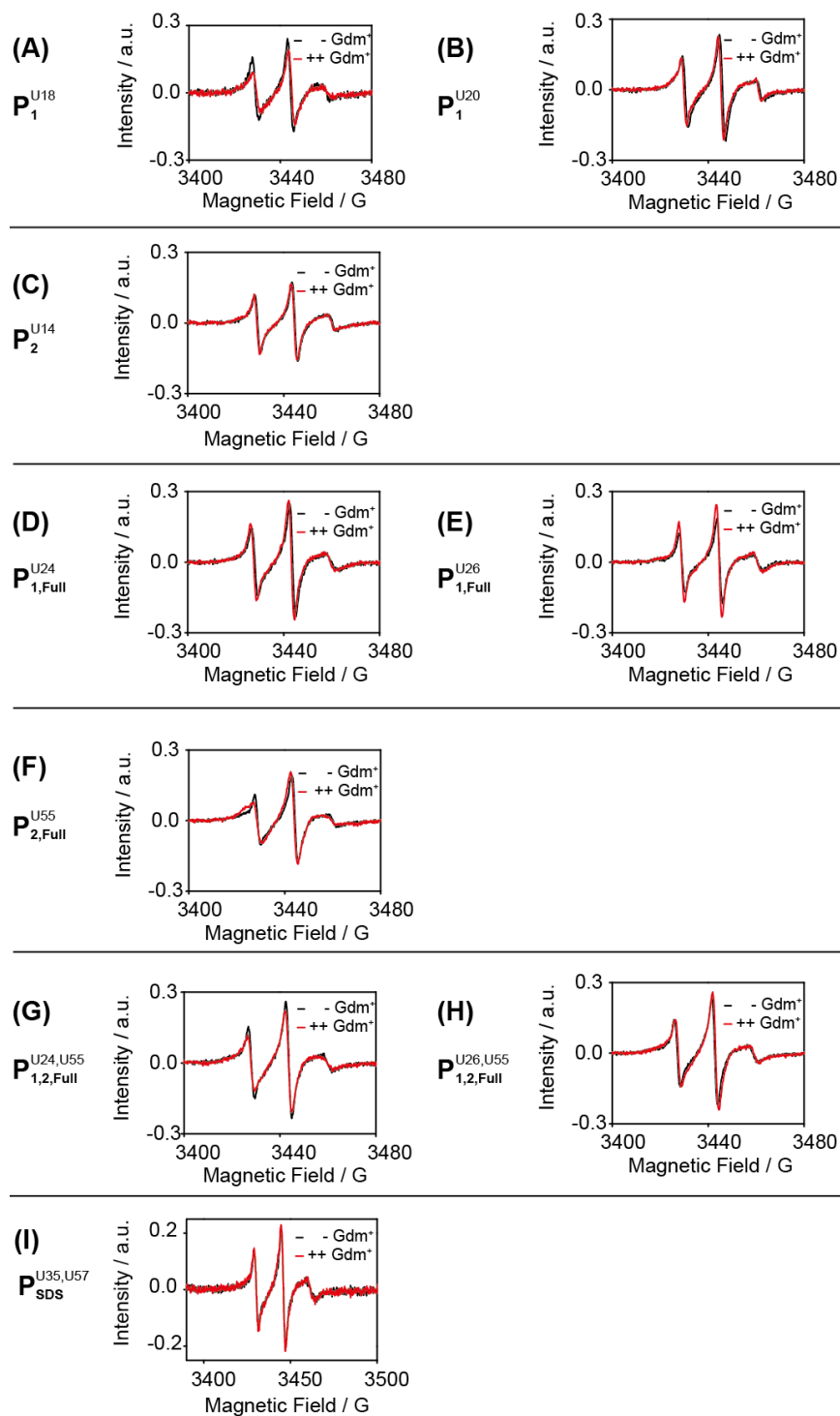


Figure 102. cwEPR spectra of the Guanidine-II riboswitch constructs.

## 6.7 PeldorFit data

### 6.7.1 Summary of the PeldorFit results

Table 29. Summary of the PeldorFit results for  $\mathbf{M}_2$ .<sup>167</sup>

Transformation <sup>[a]</sup>	$\xi / ^\circ$	$\varphi / ^\circ$	$\alpha / ^\circ$	$\beta / ^\circ$	$\gamma / ^\circ$	RMSD
Fitting result	37	16	154	56	150	0.038
Inversion of gxxA	37	16	334	124	30	0.038
Inversion of gyyA	37	16	334	124	210	0.037
Inversion of gzzA	37	16	154	56	330	0.038
Inversion of gxxB	143	344	26	124	330	0.038
Inversion of gyyB	143	344	206	56	210	0.038
Inversion of gzzB	143	344	206	56	30	0.037
Inversion of gxxA and gxxB	143	344	26	124	150	0.037
Inversion of gxxA and gyyB	143	164	206	124	330	0.037
Inversion of gxxA and gzzB	143	164	26	56	210	0.038
Inversion of gyyA and gxxB	143	164	26	56	30	0.037
Inversion of gyyA and gyyB	143	164	206	124	150	0.037
Inversion of gyyA and gzzB	37	196	334	56	150	0.037
Inversion of gzzA and gxxB	37	196	154	124	30	0.037
Inversion of gzzA and gyyB	37	196	154	124	210	0.037
Inversion of gzzA and gzzB	37	196	334	56	330	0.038

<sup>[a]</sup> gxxA, gyyA, and gzzA denote the principal components of the g-tensor of spin A; gxxB, gyyB, and gzzB denote the g tensor of spin B.

Table 30. Summary of the PeldorFit results for  $\mathbf{E}_2$ .<sup>167</sup>

Transformation <sup>[a]</sup>	$\xi / ^\circ$	$\varphi / ^\circ$	$\alpha / ^\circ$	$\beta / ^\circ$	$\gamma / ^\circ$	RMSD
Fitting result	44	155	175	34	19	0.048
Inversion of gxxA	44	155	355	146	161	0.048
Inversion of gyyA	44	155	355	146	341	0.048
Inversion of gzzA	44	155	175	34	199	0.048
Inversion of gxxB	136	205	5	146	199	0.048
Inversion of gyyB	136	205	185	34	341	0.048
Inversion of gzzB	136	205	185	34	161	0.048
Inversion of gxxA and gxxB	136	205	5	146	19	0.048
Inversion of gxxA and gyyB	136	25	185	146	199	0.048
Inversion of gxxA and gzzB	136	25	5	34	341	0.048
Inversion of gyyA and gxxB	136	25	5	34	161	0.048
Inversion of gyyA and gyyB	136	25	185	146	19	0.048
Inversion of gyyA and gzzB	44	335	355	34	19	0.048
Inversion of gzzA and gxxB	44	335	175	146	161	0.048
Inversion of gzzA and gyyB	44	335	175	146	341	0.048
Inversion of gzzA and gzzB	44	335	355	34	199	0.048

<sup>[a]</sup> gxxA, gyyA, and gzzA denote the principal components of the g-tensor of spin A; gxxB, gyyB, and gzzB denote the g tensor of spin B.

## 6.7.2 PeldorFit configuration files

### a) Original PeldorFit configuration file for M<sub>2</sub>

```
#----- PeldorFit2018 Configuration File -----  
-----  
  
# Experimental parameters  
#-----  
// filename      : name of the data file  
// detPiLength   : length of the detection pi-pulse (ns)  
// detPiHalfLength: length of the detection pi/2-pulse (ns)  
// pumpPiLength  : length of the pump pi-pulse (ns)  
// detFreq       : detection frequency (GHz)  
// pumpFreq      : pump frequency (GHz)  
// magnField     : magnetic field (T) # Field Position  
  
experimentals = (  
  {filename = "20190923_metNx16mer/metNx16mer_60MHz.dat";  
  detPiLength = 24;  
  detPiHalfLength = 12;  
  pumpPiLength = 12;  
  detFreq = 33.639484;  
  pumpFreq = 33.699562;  
  magnField = 1.19790; },  
  
  {filename = "20190923_metNx16mer/metNx16mer_80MHz.dat";  
  detPiLength = 24;  
  detPiHalfLength = 12;  
  pumpPiLength = 12;  
  detFreq = 33.619621;  
  pumpFreq = 33.699562;  
  magnField = 1.19790; },  
  
  {filename = "20190923_metNx16mer/metNx16mer_100MHz.dat";  
  detPiLength = 24;  
  detPiHalfLength = 12;  
  pumpPiLength = 12;  
  detFreq = 33.599273;  
  pumpFreq = 33.699562;  
  magnField = 1.19790; },  
  
  {filename = "20190923_metNx16mer/metNx16mer_120MHz.dat";  
  detPiLength = 24;  
  detPiHalfLength = 12;  
  pumpPiLength = 12;  
  detFreq = 33.579336;  
  pumpFreq = 33.699562;  
  magnField = 1.19950; },  
  
  {filename = "20190923_metNx16mer/metNx16mer_180MHz.dat";  
  detPiLength = 24;  
  detPiHalfLength = 12;  
  pumpPiLength = 12;  
  detFreq = 33.519883;
```

```
pumpFreq =      33.699562;
magnField =     1.19790; }
);

# Spectroscopic parameters
#-----
// nSpins      : number of spin centers
// multiSpinEffects: 0 (don't take into account multi-spin effects)
//              1 (take into account multi-spin effects)

nSpins = 2;
multiSpinEffects = 0;

// g          : g-factor
// gStrain: g-strain
// n          : number of nuclei
// I          : nuclear spin
// A          : hyperfine coupling constant A (MHz)
// AStrain: A-strain (MHz)
// lwpp      : peak-to-peak linewidth (MHz)

spinA:
{
    g = [2.0095, 2.0076, 2.0034];
    gStrain = [];
    n = [1];
    I = [1.0];
    A = [19, 18, 100];
    AStrain = [];
    lwpp = 20.4;
};

spinB:
{
    g = [2.0095, 2.0076, 2.0034];
    gStrain = [];
    n = [1];
    I = [1.0];
    A = [19, 18, 100];
    AStrain = [];
    lwpp = 20.4;
};

# Fitting parameters
#-----
// opt : 0 (not optimized), 1 (optimized), 2 (fixed)
// mode : 0 (uniform distr.), 1 (normal distr.)
//       different definition for Parameter 28:
//       0 (same pump efficiency for all time traces)
//       1 (different pump efficiency for each time trace)
// range: min and max values of the optimized parameter (for opt =
1)
// value: value of the fixed parameter (for opt = 2)

parameters = (
```

```
{opt = 1; mode = 1; range = [ 4.0, 5.0], value = 0.0},
// Parameter 1 : r1 mean
{opt = 1; mode = 1; range = [ 0.00, 0.5], value = 0.0},
// Parameter 2 : r1 width
{opt = 1; mode = 1; range = [ 0.0, 90.0], value = 0.0},
// Parameter 3 : x11 mean
{opt = 1; mode = 1; range = [ 0.0, 30.0], value = 0.0},
// Parameter 4 : x11 width
{opt = 1; mode = 1; range = [ 0.0, 180.0], value = 0.0},
// Parameter 5 : phi1 mean
{opt = 1; mode = 1; range = [ 0.0, 60.0], value = 0.0},
// Parameter 6 : phi1 width
{opt = 1; mode = 1; range = [ 0.0, 180.0], value = 0.0},
// Parameter 7 : alpha1 mean
{opt = 1; mode = 1; range = [ 0.0, 60.0], value = 0.0},
// Parameter 8 : alpha1 width
{opt = 1; mode = 1; range = [ 0.0, 90.0], value = 0.0},
// Parameter 9 : beta1 mean
{opt = 1; mode = 1; range = [ 0.0, 30.0], value = 0.0},
// Parameter 10: beta1 width
{opt = 1; mode = 1; range = [ 0.0, 180.0], value = 0.0},
// Parameter 11: gamma1 mean
{opt = 1; mode = 1; range = [ 0.0, 60.0], value = 0.0},
// Parameter 12: gamma1 width
{opt = 0; mode = 0; range = [ 1.50, 2.50], value = 0.0},
// Parameter 13: r2 mean
{opt = 0; mode = 0; range = [ 0.00, 0.10], value = 0.0},
// Parameter 14: r2 width
{opt = 0; mode = 0; range = [ 0.0, 90.0], value = 0.0},
// Parameter 15: xi2 mean
{opt = 0; mode = 0; range = [ 0.0, 90.0], value = 0.0},
// Parameter 16: xi2 width
{opt = 0; mode = 0; range = [ 0.0, 180.0], value = 0.0},
// Parameter 17: phi2 mean
{opt = 0; mode = 0; range = [ 0.0, 180.0], value = 0.0},
// Parameter 18: phi2 width
{opt = 0; mode = 0; range = [ 0.0, 180.0], value = 0.0},
// Parameter 19: alpha2 mean
{opt = 0; mode = 0; range = [ 0.0, 180.0], value = 0.0},
// Parameter 20: alpha2 width
{opt = 0; mode = 0; range = [ 0.0, 90.0], value = 0.0},
// Parameter 21: beta2 mean
{opt = 0; mode = 0; range = [ 0.0, 90.0], value = 0.0},
// Parameter 22: beta2 width
{opt = 0; mode = 0; range = [ 0.0, 180.0], value = 0.0},
// Parameter 23: gamma2 mean
{opt = 0; mode = 0; range = [ 0.0, 180.0], value = 0.0},
// Parameter 24: gamma2 width
{opt = 0; mode = 0; range = [ 0.00, 1.00], value = 0.0},
// Parameter 25: ratio between r1 and r2
{opt = 0; mode = 0; range = [ 0.00, 5.00], value = 0.0},
// Parameter 26: J mean
{opt = 0; mode = 0; range = [ 0.00, 5.00], value = 0.0},
// Parameter 27: J width
{opt = 1; mode = 1; range = [ 0.4, 1.0], value = 0.0}
// Parameter 28: scale factor for mod. depth
);
```

```
# Genetic algorithm
#-----
// num_generations_max: maximal number of generations
// size_generation    : generation size (number of chromosomes)
// prob_crossover     : crossover rate
// prob_mutation      : mutation rate
// merit_function     : merit function: 1 (RMSD), 2 (RMSD/PCC), 3
(PCC)
// num_averages      : number of Monte-Carlo samples

genetic:
{
    num_generations_max = 500;
    size_generation = 192;
    prob_crossover = 0.5;
    prob_mutation = 0.01;
    merit_function = 1;
    num_averages = 1000000;
};

# Output data
#-----
// directory          : path to the disk space where the
PeldorFit output will be saved
// record_spectrum    : record the spectrum of a spin system
// record_score       : record the goodness-of-fit vs.
optimization step
// record_parameters  : record optimized fitting parameters
// record_fit         : record the fits to the PELDOR
signals
// record_symmetric_solutions: record the symmetry-related sets of
the fitting parameters
// record_error_plot   : record the error plot
// error_plot_variables : variables of the error plot
// error_plot_size     : number of samples in the error plot

output:
{
    directory = "20190923_metNx16mer/Results/";
    record_spectrum = 0;
    record_score = 1;
    record_parameters = 1;
    record_fit = 1;
    record_symmetric_solutions = 1;
    record_error_plot = 1;
    error_plot_variables =
([1,2], [3,4], [5,6], [7,8], [9,10], [11,12]);
    error_plot_size = 1000;
};

// error_plot_only    : record the error plot for the fitting
parameters optimized previously
// enable             : switch for this mode
// error_plot_variables: variables of the error plot
```

```
// error_plot_size      : number of samples in the error plot
// input_directory      : path to the file with the optimized
fitting parameters
// output_directory     : path to the disk space where the error
plot will be saved

error_plot_only:
{
    enable = 0;
    error_plot_variables =
([1,2],[3,4],[5,6],[7,8],[9,10],[11,12]);
    error_plot_size = 1000;
    input_directory = "20190923_metNx16mer/Results/parameters.dat";
    output_directory = "20190923_metNx16mer/Results/";
};

### eof
```

## b) Original PeldorFit Configuration File for E<sub>2</sub>

```
#----- PeldorFit2018 Configuration File -----
-----

# Experimental parameters
#-----
// filename      : name of the data file
// detPiLength   : length of the detection pi-pulse (ns)
// detPiHalfLength: length of the detection pi/2-pulse (ns)
// pumpPiLength  : length of the pump pi-pulse (ns)
// detFreq       : detection frequency (GHz)
// pumpFreq      : pump frequency (GHz)
// magnField     : magnetic field (T) # Field Position

experimentals = (
    {filename = "20191004_etNx16mer/etNx16mer_60MHz.dat";
    detPiLength = 24;
    detPiHalfLength = 12;
    pumpPiLength = 12;
    detFreq = 33.643341;
    pumpFreq = 33.703445;
    magnField = 1.19850; },

    {filename = "20191004_etNx16mer/etNx16mer_80MHz.dat";
    detPiLength = 24;
    detPiHalfLength = 12;
    pumpPiLength = 12;
    detFreq = 33.623192;
    pumpFreq = 33.703445;
    magnField = 1.19850; },

    {filename = "20191004_etNx16mer/etNx16mer_100MHz.dat";
    detPiLength = 24;
    detPiHalfLength = 12;
```



```
pumpPiLength = 12;
detFreq = 33.603601;
pumpFreq = 33.703445;
magnField = 1.19850; },

{filename = "20191004_etNx16mer/etNx16mer_120MHz.dat";
detPiLength = 24;
detPiHalfLength = 12;
pumpPiLength = 12;
detFreq = 33.583239;
pumpFreq = 33.703445;
magnField = 1.20020; },

{filename = "20191004_etNx16mer/etNx16mer_180MHz.dat";
detPiLength = 24;
detPiHalfLength = 12;
pumpPiLength = 12;
detFreq = 33.523188;
pumpFreq = 33.703445;
magnField = 1.19850; }

);

# Spectroscopic parameters
#-----
// nSpins : number of spin centers
// multiSpinEffects: 0 (don't take into account multi-spin effects)
// 1 (take into account multi-spin effects)

nSpins = 2;
multiSpinEffects = 0;

// g : g-factor
// gStrain: g-strain
// n : number of nuclei
// I : nuclear spin
// A : hyperfine coupling constant A (MHz)
// AStrain: A-strain (MHz)
// lwpp : peak-to-peak linewidth (MHz)

spinA:
{
    g = [2.0095, 2.0076, 2.0034];
    gStrain = [];
    n = [1];
    I = [1.0];
    A = [19, 18, 100];
    AStrain = [];
    lwpp = 20.4;
};

spinB:
{
    g = [2.0095, 2.0076, 2.0034];
    gStrain = [];
    n = [1];
```

```
I = [1.0];
A = [19, 18, 100];
AStrain = [];
lwpp = 20.4;
};

# Fitting parameters
#-----
// opt : 0 (not optimized), 1 (optimized), 2 (fixed)
// mode : 0 (uniform distr.), 1 (normal distr.)
//      different definition for Parameter 28:
//      0 (same pump efficiency for all time traces)
//      1 (different pump efficiency for each time trace)
// range: min and max values of the optimized parameter (for opt =
1)
// value: value of the fixed parameter (for opt = 2)

parameters = (
  {opt = 1; mode = 1; range = [ 4.3, 5.3], value = 0.0},
  // Parameter 1 : r1 mean
  {opt = 1; mode = 1; range = [ 0.00, 0.5], value = 0.0},
  // Parameter 2 : r1 width
  {opt = 1; mode = 1; range = [ 0.0, 90.0], value = 0.0},
  // Parameter 3 : xi1 mean
  {opt = 1; mode = 1; range = [ 0.0, 30.0], value = 0.0},
  // Parameter 4 : xi1 width
  {opt = 1; mode = 1; range = [ 0.0, 180.0], value = 0.0},
  // Parameter 5 : phi1 mean
  {opt = 1; mode = 1; range = [ 0.0, 60.0], value = 0.0},
  // Parameter 6 : phi1 width
  {opt = 1; mode = 1; range = [ 0.0, 180.0], value = 0.0},
  // Parameter 7 : alpha1 mean
  {opt = 1; mode = 1; range = [ 0.0, 60.0], value = 0.0},
  // Parameter 8 : alpha1 width
  {opt = 1; mode = 1; range = [ 0.0, 90.0], value = 0.0},
  // Parameter 9 : beta1 mean
  {opt = 1; mode = 1; range = [ 0.0, 30.0], value = 0.0},
  // Parameter 10: beta1 width
  {opt = 1; mode = 1; range = [ 0.0, 180.0], value = 0.0},
  // Parameter 11: gamma1 mean
  {opt = 1; mode = 1; range = [ 0.0, 60.0], value = 0.0},
  // Parameter 12: gamma1 width
  {opt = 0; mode = 0; range = [ 1.50, 2.50], value = 0.0},
  // Parameter 13: r2 mean
  {opt = 0; mode = 0; range = [ 0.00, 0.10], value = 0.0},
  // Parameter 14: r2 width
  {opt = 0; mode = 0; range = [ 0.0, 90.0], value = 0.0},
  // Parameter 15: xi2 mean
  {opt = 0; mode = 0; range = [ 0.0, 90.0], value = 0.0},
  // Parameter 16: xi2 width
  {opt = 0; mode = 0; range = [ 0.0, 180.0], value = 0.0},
  // Parameter 17: phi2 mean
  {opt = 0; mode = 0; range = [ 0.0, 180.0], value = 0.0},
  // Parameter 18: phi2 width
  {opt = 0; mode = 0; range = [ 0.0, 180.0], value = 0.0},
  // Parameter 19: alpha2 mean
```

```

    {opt = 0; mode = 0; range = [ 0.0, 180.0], value = 0.0},
// Parameter 20: alpha2 width
    {opt = 0; mode = 0; range = [ 0.0, 90.0], value = 0.0},
// Parameter 21: beta2 mean
    {opt = 0; mode = 0; range = [ 0.0, 90.0], value = 0.0},
// Parameter 22: beta2 width
    {opt = 0; mode = 0; range = [ 0.0, 180.0], value = 0.0},
// Parameter 23: gamma2 mean
    {opt = 0; mode = 0; range = [ 0.0, 180.0], value = 0.0},
// Parameter 24: gamma2 width
    {opt = 0; mode = 0; range = [ 0.00, 1.00], value = 0.0},
// Parameter 25: ratio between r1 and r2
    {opt = 0; mode = 0; range = [ 0.00, 5.00], value = 0.0},
// Parameter 26: J mean
    {opt = 0; mode = 0; range = [ 0.00, 5.00], value = 0.0},
// Parameter 27: J width
    {opt = 1; mode = 1; range = [ 0.4, 1.0], value = 0.0}
// Parameter 28: scale factor for mod. depth
);

```

```

# Genetic algorithm
#-----
// num_generations_max: maximal number of generations
// size_generation      : generation size (number of chromosomes)
// probab_crossover     : crossover rate
// probab_mutation      : mutation rate
// merit_function       : merit function: 1 (RMSD), 2 (RMSD/PCC), 3
(PCC)
// num_averages        : number of Monte-Carlo samples

```

```

genetic:
{
    num_generations_max = 500;
    size_generation     = 192;
    probab_crossover    = 0.5;
    probab_mutation     = 0.01;
    merit_function      = 1;
    num_averages        = 1000000;
};

```

```

# Output data
#-----
// directory           : path to the disk space where the
PeldorFit output will be saved
// record_spectrum     : record the spectrum of a spin system
// record_score        : record the goodness-of-fit vs.
optimization step
// record_parameters   : record optimized fitting parameters
// record_fit          : record the fits to the PELDOR
signals
// record_symmetric_solutions: record the symmetry-related sets of
the fitting parameters
// record_error_plot   : record the error plot
// error_plot_variables : variables of the error plot
// error_plot_size     : number of samples in the error plot

```

```
output:
{
  directory = "20191004_etNx16mer/Results/";
  record_spectrum = 0;
  record_score = 1;
  record_parameters = 1;
  record_fit = 1;
  record_symmetric_solutions = 1;
  record_error_plot = 1;
  error_plot_variables =
  ([1,2],[3,4],[5,6],[7,8],[9,10],[11,12]);
  error_plot_size = 1000;
};

// error_plot_only      : record the error plot for the fitting
parameters optimized previously
// enable              : switch for this mode
// error_plot_variables: variables of the error plot
// error_plot_size     : number of samples in the error plot
// input_directory     : path to the file with the optimized
fitting parameters
// output_directory    : path to the disk space where the error
plot will be saved

error_plot_only:
{
  enable = 0;
  error_plot_variables =
  ([1,2],[3,4],[5,6],[7,8],[9,10],[11,12]);
  error_plot_size = 1000;
  input_directory = "20191004_etNx16mer/Results/parameters.dat";
  output_directory = "20191004_etNx16mer/Results/";
};

### eof
```

## 6.8 PELDOR data

### 6.8.1 Offset measurements

The offsets of the Guanidine-II riboswitch were measured as depicted in Table 31 and Figure 103.

Table 31. Overview of the offset measurements conducted on the Guanidine-II riboswitch constructs. The color code corresponds to the following Figures.

Pump position	Detection position	Frequency offset / MHz
a	b	60
a	c	80
a	d	100
b	e	120
a	f	180

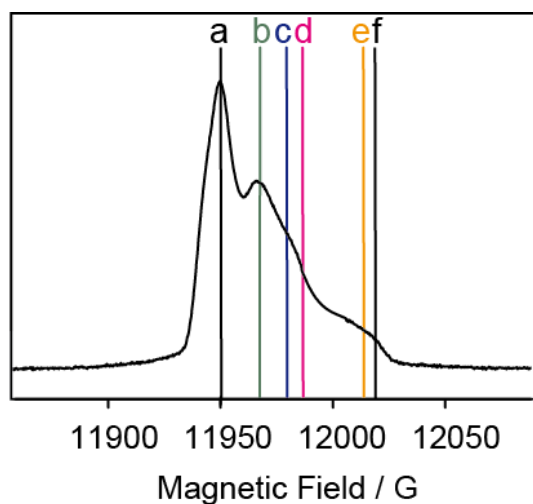


Figure 103. EDFS and marked pump and detection position of the offset measurements conducted on the guanidine-II riboswitch constructs.

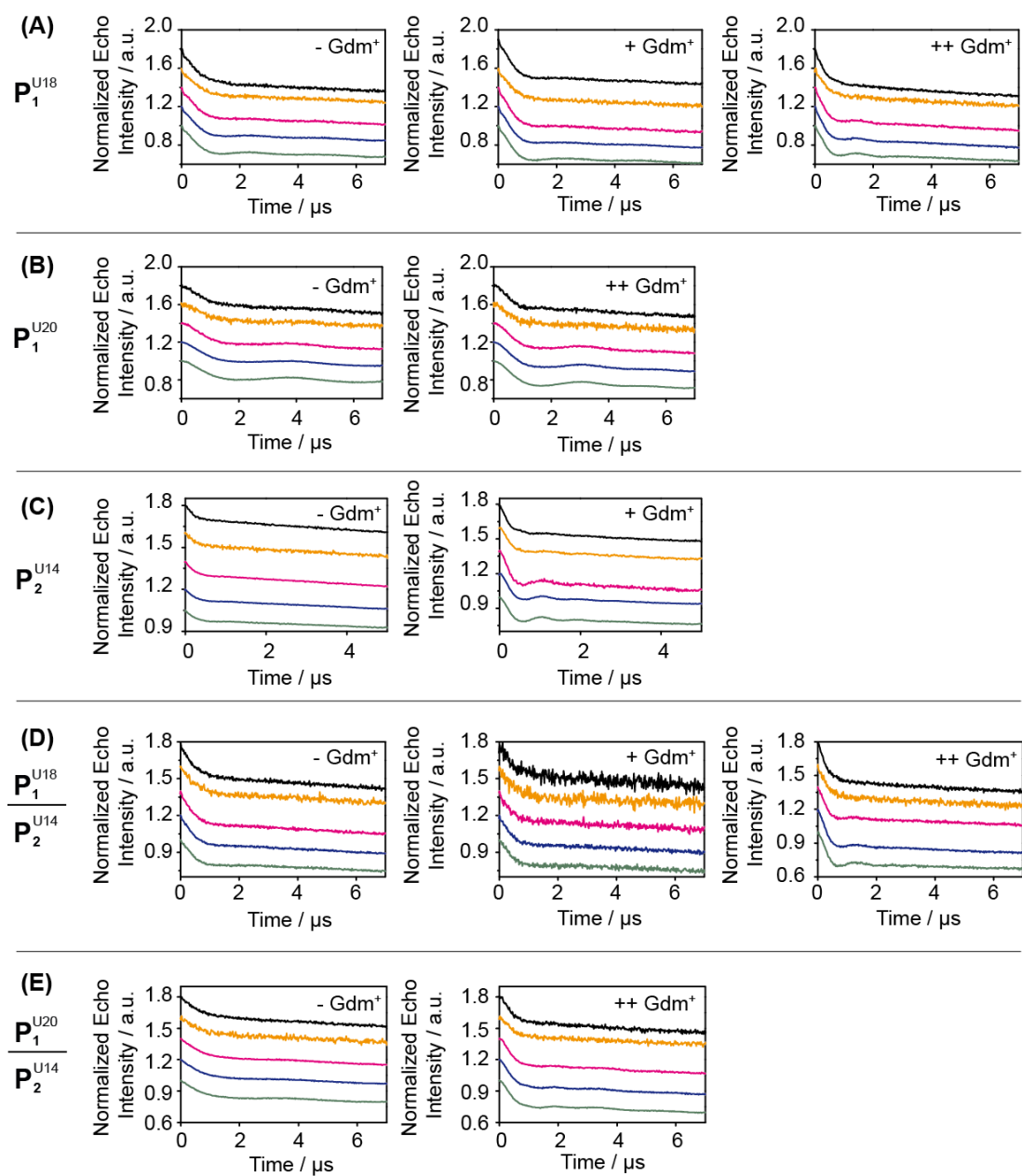


Figure 104. Raw Data of the offset measurements in absence and presence of Gdm<sup>+</sup>. (A)  $P_1^{U18}$ , (B)  $P_1^{U20}$ , (C)  $P_2^{U14}$ , (D)  $P_1^{U18}$  mixed 1:1 with  $P_2^{U14}$  and (E)  $P_1^{U20}$  mixed 1:1 with  $P_2^{U14}$ .

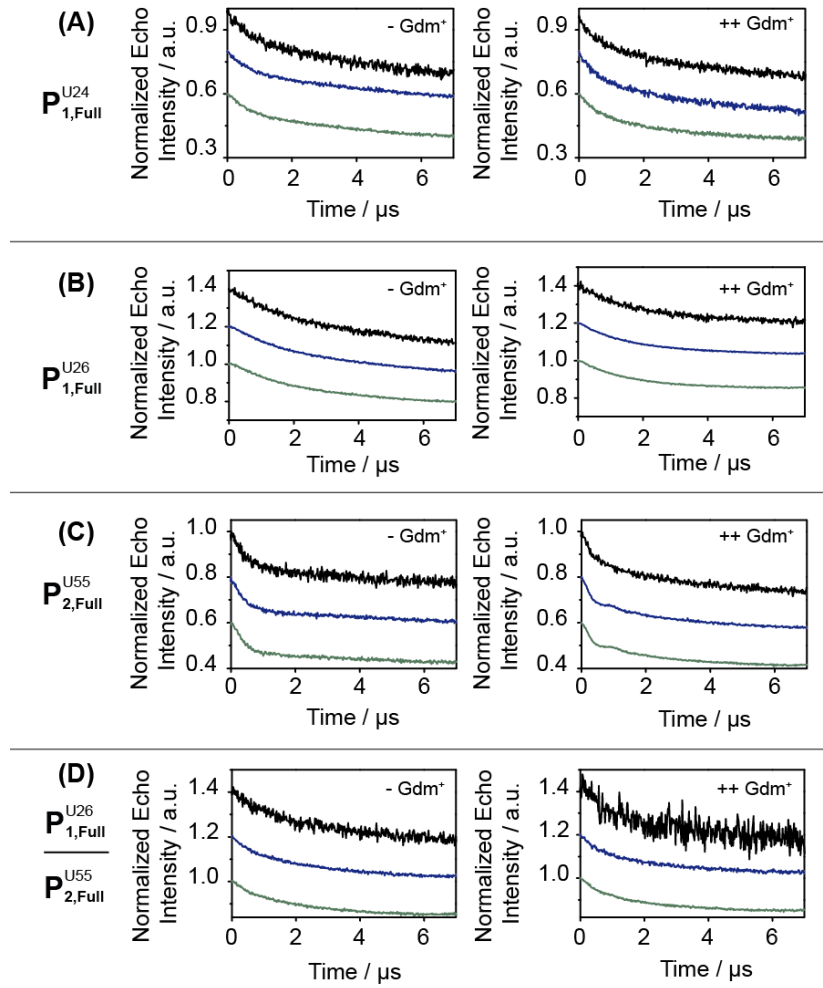


Figure 105. Raw Data of the offset measurements in absence and presence of  $\text{Gdm}^+$ . (A)  $\text{P}_{1,\text{Full}}^{\text{U24}}$ . (B)  $\text{P}_{1,\text{Full}}^{\text{U26}}$ . (C)  $\text{P}_{2,\text{Full}}^{\text{U55}}$ . (D)  $\text{P}_{1,\text{Full}}^{\text{U26}}$  mixed 1:1 with  $\text{P}_{2,\text{Full}}^{\text{U55}}$ .

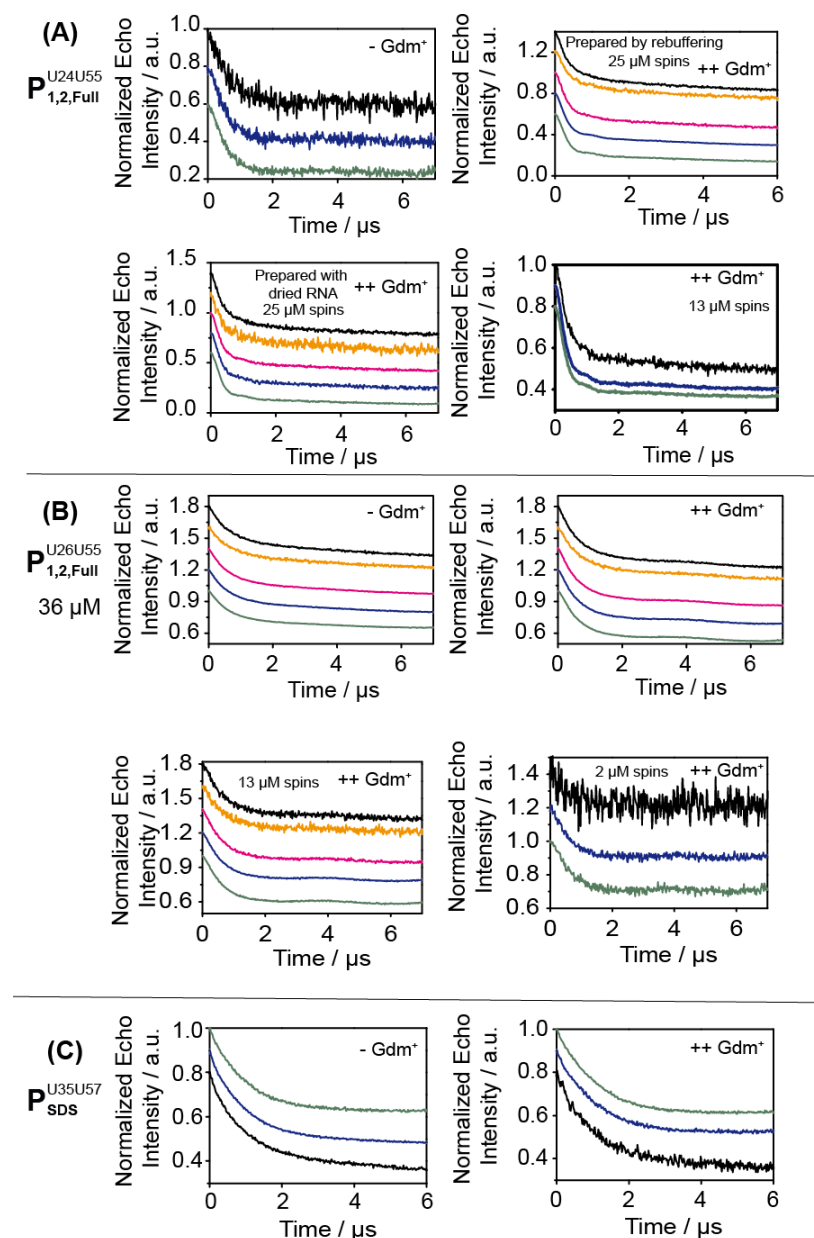


Figure 106. Raw Data of the offset measurements in absence and presence of Gdm<sup>+</sup>, and with different spin concentration as denoted. (A)  $P_{1,2,Full}^{U24U55}$ , (B)  $P_{1,2,Full}^{U26U55}$ , and (C)  $P_{sds}^{U35U57}$ .



## 6.8.2 Summed data

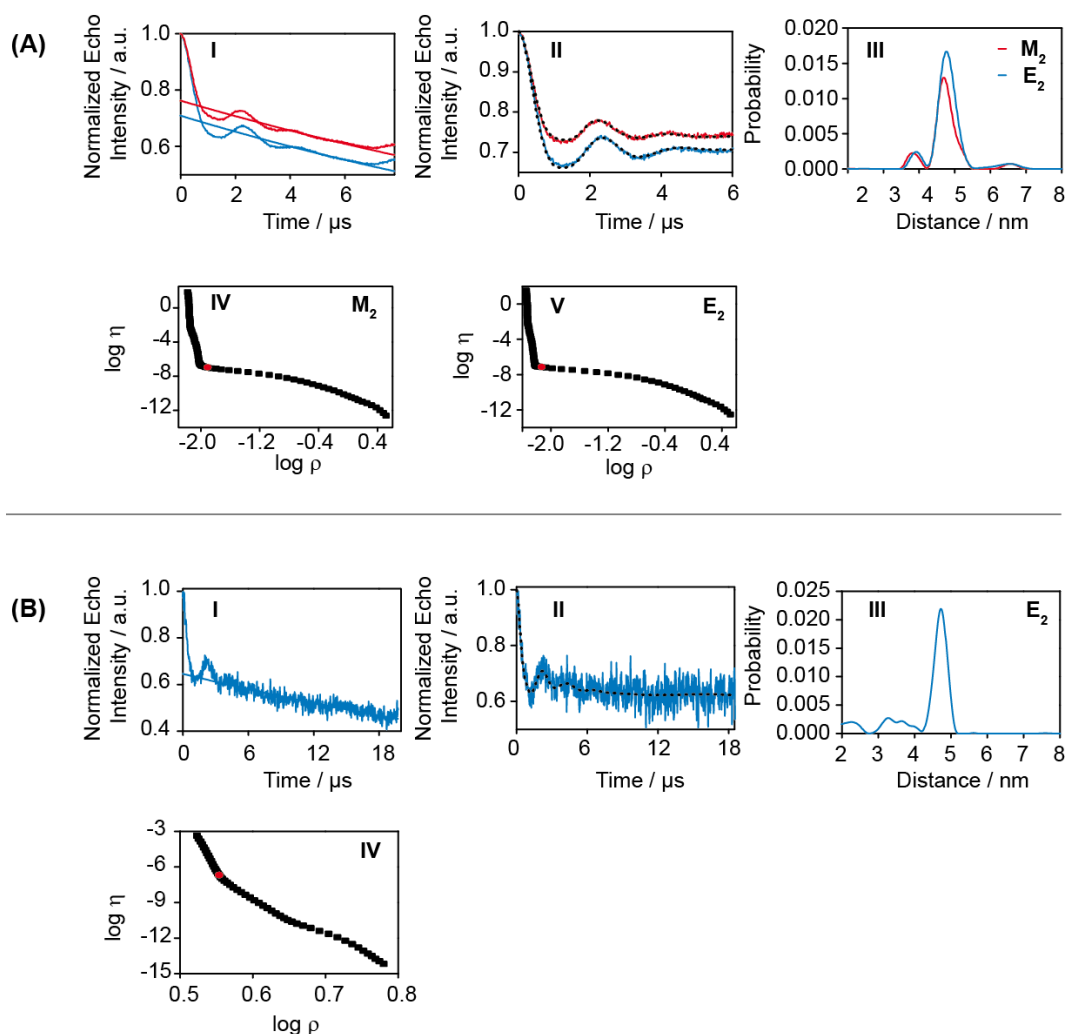


Figure 107. Data Analysis of the summed PELDOR time traces of (A)  $M_2$  and  $E_2$ , and (B) the 80 MHz offsets of  $E_2$  measured with the long acquisition window of 20  $\mu\text{s}$ . (I) Uncorrected PELDOR time traces with the intermolecular background function. (II) Background corrected PELDOR time traces with overlaid fit (dotted black line). (III) PELDOR-derived distance distributions. (IV) and (V): The corresponding L-curves.

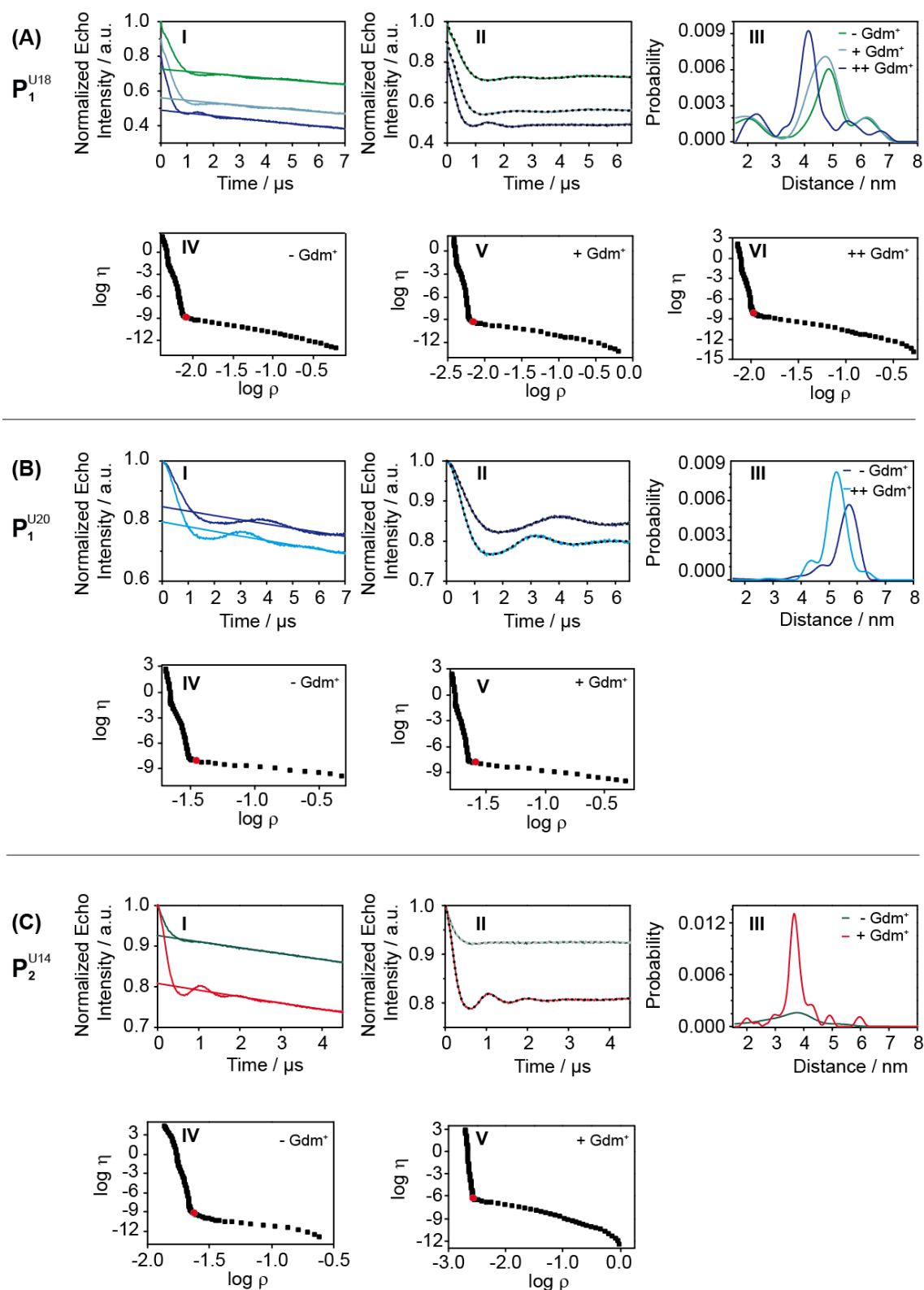


Figure 108. Data Analysis of the summed PELDOR time traces in the absence and presence of Gdm<sup>+</sup> for (A)  $P_1^{U18}$ , (B)  $P_1^{U20}$  and (C)  $P_2^{U14}$ . (I) Uncorrected PELDOR time traces with the intermolecular background function. (II) Background corrected PELDOR time traces with overlaid fit (dotted black or grey line). (III) PELDOR-derived distance distributions. (IV)-(VI): The corresponding L-curves.

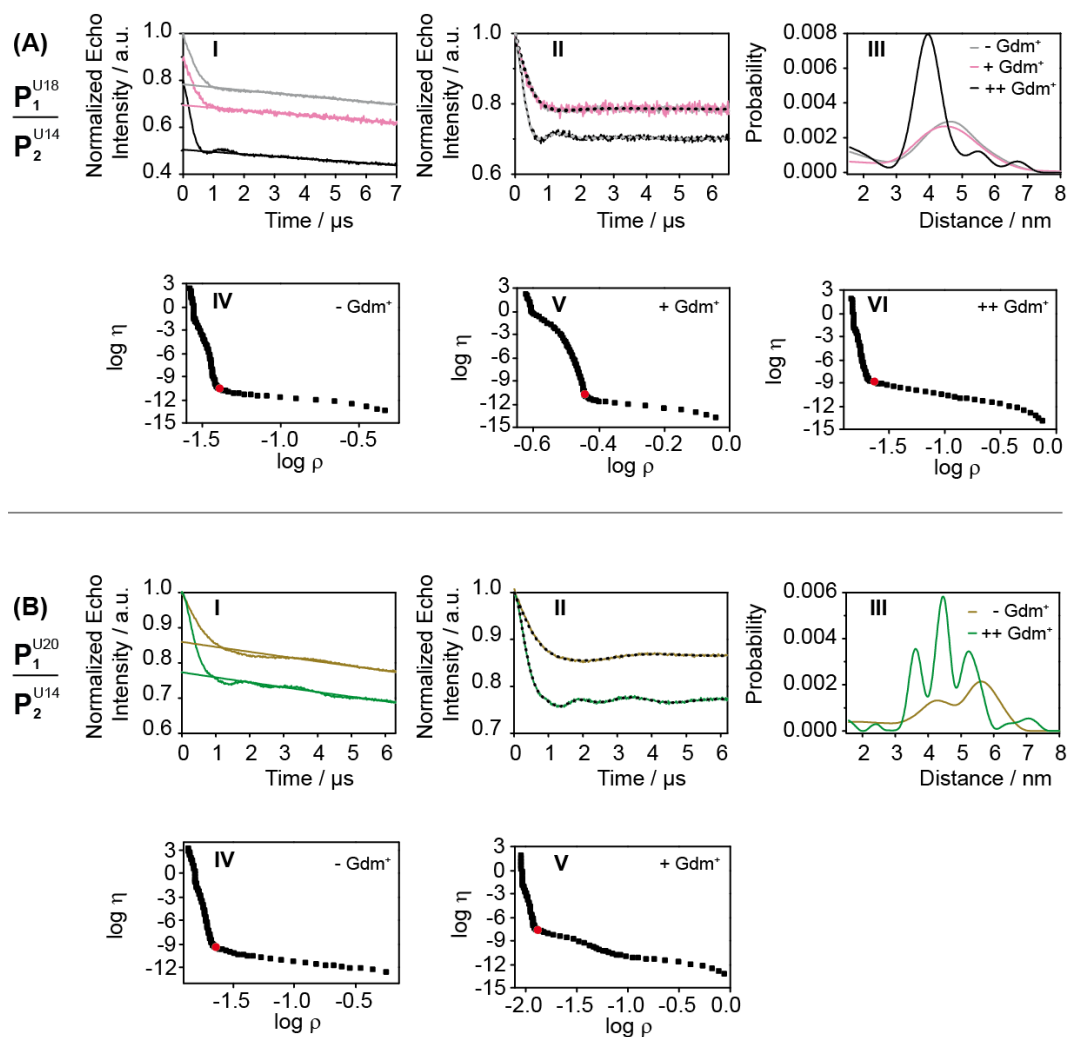


Figure 109. Data Analysis of the summed PELDOR time traces in absence and presence of Gdm<sup>+</sup>. (A)  $P_1^{U18}$  mixed 1:1 with  $P_2^{U14}$  and (B)  $P_1^{U20}$  mixed 1:1 with  $P_2^{U14}$ . (I) Uncorrected PELDOR time traces with the intermolecular background function. (II) Background corrected PELDOR time traces with fit overlaid (dotted black or grey line). (III) PELDOR-derived distance distributions. (IV)-(VI), the corresponding L-curves.

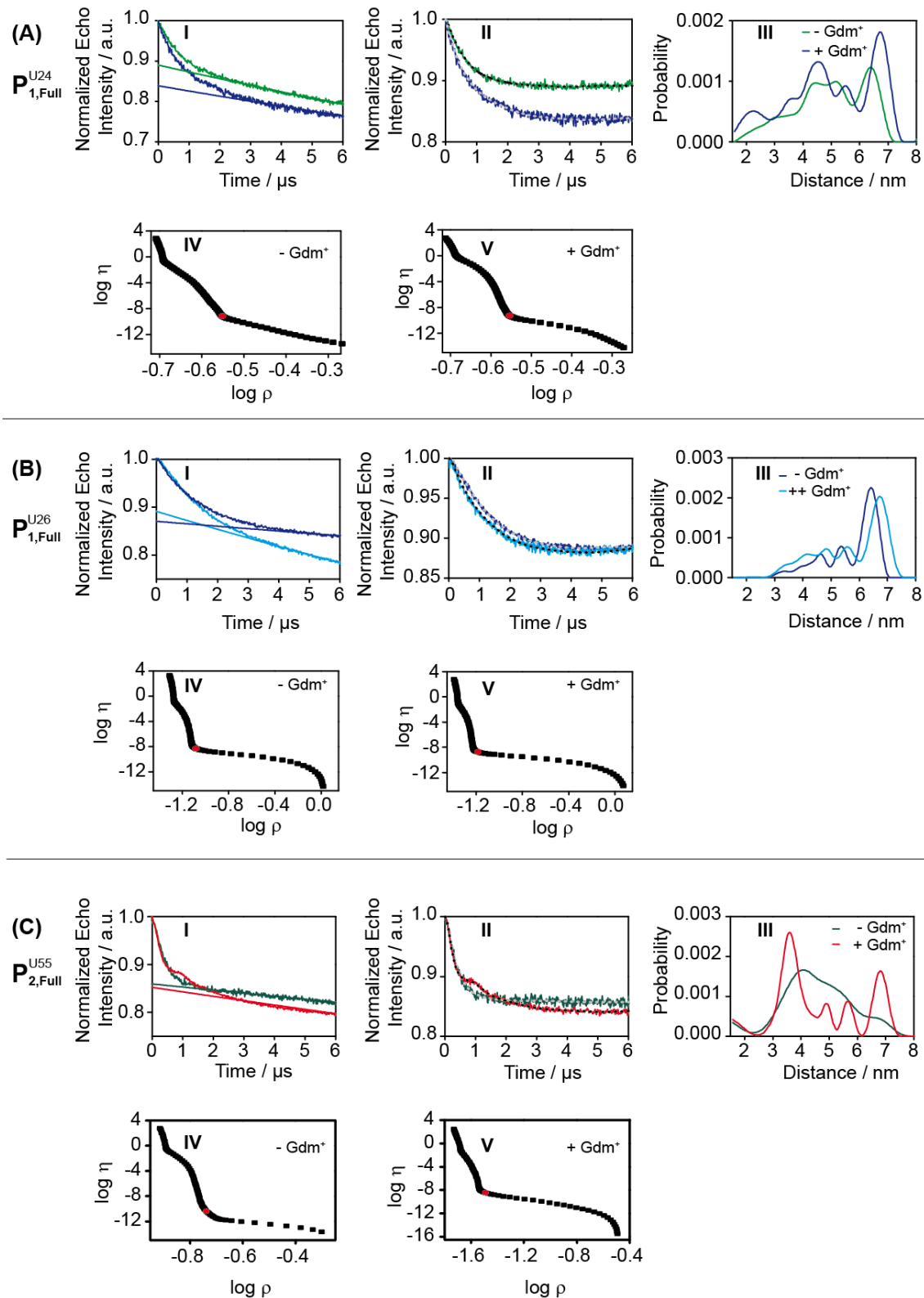


Figure 110. Data Analysis of the summed PELDOR time traces in absence and presence of Gdm<sup>+</sup>. (A)  $P_{1,Full}^{U24}$ . (B)  $P_{1,Full}^{U26}$  and (C)  $P_{2,Full}^{U55}$ . (I) Uncorrected PELDOR time traces with the intermolecular background function. (II) Background corrected PELDOR time traces with fit overlaid (dotted black or grey line). (III) PELDOR-derived distance distributions. (IV) and (V), the corresponding L-curves.

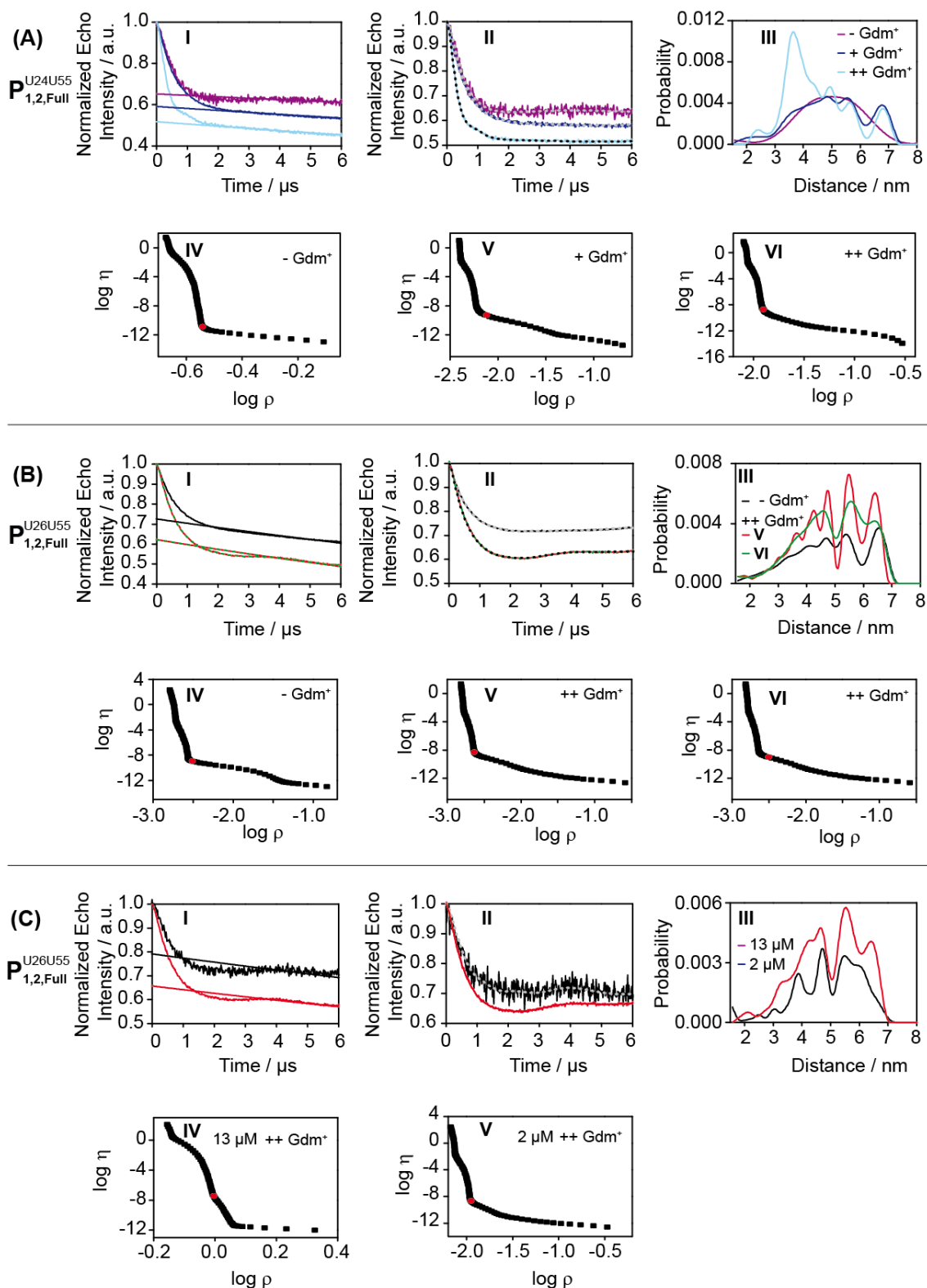


Figure 111. Data Analysis of the summed PELDOR time traces in absence and presence of Gdm<sup>+</sup>, (A)  $P_{1,2,Full}^{U24U55}$  and (B)  $P_{1,2,Full}^{U26U55}$ . (C) Data Analysis of the summed PELDOR time traces in the presence of Gdm<sup>+</sup>  $P_{1,2,Full}^{U26U55}$  diluted to 13  $\mu$ M and 2  $\mu$ M spins. (I) Uncorrected PELDOR time traces with the intermolecular background function. (II) Background corrected PELDOR time trace with fit overlaid (dotted black or grey line). (III) PELDOR derived distance distributions. (IV) and (V), the corresponding L-curves.

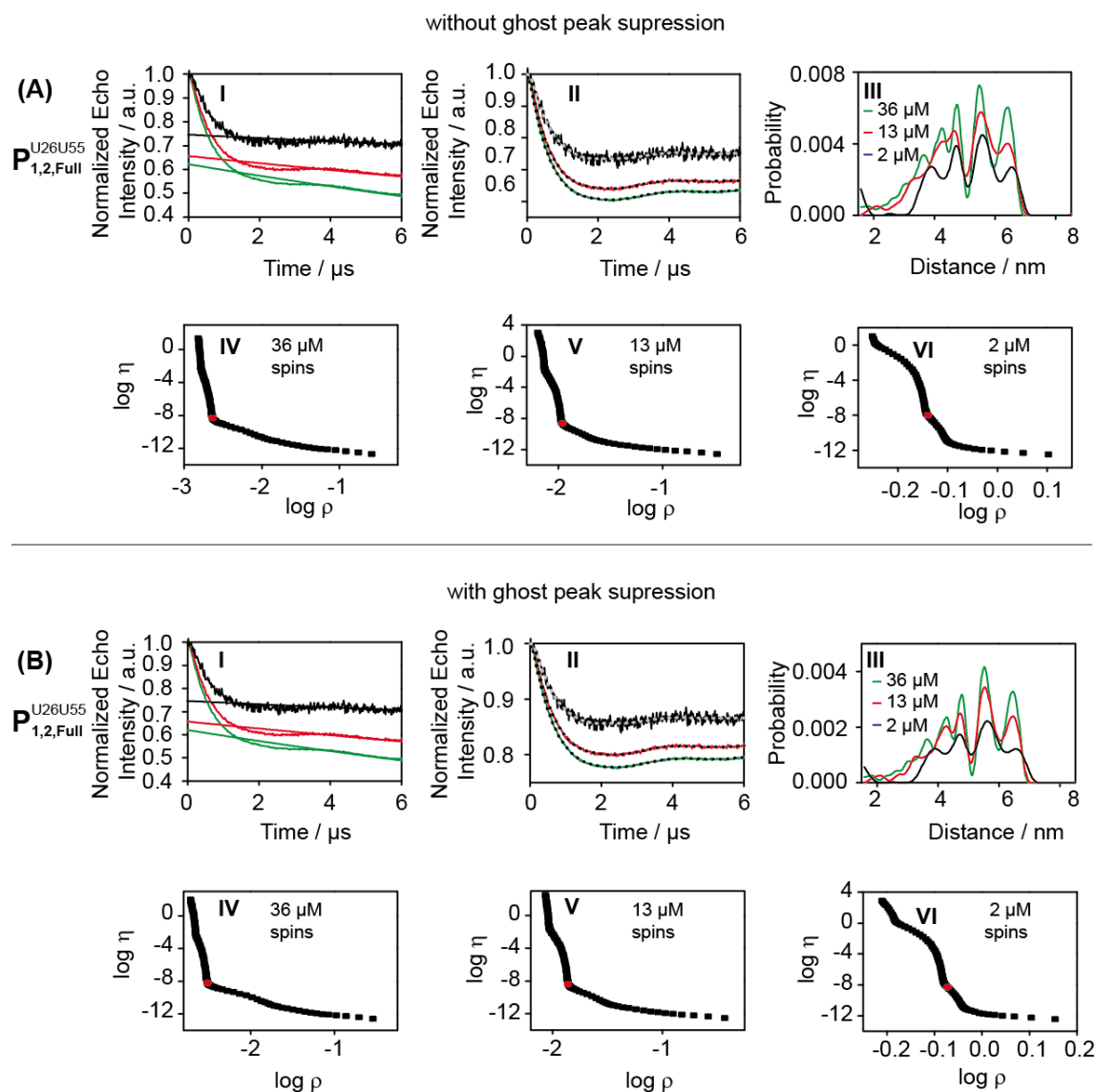


Figure 112. Data Analysis of the summed PELDOR time traces for  $P_{1,2,Full}^{U26U55}$ . In the presence of  $Gdm^+$  analyzed (A) without ghost peak suppression and (B) with ghost peak suppression (I) Uncorrected PELDOR time traces with the intermolecular background function. (II) Background corrected PELDOR time trace with fit overlaid (dotted black or grey line). (III) PELDOR derived distance distributions. (IV) and (V), the corresponding L-curves.

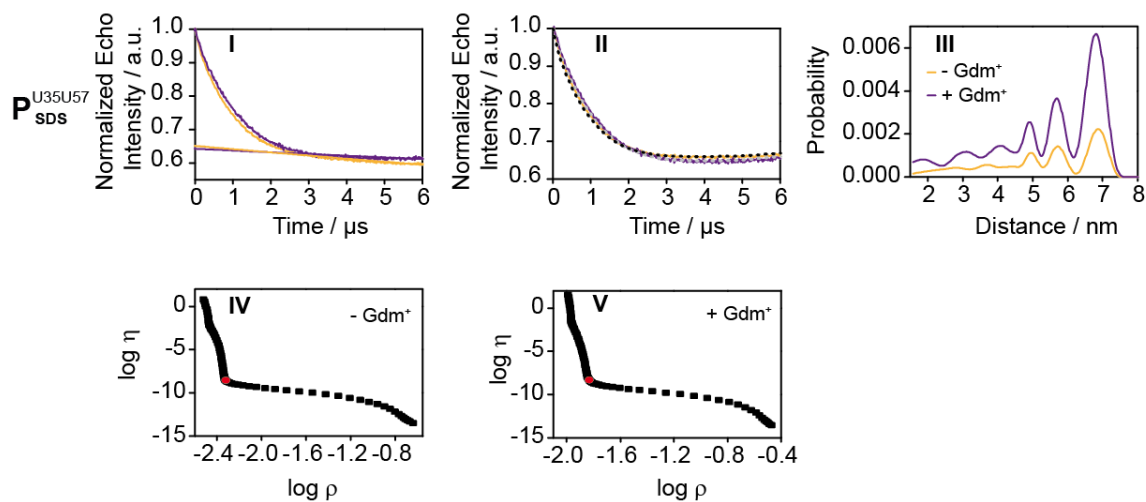


Figure 113. Data Analysis of the summed PELDOR time traces in absence (yellow line) and presence (purple line) of  $\text{Gdm}^+$  of  $P_{\text{SDS}}^{\text{U35U57}}$ . (I) Uncorrected PELDOR time traces with the intermolecular background function. (II) Background corrected PELDOR time trace with fit overlaid (dotted black line). (III) PELDOR derived distance distributions. (IV) and (V), the corresponding L-curves.

## 6.8.3 Validation

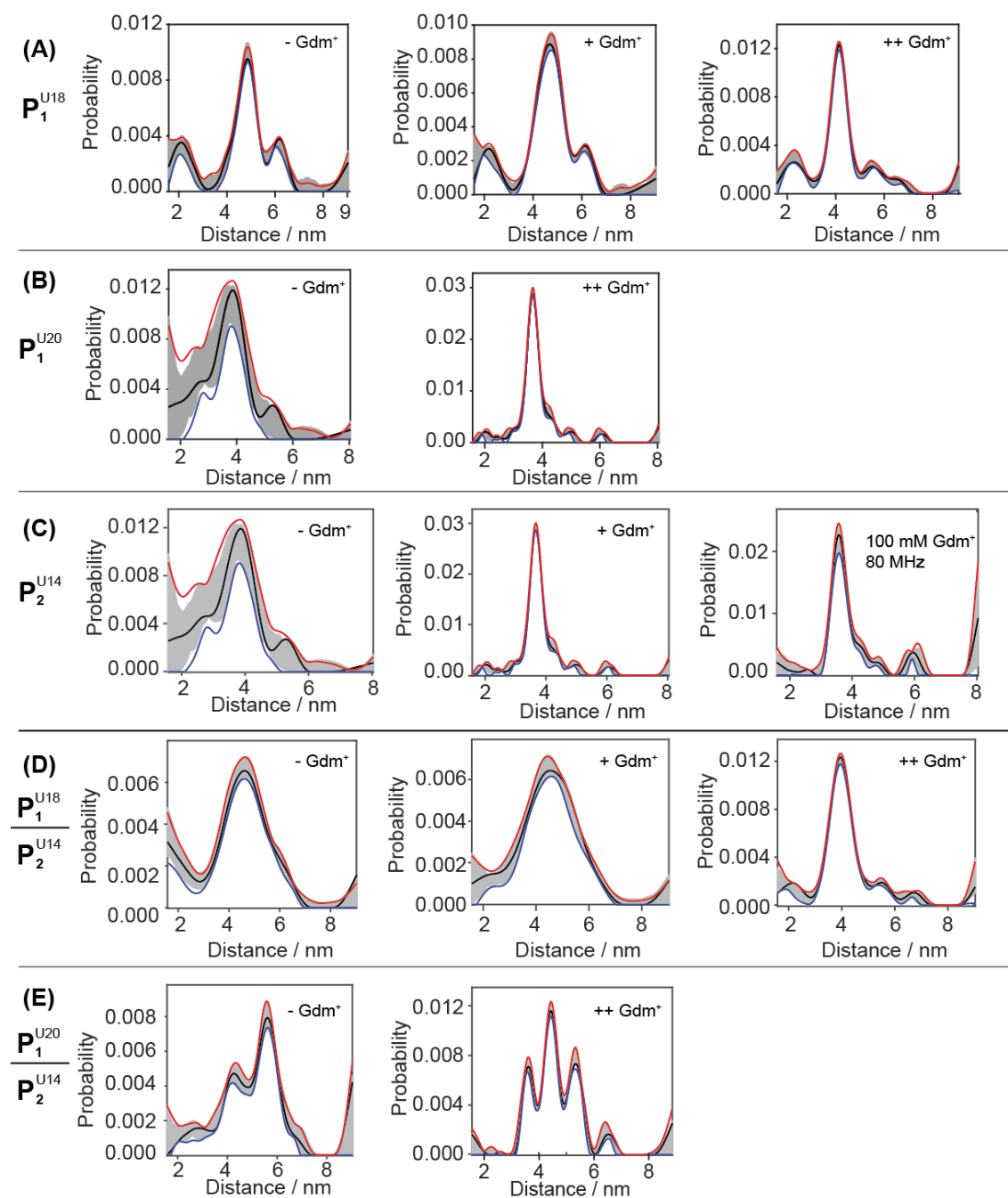


Figure 114. PELDOR data validation of the truncated hairpins.



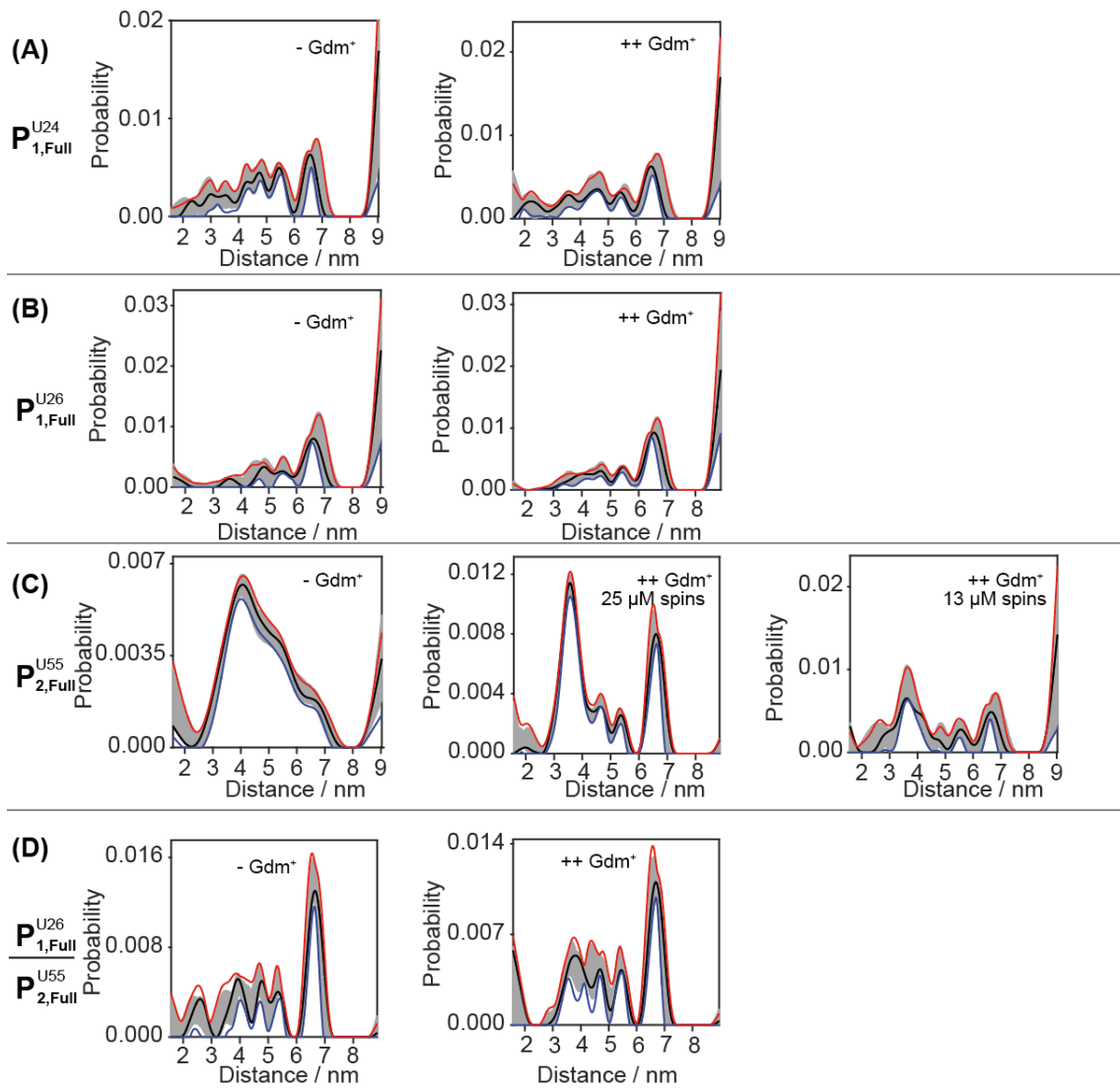


Figure 115. PELDOR data validation of the singly labeled full-length construct.

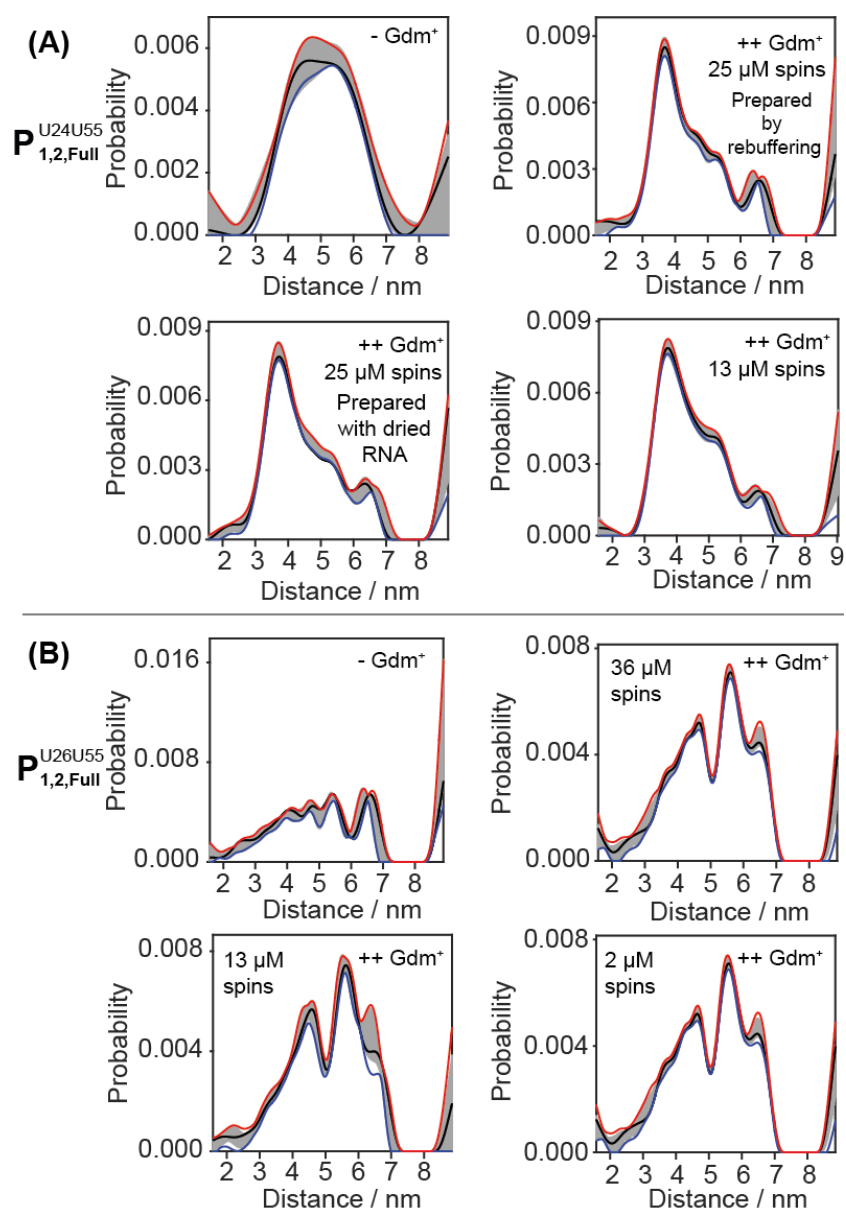


Figure 116. PELDOR data validation of the doubly labeled full-length construct.

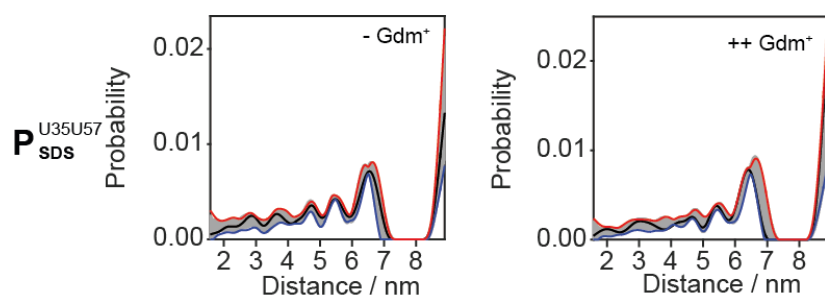


Figure 117. PELDOR data validation of the doubly labeled full-length construct with additional SDS.

## 6.8.4 In silico models and distances

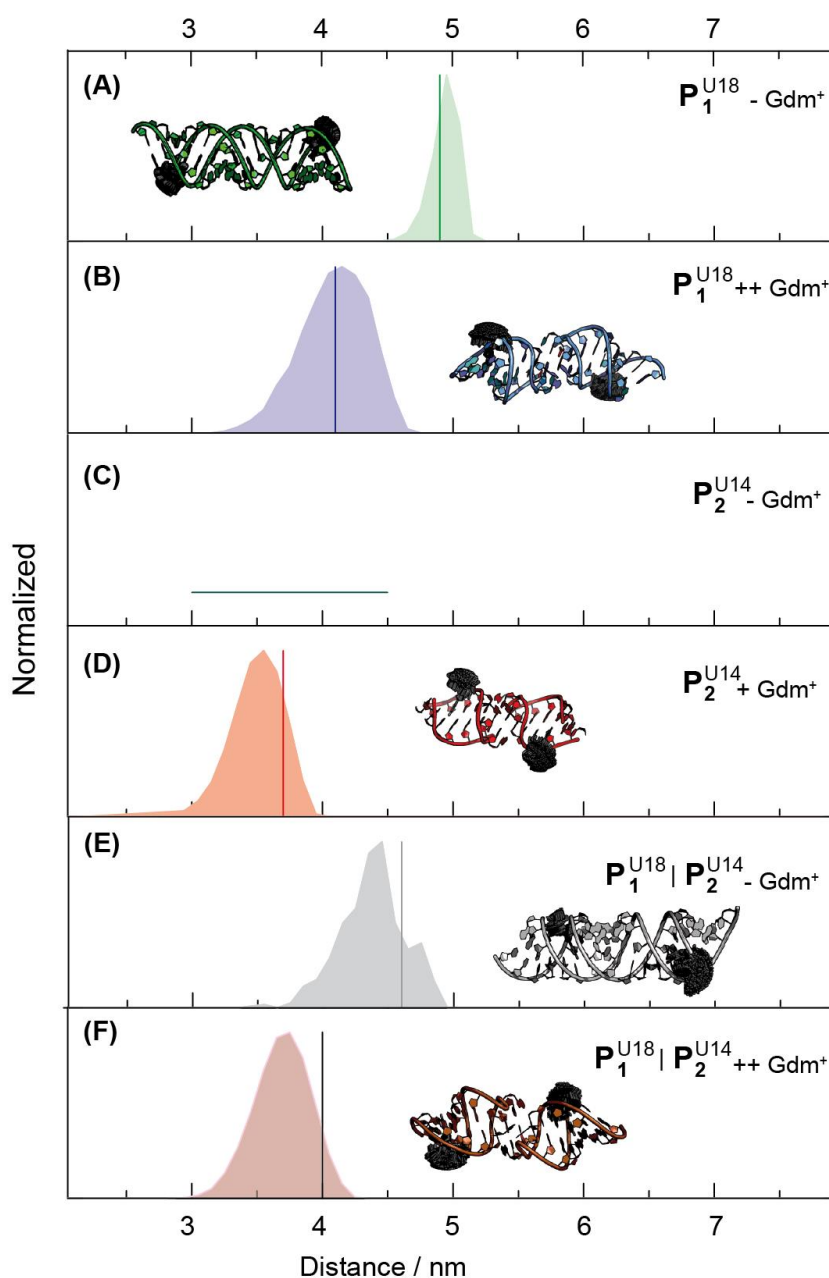


Figure 118. Predicted distance distributions via in silico spin labeling with MtsslWizard overlaid with the measured main distances as stick representation in absence and presence of Gdm<sup>+</sup> for (A) and (B)  $P_1^{U18}$ , (C) and (D)  $P_2^{U14}$ , and (E) and (F)  $P_1^{U18}$  mixed 1:1 with  $P_2^{U14}$ . The respective structure with the spin label rotamers is shown next to it.

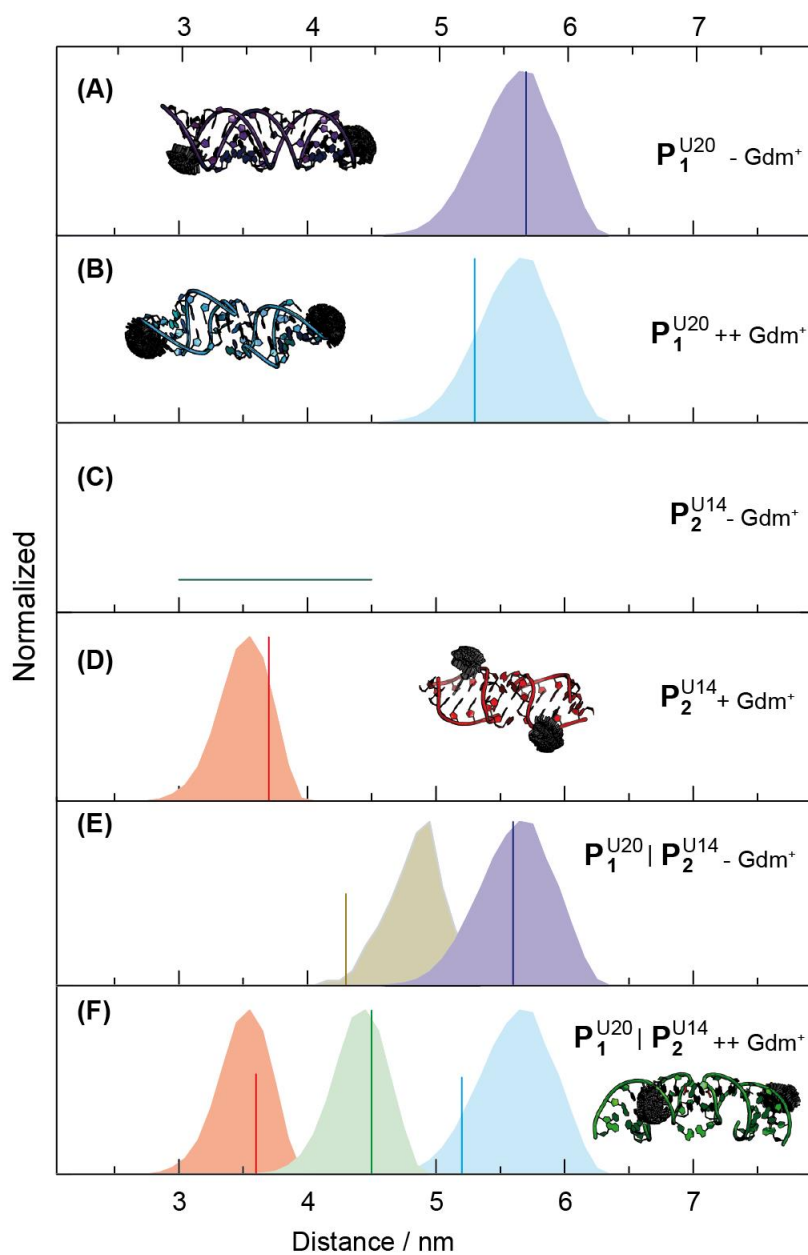


Figure 119. Predicted distance distributions via in silico spin labeling with MtsslWizard overlaid with the measured main distances as stick representation in absence and presence of  $Gdm^+$  for (A) and (B)  $P_1^{U20}$ , (C) and (D)  $P_2^{U14}$ , and (E) and (F)  $P_1^{U20}$  mixed 1:1 with  $P_2^{U14}$ . The respective structure with the spin label rotamers is shown next to it.

## 6.9 Data of the linker and hairpin length analysis

Table 32. Overview about the data of the hairpin and linker length analysis.

Species name and taxonomy <sup>[a]</sup>	Number of nt			Estimated Distance / Å		
	P1	P2	Linker	Kissing Hairpins	Linker	Linker - Kissing Hairpins
Osp-1-1	6	5	13	67.6	72.8	5.2
Pen-1-1	7	6	18	68.1	100.8	32.7
Ppu-1-1	7	4	20	67.6	112.0	44.4
Ppu-2-1	6	4	21	67.0	117.6	50.6
Pae-5-1	6	5	25	67.6	140.0	72.4
Pae-3-1	6	4	26	67.0	145.6	78.6
Oba-1-1	6	4	20	67.0	112.0	45.0
Oba-1-2	6	4	20	67.0	112.0	45.0
Sba-2-1	6	6	16	67.9	89.6	21.7
Sba-1-1	6	6	16	67.9	89.6	21.7
Ssp-5-1	6	5	17	67.6	95.2	27.6
Spu-1-1	6	4	18	67.0	100.8	33.8
Ssp-4-1	10	5	9	68.3	50.4	-17.9
Son-1-1	10	5	9	68.3	50.4	-17.9
Yps-2-1	8	5	13	68.1	72.8	4.7
Ybe-1-1	8	5	13	68.1	72.8	4.7
Yin-1-1	11	5	9	68.3	50.4	-17.9
<sup>2</sup> Yfr-1-1	11	5	10	68.3	56.0	-12.3
Bps-8-1	8	4	14	67.9	78.4	10.5
Bps-5-1	8	4	14	67.9	78.4	10.5
Bth-1-1	8	4	14	67.9	78.4	10.5
Bce-1-1	8	4	13	67.9	72.8	4.9
<sup>4</sup> Bvi-1-1	8	4	13	67.9	72.8	4.9
<sup>7</sup> env-4	7	4	14	67.6	78.4	10.8
<sup>4</sup> Bsp-1-1	7	4	14	67.6	78.4	10.8
Bam-1-1	7	4	14	67.6	78.4	10.8
Bdo-1-1	7	4	14	67.6	78.4	10.8
<sup>5</sup> env-5	7	4	14	67.6	78.4	10.8
Bxe-1-1	7	4	11	67.6	61.6	-6.0

## Appendix

---

Vch-2-1	10	4	11	68.2	61.6	-6.6
Vch-4-1	10	4	11	68.2	61.6	-6.6
Val-1-1	10	4	10	68.2	56.0	-12.2
Vpa-1-1	6	7	16	68.1	89.6	21.5
Vsp-1-1	6	4	16	67.0	89.6	22.6
Pat-1-1	6	5	15	67.6	84.0	16.4
Sen-1-1	7	4	14	67.6	78.4	10.8
Eco-16-	8	4	14	67.9	78.4	10.5
<sup>4</sup> Sdy-1-1	8	4	14	67.9	78.4	10.5
<sup>4</sup> Eco-2-1	8	4	14	67.9	78.4	10.5
<sup>4</sup> Sfl-3-1	8	4	14	67.9	78.4	10.5
<sup>4</sup> Sen-4-2	8	4	13	67.9	72.8	4.9
Gvi-1-1	7	6	14	68.1	78.4	10.3
Msp-1-1	6	6	14	67.9	78.4	10.5
<sup>5</sup> env-6	8	6	11	68.2	61.6	-6.6
<sup>2</sup> Nwi-1-1	7	6	18	68.1	100.8	32.7
<sup>8</sup> Bja-1-1	8	6	18	68.2	100.8	32.6
Nsp-1-1	9	6	17	68.3	95.2	26.9
Gsu-1-1	8	4	13	67.9	72.8	4.9
Plu-1-1	8	5	13	68.1	72.8	4.7
Rru-1-1	7	6	15	68.1	84.0	15.9
Rpa-4-1	8	6	14	68.2	78.4	10.2
Rpa-1-1	8	6	14	68.2	78.4	10.2
Rpa-3-1	8	6	14	68.2	78.4	10.2
Rpa-2-1	8	6	14	68.2	78.4	10.2
Pae-5-2	9	6	13	68.3	72.8	4.5
Pae-3-2	9	6	12	68.3	67.2	-1.1
Asp-1-1	7	6	16	68.1	89.6	21.5
Rsp-1-1	4	5	17	66.0	95.2	29.2
Rba-1-1	3	5	18	64.2	100.8	36.6
Rpa-2-3	4	6	17	67.0	95.2	28.2
Eca-1-1	8	6	13	68.2	72.8	4.6
<sup>6</sup> env-7	6	6	14	67.9	78.4	10.5
<sup>6</sup> env-8	8	6	13	68.2	72.8	4.6

Pfl-2-1	8	6	13	68.2	72.8	4.6
Pna-1-1	7	6	13	68.1	72.8	4.7
Reu-1-1	8	6	12	68.2	67.2	-1.0
Sgl-1-1	5	4	17	66.0	95.2	29.2
<sup>13</sup> Mma-1-1	9	5	13	68.2	72.8	4.6
Sde-1-1	9	5	9	68.2	50.4	-17.8
Msp-2-1	10	4	11	68.2	61.6	-6.6
Ssp-1-1	10	6	11	68.3	61.6	-6.7
Oal-1-1	4	6	19	67.0	106.4	39.4
Jsp-1-1	6	4	17	67.0	95.2	28.2
Dar-1-1	9	6	10	68.3	56.0	-12.3
Atu-1-1	8	4	18	67.9	100.8	32.9
Pfl-1-1	8	4	21	67.9	117.6	49.7
Bbr-1-1	9	5	10	68.2	56.0	-12.2
Ccr-1-1	11	5	9	68.3	50.4	-17.9
<sup>12</sup> Xau-1-1	7	6	16	68.1	89.6	21.5
Pfl-2-2	7	5	20	67.9	112.0	44.1
Xau-1-2	9	6	14	68.3	78.4	10.1
<sup>14</sup> Ret-1-1	7	6	16	68.1	89.6	21.5
<sup>2</sup> Cef-1-1	9	5	10	68.2	56.0	-12.2
Bli-1-1	8	5	13	68.1	72.8	4.7
<sup>9</sup> Asp-2-1	5	6	15	67.6	84.0	16.4
Neu-1-1	8	5	18	68.1	100.8	32.7
Ogr-1-1	13	4	15	68.3	84.0	15.7
Ret-1-2	6	6	21	67.9	117.6	49.7
Sme-1-1	4	6	25	67.0	140.0	73.0
Rnu-1-1	9	6	18	68.3	100.8	32.5
Abo-1-1	8	6	13	68.2	72.8	4.6
Wsu-1-1	8	4	16	67.9	89.6	21.7
<sup>11</sup> Cgl-1-1	7	5	14	67.9	78.4	10.5
Pae-5-3	9	4	13	68.1	72.8	4.7
Pae-6-3	9	4	13	68.1	72.8	4.7
Psy-3-1	7	6	14	68.1	78.4	10.3
Psy-2-1	7	6	14	68.1	78.4	10.3

## Appendix

---

Psy-1-1	7	5	15	67.9	84.0	16.1
<sup>3</sup> env-9	8	4	14	67.9	78.4	10.5
<sup>1</sup> Bps-8-2	14	4	12	68.4	67.2	-1.2
<sup>10</sup> env-10	8	6	12	68.2	67.2	-1.0
Xca-1-1	6	4	23	67.0	128.8	61.8
<sup>1</sup> Xor-1-1	6	4	23	67.0	128.8	61.8
Rpa-4-2	4	6	15	67.0	84.0	17.0
Rpa-3-2	4	6	15	67.0	84.0	17.0
Rpa-1-2	4	6	15	67.0	84.0	17.0
<sup>1</sup> Sfr-1-1	6	4	39	67.0	218.4	151.4
Mlo-1-1	9	6	14	68.3	78.4	10.1
Csp-1-1	12	5	11	68.3	61.6	-6.7
Aeh-1-1	8	4	16	67.9	89.6	21.7
<sup>12</sup> Acr-1-1	9	6	13	68.3	72.8	4.5
Pin-1-1	6	4	15	67.0	84.0	17.0
<sup>15</sup> Pgi-1-1	5	5	8	67.0	44.8	-22.2

[a] Data for analysis were taken from <sup>43</sup>.



## 6.10 List of abbreviations

---

2PESEEM	Two Pulse Electron Spin Echo Envelope Modulation
2D	Two dimensional
3D	Three dimensional
A	Adenosine
Anti-SDS	Anti-Shine-Dalgarno Sequence
APS	Ammonium persulfate
C	Cytosine
DD	Dipole-dipole coupling
cryo-EM	cryo-Electron Microscopy
cwEPR	continuous wave Electron Paramagnetic Resonance
EZ	Electron Zeeman interaction
DEER	Double Electron-Electron Resonance
DNA	Deoxyribonucleic Acid
DPA	2,2'-Dipicolylamine Phosphoramidite
EPR	Electron Paramagnetic Resonance
EZ	Electron Zeeman
FRET	Förster Resonance Energy Transfer
G	Guanine
Gdm <sup>+</sup>	Guanidinium
GMPs	Guanosine Monophosphorthioate
H	Hamiltonian
HF	Hyperfine coupling interaction
HIV	Human Immunodeficiency Virus
HPLC	High Performance Liquid Chromatography
LCMS	Liquid Chromatography mass Spectrometry
MeCN	Acetonitrile
mRNA	messenger RNA
NMR	Nuclear Magnetic Resonance

NZ	Nuclear Zeeman interaction
NQ	Nuclear Quadrupole
nt	Nucleotides
NZ	Nuclear Zeemann Interaction
PAGE	Polyacrylamide gel electrophoresis
PDS	Pulsed Dipolar EPS Spectroscopy
PELDOR	Pulsed Electron-Electron Double Resonance
pdb	Protein Data Bank
RNA	Ribonucleic acid
RP HPLC	Reverse Phase High Performance Liquid Chromatography
rRNA	ribosomal RNA
SDS	Shine-Dalgarno Sequence
smFRET	Single molecule Förster Resonance Energy Transfer
SNR	Signal-to-Noise Ratio
SRT	Shot-repetition time
T	Thymine
TAR	trans-activation Responsive Region
TEAA	Triethyl ammonium acetate
TEMED	Tetramethylethylenediamine
tRNA	transfer RNA
U	Uracil
XFELs	X-Ray Free Electron Lasers
ZFS	Zero Field Splitting

---

## 6.11 List of figures

Figure 1. Ingredients of a cell (adapted from reference 3).....	1
Figure 2. (A) Chemical structure of a nucleotide composed of a phosphate group, a base and the pentose sugar, which is either ribose in the case of RNA or deoxyribose in DNA. (B) Chemical structure of the purine and (C) pyrimidine bases.....	2
Figure 3. Overview of the riboswitch mechanisms ordered in “common” and “rare” in context of their natural abundance.....	3
Figure 4. (A) Transcriptional control of a riboswitch. “UUUU” denotes the poly-uracil region. The grey dot represents the RNA polymerase. The orange boxes represent the stable stem of the terminator hairpin. (B) Translational control of a riboswitch. “SDS” denotes the Shine-Dalgarno Sequence and “AUG” the start codon where the ribosome binds. The orange body represents the ribosome that, in case it can bind, expresses polypeptides visualized as black dots. ....	4
Figure 5. Overview of the riboswitch ligands (adapted from reference 12, 17, and 31, abbreviations are found in the appendix).....	5
Figure 6. (A) Crystal structure of the F <sup>-</sup> riboswitch with (B) a Zoom-in to the F <sup>-</sup> binding pocket (PDB ID: 4ENC). <sup>37</sup> The F <sup>-</sup> anion (red) is coordinated by three Mg <sup>2+</sup> cations (yellow), which are in turn coordinated by the non-bridging oxygens (blue) of five phosphates (green). In purple an additional K <sup>+</sup> ion is shown. <sup>37</sup> ..	6
Figure 7. Abundance of the Guanidine-II riboswitch in different organisms.....	8
Figure 8. (A) Proposed switching mechanism of the Guanidine-II riboswitch. “SDS” denotes the Shine-Dalgarno Sequence and “Anti-SDS” the complementary Anti-Shine-Dalgarno Sequence. The hairpins <b>P1</b> and <b>P2</b> are colour coded in yellow and blue, respectively (representation based on reference 47). (B) Crystal structure of <b>P2</b> (PDB ID: 5VJ9) <sup>48</sup> with Gdm <sup>+</sup> marked in red. (C)-(F) Visualisation of the interaction of the hairpins and the Gdm <sup>+</sup> binding. The description of the nucleotides follows (A). The dark and the light blue colour marks the two different hairpins. Gdm <sup>+</sup> is coloured in red. Interactions are illustrated with black lines. ....	10
Figure 9. Statistic of the total number of entries available in the Protein Data Bank. Data are obtained from reference 83 on July 9, 2020. ....	13

- Figure 10. (A) Electron Zeeman splitting for an electron spin in an applied magnetic field  $B_0$ . (B) Absorption line, which is obtained when the resonance condition  $\Delta E = h\nu$  is matched. (C) Resulting cwEPR spectrum obtained as first derivative of the absorption line (Adapted from reference 148). ..... 17
- Figure 11. Energy scheme a nitroxide with  $s = 1/2$  and  $I = 1$  in an applied magnetic field in the case that the hyperfine interaction exceeded the nuclear Zeeman interaction. (A) The electron Zeeman interaction with the resulting magnetic moments of the electron spins marked as red arrows. (B) The hyperfine interaction yielding the magnetic moments of the nuclear spins marked as blue arrows. (C) The nuclear Zeeman interaction inducing an increase and decrease of the energy levels. (D) The selection rules  $\Delta m_s = \pm 1$  and  $\Delta m_I = 0$  give three allowed transitions indicated as green arrows in (C), which yield (E) the absorption lines and (F) the final cwEPR spectrum as first derivative. .... 19
- Figure 12. (A) Structure of spin label **1**<sup>\*</sup>. (B) cwEPR spectrum of **1**<sup>\*</sup> in liquid, degassed toluene at room temperature. The hyperfine couplings of <sup>14</sup>N and <sup>13</sup>C are indicated. (C) Zoom of (B) to visualize the <sup>1</sup>H hyperfine coupling. The simulation is overlaid as red line. .... 20
- Figure 13. Absorption spectrum of a nitroxide recorded at 50 K at Q-band. The  $g$  anisotropy is resolved yielding  $g_{xx}$ ,  $g_{yy}$ ,  $g_{zz}$ , whereas the components of the  $A$  anisotropy can be found in different areas of the spectrum (adapted from reference 149). .... 20
- Figure 14. Simulated cwEPR spectra to illustrate the nitroxide spin label dynamic. The program EasySpin<sup>157</sup> was used with the parameters  $g = 2.003, 2.006, 2.008$  and  $A = 20 \text{ MHz}, 20 \text{ MHz}, 90 \text{ MHz}$ . .... 21
- Figure 15. (A) Scheme of the dipole-dipole coupling of two spins (A spins and B spins) that depends on the interspin distance vector  $r_{AB}$  and on the angle  $\theta$ , which is assigned between the magnetic field vector  $B_0$  and the interspin distance vector  $r_{AB}$ . (B) Dipolar spectrum called Pake pattern that is obtained if a spin pair is randomly oriented in a sample and a complete distribution of dipolar frequencies is obtained. .... 22

Figure 16. (A) Hahn echo pulse sequence. (B) Illustration of the net spin magnetization in z-direction. (C) Illustration of the dephasing of the spins after applying a $\pi/2$ pulse. (D) Illustration of the refocussing of the spins after applying a $\pi$ pulse. The resulting magnetization is detected as Hahn echo. ....	24
Figure 17. 2PESEEM sequence. The integrated echo is measured as function between the two pulses. The observed decay is analyzed as function of $T_M$ . ....	25
Figure 18. (A) Four-pulse PELDOR sequence. (B) PELDOR time trace. The modulation depth $\Delta$ and a fully oscillation are indicated. ....	27
Figure 19. (A) 3' termini spin label and (B) 5' termini spin label. ....	28
Figure 20. Spin labeling reactions performed on the phosphate group. ....	29
Figure 21. Spin labeling reactions performed on the ribose. ....	30
Figure 22. Spin labeling reactions performed on the nucleotide base. ....	31
Figure 23. Rigid spin labels. ....	33
Figure 24. Non-covalent spin labels with the ability to build hydrogen-bonds for base pairing shown as dotted lines. ....	33
Figure 25. Ligation strategies utilizing the (A) T4 RNA Ligase, (B) the T4 DNA Ligase, and (C) a DNAzyme. ....	34
Figure 26. Spin labeling reaction based on the site directed complementary addressed approach. ....	35
Figure 27. (A) Novel nitroxide carrying RNA triphosphate (TPT3-NO $\cdot$ TP). (B) RNA labeling strategy using the DNA template constructed with two additional nucleotides (dNAM and dTPT3). The genetic alphabet expansion transcription introduces TPT3-NO $\cdot$ TP at specific positions. ....	35
Figure 28. (A) Finland Trityl. (B) First spin labeling approach using a Trityl radical on the 5' termini of a DNA duplex. (C) Improved spin labeling strategy using a shorter linker. (D) Internal spin labeling approach with a non-nucleotide phosphoramidite. ....	36
Figure 29. Gd $^{3+}$ spin labeling strategies. ....	37
Figure 30. Cu $^{2+}$ based spin labeling. ....	38

- Figure 31. (A) Spin labeling reaction based on the CuAAC Click-reaction introducing **1\*** and **2\*** into RNA strands. (B) Sequence of the single strand RNA and the annealed duplex. “**U**” corresponds to the labeling positions. In the following, the RNA single strand labeled with **1\*** is referred to as **E**, while the one labeled with **2\*** is titled **M**. The spin labeled single stranded RNAs **E** and **M** were annealed to obtain duplexes **E<sub>2</sub>** and **M<sub>2</sub>**, respectively. ....41
- Figure 32. (A) Overlay of the HPLC runs of the unmodified (black line) and labeled RNAs **M** (red line) and **E** (blue line). (B) LCMS UV chromatogram and (C) deconvoluted mass of **M** (calculated mass 5305.03, found mass 5304.78). (D) LCMS UV chromatogram and (E) deconvoluted mass of **E** (calculated mass 5361.03, found mass 5361.59). (F) Experimental cwEPR spectra of 35  $\mu\text{M}$  **M<sub>2</sub>** (red line) and 35  $\mu\text{M}$  **E<sub>2</sub>** (blue line). The measured spin concentrations using the spin counting tool are 32  $\mu\text{M}$  for **M<sub>2</sub>** and 31  $\mu\text{M}$  for **E<sub>2</sub>**. (G) Temperature dependent UV VIS curves of the unmodified (black line,  $T_m = 66^\circ\text{C}$ ) and labeled RNAs **M<sub>2</sub>** (red line,  $T_m = 58^\circ\text{C}$ ) and **E<sub>2</sub>** (blue line,  $T_m = 55^\circ\text{C}$ ). (H) CD spectra of the unmodified (black line) and labeled RNAs **M<sub>2</sub>** (red line) and **E<sub>2</sub>** (blue line).....42
- Figure 33. 2PESEEM traces of **M<sub>2</sub>** (red line) and **E<sub>2</sub>** (blue line) at temperatures between 10 K – 120 K overlaid with their fits (black line). The fit data are listed in Table 1.....44
- Figure 34. Plot of the fitted phase memory time relaxation parameters of **M<sub>2</sub>** (red) and **E<sub>2</sub>** (blue). The vertical line symbol displays the parameter with the subscript “1”, whereas the horizontal line symbol displays the parameter with the subscript “2”. (A) shows the variation of the phase memory times components  $T_{M1}$  and  $T_{M2}$  in dependence of the temperature, (B) the stretched exponents  $x_1$  and  $x_2$  and (C) the weighting factors  $A_1$  and  $A_2$ . Lines are shown as eye guidance in the same color code. For **E<sub>2</sub>** at 30 K an outlier is suspected, so that this data point is excluded from the discussion. ....45
- Figure 35. (A) 2PESEEM decay curves of **E<sub>2</sub>** in deuterated buffer (blue line) and in deuterated buffer with 17% additional water content (green line) both obtained at 50 K. (B) Comparison of the 2PESEEM traces of **M<sub>2</sub>** (yellow line) and **E<sub>2</sub>** (green line) in deuterated buffer with additional 17 % water recorded at 50 K. ....47

Figure 36. Illustration of the critical range of spin label <b>1*</b> (blue) and <b>2*</b> (red) attached to the RNA. The RNA model generation is explained in the appendix.....	48
Figure 37. 2PESEEM measurements of <b>E<sub>2</sub></b> in dependence of the magnetic field recorded at 50 K.....	48
Figure 38. Inversion recovery measurement of <b>E<sub>2</sub></b> recorded at 50 K. The marked data point reflects the SRT of 3 ms that is in the partially saturated region of the trace. ....	49
Figure 39. Echo detected field sweep (EDFS) of <b>E<sub>2</sub></b> recorded at 50 K with the different pump and detection positions indicated as lines.....	50
Figure 40. (A) Comparison of the generated distance distributions received from the sum of the time traces of <b>M<sub>2</sub></b> (red line) and <b>E<sub>2</sub></b> (blue line), and the distances calculated from the dipolar coupling frequency of the 2PESEEM pattern of <b>M<sub>2</sub></b> (dotted red line) and <b>E<sub>2</sub></b> (dotted blue line) indicated as dotted lines. (B) Frequency domain 2PESEEM spectrum of <b>M<sub>2</sub></b> (red line) and <b>E<sub>2</sub></b> (blue line). The inset is a Zoom-in for the frequency range 0-1 MHz. The dipolar coupling frequency of ~0.49 MHz is translated into the distance in (A). ....	50
Figure 41. Geometric model used by PeldorFit. <sup>167</sup> .....	51
Figure 42. Background corrected Q-band PELDOR time traces acquired at different offsets (black lines) are overlaid with their PeldorFit <sup>167</sup> simulations (grey lines) for (A) <b>M<sub>2</sub></b> and (B) <b>E<sub>2</sub></b> . RMSD between experimental and simulated PELDOR time traces as a function of the geometric parameter of PeldorFit <sup>167</sup> for (C) <b>M<sub>2</sub></b> and (D) <b>E<sub>2</sub></b> . ....	52
Figure 43. Spin label attached to the base with the denoted angles $\chi_1$ and $\chi_2$ . ....	54
Figure 44. (A) PELDOR time trace of <b>E<sub>2</sub></b> with an 80 MHz offset in deuterated buffer at 50 K and (B) the corresponding distance distribution. ....	55
Figure 45. Plot of the maximum dipolar evolution time required for a reliable distance $r$ (Adapted from Reference 256). The marked data point corresponds to the maximal phase memory time of ~21 $\mu$ s obtained for <b>E<sub>2</sub></b> . ....	55
Figure 46. Stability decay curves of MTSL in ascorbate (green line) and HeLa extract (blue line), and <b>1*</b> attached to DNA in ascorbate (red line) and HeLa extract (purple line). ....	56

Figure 47. (A) Background corrected PELDOR time traces of **1\*** attached to the DNA duplex at 50 K in MBS buffer and (B) the corresponding distance distribution.

.....56

Figure 48. (A) RNA sequence of **P2**. Introduction of spin label **1\*** at the position marked with the bold “**U**” leads the spin labeled construct referred to as **P2U14**. (B) HPLC run of the unmodified RNA performed at room temperature (orange line) and with the column heated to 60 °C (black line). (C) HPLC run of the unmodified RNA (black line) and labeled RNA (red line) performed at 60 °C column temperature. (D) LCMS UV chromatogram at 254 nm and the deconvoluted ESI-mass shown as inlet of **P2U14**. The calculated mass  $M_{\text{calc}}(\mathbf{P2U14}) = 5443.10$  matched the found mass  $M_{\text{found}}(\mathbf{P2U14}) = 5467.71$ , which was assigned to  $[M+^{23}\text{Na}]^+$ . (E) CD spectra and (F) UV-VIS melting curves of the unmodified **P2unmod** (black line) and labeled **P2U14** (red line) in the presence of  $\text{Gdm}^+$ .  $T_m(\mathbf{P2unmod}) = 56.9$  °C and  $T_m(\mathbf{P2labeled}) = 50.0$  °C. (G) 15 % native PAGE analysis of **P2unmod** and **P2U14** prepared in the absence (-) and presence (+) of  $\text{Gdm}^+$  during the fast annealing, and without  $\text{Gdm}^+$  in the running buffer. (H) 15 % native PAGE analysis of **P2unmod** and **P2U14** prepared in the absence (-) and presence (+) of  $\text{Gdm}^+$  during the fast annealing, and with  $\text{Gdm}^+$  in the running buffer. “L” depicts the GeneRuler ultra low range DNA ladder (ThermoFisher) with the base pair sizes on the left. .58

Figure 49. (A) EDFS with assigned pump and detection position. (B) Offset measurements of **P2U14** in the presence of 40 mM  $\text{Gdm}^+$  with the offsets measurements marked in (A), where  $v_{\text{ab}} = 60$  MHz,  $v_{\text{ac}} = 80$  MHz,  $v_{\text{ad}} = 100$  MHz,  $v_{\text{be}} = 120$  MHz,  $v_{\text{af}} = 180$  MHz.....60

Figure 50. (A) Background corrected PELDOR time traces of **P2U14** in the absence (dark green line) and presence (red line) of  $\text{Gdm}^+$  and prepared with the Fast Annealing (FA). The fits are overlaid as grey or black dotted line, respectively. The modulation depths are indicated in percentages. (B) and (C) The corresponding distance distributions to the time traces in (A) shown as solid lines following the same color code as in (A). The *in silico* generated distance distribution is shown in orange. The structure used in MtsslWizard assigned to the distribution is shown next to it. ....60



- Figure 51. 25  $\mu\text{M}$  cwEPR measurements of **P2U14**. (A) The Fast Annealed (FA) RNA in the absence (- Gdm<sup>+</sup>, blue line) and presence (+ Gdm<sup>+</sup>, yellow line) of Gdm<sup>+</sup> and (D) the Slow Annealed (SA) RNA in the absence (- Gdm<sup>+</sup>, grey line) and presence (+ Gdm<sup>+</sup>, green line) of Gdm<sup>+</sup>. Spin counting revealed the following concentrations: FA: c(- Gdm<sup>+</sup>) = 23  $\mu\text{M}$  and c(+ Gdm<sup>+</sup>) = 27  $\mu\text{M}$ . SA: c(- Gdm<sup>+</sup>) = 23  $\mu\text{M}$  and c(+ Gdm<sup>+</sup>) = 24  $\mu\text{M}$ . ..... 62
- Figure 52. (A) Background corrected PELDOR time traces for the slowly annealed **P2U14** in the absence (dark green line) and presence (red line) of Gdm<sup>+</sup>. The fits are overlaid as grey or black dotted line, respectively. The modulation depths are indicated in percentages. (B) and (C) show the corresponding distance distributions to the time traces in (A) shown as solid lines following the same color code as in (A). The *in silico* generated distance distribution is shown in grey. The structure used in MtsslWizard assigned to the distribution is shown next to it. .... 62
- Figure 53. 15 % native PAGE of the unmodified **P2** RNA with the different annealings in absence and presence of Gdm<sup>+</sup>. The native PAGE was facilitated without Gdm<sup>+</sup> in the running buffer. .... 63
- Figure 54. 25  $\mu\text{M}$  circular dichroism spectroscopic measurements of the different annealed unmodified **P2** in absence and presence of Gdm<sup>+</sup>. .... 64
- Figure 55. Secondary structure of (A) the **P2** kissing hairpin and (B) the **P2** duplex. The point symmetric plane is visualized as grey line. (C)-(F) <sup>1</sup>H NMR spectra of the iminio region of the differently annealed samples in the absence and presence of Gdm<sup>+</sup>. The asterisk indicates an impurity of the NMR tube. .... 65
- Figure 56. **P2** <sup>1</sup>H NMR spectra of (A) the Fast annealed sample subsequent to <sup>14</sup>N-Gdm<sup>+</sup> addition and (B) of the Fast annealed sample subsequent to <sup>15</sup>N-Gdm<sup>+</sup> addition. .... 65
- Figure 57. Comparison of the <sup>1</sup>H NMR spectra of the <sup>14</sup>N-Gdm<sup>+</sup> (yellow line) and <sup>15</sup>N-Gdm<sup>+</sup> (red line) free in solution. .... 65
- Figure 58. **P2** <sup>1</sup>H NMR spectra of (A) the SA sample after addition of Gdm<sup>+</sup> and (B) of the reannealed sample. .... 66
- Figure 59. Comparison of the abundance of the events that the **P1** stem length is shorter (**P1**<**P2**), has the same length (**P1**=**P2**) or exceeds the **P2** stem length (**P1**>**P2**). .... 67

Figure 60. (A) RNA sequence of **P1**. Introduction of spin label **1\*** at the position marked with a bold “**U**” leads to the spin labeled construct referred to as **P1U18**. (B) HPLC run of the unmodified RNA (**P1unmod**) (black line) and the labeled RNA (**P1U18**) (red line) performed at 60 °C column temperature. (C) LCMS UV chromatogram and the deconvoluted ESI-mass of the labeled RNA shown as inset. The calculated mass  $M_{\text{calc}}(\mathbf{P1U18}) = 7365.23$  matched the found mass  $M_{\text{found}}(\mathbf{P1U18}) = 7428.44$ , which was assigned to  $[M+^{23}\text{Na}+^{39}\text{K}]^+$ . (D) 25  $\mu\text{M}$  cwEPR spectra in the absence (black line) and presence (red line) of  $\text{Gdm}^+$ . Spin counting revealed the following concentrations:  $c(-\text{Gdm}^+) = 26 \mu\text{M}$  and  $c(+\text{Gdm}^+) = 21 \mu\text{M}$ . (E) UV-VIS melting curve of **P1unmod** (black line) and **P1U18** (red line) RNA in the presence of  $\text{Gdm}^+$ .  $T_m(\mathbf{P1unmod}) = 51.0 \text{ }^\circ\text{C}$  and  $T_m(\mathbf{P1U18}) = 54.4 \text{ }^\circ\text{C}$ . (F) CD spectra of **P1unmod** (black line) and **P1U18** (red line) in the presence of  $\text{Gdm}^+$ . (G) 15 % native PAGE analysis of **P1unmod** and **P1U18** prepared in the absence (-) and presence (+) of  $\text{Gdm}^+$  during the fast annealing, and without  $\text{Gdm}^+$  in the running buffer. (H) 15 % native PAGE analysis of **P1unmod** and **P1U18** prepared in the absence (-) and presence (+) of  $\text{Gdm}^+$  during the fast annealing, and with  $\text{Gdm}^+$  in the running buffer. “L” depicts the GeneRuler ultra low range DNA ladder (ThermoFisher) with the base pair sizes on the left. ....68

Figure 61. (A) Background corrected PELDOR time traces for **P1U18** in the absence (green line) and presence of 0.4 mM (blue line) and 40 mM (purple line)  $\text{Gdm}^+$ . The fits are overlaid as black dotted lines, respectively. The modulation depths are indicated in percentages. (B) and (C) The corresponding distance distributions to the time traces in (A) shown as solid lines following the same color code as in (A). The *in silico* generated distance distributions are shown as green and purple areas, respectively. The structure used in MtssiWizard assigned to the distribution is shown next to it. ....69

Figure 62. Gaussian fits of the normalized distance distributions corresponding to the PELDOR measurements of **P1U18** (solid lines) overlaid with the experimental measurements (dotted lines). ....70

Figure 63. (A) Secondary structure of **P1** forming the kissing hairpin.  $^1\text{H}$  NMR spectra of the iminio region (B) upon FA in the absence of  $\text{Gdm}^+$  and (C) in the presence of  $\text{Gdm}^+$ . (D) Secondary structure of the **P1** duplex.  $^1\text{H}$  NMR spectra of the iminio region (E) upon SA in the absence of  $\text{Gdm}^+$  and (F) after addition of  $\text{Gdm}^+$ . The asterisk indicates an impurity signal of the NMR tube. ....71

Figure 64. (A) Background corrected PELDOR time traces for **P2U14** mixed equivalently with **P1U18** in the absence (light grey line) and presence of 40 mM (black line)  $\text{Gdm}^+$ . The fits are overlaid as black or grey dotted lines, respectively. The modulation depths are indicated in percentages. (B) and (C) show the corresponding distance distributions to the time traces in (A) as solid lines following the same color code as in (A). The *in silico* generated distance distributions are shown as filled areas and follow the same color code as in Figure 50 and Figure 61. The structure used in MtsslWizard assigned to the respective distribution is shown next to it. .... 72

Figure 65. (A) RNA sequence of **P1**. Introduction of spin label **1\*** at the position marked with a bold "**U**" leads to the spin labeled construct referred to as **P1U20**. (B) LCMS UV chromatogram and the deconvoluted ESI<sup>-</sup>-mass of the labeled RNA shown as inset. The calculated mass  $M_{\text{calc}}(\mathbf{P1U20}) = 7365.23$  matched the found mass  $M_{\text{found}}(\mathbf{P1U20}) = 73647.26$ , which was assigned to  $[\text{M}+^1\text{H}]^+$ . (C) 25  $\mu\text{M}$  cwEPR spectra in the absence (black line) and presence (red line) of  $\text{Gdm}^+$ . Spin counting revealed the following concentrations:  $c(-\text{Gdm}^+) = 25 \mu\text{M}$  and  $c(+\text{Gdm}^+) = 22 \mu\text{M}$ . (D) UV-VIS melting curve of the unmodified (black line) and labeled (red line) RNA in the presence of  $\text{Gdm}^+$ .  $T_m(\mathbf{P1unmod}) = 51.0 \text{ }^\circ\text{C}$  and  $T_m(\mathbf{P1U20}) = 51.7 \text{ }^\circ\text{C}$ . (E) 15 % native PAGE analysis for **P1unmod**, **P1U18** and **P1U20** prepared in the absence (-) and presence (+) of  $\text{Gdm}^+$  during the fast annealing, and without  $\text{Gdm}^+$  in the running buffer. (F) 15 % native PAGE analysis for **P1unmod**, **P1U18** and **P1U20** prepared in the absence (-) and presence (+) of  $\text{Gdm}^+$  during the fast annealing, and with  $\text{Gdm}^+$  in the running buffer. "L" depicts the GeneRuler ultra low range DNA ladder (ThermoFisher) with the base pair sizes on the left. .... 73

Figure 66. (A) Background corrected PELDOR time traces for **P1U20** in the absence (purple line) and presence (blue line) of  $\text{Gdm}^+$ . The fits are overlaid as black dotted lines. The modulation depths are indicated in percentages. (B) and (C) show the distance distributions corresponding to the time traces in (A) as solid lines following the same color code as in (A). The fully shaded shapes are the distance distributions derived from MtsslWizard. The structure assigned to the distribution is shown next to it. .... 75

Figure 67. (A) Background corrected PELDOR time traces for the 1:1 mixture of **P1U20 | P2U14** in the absence (olive line) and presence (green line) of  $\text{Gdm}^+$ . The fits are overlaid as black dotted lines. The modulation depths are indicated in percentages. (B) and (C) show the distance distributions corresponding to the time traces in (A) as solid lines following the same color code as in (A). The fully shaded shapes are the distance distributions derived from MtssWizard. The structure assigned to the distribution is shown next to it. ....76

Figure 68. Gaussian fitted peaks corresponding to the distance distribution obtained of **P1U20 | P2U14** in presence of  $\text{Gdm}^+$ . ....76

Figure 69. (A) Proposed switching mechanism of the Guanidine-II riboswitch with the base sequence used in this analysis (the representation is based on reference 48). (B) Overview of the modifications and the corresponding abbreviations of the RNA sequences. If it reads “unmod”, the strand is not labeled. The subscripts “1” or “2” denotes if the spin labeled position is in hairpin **P1** and/or **P2**. The subscript “Full” shows that it is the full-length construct. The superscript denotes the base that is spin labeled. If it is “**UX = U**”, the designated base is a natural uridine. If it is “**UX = U + 1**”, the mentioned base was spin labeled with **1**. ....78

Figure 70. Characterization of the singly labeled full-length constructs. **Top part left panel:** UV-VIS chromatograms. **Top part right panel:** Deconvoluted masses. **Bottom part:** cwEPR spectra in the absence (red line) and in the presence of  $\text{Gdm}^+$  (black line). (A) and (D) **P1,FullU24**, (B) and (E) **P1,FullU26** and (C) and (E) **P2,FullU55**. It was not possible to obtain a deconvoluted mass for **P1,FullU26**, thus the raw spectrum is shown. For the discussion, see the text. The calculated mass is  $M_{\text{calc}}(\text{PX,FullUX}) = 19186.28$ . Spin counting concentrations are given in Table 10. ....79

Figure 71. MALDI TOF<sup>+</sup> spectra. (A) 100  $\mu\text{M}$  **PFullunmod** in  $\text{H}_2\text{O}$ . (B) 1  $\mu\text{M}$  **PFullunmod** in  $\text{H}_2\text{O}$ . (C) 7  $\mu\text{M}$  **P1,FullU26** in Folding Buffer. (D) 19  $\mu\text{M}$  **PFullunmod** in Folding Buffer.  $M_{\text{calc}}(\text{PFullunmod}): [\text{M}]^+ = 18892.36$ .  $M_{\text{found}}(\text{PFullunmod}): [\text{M}]^+ = 18882.6$ ,  $[\text{M}]^{2+} = 9444.5$ ,  $[\text{M}]^{3+} = 6294.3$ .  $M_{\text{calc}}(\text{P1,FullU26}): [\text{M}]^+ = 19186.28$ . ....80

Figure 72. (A) CD spectra of **PFullunmod** (black line), **P1,FullU24** (blue line) and **P2,FullU55** (red line) in presence of 40 mM  $\text{Gdm}^+$ . (B) UV-VIS melting curves with the same color code as shown in (A) in presence of 40 mM  $\text{Gdm}^+$ . ....81

- Figure 73. 15% Native PAGE analysis of the singly labeled full-length constructs without Gdm<sup>+</sup> in the running buffer in the absence (-) and presence (+) of 40 mM Gdm<sup>+</sup> “L” depicts the GeneRuler ultra low range DNA ladder (ThermoFisher) with the base pair sizes on the left. .... 82
- Figure 74. Illustration of the (A) intrastrand and (B)-(F) potential interstrand interactions of the Guanidine-II riboswitch. .... 83
- Figure 75. **Left panel** PELDOR time traces and **right panel** distance distributions for (A) and (B) **P1,FullU24**, (C) and (D) **P1,FullU26** and (E) and (F) **P2,FullU55**. **Top panel:** (A) Background corrected PELDOR time traces for **P1,FullU24** in the absence (green line) and presence (dark blue line) of Gdm<sup>+</sup>. The fits are overlaid as black dotted lines. The modulation depths are indicated in percentages. (B) shows the distance distributions corresponding to the time traces in (A) as solid lines following the same color code as in (A). **Middle panel:** (C) Background corrected PELDOR time traces for **P1,FullU26** in the absence (light blue line) and presence (blue line) of Gdm<sup>+</sup>. The fits are overlaid as black dotted lines. The modulation depths are indicated in percentages. (D) shows the distance distributions corresponding to the time traces in (C) as solid lines following the same color code as in (C). **Bottom Panel:** (E) Background corrected PELDOR time traces for **P2,FullU55**. in the absence (dark green line) and presence (red line) of Gdm<sup>+</sup>. The fits are overlaid as black dotted lines. The modulation depths are indicated in percentages. (F) shows the distance distributions corresponding to the time traces in (E) as solid lines following the same color code as in (E). .... 84
- Figure 76. (A) Background corrected PELDOR time traces for the 80 MHz offset of 25 μM (red line) and 12.5 μM (yellow line) **P2,FullU55** in the presence of Gdm<sup>+</sup>. The fits are overlaid as black dotted lines. The modulation depths are indicated in percentages. (B) shows the distance distributions corresponding to the time traces in (A) as solid lines following the same color code as in (A). .... 85

Figure 77. Characterization of the doubly labeled full-length constructs. **Top part left panel:** UV-VIS chromatograms. **Top part right panel:** Deconvoluted masses. **Bottom part:** cwEPR spectra in the absence (red line) and in the presence of Gdm<sup>+</sup> (black line). (A) and (C) **P1,2,FullIU24U55**, (B) and (D) **P1,2,FullIU26U55**. It was not possible to obtain a deconvoluted mass for **P1,2,FullIU26U55**, thus the raw spectrum is shown. For the discussion, see the text. The calculated masses are  $M_{\text{calc}}(\mathbf{P1,2,FullIU24U55}) = M_{\text{calc}}(\mathbf{P1,2,FullIU26U55}) = 19480.20$ . Spin counting concentrations are given in Table 11.....86

Figure 78. 15% Native PAGE analysis of the doubly labeled full-length constructs without Gdm<sup>+</sup> in the running buffer in the absence (-) and presence (+) of 40 mM Gdm<sup>+</sup> “L” depicts the GeneRuler ultra low range DNA ladder (ThermoFisher) with the base pair sizes on the left. ....87

Figure 79. (A) Background corrected PELDOR time traces for **P1,2,FullIU24U55** in the absence (purple line) and presence (light blue line) of Gdm<sup>+</sup>. The fits are overlaid as black dotted lines. The modulation depths are indicated in percentages. (B) shows the distance distributions corresponding to the time traces in (A) as solid lines following the same color code as in (A). ....88

Figure 80. (A) Background corrected PELDOR time traces for **P1,2,FullIU24U55** of 25 μM (light blue line) and 12.5 μM (dark blue line) in the presence of Gdm<sup>+</sup>. The fits are overlaid as black and grey dotted lines, respectively. The modulation depths are indicated in percentages. (B) shows the distance distributions corresponding to the time traces in (A) as solid lines following the same color code as in (A). ....89

Figure 81. (A) Background corrected PELDOR time traces for **P1,2,FullIU26U55** in the absence (light purple line) and presence (light green line) of Gdm<sup>+</sup>. The fits are overlaid as black dotted lines. The modulation depths are indicated in percentages. (B) shows the distance distributions corresponding to the time traces in (A) as solid lines following the same color code as in (A). ....89

Figure 82. (A) Background corrected PELDOR time traces for **P1,2,FullIU26U55** of 36 μM (light green line), 13 μM (green line) and 2 μM (black line) in the presence of Gdm<sup>+</sup>. The fits are overlaid as black or grey dotted lines, respectively. (B) shows the distance distributions corresponding to the time traces in (A) as solid lines following the same color code as in (A). ....90

- Figure 83. (A) Background corrected PELDOR time traces for **P1,FullIU26** mixed equivalently with **P2,FullIU55** in the absence (dark red line) and presence of 40 mM (light green line)  $Gdm^+$ . The fits are overlaid as black dotted lines. The modulation depths are indicated in percentages. (B) shows the corresponding distance distributions to the time traces in (A) as solid lines following the same color code as in (A). ..... 91
- Figure 84. Cross interactions, which might contribute to the PELDOR measurement. 91
- Figure 85. Overview of the abundance of a certain linker length in nt. .... 94
- Figure 86. Overview about the abundance that the estimated linker length is either smaller ( $Linker < P1 + P2$ ), has the same size ( $Linker = P1 + P2$ ) or exceed the estimated length of the kissing hairpin ( $Linker > P1 + P2$ ). ..... 95
- Figure 87. Proposed switching mechanism of the Guanidine-II riboswitch with the base sequence used in this study and additional SDS (the representation is based on reference 48). The bold "X" represents the spin labeling position. .... 97
- Figure 88. (A) HPLC Run of the unmodified RNA (black line) and labeled RNA (red line) performed at 60 °C column temperature. (B) cwEPR spectrum of **PSDSU35U57** in the absence (yellow line) and presence (purple line) of  $Gdm^+$ . (C) 15% native PAGE analysis without  $Gdm^+$  in the running buffer in the absence (-) and presence (+) of  $Gdm^+$  for **PSDSunmod** and **PSDSU35U57**. "L" depicts the GeneRuler ultra low range DNA ladder (ThermoFisher) with the base pair sizes on the left. .... 98
- Figure 89. (A) Background corrected PELDOR time traces for **PSDSU35U57** in the absence (yellow line) and presence (purple line) of  $Gdm^+$ . The fits are overlaid as black or grey dotted lines, respectively. The modulation depths are indicated in percentages. (B) shows the distance distributions corresponding to the time traces in (A) as solid lines following the same color code as in (A). .... 99
- Figure 90. cwEPR spectrum of a reference  $Mn^{2+}$  measurement (green line) and the same concentrated  $Mn^{2+}$  binding to the Dzwt:RNA complex (black line). .... 100
- Figure 91. cwEPR  $Mn^{2+}$  titration data analysis. (A) Raw spectrum. (B) Single integrated spectrum. (C) Baseline corrected single integrated spectrum. (D) Double integrated spectrum. .... 103

Figure 92. Plot of the corrected double integral against the titrated $Mn^{2+}$ of a reference solution (green line) and an exemplary DNAzyme:RNA complex (black line). .....	103
Figure 93. $Mn^{2+}$ binding isotherms for 40 $\mu M$ Dzwt:RNA complex (A) in the absence of NaCl, (B) in the presence of 100 mM NaCl and (C) in the presence of 1000 mM NaCl.....	104
Figure 94. $Mn^{2+}$ binding isotherms for 40 $\mu M$ Dz <sup>5C</sup> :RNA complex in the presence of 100 mM NaCl analyzed with <b>left panel</b> : the non-cooperative fit and <b>right panel</b> : a cooperative fit in the concentration range of (A) and (B) 0-0.5 mM, and (C) and (D) 0-6.5 mM of free $Mn^{2+}$ .....	105
Figure 95 Double Integral vs concentration of the respective divalent metal ion. In black the sample of (A) containing 40 $\mu M$ Dz <sup>5C</sup> :RNA complex and 100 mM NaCl titrated with $Mn^{2+}$ , in blue the reference $Mn^{2+}$ measurement, and in red the sample containing 40 $\mu M$ Dz5C:RNA complex, 100 mM NaCl, 600 $\mu M$ $Mn^{2+}$ titrated with $Mg^{2+}$ .....	106
Figure 96. Conclusion regarding the truncated hairpins <b>P1</b> and <b>P2</b> . Binding of $Gdm^+$ (red triangle) was found to form hetero kissing hairpins alongside of homo kissing hairpins in a statistical 1:2:1 fashion. ....	108
Figure 97. Conclusion regarding the full-length Guanidine-II riboswitch. Intrastrand and interstrand interaction of the hetero kissing hairpins could not be distinguished. ....	108
Figure 98. Linear regression of the absorbance at 260 nm of spin label <b>1*</b> plotted against the respective concentration. ....	111
Figure 99. HPLC spectra of the Guanidine-II riboswitch constructs. ....	129
Figure 100. LCMS spectra of the Guanidine-II riboswitch constructs.....	131
Figure 101. 15% Native PAGEs of the full-length constructs in the absence (-) or presence of 40 mM (+) $Gdm^+$ . The ladder is denoted as "L". The respective band sizes are shown in (A). In (C) and (D) the $Gdm^+$ concentrations is varied as depicted. ....	132
Figure 102. cwEPR spectra of the Guanidine-II riboswitch constructs. ....	135
Figure 103. EDFS and marked pump and detection position of the offset measurements conducted on the guanidine-II riboswitch constructs. ....	147



- Figure 104. Raw Data of the offset measurements in absence and presence of  $\text{Gdm}^+$ .  
 (A) **P1U18**, (B) **P1U20**, (C) **P2U14**, (D) **P1U18** mixed 1:1 with **P2U14** and (E) **P1U20** mixed 1:1 with **P2U14**. ..... 148
- Figure 105. Raw Data of the offset measurements in absence and presence of  $\text{Gdm}^+$ .  
 (A) **P1,FullU24**, (B) **P1,FullU26**, (C) **P2,FullU55**, (D) **P1,FullU26** mixed 1:1 with **P2,FullU55**. ..... 149
- Figure 106. Raw Data of the offset measurements in absence and presence of  $\text{Gdm}^+$ , and with different spin concentration as denoted. (A) **P1,2,FullU24U55**, (B) **P1,2,FullU26U55**, and (C) **PSDSU35U57**. ..... 150
- Figure 107. Data Analysis of the summed PELDOR time traces of (A)  $\mathbf{M}_2$  and  $\mathbf{E}_2$ , and (B) the 80 MHz offsets of  $\mathbf{E}_2$  measured with the long acquisition window of 20  $\mu\text{s}$ . (I) Uncorrected PELDOR time traces with the intermolecular background function. (II) Background corrected PELDOR time traces with overlaid fit (dotted black line). (III) PELDOR-derived distance distributions. (IV) and (V): The corresponding L-curves. .... 151
- Figure 108. Data Analysis of the summed PELDOR time traces in the absence and presence of  $\text{Gdm}^+$  for (A) **P1U18**, (B) **P1U20** and (C) **P2U14**. (I) Uncorrected PELDOR time traces with the intermolecular background function. (II) Background corrected PELDOR time traces with overlaid fit (dotted black or grey line). (III) PELDOR-derived distance distributions. (IV)-(VI): The corresponding L-curves. .... 152
- Figure 109. Data Analysis of the summed PELDOR time traces in absence and presence of  $\text{Gdm}^+$ . (A) **P1U18** mixed 1:1 with **P2U14** and (B) **P1U20** mixed 1:1 with **P2U14**. (I) Uncorrected PELDOR time traces with the intermolecular background function. (II) Background corrected PELDOR time traces with fit overlaid (dotted black or grey line). (III) PELDOR-derived distance distributions. (IV)-(VI), the corresponding L-curves. .... 153
- Figure 110. Data Analysis of the summed PELDOR time traces in absence and presence of  $\text{Gdm}^+$ . (A) **P1,FullU24**, (B) **P1,FullU26** and (C) **P2,FullU55**. (I) Uncorrected PELDOR time traces with the intermolecular background function. (II) Background corrected PELDOR time traces with fit overlaid (dotted black or grey line). (III) PELDOR-derived distance distributions. (IV) and (V), the corresponding L-curves. .... 154

- Figure 111. Data Analysis of the summed PELDOR time traces in absence and presence of Gdm<sup>+</sup>, (A) **P1,2,FullU24U55** and (B) **P1,2,FullU26U55**. (C) Data Analysis of the summed PELDOR time traces in the presence of Gdm<sup>+</sup> **P1,2,FullU26U55** diluted to 13 μM and 2 μM spins. (I) Uncorrected PELDOR time traces with the intermolecular background function. (II) Background corrected PELDOR time trace with fit overlaid (dotted black or grey line). (III) PELDOR derived distance distributions. (IV) and (V), the corresponding L-curves. .... 155
- Figure 112. Data Analysis of the summed PELDOR time traces for **P1,2,FullU26U55**. In the presence of Gdm<sup>+</sup> analyzed (A) without ghost peak suppression and (B) with ghost peak suppression (I) Uncorrected PELDOR time traces with the intermolecular background function. (II) Background corrected PELDOR time trace with fit overlaid (dotted black or grey line). (III) PELDOR derived distance distributions. (IV) and (V), the corresponding L-curves. .... 156
- Figure 113. Data Analysis of the summed PELDOR time traces in absence (yellow line) and presence (purple line) of Gdm<sup>+</sup> of **PSDSU35U57**. (I) Uncorrected PELDOR time traces with the intermolecular background function. (II) Background corrected PELDOR time trace with fit overlaid (dotted black line). (III) PELDOR derived distance distributions. (IV) and (V), the corresponding L-curves. ... 157
- Figure 114. PELDOR data validation of the truncated hairpins. .... 158
- Figure 115. PELDOR data validation of the singly labeled full-length construct. .... 159
- Figure 116. PELDOR data validation of the doubly labeled full-length construct. .... 160
- Figure 117. PELDOR data validation of the doubly labeled full-length construct with additional SDS. .... 160
- Figure 118. Predicted distance distributions via in silico spin labeling with MtssiWizard overlaid with the measured main distances as stick representation in absence and presence of Gdm<sup>+</sup> for (A) and (B) **P1U18**, (C) and (D) **P2U14**, and (E) and (F) **P1U18** mixed 1:1 with **P2U14**. The respective structure with the spin label rotamers is shown next to it. .... 161
- Figure 119. Predicted distance distributions via in silico spin labeling with MtssiWizard overlaid with the measured main distances as stick representation in absence and presence of Gdm<sup>+</sup> for (A) and (B) **P1U20**, (C) and (D) **P2U14**, and (E) and (F) **P1U20** mixed 1:1 with **P2U14**. The respective structure with the spin label rotamers is shown next to it. .... 162

## 6.12 List of tables

Table 1. Fitted parameters of the 2PESEEM traces of <b>M<sub>2</sub></b> and <b>E<sub>2</sub></b> in dependence of the temperature.....	45
Table 2. Fitting parameters of the 2PESEEM decay curves of <b>M<sub>2</sub></b> and <b>E<sub>2</sub></b> in dependence of the solvent.....	47
Table 3. Notation of the frequency offsets shown in Figure 39. ....	50
Table 4. Geometric parameters of the PeldorFit <sup>167</sup> analysis of <b>M<sub>2</sub></b> and <b>E<sub>2</sub></b> . ....	52
Table 5. Comparison of the three methods receiving the interspin distance of the two spin labels for <b>M<sub>2</sub></b> and <b>E<sub>2</sub></b> i.e., the analysis with DeerAnalysis <sup>275</sup> of the summed PELDOR time traces, the translation of the dipolar coupling frequency obtained in the 2PESEEM spectrum, and the analysis with PeldorFit. <sup>167</sup> .....	53
Table 6. Comparison of the PeldorFit <sup>167</sup> data for <b>M<sub>2</sub></b> and <b>E<sub>2</sub></b> with the parameters from their <i>in silico</i> generated models. ....	54
Table 7. Results of the amplitude based analysis corresponding to the distance distribution obtained of <b>P1U20</b>   <b>P2U14</b> in presence of Gdm <sup>+</sup> .....	77
Table 8. Results of the Gaussian Fit based analysis corresponding to the distance distribution obtained of <b>P1U20</b>   <b>P2U14</b> in presence of Gdm <sup>+</sup> .....	77
Table 9. Spin concentrations of the singly labeled full-length constructs.....	81
Table 10. Spin concentrations of the doubly labeled full-length constructs. ....	87
Table 11. Overview of the number of nt per linker. ....	92
Table 12. Overview of the measured 5' hydroxy distance of the duplex. ....	94
Table 13. Overview of the estimated linker length. ....	94
Table 14. Overview of the number of nt per <b>P1</b> and <b>P2</b> stem.....	94
Table 15. Overview of the measured distance stretched by the conserved GG ACGA CC binding pocket region.....	95
Table 16. Overview of the distance estimation connected to the specific sequence used in this study. ....	96
Table 17. List of the RNA constructs used in this study. The marked <b>X</b> depicted the 5-deoxy-2'-ethynyl-Uridine, thus the spin labeling position. ....	110
Table 18. Extinction coefficients of the RNA constructs. ....	111

Table 19. HPLC Methods.....	113
Table 20. List of buffers.....	114
Table 21. Amounts of RNA and staining procedure employed for the native PAGE analysis.....	118
Table 22. RNA concentrations for the cwEPR measurements of the Guanidine-II constructs. ....	119
Table 23. PELDOR spin concentrations of the Guanidine-II constructs. ....	123
Table 24. Spectroscopic parameters used for PeldorFit. ....	125
Table 25. Geometric parameters used for PeldorFit. ....	125
Table 26. Overview of the riboswitch ligands and their abbreviations utilized in Figure 5. ....	128
Table 27. Spin labeling yields. ....	130
Table 28. List of the spin countings of the cwEPR spectra of the Guanidine-II riboswitch constructs. ....	134
Table 29. Summary of the PeldorFit results for <b>M<sub>2</sub></b> . <sup>167</sup> ....	136
Table 30. Summary of the PeldorFit results for <b>E<sub>2</sub></b> . <sup>167</sup> ....	137
Table 31. Overview of the offset measurements conducted on the Guanidine-II riboswitch constructs. The color code corresponds to the following Figures. ....	147
Table 32. Overview about the data of the hairpin and linker length analysis. ....	163

---

## 7. References

- (1) World Health Organization. WHO announces COVID-19 outbreak a pandemic. <https://www.euro.who.int/en/health-topics/health-emergencies/coronavirus-covid-19/news/news/2020/3/who-announces-covid-19-outbreak-a-pandemic>. **2020**.
- (2) World Health Organization. DRAFT landscape of COVID-19 candidate vaccines - 9 September 2020. <https://www.who.int/publications/m/item/draft-landscape-of-covid-19-candidate-vaccines>. **2020**.
- (3) Alberts, B.; Johnson, A.; Lewis, J.; Morgan, D.; Raff, M.; Roberts, K.; Walter, P. *Molecular Biology of the Cell*, Sixth edition; Garland Science Taylor and Francis Group: New York, NY, Abingdon, UK **2014**.
- (4) Crick, F. H. C. On protein synthesis. *Symposia of the Society for Experimental Biology*. **1958**, *12*, 138–163.
- (5) Crick, F. Central dogma of molecular biology. *Nature*. **1970**, *227*, 561–563.
- (6) Westhof, E.; Auffinger, P. RNA Tertiary Structure. In *Encyclopedia of Analytical Chemistry*; Meyers, R. A., Ed.; John Wiley & Sons, Ltd: Chichester, UK **2006**.
- (7) Klostermeier, D.; Hammann, C., Eds. *RNA Structure and Folding: Biophysical Techniques and Prediction Methods*; De Gruyter: Berlin/Boston **2013**.
- (8) Carell, T.; Brandmayr, C.; Hienzsch, A.; Müller, M.; Pearson, D.; Reiter, V.; Thoma, I.; Thumbs, P.; Wagner, M. Structure and function of noncanonical nucleobases. *Angewandte Chemie International Edition*. **2012**, *51*, 7110–7131.
- (9) Barrick, J. E.; Breaker, R. R. The distributions, mechanisms, and structures of metabolite-binding riboswitches. *Genome Biology*. **2007**, *8*, 1–8.
- (10) Breaker, R. R. Riboswitches and the RNA world. *Cold Spring Harbor Perspectives in Biology*. **2012**, *4*, 1–15.
- (11) Breaker, R. R. Riboswitches and Translation Control. *Cold Spring Harbor Perspectives in Biology*. **2018**, *10*, 1–14.
- (12) Breaker, R. R. Imaginary Ribozymes. *ACS Chemical Biology*. **2020**, *15*, 2020-2030.
- (13) Garst, A. D.; Edwards, A. L.; Batey, R. T. Riboswitches: structures and mechanisms. *Cold Spring Harbor Perspectives in Biology*. **2011**, *3*, 1–13.
- (14) Lotz, T. S.; Suess, B. Small-Molecule-Binding Riboswitches. *Microbiology Spectrum*. **2018**, *6*, 1–12.

- (15) Serganov, A.; Nudler, E. A Decade of Riboswitches. *Cell*. **2013**, *152*, 17–24.
- (16) Sherlock, M. E.; Breaker, R. R. Former orphan riboswitches reveal unexplored areas of bacterial metabolism, signaling, and gene control processes. *RNA*. **2020**, *26*, 675–693.
- (17) McCown, P. J.; Corbino, K. A.; Stav, S.; Sherlock, M. E.; Breaker, R. R. Riboswitch diversity and distribution. *RNA*. **2017**, *23*, 995–1011.
- (18) Mandal, M.; Breaker, R. R. Gene Regulation by Riboswitches. *Nature Reviews. Molecular Cell Biology*. **2004**, *5*, 451–463.
- (19) Wilson, K. S.; Hippel, P. H. von. Transcription termination at intrinsic terminators: the role of the RNA hairpin. *Proceedings of the National Academy of Sciences of the United States of America*. **1995**, *92*, 8793–8797.
- (20) Winkler, W. C.; Cohen-Chalamish, S.; Breaker, R. R. An mRNA structure that controls gene expression by binding FMN. *Proceedings of the National Academy of Sciences of the United States of America*. **2002**, *99*, 15908–15913.
- (21) Cheng, H.; Bjerknes, M.; Kumar, R.; Jay, E. Determination of the optimal aligned spacing between the Shine-Dalgarno sequence and the translation initiation codon of Ecoli mRNAs. *Nucleic Acids Research*. **1994**, *22*, 4953–4957.
- (22) Ringquist, S.; Shinedling, S.; Barrick, D.; Green, L.; Binkley, J.; Stormo, G. D.; Gold, L. Translation initiation in Escherichia coli: sequences within the ribosome-binding site. *Molecular Microbiology*. **1992**, *6*, 1219–1229.
- (23) Mironov, A. S.; Gusarov, I.; Rafikov, R.; Lopez, L. E.; Shatalin, K.; Kreneva, Rimma, A.; Perumov, D. A.; Nudler, E. Sensing Small Molecules by Nascent RNA: A Mechanism to Control Transcription in Bacteria. *Cell*. **2002**, *111*, 747–756.
- (24) Nahvi, A.; Sudarsan, N.; Ebert, Margaret, S.; Zou, X.; Brown, K. L.; Breaker, R. R. Genetic Control by a Metabolite Binding mRNA. *Chemistry & Biology*. **2002**, *9*, 1043–1049.
- (25) Winkler, W.; Nahvi, A.; Breaker, R. R. Thiamine derivatives bind messenger RNAs directly to regulate bacterial gene expression. *Nature*. **2002**, *419*, 952–956.
- (26) Gelfand, M. S.; Mironov, A. A.; Jomantas, J.; Kozolov, Y. I.; Perumov, D. A. A conserved RNA structure element involved in the regulation of bacterial riboflavin synthesis genes. *Trends in Genetics*. **1999**, *15*, 439–442.

- (27) Kil, Y. V.; Mironov, V. N.; Gorishin, I. Y.; Kreneva, R. A.; Perumov, D. A. Riboflavin operon of *Bacillus subtilis*: unusual symmetric arrangement of the regulatory region. *Molecular and General Genetics*. **1992**, *233*, 483–486.
- (28) Miranda-Ríos, J.; Navarro, M.; Soberón, M. A conserved RNA structure (thi box) is involved in regulation of thiamin biosynthetic gene expression in bacteria. *Proceedings of the National Academy of Sciences of the United States of America*. **2001**, *98*, 9736–9741.
- (29) Nou, X.; Kadner, R. J. Coupled changes in translation and transcription during cobalamin-dependent regulation of *btuB* expression in *Escherichia coli*. *Journal of Bacteriology*. **1998**, *180*, 6719–6728.
- (30) Stormo, G. D.; Ji, Y. Do mRNAs act as direct sensors of small molecules to control their expression? *Proceedings of the National Academy of Sciences of the United States of America*. **2001**, *98*, 9465–9467.
- (31) Panchapakesan, S. S. S.; Breaker, R. R. The case of the missing allosteric ribozymes. *Nature Chemical Biology*. **2021**, DOI 10.1038/s41589-020-00713-2.
- (32) Serganov, A.; Polonskaia, A.; Phan, A. T.; Breaker, R. R.; Patel, D. J. Structural basis for gene regulation by a thiamine pyrophosphate-sensing riboswitch. *Nature*. **2006**, *441*, 1167–1171.
- (33) Thore, S.; Leibundgut, M.; Ban, N. Structure of the Eukaryotic Thiamine Pyrophosphate Riboswitch with Its Regulatory Ligand. *Science*. **2006**, *312*, 1208–1211.
- (34) Cheah, M. T.; Wachter, A.; Sudarsan, N.; Breaker, R. R. Control of alternative RNA splicing and gene expression by eukaryotic riboswitches. *Nature*. **2007**, *447*, 497–500.
- (35) Croft, M. T.; Moulin, M.; Webb, M. E.; Smith, A. G. Thiamine biosynthesis in algae is regulated by riboswitches. *Proceedings of the National Academy of Sciences of the United States of America*. **2007**, *104*, 20770–20775.
- (36) Sudarsan, N.; Barrick, J. E.; Breaker, R. R. Metabolite-binding RNA domains are present in the genes of eukaryotes. *RNA*. **2003**, *9*, 644–647.
- (37) Ren, A.; Rajashankar, K. R.; Patel, D. J. Fluoride ion encapsulation by Mg<sup>2+</sup> ions and phosphates in a fluoride riboswitch. *Nature*. **2012**, *486*, 85–89.
- (38) Collins, J. A.; Irnov, I.; Baker, S.; Winkler, W. C. Mechanism of mRNA destabilization by the *glmS* ribozyme. *Genes & Development*. **2007**, *21*, 3356–3368.

- (39) Barrick, J. E.; Corbino, K. A.; Winkler, W. C.; Nahvi, A.; Mandal, M.; Collins, J.; Lee, M.; Roth, A.; Sudarsan, N.; Jona, I.; *et al.* New RNA motifs suggest an expanded scope for riboswitches in bacterial genetic control. *Proceedings of the National Academy of Sciences of the United States of America*. **2004**, *101*, 6421–6426.
- (40) Nelson, J. W.; Atilho, R. M.; Sherlock, M. E.; Stockbridge, R. B.; Breaker, R. R. Metabolism of Free Guanidine in Bacteria Is Regulated by a Widespread Riboswitch Class. *Molecular Cell*. **2017**, *65*, 220–230.
- (41) Kazanov, M. D.; Vitreschak, A. G.; Gelfand, M. S. Abundance and functional diversity of riboswitches in microbial communities. *BMC genomics*. **2007**, *8*, 1–9.
- (42) Meyer, M. M.; Hammond, M. C.; Salinas, Y.; Roth, A.; Sudarsan, N.; Breaker, R. R. Challenges of ligand identification for riboswitch candidates. *RNA Biology*. **2011**, *8*, 5–10.
- (43) Weinberg, Z.; Barrick, J. E.; Yao, Z.; Roth, A.; Kim, J. N.; Gore, J.; Wang, J. X.; Lee, E. R.; Block, K. F.; Sudarsan, N.; *et al.* Identification of 22 candidate structured RNAs in bacteria using the CMfinder comparative genomics pipeline. *Nucleic Acids Research*. **2007**, *35*, 4809–4819.
- (44) Weinberg, Z.; Wang, J. X.; Bogue, J.; Yang, J.; Corbino, K.; Moy, Ryan, H.; Breaker, Ronald, R. Comparative genomics reveals 104 candidate structured RNAs from bacteria, archaea, and their metagenomes. *Genome Biology*. **2010**, *11*, 1–17.
- (45) Battaglia, R. A.; Ke, A. Guanidine-sensing riboswitches: How do they work and what do they regulate? *Wiley Interdisciplinary Reviews. RNA*. **2018**, 1–10.
- (46) Sherlock, M. E.; Malkowski, S. N.; Breaker, R. R. Biochemical Validation of a Second Guanidine Riboswitch Class in Bacteria. *Biochemistry*. **2017**, *56*, 352–358.
- (47) Sherlock, M. E.; Breaker, R. R. Biochemical Validation of a Third Guanidine Riboswitch Class in Bacteria. *Biochemistry*. **2017**, *56*, 359–363.
- (48) Reiss, C. W.; Strobel, S. A. Structural basis for ligand binding to the guanidine-II riboswitch. *RNA*. **2017**, *23*, 1338–1343.
- (49) Huang, L.; Wang, J.; Lilley, D. M. J. The Structure of the Guanidine-II Riboswitch. *Cell Chemical Biology*. **2017**, *24*, 695–702.
- (50) Huang, L.; Wang, J.; Wilson, T. J.; Lilley, D. M. J. Structure-guided design of a high-affinity ligand for a riboswitch. *RNA*. **2019**, *25*, 423–430.



- (51) NobelPrize.org. The Nobel Prize in Chemistry 1989. Press release. <https://www.nobelprize.org/prizes/chemistry/1989/press-release>. **1989**.
- (52) Cech, T. R. The Ribosome Is a Ribozyme. *Science*. **2000**, *289*, 878–879.
- (53) Micura, R.; Höbartner, C. Fundamental studies of functional nucleic acids: aptamers, riboswitches, ribozymes and DNAzymes. *Chemical Society Reviews*. **2020**, *49*, 7331–7353.
- (54) Scott, W. G.; Horan, L. H.; Martick, M. The Hammerhead Ribozyme: Structure, Catalysis and Gene Regulation. *Progress in molecular biology and translational science*. **2013**, *120*, 1–23.
- (55) Ke, A.; Zhou, K.; Ding, F.; Cate, J. H. D.; Doudna, J. A. A conformational switch controls hepatitis delta virus ribozyme catalysis. *Nature*. **2004**, *429*, 201–205.
- (56) Ferré-D'Amaré, A. R.; Zhou, K.; Doudna, J. A. Crystal structure of a hepatitis delta virus ribozyme. *Nature*. **1998**, *395*, 567–574.
- (57) Liu, Y.; Wilson, T. J.; McPhee, S. A.; Lilley, D. M. J. Crystal structure and mechanistic investigation of the twister ribozyme. *Nature Chemical Biology*. **2014**, *10*, 739–744.
- (58) Klein, D. J.; Ferré-D'Amaré, A. R. Structural basis of glmS ribozyme activation by glucosamine-6-phosphate. *Science*. **2006**, *313*, 1752–1756.
- (59) Breaker, R. R.; Joyce, G. F. The expanding view of RNA and DNA function. *Chemistry & Biology*. **2014**, *21*, 1059–1065.
- (60) Wawrzyniak-Turek, K.; Höbartner, C. Deoxyribozyme-mediated ligation for incorporating EPR spin labels and reporter groups into RNA. *Methods in Enzymology*. **2014**, *549*, 85–104.
- (61) Rosenbach, H.; Victor, J.; Etkorn, M.; Steger, G.; Riesner, D.; Span, I. Molecular Features and Metal Ions That Influence 10-23 DNAzyme Activity. *Molecules*. **2020**, *25*, 1–25.
- (62) Breaker, R. R.; Joyce, G. F. A DNA enzyme that cleaves RNA. *Chemistry & Biology*. **1994**, *1*, 223–229.
- (63) Santoro, S. W.; Joyce, G. F. A general purpose RNA-cleaving DNA enzyme. *Proceedings of the National Academy of Sciences of the United States of America*. **1997**, *94*, 4262–4266.

- (64) Flynn-Charlebois, A.; Wang, Y.; Prior, T. K.; Rashid, I.; Hoadley, K. A.; Coppins, R. L.; Wolf, A. C.; Silverman, S. K. Deoxyribozymes with 2'-5' RNA ligase activity. *Journal of the American Chemical Society*. **2003**, *125*, 2444–2454.
- (65) Chandra, M.; Sachdeva, A.; Silverman, S. K. DNA-catalyzed sequence-specific hydrolysis of DNA. *Nature Chemical Biology*. **2009**, *5*, 718–720.
- (66) Cuenoud, B.; Szostak, J. W. A DNA metalloenzyme with DNA ligase activity. *Nature*. **1995**, *375*, 611–614.
- (67) Pradeepkumar, P. I.; Höbartner, C.; Baum, D. A.; Silverman, S. K. DNA-catalyzed formation of nucleopeptide linkages. *Angewandte Chemie (International ed. in English)*. **2008**, *47*, 1753–1757.
- (68) Chandra, M.; Silverman, S. K. DNA and RNA can be equally efficient catalysts for carbon-carbon bond formation. *Journal of the American Chemical Society*. **2008**, *130*, 2936–2937.
- (69) Dass, C. R.; Choong, P. F. M.; Khachigian, L. M. DNAzyme technology and cancer therapy: cleave and let die. *Molecular cancer therapeutics*. **2008**, *7*, 243–251.
- (70) Mathews, D. H.; Moss, W. N.; Turner, D. H. Folding and Finding RNA secondary structure. *Cold Spring Harbor Perspectives in Biology*. **2010**, *2*, a003665.
- (71) Tahi, F.; van T Tran; Boucheham, A. In Silico Prediction of RNA Secondary Structure. *Methods in Molecular Biology*. **2017**, *1543*, 145–168.
- (72) Zuker, M. Mfold web server for nucleic acid folding and hybridization prediction. *Nucleic Acids Research*. **2003**, *31*, 3406–3415.
- (73) Lorenz, R.; Bernhart, S. H.; Höner Zu Siederdisen, C.; Tafer, H.; Flamm, C.; Stadler, P. F.; Hofacker, I. L. ViennaRNA Package 2.0. *Algorithms for Molecular Biology*. **2011**, *6*, 26.
- (74) Reuter, J. S.; Mathews, D. H. RNAstructure: software for RNA secondary structure prediction and analysis. *BMC Bioinformatics*. **2010**, *11*, 129.
- (75) Kubota, M.; Tran, C.; Spitale, R. C. Progress and challenges for chemical probing of RNA structure inside living cells. *Nature Chemical Biology*. **2015**, *11*, 933–941.
- (76) Brunel, C.; Romby, P. Probing RNA Structure and RNA-Ligand Complexes with Chemical Probes. *Methods in Enzymology*. **2000**, *318*, 3–21.
- (77) Cressey, D.; Callaway, E. Cryo-electron microscopy wins chemistry Nobel. *Nature*. **2017**, *550*, 167.

- (78) NobelPrize.org. The Nobel Prize in Chemistry 2017. Press release. <https://www.nobelprize.org/prizes/chemistry/2017/press-release>. **2017**.
- (79) Cheng, Y. Single-particle cryo-EM-How did it get here and where will it go. *Science*. **2018**, *361*, 876–880.
- (80) Cheng, Y.; Grigorieff, N.; Penczek, P. A.; Walz, T. A primer to single-particle cryo-electron microscopy. *Cell*. **2015**, *161*, 438–449.
- (81) Kaledhonkar, S.; Fu, Z.; Caban, K.; Li, W.; Chen, B.; Sun, M.; Gonzalez, R. L.; Frank, J. Late steps in bacterial translation initiation visualized using time-resolved cryo-EM. *Nature*. **2019**, *570*, 400–404.
- (82) Kappel, K.; Zhang, K.; Su, Z.; Watkins, A. M.; Kladwang, W.; Li, S.; Pintilie, G.; Topkar, V. V.; Rangan, R.; Zheludev, I. N.; *et al.* Accelerated cryo-EM-guided determination of three-dimensional RNA-only structures. *Nature Methods*. **2020**, *17*, 699–707.
- (83) Berman, H.; Henrick, K.; Nakamura, H. Announcing the worldwide Protein Data Bank. *Nature Structural Biology*. **2003**, *10*, 980, can be found under <https://www ww pdb.org/>.
- (84) Baronti, L.; Karlsson, H.; Marušič, M.; Petzold, K. A guide to large-scale RNA sample preparation. *Analytical and Bioanalytical Chemistry*. **2018**, *410*, 3239–3252.
- (85) Reyes, Francis, E.; Garst, A. D.; Batey, R. T. Strategies in RNA Crystallography. *Methods in Enzymology*. **2009**, *6*, 119–139.
- (86) Boutet, S.; Fromme, P.; Hunter, M. S., Eds. *X-ray Free Electron Lasers: A Revolution in Structural Biology*; Springer International Publishing: Cham **2018**.
- (87) Hebert, H. CryoEM: a crystals to single particles round-trip. *Current Opinion in Structural Biology*. **2019**, *58*, 59–67.
- (88) Stagno, J. R.; Liu, Y.; Bhandari, Y. R.; Conrad, C. E.; Panja, S.; Swain, M.; Fan, L.; Nelson, G.; Li, C.; Wendel, D. R.; *et al.* Structures of riboswitch RNA reaction states by mix-and-inject XFEL serial crystallography. *Nature*. **2017**, *541*, 242–246.
- (89) Liu, H.; Spence, J. C. H. XFEL data analysis for structural biology. *Quantitative Biology*. **2016**, *4*, 159–176.
- (90) Marušič, M.; Schlagnitweit, J.; Petzold, K. RNA Dynamics by NMR Spectroscopy. *ChemBioChem*. **2019**, *20*, 2685–2710.

- (91) Schnieders, R.; Keyhani, S.; Schwalbe, H.; Fürtig, B. More than Proton Detection- New Avenues for NMR Spectroscopy of RNA. *Chemistry - A European Journal*. **2020**, *26*, 102–113.
- (92) Sakamoto, T.; Otsu, M.; Kawai, G. NMR Studies on RNA. In *Experimental Approaches of NMR Spectroscopy*; The Nuclear Magnetic Resonance Society of Japan, Ed.; Springer Singapore: Singapore **2018**; pp 439–459.
- (93) Fürtig, B.; Richter, C.; Wöhnert, J.; Schwalbe, H. NMR spectroscopy of RNA. *ChemBioChem*. **2003**, *4*, 936–962.
- (94) Hellenkamp, B.; Schmid, S.; Doroshenko, O.; Opanasyuk, O.; Kühnemuth, R.; Rezaei Adariani, S.; Ambrose, B.; Aznauryan, M.; Barth, A.; Birkedal, V.; *et al.* Precision and accuracy of single-molecule FRET measurements-a multi-laboratory benchmark study. *Nature Methods*. **2018**, *15*, 669–676.
- (95) Pietraszewska-Bogiel, A.; Gadella, T. W. J. FRET microscopy: from principle to routine technology in cell biology. *Journal of Microscopy*. **2011**, *241*, 111–118.
- (96) Coullomb, A.; Bidan, C. M.; Qian, C.; Wehnekamp, F.; Oddou, C.; Albigès-Rizo, C.; Lamb, D. C.; Dupont, A. QuantI-FRET: a framework for quantitative FRET measurements in living cells. *Scientific Reports*. **2020**, *10*, 1–11.
- (97) Haller, A.; Rieder, U.; Aigner, M.; Blanchard, S. C.; Micura, R. Conformational capture of the SAM-II riboswitch. *Nature Chemical Biology*. **2011**, *7*, 393–400.
- (98) Lemay, J.-F.; Penedo, J. C.; Tremblay, R.; Lilley, D. M. J.; Lafontaine, D. A. Folding of the Adenine Riboswitch. *Chemistry & Biology*. **2006**, *13*, 857–868.
- (99) Manz, C.; Kobitski, A. Y.; Samanta, A.; Keller, B. G.; Jäschke, A.; Nienhaus, G. U. Single-molecule FRET reveals the energy landscape of the full-length SAM-I riboswitch. *Nature Chemical Biology*. **2017**, *13*, 1172–1178.
- (100) Tippana, R.; Chen, M. C.; Demeshkina, N. A.; Ferré-D'Amaré, A. R.; Myong, S. RNA G-quadruplex is resolved by repetitive and ATP-dependent mechanism of DHX36. *Nature Communications*. **2019**, *10*, 1855.
- (101) Uhm, H.; Kang, W.; Ha, K. S.; Kang, C.; Hohng, S. Single-molecule FRET studies on the cotranscriptional folding of a thiamine pyrophosphate riboswitch. *Proceedings of the National Academy of Sciences of the United States of America*. **2018**, *115*, 331–336.

- (102) Warnasooriya, C.; Ling, C.; Belashov, I. A.; Salim, M.; Wedekind, J. E.; Ermolenko, D. N. Observation of preQ1-II riboswitch dynamics using single-molecule FRET. *RNA Biology*. **2019**, *16*, 1086–1092.
- (103) Albizu, L.; Cottet, M.; Kralikova, M.; Stoev, S.; Seyer, R.; Brabet, I.; Roux, T.; Bazin, H.; Bourrier, E.; Lamarque, L.; *et al.* Time-resolved FRET between GPCR ligands reveals oligomers in native tissues. *Nature Chemical Biology*. **2010**, *6*, 587–594.
- (104) Maurel, D.; Comps-Agrar, L.; Brock, C.; Rives, M.-L.; Bourrier, E.; Ayoub, M. A.; Bazin, H.; Tinel, N.; Durroux, T.; Prézeau, L.; *et al.* Cell-surface protein-protein interaction analysis with time-resolved FRET and snap-tag technologies: application to GPCR oligomerization. *Nature Methods*. **2008**, *5*, 561–567.
- (105) Xu, Q.-H.; Wang, S.; Korystov, D.; Mikhailovsky, A.; Bazan, G. C.; Moses, D.; Heeger, A. J. The fluorescence resonance energy transfer (FRET) gate: a time-resolved study. *Proceedings of the National Academy of Sciences of the United States of America*. **2005**, *102*, 530–535.
- (106) Sanabria, H.; Rodnin, D.; Hemmen, K.; Peulen, T.-O.; Felekyan, S.; Fleissner, M. R.; Dimura, M.; Koberling, F.; Kühnemuth, R.; Hubbell, W.; *et al.* Resolving dynamics and function of transient states in single enzyme molecules. *Nature Communications*. **2020**, *11*, 1231.
- (107) Jeschke, G. DEER Distance Measurements on Proteins. *Annual Review of Physical Chemistry*. **2012**, *63*, 419–446.
- (108) Hunsicker-Wang, L.; Vogt, M.; DeRose, V. J. EPR Methods to Study Specific Metal-Ion Binding Sites in RNA. *Methods in Enzymology*. **2009**, *468*, 335–367.
- (109) Abdullin, D.; Schiemann, O. Pulsed Dipolar EPR Spectroscopy and Metal Ions: Methodology and Biological Applications. *ChemPlusChem*. **2020**, *85*, 353–372.
- (110) Nguyen, P.; Qin, P. Z. RNA dynamics: perspectives from spin labels. *Wiley Interdisciplinary Reviews. RNA*. **2012**, *3*, 62–72.
- (111) Zhang, X.; Cekan, P.; Sigurdsson, S. T.; Qin, P. Z. Studying RNA Using Site-Directed Spin-Labeling and Continuous-Wave Electron Paramagnetic Resonance Spectroscopy. *Methods in Enzymology*. **2009**, *469*, 303–328.
- (112) Borbat, P. P.; Costa-Filho, A. J.; Earle, K. A.; Moscicki, J. K.; Freed, J. H. Electron Spin Resonance in Studies of Membranes and Proteins. *Science*. **2001**, *291*, 266–269.

- (113) Roser, P.; Schmidt, M. J.; Drescher, M.; Summerer, D. Site-directed spin labeling of proteins for distance measurements in vitro and in cells. *Organic & Biomolecular Chemistry*. **2016**, *14*, 5468–5476.
- (114) Qin, P. Z. Site-directed Spin Labeling Studies on Nucleic Acid Structure and Dynamics. In *Progress in Nucleic Acid Research and Molecular Biology*, 82nd ed.; Conn, P. M., Ed.; Progress in Molecular Biology and Translational Science; Elsevier: Burlington **2008**; pp 147–197.
- (115) Esquiaqui, J. M.; Sherman, E. M.; Ye, J.-D.; Fanucci, G. E. Site-directed Spin-Labeling Strategies and Electron Paramagnetic Resonance Spectroscopy for Large Riboswitches. *Methods in Enzymology*. **2014**, *549*, 287–311.
- (116) Shelke, S. A.; Sigurdsson, S. T. Site-Directed Spin Labeling for EPR Studies of Nucleic Acids. In *Modified Nucleic Acids*; Nakatani, K., Tor, Y., Eds.; Nucleic Acids and Molecular Biology; Springer International Publishing: Cham **2016**; pp 159–187.
- (117) Shelke, S. A.; Sigurdsson, S. T. Site-Directed Nitroxide Spin Labeling of Biopolymers. In *Structural Information from Spin-Labels and Intrinsic Paramagnetic Centres in the Biosciences*; Timmel, C. R., Harmer, J. R., Eds.; Structure and Bonding; Springer: Berlin, Heidelberg **2013**; pp 121–162.
- (118) Fleck, N.; Heubach, C. A.; Hett, T.; Haege, F. R.; Bawol, P. P.; Baltruschat, H.; Schiemann, O. SLIM: A Short-Linked, Highly Redox-Stable Trityl Label for High-Sensitivity In-Cell EPR Distance Measurements. *Angewandte Chemie International Edition*. **2020**, *59*, 9767–9772.
- (119) Jassoy, J. J.; Berndhäuser, A.; Duthie, F.; Kühn, S. P.; Hagelueken, G.; Schiemann, O. Versatile Trityl Spin Labels for Nanometer Distance Measurements on Biomolecules In Vitro and within Cells. *Angewandte Chemie International Edition*. **2017**, *56*, 177–181.
- (120) Kuzhelev, A. A.; Trukhin, D. V.; Krumkacheva, O. A.; Strizhakov, R. K.; Rogozhnikova, O. Y.; Troitskaya, T. I.; Fedin, M. V.; Tormyshev, V. M.; Bagryanskaya, E. G. Room-Temperature Electron Spin Relaxation of Triarylmethyl Radicals at the X- and Q-Bands. *The Journal of Physical Chemistry. B*. **2015**, *119*, 13630–13640.
- (121) Shevelev, G. Y.; Krumkacheva, O. A.; Lomzov, A. A.; Kuzhelev, A. A.; Rogozhnikova, O. Y.; Trukhin, D. V.; Troitskaya, T. I.; Tormyshev, V. M.; Fedin, M. V.; Pyshnyi, D. V.; *et al.* Physiological-Temperature Distance Measurement in Nucleic

- Acid using Triarylmethyl-based Spin Labels and Pulsed Dipolar EPR Spectroscopy. *Journal of the American Chemical Society*. **2014**, *136*, 9874–9877.
- (122) Yang, Y.; Pan, B.-B.; Tan, X.; Yang, F.; Liu, Y.; Su, X.-C.; Goldfarb, D. In-Cell Trityl-Trityl Distance Measurements on Proteins. *The Journal of Physical Chemistry Letters*. **2020**, *11*, 1141–1147.
- (123) Yang, Y.; Yang, F.; Li, X.-Y.; Su, X.-C.; Goldfarb, D. In-Cell EPR Distance Measurements on Ubiquitin Labeled with a Rigid PyMTA-Gd(III) Tag. *The Journal of Physical Chemistry. B*. **2019**, *123*, 1050–1059.
- (124) Kucher, S.; Korneev, S.; Klare, J. P.; Klose, D.; Steinhoff, H.-J. In cell Gd<sup>3+</sup>-based site-directed spin labeling and EPR spectroscopy of eGFP. *Physical Chemistry Chemical Physics*. **2020**, *22*, 13358–13362.
- (125) Collauto, A.; Bülow, S. von; Gophane, D.; Saha, S.; Stelzl, L.; Hummer, G.; Sigurdsson, S. T.; Prisner, T. Compaction of RNA duplexes in the cell. *Angewandte Chemie International Edition*. **2020**, DOI 10.1002/anie.202009800.
- (126) Karthikeyan, G.; Bonucci, A.; Casano, G.; Gerbaud, G.; Abel, S.; Thomé, V.; Kodjabachian, L.; Magalon, A.; Guigliarelli, B.; Belle, V.; *et al.* A Bioresistant Nitroxide Spin Label for In-Cell EPR Spectroscopy: In Vitro and In Oocytes Protein Structural Dynamics Studies. *Angewandte Chemie International Edition*. **2018**, *57*, 1366–1370.
- (127) Widder, P.; Schuck, J.; Summerer, D.; Drescher, M. Combining site-directed spin labeling in vivo and in-cell EPR distance determination. *Physical Chemistry Chemical Physics*. **2020**, *22*, 4875–4879.
- (128) Teucher, M.; Zhang, H.; Bader, V.; Winklhofer, K. F.; García-Sáez, A. J.; Rajca, A.; Bleicken, S.; Bordignon, E. A new perspective on membrane-embedded Bax oligomers using DEER and bioresistant orthogonal spin labels. *Scientific Reports*. **2019**, *9*, 13013.
- (129) Schmidt, M. J.; Borbas, J.; Drescher, M.; Summerer, D. A genetically encoded spin label for electron paramagnetic resonance distance measurements. *Journal of the American Chemical Society*. **2014**, *136*, 1238–1241.
- (130) Lawless, M. J.; Shimshi, A.; Cunningham, T. F.; Kinde, M. N.; Tang, P.; Saxena, S. Analysis of Nitroxide-Based Distance Measurements in Cell Extracts and in Cells by Pulsed ESR Spectroscopy. *ChemPhysChem*. **2017**, *18*, 1653–1660.

- (131) Krstić, I.; Hänsel, R.; Romainczyk, O.; Engels, J. W.; Dötsch, V.; Prisner, T. F. Long-range distance measurements on nucleic acids in cells by pulsed EPR spectroscopy. *Angewandte Chemie International Edition*. **2011**, *50*, 5070–5074.
- (132) Igarashi, R.; Sakai, T.; Hara, H.; Tenno, T.; Tanaka, T.; Tochio, H.; Shirakawa, M. Distance determination in proteins inside *Xenopus laevis* oocytes by double electron-electron resonance experiments. *Journal of the American Chemical Society*. **2010**, *132*, 8228–8229.
- (133) Hänsel, R.; Luh, L. M.; Corbeski, I.; Trantirek, L.; Dötsch, V. In-cell NMR and EPR spectroscopy of biomacromolecules. *Angewandte Chemie International Edition*. **2014**, *53*, 10300–10314.
- (134) Bonucci, A.; Ouari, O.; Guigliarelli, B.; Belle, V.; Mileo, E. In-Cell EPR: Progress towards Structural Studies Inside Cells. *ChemBioChem*. **2020**, *21*, 451–460.
- (135) Azarkh, M.; Singh, V.; Okle, O.; Seemann, I. T.; Dietrich, D. R.; Hartig, J. S.; Drescher, M. Site-directed spin-labeling of nucleotides and the use of in-cell EPR to determine long-range distances in a biologically relevant environment. *Nature Protocols*. **2013**, *8*, 131–147.
- (136) Azarkh, M.; Okle, O.; Singh, V.; Seemann, I. T.; Hartig, J. S.; Dietrich, D. R.; Drescher, M. Long-range distance determination in a DNA model system inside *Xenopus laevis* oocytes by in-cell spin-label EPR. *ChemBioChem*. **2011**, *12*, 1992–1995.
- (137) Cohn, M.; Townsend, J. A Study of Manganous Complexes by Paramagnetic Resonance Absorption. *Nature*. **1954**, *173*, 1090–1091.
- (138) Danchin, A.; Guéron, M. Cooperative Binding of Manganese (II) to Transfer RNA. *European Journal of Biochemistry*. **1970**, *16*, 532–536.
- (139) Horton, T. E.; Clardy, D. R.; DeRose, V. J. Electron Paramagnetic Resonance Spectroscopic Measurement of Mn<sup>2+</sup> Binding Affinities to the Hammerhead Ribozyme and Correlation with Cleavage Activity. *Biochemistry*. **1998**, *37*, 18094–18101.
- (140) Horton, T. E.; DeRose, V. J. Cobalt Hexammine Inhibition of the Hammerhead Ribozyme. *Biochemistry*. **2000**, *39*, 11408–11416.
- (141) Hunsicker, L. M.; DeRose, V. J. Activities and relative affinities of divalent metals in unmodified and phosphorothioate-substituted hammerhead ribozymes. *Journal of Inorganic Biochemistry*. **2000**, *80*, 271–281.



- (142) Kisseleva, N.; Khvorova, A.; Westhof, E.; Schiemann, O. Binding of manganese(II) to a tertiary stabilized hammerhead ribozyme as studied by electron paramagnetic resonance spectroscopy. *RNA*. **2005**, *11*, 1–6.
- (143) Kisseleva, N.; Kraut, S.; Jäschke, A.; Schiemann, O. Characterizing multiple metal ion binding sites within a ribozyme by cadmium-induced EPR silencing. *HFSP Journal*. **2007**, *1*, 127–136.
- (144) Schiemann, O.; Fritscher, J.; Kisseleva, N.; Sigurdsson, S. T.; Prisner, T. F. Structural Investigation of a High-Affinity MnII Binding Site in the Hammerhead Ribozyme by EPR Spectroscopy and DFT Calculations. Effects of Neomycin B on Metal-Ion Binding. *ChemBioChem*. **2003**, *4*, 1057–1065.
- (145) Wang, K. Y.; Gerena, L.; Swaminathan, S.; Colton, P. H. Determination of the number and location of the manganese binding sites of DNA quadruplexes in solution by EPR and NMR. *Nucleic Acids Research*. **1995**, *23*, 844–848.
- (146) Woody, A. Y.; Eaton, S. S.; Osumi-Davis, P. A.; Woody, R. W. Asp537 and Asp812 in Bacteriophage T7 RNA Polymerase as Metal Ion-Binding Sites Studied by EPR, Flow-Dialysis, and Transcription. *Biochemistry*. **1996**, *35*, 144–152.
- (147) Schweiger, A.; Jeschke, G. *Principles of pulse electron paramagnetic resonance*; Oxford University Press: Oxford **2001**.
- (148) Schiemann, O. EPR Spektroskopie an Biologischen Systemen. In *Bioanalytik*, 3. Auflage; Lottspeich, F., Engels, J. W., Eds.; Springer Spektrum: Berlin, Heidelberg **2012**; pp 509–526.
- (149) Junk, M. J. N. *Assessing the functional structure of molecular transporters by EPR spectroscopy*. Johannes Gutenberg-University, Dissertation; Springer theses; Springer: Berlin, Heidelberg **2012**.
- (150) Goldfarb, D.; Stoll, S., Eds. *EPR spectroscopy: Fundamentals and Methods*; eMagRes books; Wiley: Chichester, UK **2018**.
- (151) Berliner, L. J.; Eaton, G. R.; Eaton, S. S. *Distance Measurements in Biological Systems by EPR*, 19th ed.; Biological Magnetic Resonance; Kluwer Academic Publishers: New York, Boston, Dodrecht, London, Moscow **2000**.
- (152) Bode, B. E.; Norman, D. G. Pulsed Electron-Electron Double Resonance (PELDOR) and Electron Spin Echo Envelope Modulation (ESEEM) Spectroscopy in Bioanalysis. In *Radiation in Bioanalysis*; Pereira, A. S., Tavares, P., Limão-Vieira, P., Eds.; Bioanalysis; Springer International Publishing: Cham **2019**; pp 195–212.

- (153) Tsvetkov, Y. D.; Bowman, M. K.; Grishin, Y. A. *Pulsed Electron-Electron Double Resonance: Nanoscale Distance Measurement in the Biological, Materials and Chemical Sciences*; Springer International Publishing: Cham **2019**.
- (154) Weil, J. A.; Bolton, J. R. *Electron paramagnetic resonance: Elementary theory and practical applications*, 2nd ed.; Wiley-Interscience: Hoboken, NJ **2007**.
- (155) Levitt, M. H. *Spin dynamics: Basics of nuclear magnetic resonance*, 2. ed.; Wiley: Chichester **2008**.
- (156) Brustolon, M.; Giamello, G., Eds. *Electron paramagnetic resonance: A practitioner's toolkit*; Wiley: Hoboken, NJ **2009**.
- (157) Stoll, S.; Schweiger, A. EasySpin, a comprehensive software package for spectral simulation and analysis in EPR. *Journal of Magnetic Resonance*. **2006**, *178*, 42–55.
- (158) Sproules, S. Molecules as electron spin qubits. In *Electron Paramagnetic Resonance: A review of the recent literature*, 25th ed.; Chechik, V., Murphy, D., Eds.; A specialist periodical report; Royal Society of Chemistry: Cambridge **2017**; pp 61–97.
- (159) Lindgren, M.; Eaton, G. R.; Eaton, S. S.; Jonsson, B.-H.; Hammarström, P.; Svensson, M.; Carlsson, U. Electron spin echo decay as a probe of aminoxyl environment in spin-labeled mutants of human carbonic anhydrase II. *Journal of the Chemical Society, Perkin Transactions 2*. **1997**, 2549–2554.
- (160) Huber, M.; Lindgren, M.; Hammarström, P.; Mårtensson, L.-G.; Carlsson, U.; Eaton, G.R.; Eaton, S.S. Phase memory relaxation times of spin labels in human carbonic anhydrase II: pulsed EPR to determine spin label location. *Biophysical Chemistry*. **2001**, *94*, 245–256.
- (161) Zecevic, A.; Eaton, G. R.; Eaton, S. S.; Lindgren, M. Dephasing of electron spin echoes for nitroxyl radicals in glassy solvents by non-methyl and methyl protons. *Molecular Physics*. **1998**, *95*, 1255–1263.
- (162) Ward, R.; Bowman, A.; Sozudogru, E.; El-Mkami, H.; Owen-Hughes, T.; Norman, D. G. EPR distance measurements in deuterated proteins. *Journal of Magnetic Resonance*. **2010**, *207*, 164–167.
- (163) El Mkami, H.; Ward, R.; Bowman, A.; Owen-Hughes, T.; Norman, D. G. The spatial effect of protein deuteration on nitroxide spin-label relaxation: implications for EPR distance measurement. *Journal of Magnetic Resonance*. **2014**, *248*, 36–41.

- (164) Schmidt, T.; Wälti, M. A.; Baber, J. L.; Hustedt, E. J.; Clore, G. M. Long Distance Measurements up to 160 Å in the GroEL Tetradecamer Using Q-Band DEER EPR Spectroscopy. *Angewandte Chemie International Edition*. **2016**, *55*, 15905–15909.
- (165) Kathirvelu, V.; Smith, C.; Parks, C.; Mannan, M. A.; Miura, Y.; Takeshita, K.; Eaton, S. S.; Eaton, G. R. Relaxation rates for spirocyclohexyl nitroxyl radicals are suitable for interspin distance measurements at temperatures up to about 125 K. *Chemical Communications*. **2009**, 454–456.
- (166) Rajca, A.; Kathirvelu, V.; Roy, S. K.; Pink, M.; Rajca, S.; Sarkar, S.; Eaton, S. S.; Eaton, G. R. A spirocyclohexyl nitroxide amino acid spin label for pulsed EPR spectroscopy distance measurements. *Chemistry - A European Journal*. **2010**, *16*, 5778–5782.
- (167) Abdullin, D.; Hagelueken, G.; Hunter, R. I.; Smith, G. M.; Schiemann, O. Geometric model-based fitting algorithm for orientation-selective PELDOR data. *Molecular Physics*. **2015**, *113*, 544–560.
- (168) Marko, A.; Margraf, D.; Cekan, P.; Sigurdsson, S. T.; Schiemann, O.; Prisner, T. F. Analytical method to determine the orientation of rigid spin labels in DNA. *Physical Review E*. **2010**, *81*, 21911.
- (169) Prisner, T. F.; Marko, A.; Sigurdsson, S. T. Conformational dynamics of nucleic acid molecules studied by PELDOR spectroscopy with rigid spin labels. *Journal of Magnetic Resonance*. **2015**, *252*, 187–198.
- (170) Jeschke, G. Dipolar Spectroscopy - Double-Resonance Methods. *eMagRes*. **2016**, *5*, 1459–1476.
- (171) Saha, S.; Jagtap, A. P.; Sigurdsson, S. T. Site-Directed Spin Labeling of RNA by Postsynthetic Modification of 2'-Amino Groups. *Methods in Enzymology*. **2015**, *563*, 397–414.
- (172) Haugland, M. M.; Lovett, J. E.; Anderson, E. A. Advances in the synthesis of nitroxide radicals for use in biomolecule spin labelling. *Chemical Society Reviews*. **2018**, *47*, 668–680.
- (173) Saha, S.; Hetzke, T.; Prisner, T. F.; Sigurdsson, S. T. Noncovalent spin-labeling of RNA: the aptamer approach. *Chemical Communications*. **2018**, *54*, 11749–11752.
- (174) Heinz, M.; Erlenbach, N.; Stelzl, L. S.; Thierolf, G.; Kamble, N. R.; Sigurdsson, S. T.; Prisner, T. F.; Hummer, G. High-resolution EPR distance measurements on RNA

- and DNA with the non-covalent  $\dot{G}$  spin label. *Nucleic Acids Research*. **2020**, *48*, 924–933.
- (175) Domnick, C.; Eggert, F.; Wuebben, C.; Bornewasser, L.; Hagelueken, G.; Schiemann, O.; Kath-Schorr, S. EPR Distance Measurements on Long Non-coding RNAs Empowered by Genetic Alphabet Expansion Transcription. *Angewandte Chemie International Edition*. **2020**, *59*, 7891–7896.
- (176) Wang, Y.; Kathiresan, V.; Chen, Y.; Hu, Y.; Jiang, W.; Bai, G.; Liu, G.; Qin, P.; Fang, X. Posttranscriptional site-directed spin labeling of large RNAs with an unnatural base pair system under non-denaturing conditions. *Chemical Science*. **2020**, *11*, 9655–9664.
- (177) Caron, M.; Dugas, H. Specific spin-labeling of transfer ribonucleic acid molecules. *Nucleic Acids Research*. **1976**, *3*, 19–34.
- (178) Pscheidt, R. H.; Wells, B. D. Different conformations of the 3' termini of initiator and elongator transfer ribonucleic acids. An EPR study. *The Journal of Biological Chemistry*. **1986**, *261*, 7253–7256.
- (179) Macosko, J. C.; Pio, M. S.; Tinoco, I.; Shin, Y. K. A novel 5 displacement spin-labeling technique for electron paramagnetic resonance spectroscopy of RNA. *RNA*. **1999**, *5*, 1158–1166.
- (180) Grant, G. P. G.; Qin, P. Z. A facile method for attaching nitroxide spin labels at the 5' terminus of nucleic acids. *Nucleic Acids Research*. **2007**, *35*, 1–8.
- (181) Qin, P. Z.; Butcher, S. E.; Feigon, J.; Hubbell, W. L. Quantitative Analysis of the Isolated GAAA Tetraloop/Receptor Interaction in Solution: A Site-Directed Spin Labeling Study. *Biochemistry*. **2001**, *40*, 6929–6936.
- (182) Cai, Q.; Kusnetzow, A. K.; Hideg, K.; Price, E. A.; Haworth, I. S.; Qin, P. Z. Nanometer distance measurements in RNA using site-directed spin labeling. *Biophysical Journal*. **2007**, *93*, 2110–2117.
- (183) Qin, P. Z.; Haworth, I. S.; Cai, Q.; Kusnetzow, A. K.; Grant, G. P. G.; Price, E. A.; Sowa, G. Z.; Popova, A.; Herreros, B.; He, H. Measuring nanometer distances in nucleic acids using a sequence-independent nitroxide probe. *Nature Protocols*. **2007**, *2*, 2354–2365.
- (184) Nguyen, P. H.; Popova, A. M.; Hideg, K.; Qin, P. Z. A nucleotide-independent cyclic nitroxide label for monitoring segmental motions in nucleic acids. *BMC Biophysics*. **2015**, *8*, 1–8.

- (185) Edwards, T. E.; Okonogi, T. M.; Robinson, B. H.; Sigurdsson, S. T. Site-Specific Incorporation of Nitroxide Spin-Labels into Internal Sites of the TAR RNA; Structure-Dependent Dynamics of RNA by EPR spectroscopy. *Journal of the American Chemical Society*. **2001**, *123*, 1527–1528.
- (186) Edwards, T. E.; Robinson, B. H.; Sigurdsson, S. T. Identification of amino acids that promote specific and rigid TAR RNA-tat protein complex formation. *Chemistry & Biology*. **2005**, *12*, 329–337.
- (187) Edwards, T. E.; Sigurdsson, S. T. EPR spectroscopic analysis of TAR RNA–metal ion interactions. *Biochemical and Biophysical Research Communications*. **2003**, *303*, 721–725.
- (188) Edwards, T. E.; Sigurdsson, S. T. Site-specific incorporation of nitroxide spin-labels into 2'-positions of nucleic acids. *Nature Protocols*. **2007**, *2*, 1954–1962.
- (189) Edwards, T. E.; Sigurdsson, S. T. Electron paramagnetic resonance dynamic signatures of TAR RNA-small molecule complexes provide insight into RNA structure and recognition. *Biochemistry*. **2002**, *41*, 14843–14847.
- (190) Kim, N.-K.; Murali, A.; DeRose, V. J. Separate metal requirements for loop interactions and catalysis in the extended hammerhead ribozyme. *Journal of the American Chemical Society*. **2005**, *127*, 14134–14135.
- (191) Schiemann, O.; Weber, A.; Edwards, T. E.; Prisner, T. F.; Sigurdsson, S. T. Nanometer Distance Measurements on RNA using PELDOR. *Journal of the American Chemical Society*. **2003**, *125*, 3434–3435.
- (192) Saha, S.; Jagtap, A. P.; Sigurdsson, S. T. Site-directed spin labeling of 2'-amino groups in RNA with isoindoline nitroxides that are resistant to reduction. *Chemical Communications*. **2015**, *51*, 13142–13145.
- (193) Braun, T. S.; Widder, P.; Osswald, U.; Groß, L.; Williams, L.; Schmidt, M.; Helmle, I.; Summerer, D.; Drescher, M. Isoindoline-Based Nitroxides as Bioresistant Spin Labels for Protein Labeling through Cysteines and Alkyne-Bearing Noncanonical Amino Acids. *ChemBioChem*. **2020**, *21*, 958–962.
- (194) Jagtap, A. P.; Krstic, I.; Kunjir, N. C.; Hänsel, R.; Prisner, T. F.; Sigurdsson, S. T. Sterically shielded spin labels for in-cell EPR spectroscopy: Analysis of stability in reducing environment. *Free Radical Research*. **2015**, *49*, 78–85.
- (195) Marx, L.; Chiarelli, R.; Guiberteau, T.; Rassat, A. A comparative study of the reduction by ascorbate of 1,1,3,3-tetraethylisoindolin-2-yloxy and of 1,1,3,3-

- tetramethylisoindolin-2-yloxyl. *Journal of the Chemical Society, Perkin Transactions 1*. **2000**, 1181–1182.
- (196) Juliusson, H. Y.; Sigurdsson, S. T. Reduction Resistant and Rigid Nitroxide Spin-Labels for DNA and RNA. *The Journal of Organic Chemistry*. **2020**, *85*, 4036–4046.
- (197) Hara, H.; Horiuchi, T.; Saneyoshi, M.; Nishimura, S. 4thiouridine-specific spin-labeling of E.coli transfer RNA. *Biochemical and Biophysical Research Communications*. **1970**, *38*, 305–311.
- (198) Qin, P. Z.; Hideg, K.; Feigon, J.; Hubbell, W. L. Monitoring RNA Base Structure and Dynamics Using Site-Directed Spin Labeling. *Biochemistry*. **2003**, *42*, 6772–6783.
- (199) Rostovtsev, V. V.; Green, L. G.; Fokin, V. V.; Sharpless, K. B. A Stepwise Huisgen Cycloaddition Process: Copper(I)-Catalyzed Regioselective “Ligation” of Azides and Terminal Alkynes. *Angewandte Chemie International Edition*. **2002**, *41*, 2596–2599.
- (200) Kolb, H. C.; Finn, M. G.; Sharpless, K. B. Click Chemistry: Diverse Chemical Function from a Few Good Reactions. *Angewandte Chemie International Edition*. **2001**, *40*, 2004–2021.
- (201) Burley, G. A.; Gierlich, J.; Mofid, M. R.; Nir, H.; Tal, S.; Eichen, Y.; Carell, T. Directed DNA Metallization. *Journal of the American Chemical Society*. **2006**, *128*, 1398–1399.
- (202) El-Sagheer, A. H.; Brown, T. Click chemistry with DNA. *Chemical Society Reviews*. **2010**, *39*, 1388–1405.
- (203) Gierlich, J.; Burley, G. A.; Gramlich, P. M. E.; Hammond, D. M.; Carell, T. Click Chemistry as a Reliable Method for the High-Density Postsynthetic Functionalization of Alkyne-Modified DNA. *Organic Letters*. **2006**, *8*, 3639–3642.
- (204) Kocalka, P.; Andersen, N. K.; Jensen, F.; Nielsen, P. Synthesis of 5-(1,2,3-triazol-4-yl)-2'-deoxyuridines by a click chemistry approach: stacking of triazoles in the major groove gives increased nucleic acid duplex stability. *ChemBioChem*. **2007**, *8*, 2106–2116.
- (205) Park, S. M.; Shen, Y.; Kim, B. H. Water gelation abilities of alkylbenzyltriazole-appended 2'-deoxyribonucleoside and ribonucleoside. *Organic & Biomolecular Chemistry*. **2007**, *5*, 610–612.
- (206) Seela, F.; Sirivolu, V. R. Nucleosides and Oligonucleotides with Diynyl Side Chains: Base Pairing and Functionalization of 2'-Deoxyuridine Derivatives by the

- Copper(I)-Catalyzed Alkyne-Azide 'Click' Cycloaddition. *Helvetica Chimica Acta*. **2007**, *90*, 535–552.
- (207) Jakobsen, U.; Shelke, S. A.; Vogel, S.; Sigurdsson, S. T. Site-Directed Spin-Labeling of Nucleic Acids by Click Chemistry: Detection of Abasic Sites in Duplex DNA by EPR spectroscopy. *Journal of the American Chemical Society*. **2010**, *132*, 10424–10428.
- (208) Tornøe, C. W.; Christensen, C.; Meldal, M. Peptidotriazoles on Solid Phase: 1,2,3-Triazoles by Regiospecific Copper(I)-Catalyzed 1,3-Dipolar Cycloadditions of Terminal Alkynes to Azides. *The Journal of Organic Chemistry*. **2002**, *67*, 3057–3064.
- (209) Kerzhner, M.; Abdullin, D.; Więcek, J.; Matsuoka, H.; Hagelueken, G.; Schiemann, O.; Famulok, M. Post-synthetic Spin-Labeling of RNA through Click Chemistry for PELDOR Measurements. *Chemistry - A European Journal*. **2016**, *22*, 12113–12121.
- (210) Kerzhner, M.; Matsuoka, H.; Wuebben, C.; Famulok, M.; Schiemann, O. High-Yield Spin Labeling of Long RNAs for Electron Paramagnetic Resonance Spectroscopy. *Biochemistry*. **2018**, *57*, 2923–2931.
- (211) Kerzhner, M. Site-Directed Spin Labeling of Large Riboswitches Using Click Chemistry. *Dissertation*, Rheinische Friedrich-Wilhelms Universität, Bonn. **2018**.
- (212) Strube, T.; Schiemann, O.; MacMillan, F.; Prisner, T.; Engels, J. W. A new facile method for spin-labeling of oligonucleotides. *Nucleosides, Nucleotides and Nucleic Acids*. **2001**, *20*, 1271–1274.
- (213) Piton, N.; Schiemann, O.; Mu, Y.; Stock, G.; Prisner, T.; Engels, J. W. Synthesis of spin-labeled RNAs for long range distance measurements by peldor. *Nucleosides, Nucleotides and Nucleic Acids*. **2005**, *24*, 771–775.
- (214) Piton, N.; Mu, Y.; Stock, G.; Prisner, T. F.; Schiemann, O.; Engels, J. W. Base-specific spin-labeling of RNA for structure determination. *Nucleic Acids Research*. **2007**, *35*, 3128–3143.
- (215) Schiemann, O.; Piton, N.; Plackmeyer, J.; Bode, B. E.; Prisner, T. F.; Engels, J. W. Spin labeling of oligonucleotides with the nitroxide TPA and use of PELDOR, a pulse EPR method, to measure intramolecular distances. *Nature Protocols*. **2007**, *2*, 904–923.
- (216) Sicoli, G.; Wachowius, F.; Bennati, M.; Höbartner, C. Probing Secondary Structures of Spin-Labeled RNA by Pulsed EPR Spectroscopy. *Angewandte Chemie International Edition*. **2010**, *49*, 6443–6447.

- (217) Höbartner, C.; Sicoli, G.; Wachowius, F.; Gophane, D. B.; Sigurdsson, S. T. Synthesis and Characterization of RNA Containing a Rigid and Nonperturbing Cytidine-Derived Spin Label. *The Journal of Organic Chemistry*. **2012**, *77*, 7749–7754.
- (218) Tkach, I.; Pornsuwan, S.; Höbartner, C.; Wachowius, F.; Sigurdsson, S. T.; Baranova, T. Y.; Diederichsen, U.; Sicoli, G.; Bennati, M. Orientation selection in distance measurements between nitroxide spin labels at 94 GHz EPR with variable dual frequency irradiation. *Physical Chemistry Chemical Physics*. **2013**, *15*, 3433–3437.
- (219) Hetzke, T.; Vogel, M.; Gophane, D. B.; Weigand, J. E.; Suess, B.; Sigurdsson, S. T.; Prisner, T. F. Influence of Mg<sup>2+</sup> on the conformational flexibility of a tetracycline aptamer. *RNA*. **2019**, *25*, 158–167.
- (220) Juliusson, H. Y.; Segler, A.-L. J.; Sigurdsson, S. T. Benzoyl-Protected Hydroxylamines for Improved Chemical Synthesis of Oligonucleotides Containing Nitroxide Spin Labels. *European Journal of Organic Chemistry*. **2019**, *2019*, 3799–3805.
- (221) Shelke, S. A.; Sandholt, G. B.; Sigurdsson, S. T. Nitroxide-labeled pyrimidines for non-covalent spin-labeling of abasic sites in DNA and RNA duplexes. *Organic & Biomolecular Chemistry*. **2014**, *12*, 7366–7374.
- (222) Kamble, N. R.; Gränz, M.; Prisner, T. F.; Sigurdsson, S. T. Noncovalent and site-directed spin labeling of duplex RNA. *Chemical Communications*. **2016**, *52*, 14442–14445.
- (223) Kamble, N. R.; Sigurdsson, S. T. Purine-Derived Nitroxides for Noncovalent Spin-Labeling of Abasic Sites in Duplex Nucleic Acids. *Chemistry - A European Journal*. **2018**, *24*, 4157–4164.
- (224) Kamble, N.; Wolfrum, M.; Halbritter, T.; Sigurdsson, S. T.; Richert, C. Noncovalent Spin-Labeling of DNA and RNA Triplexes. *Chemistry & Biodiversity*. **2020**, *17*, 1-7.
- (225) Lang, K.; Micura, R. The preparation of site-specifically modified riboswitch domains as an example for enzymatic ligation of chemically synthesized RNA fragments. *Nature Protocols*. **2008**, *3*, 1457–1466.
- (226) Moore, M. J.; Query, C. C. Joining of RNAs by Splinted Ligation. *Methods in Enzymology*. **2000**, *317*, 109–123.



- (227) Rieder, R.; Höbartner, C.; Micura, R. Enzymatic ligation strategies for the preparation of purine riboswitches with site-specific chemical modifications. *Methods in Molecular Biology*. **2009**, *540*, 15–24.
- (228) Lebars, I.; Vileno, B.; Bourbigot, S.; Turek, P.; Wolff, P.; Kieffer, B. A fully enzymatic method for site-directed spin labeling of long RNA. *Nucleic Acids Research*. **2014**, *42*, 1-10.
- (229) Esquiaqui, J. M.; Sherman, E. M.; Ionescu, S. A.; Ye, J.-D.; Fanucci, G. E. Characterizing the Dynamics of the Leader-Linker Interaction in the Glycine Riboswitch with Site-Directed Spin Labeling. *Biochemistry*. **2014**, *53*, 3526–3528.
- (230) Duss, O.; Yulikov, M.; Jeschke, G.; Allain, F. H.-T. EPR-aided approach for solution structure determination of large RNAs or protein-RNA complexes. *Nature Communications*. **2014**, *5*, 1–9.
- (231) Duss, O.; Michel, E.; Yulikov, M.; Schubert, M.; Jeschke, G.; Allain, F. H.-T. Structural basis of the non-coding RNA RsmZ acting as a protein sponge. *Nature*. **2014**, *509*, 588–592.
- (232) Büttner, L.; Seikowski, J.; Wawrzyniak, K.; Ochmann, A.; Höbartner, C. Synthesis of spin-labeled riboswitch RNAs using convertible nucleosides and DNA-catalyzed RNA ligation. *Bioorganic & Medicinal Chemistry*. **2013**, *21*, 6171–6180.
- (233) Babaylova, E. S.; Ivanov, A. V.; Malygin, A. A.; Vorobjeva, M. A.; Venyaminova, A. G.; Polienko, Y. F.; Kirilyuk, I. A.; Krumkacheva, O. A.; Fedin, M. V.; Karpova, G. G.; *et al.* A versatile approach for site-directed spin labeling and structural EPR studies of RNAs. *Organic & Biomolecular Chemistry*. **2014**, *12*, 3129–3136.
- (234) Babaylova, E. S.; Malygin, A. A.; Lomzov, A. A.; Pyshnyi, D. V.; Yulikov, M.; Jeschke, G.; Krumkacheva, O. A.; Fedin, M. V.; Karpova, G. G.; Bagryanskaya, E. G. Complementary-addressed site-directed spin labeling of long natural RNAs. *Nucleic Acids Research*. **2016**, *44*, 7935–7943.
- (235) Thaning, M. Triarylmethyl Free Radicals as Image enhancing Agents. (*Nycomed Imaging AS*), *International Patent GB98/00672, WO 98/39277* **1997**.
- (236) Ardenkjaer-Larsen, J. H. A Method of Determinating Oxygen Concentration in a sample. (*Nycomed Imaging A/S*), *International Patent GB96/02198, WO 97/09633* **1997**.
- (237) Andersson, S.; Radner, F.; Servin, R.; Wistrand, L.-G. Free Radicals. (*Nycomed Imaging AS*), *United States Patent 5728370* **1998**.

- (238) Andersson, S.; Radner, F.; Rydbeck, A.; Servin, R.; Wistrand, L.-G. Free Radicals. (*Nycomed Imaging AS*), *United States Patent 5530140* **1996**.
- (239) Fleck, N.; Heubach, C.; Hett, T.; Spicher, S.; Grimme, S.; Schiemann, O. Ox-SLIM: Synthesis of and Site-Specific Labelling with a Highly Hydrophilic Trityl Spin Label. *Chemistry - A European Journal*. **2021**, DOI 10.1002/chem.202100013.
- (240) Owenius, R.; Eaton, G. R.; Eaton, S. S. Frequency (250 MHz to 9.2 GHz) and viscosity dependence of electron spin relaxation of triarylmethyl radicals at room temperature. *Journal of Magnetic Resonance*. **2005**, *172*, 168–175.
- (241) Lomzov, A. A.; Sviridov, E. A.; Shernuykov, A. V.; Shevelev, G. Y.; Pyshnyi, D. V.; Bagryanskaya, E. G. Study of a DNA Duplex by Nuclear Magnetic Resonance and Molecular Dynamics Simulations. Validation of Pulsed Dipolar Electron Paramagnetic Resonance Distance Measurements Using Triarylmethyl-Based Spin Labels. *The Journal of Physical Chemistry. B*. **2016**, *120*, 5125–5133.
- (242) Shevelev, G. Y.; Krumkacheva, O. A.; Lomzov, A. A.; Kuzhelev, A. A.; Trukhin, D. V.; Rogozhnikova, O. Y.; Tormyshev, V. M.; Pyshnyi, D. V.; Fedin, M. V.; Bagryanskaya, E. G. Triarylmethyl Labels: Toward Improving the Accuracy of EPR Nanoscale Distance Measurements in DNAs. *The Journal of Physical Chemistry. B*. **2015**, *119*, 13641–13648.
- (243) Fedin, M. V.; Shevelev, G. Y.; Pyshnyi, D. V.; Tormyshev, V. M.; Jeschke, G.; Yulikov, M.; Bagryanskaya, E. G. Interaction of triarylmethyl radicals with DNA termini revealed by orientation-selective W-band double electron-electron resonance spectroscopy. *Physical Chemistry Chemical Physics*. **2016**, *18*, 29549–29554.
- (244) Kuzhelev, A.; Akhmetzyanov, D.; Denysenkov, V.; Shevelev, G.; Krumkacheva, O.; Bagryanskaya, E.; Prisner, T. High-frequency pulsed electron-electron double resonance spectroscopy on DNA duplexes using trityl tags and shaped microwave pulses. *Physical Chemistry Chemical Physics*. **2018**, *20*, 26140–26144.
- (245) Kuzhelev, A. A.; Shevelev, G. Y.; Krumkacheva, O. A.; Tormyshev, V. M.; Pyshnyi, D. V.; Fedin, M. V.; Bagryanskaya, E. G. Saccharides as Prospective Immobilizers of Nucleic Acids for Room-Temperature Structural EPR Studies. *The Journal of Physical Chemistry Letters*. **2016**, *7*, 2544–2548.
- (246) Shevelev, G. Y.; Gulyak, E. L.; Lomzov, A. A.; Kuzhelev, A. A.; Krumkacheva, O. A.; Kupryushkin, M. S.; Tormyshev, V. M.; Fedin, M. V.; Bagryanskaya, E. G.; Pyshnyi, D. V. A Versatile Approach to Attachment of Triarylmethyl Labels to DNA for

- Nanoscale Structural EPR Studies at Physiological Temperatures. *The Journal of Physical Chemistry. B.* **2018**, *122*, 137–143.
- (247) Goldfarb, D. Gd<sup>3+</sup> spin labeling for distance measurements by pulse EPR spectroscopy. *Physical Chemistry Chemical Physics.* **2014**, *16*, 9685–9699.
- (248) Feintuch, A.; Otting, G.; Goldfarb, D. Gd<sup>3+</sup> Spin Labeling for Measuring Distances in Biomacromolecules: Why and How? *Methods in Enzymology.* **2015**, *563*, 415–457.
- (249) Martorana, A.; Bellapadrona, G.; Feintuch, A.; Di Gregorio, E.; Aime, S.; Goldfarb, D. Probing protein conformation in cells by EPR distance measurements using Gd<sup>3+</sup> spin labeling. *Journal of the American Chemical Society.* **2014**, *136*, 13458–13465.
- (250) Qi, M.; Gross, A.; Jeschke, G.; Godt, A.; Drescher, M. Gd(III)-PyMTA label is suitable for in-cell EPR. *Journal of the American Chemical Society.* **2014**, *136*, 15366–15378.
- (251) Wojciechowski, F.; Groß, A.; Holder, I. T.; Knörr, L.; Drescher, M.; Hartig, J. S. Pulsed EPR spectroscopy distance measurements of DNA internally labelled with Gd(3+)-DOTA. *Chemical Communications.* **2015**, *51*, 13850–13853.
- (252) Yang, Y.; Chen, S.-N.; Yang, F.; Li, X.-Y.; Feintuch, A.; Su, X.-C.; Goldfarb, D. In-cell destabilization of a homodimeric protein complex detected by DEER spectroscopy. *Proceedings of the National Academy of Sciences of the United States of America.* **2020**, *117*, 20566–20575.
- (253) Yang, Y.; Yang, F.; Gong, Y.-J.; Bahrenberg, T.; Feintuch, A.; Su, X.-C.; Goldfarb, D. High Sensitivity In-Cell EPR Distance Measurements on Proteins using an Optimized Gd(III) Spin Label. *The Journal of Physical Chemistry Letters.* **2018**, *9*, 6119–6123.
- (254) Yang, Y.; Yang, F.; Gong, Y.-J.; Chen, J.-L.; Goldfarb, D.; Su, X.-C. A Reactive, Rigid GdIII Labeling Tag for In-Cell EPR Distance Measurements in Proteins. *Angewandte Chemie International Edition.* **2017**, *56*, 2914–2918.
- (255) Song, Y.; Meade, T. J.; Astashkin, A. V.; Klein, E. L.; Enemark, J. H.; Raitsimring, A. Pulsed dipolar spectroscopy distance measurements in biomacromolecules labeled with Gd(III) markers. *Journal of Magnetic Resonance.* **2011**, *210*, 59–68.
- (256) Clever, G. H.; Reitmeier, S. J.; Carell, T.; Schiemann, O. Antiferromagnetic coupling of stacked Cu(II)-salen complexes in DNA. *Angewandte Chemie International Edition.* **2010**, *49*, 4927–4929.

- (257) Donohue, M. P.; Szalai, V. A. Distance measurements between paramagnetic ligands bound to parallel stranded guanine quadruplexes. *Physical Chemistry Chemical Physics*. **2016**, *18*, 15447–15455.
- (258) Engelhard, D. M.; Meyer, A.; Berndhäuser, A.; Schiemann, O.; Clever, G. H. Di-copper(II) DNA G-quadruplexes as EPR distance rulers. *Chemical Communications*. **2018**, *54*, 7455–7458.
- (259) Stratmann, L. M.; Kutin, Y.; Kasanmascheff, M.; Clever, G. H. Precise Distance Measurements in DNA G-Quadruplex Dimers and Sandwich Complexes by Pulsed Dipolar EPR Spectroscopy. *Angewandte Chemie International Edition*. **2020**, *59*, 2–11.
- (260) Ghosh, S.; Lawless, M. J.; Brubaker, H. J.; Singewald, K.; Kurpiewski, M. R.; Jen-Jacobson, L.; Saxena, S. Cu<sup>2+</sup>-based distance measurements by pulsed EPR provide distance constraints for DNA backbone conformations in solution. *Nucleic Acids Research*. **2020**, *48*, 1-11.
- (261) Lawless, M. J.; Sarver, J. L.; Saxena, S. Nucleotide-Independent Copper(II)-Based Distance Measurements in DNA by Pulsed ESR Spectroscopy. *Angewandte Chemie International Edition*. **2017**, *56*, 2115–2117.
- (262) Gamble Jarvi, A.; Bogetti, X.; Singewald, K.; Ghosh, S.; Saxena, S. Going the dHis-tance: Site-Directed Cu<sup>2+</sup> Labeling of Proteins and Nucleic Acids. *Accounts of chemical research*. **2021**, DOI 10.1021/acs.accounts.0c00761.
- (263) Wu, M. T.-P.; D'Souza, V. Alternate RNA Structures. *Cold Spring Harbor Perspectives in Biology*. **2020**, *12*, DOI 10.1101/cshperspect.a032425.
- (264) Sharp, P. A. The centrality of RNA. *Cell*. **2009**, *136*, 577–580.
- (265) Dethoff, E. A.; Chugh, J.; Mustoe, A. M.; Al-Hashimi, H. M. Functional Complexity and Regulation through RNA dynamics. *Nature*. **2012**, *482*, 322–330.
- (266) Reginsson, G. W.; Schiemann, O. Pulsed electron-electron double resonance: beyond nanometre distance measurements on biomacromolecules. *The Biochemical Journal*. **2011**, *434*, 353–363.
- (267) Jeschke, G.; Polyhach, Y. Distance measurements on spin-labelled biomacromolecules by pulsed electron paramagnetic resonance. *Physical Chemistry Chemical Physics*. **2007**, *9*, 1895–1910.
- (268) Haugland, M. M.; El-Sagheer, A. H.; Porter, R. J.; Peña, J.; Brown, T.; Anderson, E. A.; Lovett, J. E. 2'-Alkynylnucleotides: A Sequence- and Spin Label-Flexible

- Strategy for EPR Spectroscopy in DNA. *Journal of the American Chemical Society*. **2016**, *138*, 9069–9072.
- (269) Brajtenbach, D. Synthese eines Tetraethylisoindolin Spinlabels sowie Labeling einer Modell RNA zur EPR spektroskopischen Untersuchung. *Bachelor Thesis*, Rheinische Friedrich-Wilhelms Universität, Bonn. **2017**.
- (270) Blume, S. Synthese und Untersuchung der Relaxationszeit von 1,1,3,3-Tetramethylisoindolin-2-oxyl als Spinlabel für die EPR-Spektroskopie. *Bachelor Thesis*, Rheinische Friedrich-Wilhelms Universität, Bonn. **2019**.
- (271) Schmidt, F. Abstandsmessungen an Nukleinsäuren in Zellen mittels gepulster EPR-Spektroskopie. *Bachelor Thesis*, Rheinische Friedrich-Wilhelms Universität, Bonn. **2019**.
- (272) Haege, F. A stability study of trityl and nitroxide spin labels for in-cell EPR Spectroscopy. *Master Thesis*, Rheinische Friedrich-Wilhelms Universität, Bonn. **2019**.
- (273) Schiemann, O.; Piton, N.; Mu, Y.; Stock, G.; Engels, J. W.; Prisner, T. F. A PELDOR-based nanometer distance ruler for oligonucleotides. *Journal of the American Chemical Society*. **2004**, *126*, 5722–5729.
- (274) Romainczyk, O.; Endeward, B.; Prisner, T. F.; Engels, J. W. The RNA-DNA hybrid structure determined by EPR, CD and RNase H1. *Molecular bioSystems*. **2011**, *7*, 1050–1052.
- (275) Jeschke, G.; Chechik, V.; Ionita, P.; Godt, A.; Zimmermann, H.; Banham, J.; Timmel, C. R.; Hilger, D.; Jung, H. DeerAnalysis2006—a comprehensive software package for analyzing pulsed ELDOR data. *Applied Magnetic Resonance*. **2006**, *30*, 473–498.
- (276) Kulik, L. V.; Dzuba, S. A.; Grigoryev, I. A.; Tsvetkov, Y.D. Electron dipole–dipole interaction in ESEEM of nitroxide biradicals. *Chemical Physics Letters*. **2001**, *343*, 315–324.
- (277) Nowacka, M.; Fernandes, H.; Kiliszek, A.; Bernat, A.; Lach, G.; Bujnicki, J. M. Specific interaction of zinc finger protein Com with RNA and the crystal structure of a selfcomplementary RNA duplex recognized by Com. *PLoS ONE*. **2019**, *14*, 1–19.
- (278) Lu, X.-J.; Olson, W. K. 3DNA: a software package for the analysis, rebuilding and visualization of three-dimensional nucleic acid structures. *Nucleic Acids Research*. **2003**, *31*, 5108–5121.

- (279) Berendsen, H. J. C.; van der Spoel, D.; van Drunen, R. GROMACS: A message-passing parallel molecular dynamics implementation. *Computer Physics Communications*. **1995**, *91*, 43–56.
- (280) Pronk, S.; Páll, S.; Schulz, R.; Larsson, P.; Bjelkmar, P.; Apostolov, R.; Shirts, M. R.; Smith, J. C.; Kasson, P. M.; van der Spoel, D.; *et al.* GROMACS 4.5: a high-throughput and highly parallel open source molecular simulation toolkit. *Bioinformatics*. **2013**, *29*, 845–854.
- (281) van der Spoel, D.; Lindahl, E.; Hess, B.; Groenhof, G.; Mark, A. E.; Berendsen, H. J. C. GROMACS: fast, flexible, and free. *Journal of Computational Chemistry*. **2005**, *26*, 1701–1718.
- (282) Abraham, M. J.; Murtola, T.; Schulz, R.; Páll, S.; Smith, J. C.; Hess, B.; Lindahl, E. GROMACS: High performance molecular simulations through multi-level parallelism from laptops to supercomputers. *SoftwareX*. **2015**, *1-2*, 19–25.
- (283) Best, R. B.; Zhu, X.; Shim, J.; Lopes, P. E. M.; Mittal, J.; Feig, M.; Mackerell, A. D., JR. Optimization of the additive CHARMM all-atom protein force field targeting improved sampling of the backbone  $\phi$ ,  $\psi$  and side-chain  $\chi_1$  and  $\chi_2$  dihedral angles. *Journal of Chemical Theory and Computation*. **2012**, *8*, 3257–3273.
- (284) Denning, E. J.; Priyakumar, U. D.; Nilsson, L.; Mackerell, A. D. Impact of 2'-hydroxyl sampling on the conformational properties of RNA: update of the CHARMM all-atom additive force field for RNA. *Journal of Computational Chemistry*. **2011**, *32*, 1929–1943.
- (285) Hagelueken, G.; Abdullin, D.; Schiemann, O. mtsslSuite: Probing Biomolecular Conformation by Spin-Labeling Studies. *Methods in Enzymology*. **2015**, *563*, 595–622.
- (286) Hagelueken, G.; Abdullin, D.; Ward, R.; Schiemann, O. mtsslSuite: In silico spin labelling, trilateration and distance-constrained rigid body docking in PyMOL. *Molecular Physics*. **2013**, *111*, 2757–2766.
- (287) Hagelueken, G.; Ward, R.; Naismith, J. H.; Schiemann, O. MtsslWizard: In Silico Spin-Labeling and Generation of Distance Distributions in PyMOL. *Applied Magnetic Resonance*. **2012**, *42*, 377–391.
- (288) Vicino, M. F. Conformational studies of the P2 stem loop of the guanidine-II riboswitch from *Pseudomonas aeruginosa*. *Master Thesis*, Rheinische Friedrich-Wilhelms Universität, Bonn. **2018**.

- (289) Woodson, S. A.; Koculi, E. Analysis of RNA Folding by Native Polyacrylamide Gel Electrophoresis. *Methods in Enzymology*. **2009**, *469*, 189–208.
- (290) Höbartner, C.; Ebert, M.-O.; Jaun, B.; Micura, R. RNA-Konformationsgleichgewichte und der Einfluss der Methylierung von Nucleobasen auf die Gleichgewichtslage. *Angewandte Chemie*. **2002**, *114*, 619–623.
- (291) Micura, R.; Höbartner, C. On secondary structure rearrangements and equilibria of small RNAs. *ChemBioChem*. **2003**, *4*, 984–990.
- (292) Tanaka, Y.; Hori, T.; Tagaya, M.; Sakamoto, T.; Kurihara, Y.; Katahira, M.; Uesugi, S. Imino proton NMR analysis of HDV ribozymes: nested double pseudoknot structure and Mg<sup>2+</sup> ion-binding site close to the catalytic core in solution. *Nucleic Acids Research*. **2002**, *30*, 766–774.
- (293) Wacker, A.; Buck, J.; Mathieu, D.; Richter, C.; Wöhnert, J.; Schwalbe, H. Structure and dynamics of the deoxyguanosine-sensing riboswitch studied by NMR-spectroscopy. *Nucleic Acids Research*. **2011**, *39*, 6802–6812.
- (294) Müller, M. Structure investigations on the P1 stem-loop of the guanidine-II riboswitch from *Pseudomonas Aeruginosa* in dependence of guanidine. *Bachelor Thesis*, Rheinische Friedrich-Wilhelms Universität, Bonn. **2018**.
- (295) Reiss, C. W. Structural basis for functional versatility in riboswitches. *Dissertation*, Yale University, New Haven, CT. **2018**.
- (296) Hagens, T. von; Polyhach, Y.; Sajid, M.; Godt, A.; Jeschke, G. Suppression of ghost distances in multiple-spin double electron-electron resonance. *Physical Chemistry Chemical Physics*. **2013**, *15*, 5854–5866.
- (297) Freisinger, E.; Sigel, R. K.O. From nucleotides to ribozymes—A comparison of their metal ion binding properties. *Coordination Chemistry Reviews*. **2007**, *251*, 1834–1851.
- (298) Sigel, A.; Sigel, H.; Sigel, R. K. O., Eds. *Interplay between Metal Ions and Nucleic Acids*, 1. Aufl.; Metal Ions in Life Sciences, 10; Springer: Dordrecht **2012**.
- (299) Wittig, M. Ermittlung von Mangan(II)-Bindungsstellen an der P2-Haarnadel des Guanidin-2 Riboswitches. *Bachelor Thesis*, Rheinische Friedrich-Wilhelms Universität, Bonn. **2019**.
- (300) Stockmeier, M. Bindung von Mangan(II) an den P2 Hairpin des Guanidin-II Riboswitches, untersucht anhand von Elektronen Paramagnetischer Resonanz

- Spektroskopie. *Bachelor Thesis*, Rheinische Friedrich-Wilhelms Universität, Bonn. **2019**.
- (301) Eaton, G. R.; Barr, D. P.; Eaton, S. S.; Weber, R. T. *Quantitative EPR: A Practitioners Guide*; Springer-Verlag Vienna: Vienna **2010**.
- (302) Hartmann, R. K.; Bindereif, A.; Schön, A.; Westhof, E., Eds. *Handbook of RNA Biochemistry*; Wiley-VCH: Weinheim **2014**.
- (303) Thermo Scientific. NanoDrop 1000 Spectrophotometer. **2010**, *Thermo Fisher Scientific, Wilmington, DE*, User's Manual Version 3.8.
- (304) Rosenbach, H.; Borggräfe, J.; Victor, J.; Wuebben, C.; Schiemann, O.; Hoyer, W.; Steger, G.; Eitzkorn, M.; Span, I. Influence of monovalent metal ions on metal binding and catalytic activity of the 10-23 DNAzyme. *Biological Chemistry*. **2020**, *402*, 99-111.